TESIS DE LA UNIVERSIDAD DE ZARAGOZA

2013

107

Carlos Borau Zamora

# Multiscale computational modeling of single cell migration in 3D

Departamento
Ingeniería Mecánica

Director/es
García Aznar, José Manuel
Kamm, Roger



ISSN 2254-7606

Prensas de la Universidad
Universidad Zaragoza

Universidad Zaragoza
1542

Tesis Doctoral

# MULTISCALE COMPUTATIONAL MODELING OF SINGLE CELL MIGRATION IN 3D


Autor

Carlos Borau Zamora

Director/es

García Aznar, José Manuel
Kamm, Roger

**UNIVERSIDAD DE ZARAGOZA**

Ingeniería Mecánica


2013

# Multiscale computational modeling of single cell migration in 3D

DISSERTATION

*submitted in partial satisfaction of the requirements for the degree of*

DOCTOR OF PHILOSOPHY

*in Computational Mechanics*

*by*

**Carlos Borau Zamora**

*Faculty advisors*

**José Manuel García Aznar**

**Roger D. Kamm**

*Multiscale in mechanical and biological engineering*

*Aragon Institute of Engineering Research*

*Department of Mechanical Engineering, University of Zaragoza*

*Spain*

*&*

*Departments of Biological and Mechanical Engineering, Massachusetts Institute of Technology*

*United States of America*

*Zaragoza, September 2013*

*To learn something new, take the path that you took yesterday.*

*~John Burroughs*

# SINOPSIS

La migración celular es un proceso complejo, orquestado por factores químicos y biológicos, por la microestructura y por las propiedades mecánicas de la matriz extracelular. Este fenómeno es fundamental para el desarrollo de tejidos en los organismos pluricelulares, y como seres humanos, nos acompaña durante toda la vida, desde el mismo momento de la concepción hasta la muerte. Juega un papel fundamental durante el desarrollo embrionario determinando la formación de los diferentes órganos (morfogénesis) y es clave en todos los procesos regenerativos como la renovación de la piel, la respuesta inflamatoria o la cicatrización de heridas. Sin embargo, también contribuye al desarrollo de procesos patológicos como la metástasis, el retraso mental, la osteoporosis o enfermedades vasculares entre otros. Es por ello de vital importancia el conocer los mecanismos fundamentales que controlan la migración celular con el fin de tratar de manera efectiva las diferentes patologías, así como avanzar en el trasplante de órganos y el desarrollo de tejidos artificiales. Así pues, el objetivo de esta Tesis es el desarrollo de modelos a distintas escalas y centrados en diversos aspectos de la migración, de manera que faciliten la compresión de fenómenos específicos y sirvan como guía para el diseño de experimentos. Dada la complejidad y las grandes diferencias respecto a la migración colectiva, todos los modelos y análisis de esta Tesis se centran en células individuales.

En primer lugar se ha estudiado la migración tridimensional de una célula individual embebida en una matriz extracelular donde su velocidad y orientación se consideran reguladas por estímulos mecánicos. Para ello se ha desarrollado un modelo mecanosensor basado en elementos finitos y se ha analizado el comportamiento celular en función de diferentes rigideces y condiciones de contorno a escala celular. A medida que el trabajo ha progresado, los resultados del modelo unidos a nuevos avances científicos publicados en este ámbito, han reforzado la idea de que el mecansimo mecanosensor juega un papel crítico en los procesos que dirigen la migración celular. Por ello, se ha necesitado un estudio más profundo de este fenómeno para lo que se ha utilizado un modelo mucho más detallado a escala intracelular.

Así pues, se ha explorado la estructura interna del citoesqueleto y su comportamiento ante cambios mecánicos en la matriz extracelular, utilizando un modelo discreto de partículas basado en dinámica Browniana con el que se ha simulado la formación de una red de actina (polimerización) entrecruzada con proteínas y motores

moleculares. En concreto, se ha estudiado el comportamiento activo de estos motores y su papel como sensores de estímulos mecánicos externos (mecanosensores) de manera que los resultados obtenidos con este modelo "micro" han permitido validar las hipótesis del modelo previo. Consecuentemente, se ha revisado el modelo mecánico y se le ha añadido dependencia temporal, obteniendo un modelo continuo capaz de predecir respuestas celulares macroscópicas basadas en el comportamiento de los componentes microestructurales. En otras palabras, esta simplificación ha permitido la introducción de la respuesta macroscópica emergente obtenida del comportamiento dinámico de la microestructura, disminuyendo enormemente el coste computacional y por tanto permitiendo simulaciones a mayores escalas espacio-temporales.

A continuación se han introducido las nuevas hipótesis en un modelo probabilístico de migración a escala celular basado en elementos finitos que permite al mismo tiempo el estudio de factores tanto a escala macroscópica (velocidades, trayectorias) como a escala celular (orientación, área de adhesión, tensiones celulares, desplazamientos de la matriz etc.). Adicionalmente, este modelo es sensible no sólo a la mecánica sino a las condiciones fluido-químicas del entorno, las cuales han sido analizadas igualmente mediante simulaciones por elementos finitos.

Con todo esto, los modelos desarrollados todavía no incluyen una descripción detallada de procesos importantes envueltos en la migración celular como la protrusión de la membrana, la polimerización de actina en el frente celular o la formación de adhesiones focales. Por lo tanto, para completar la Tesis, se ha desarrollado un modelo continuo basado en diferencias finitas que permite el estudio del comportamiento dinámico del lamelipodio y el papel fundamental que juegan la polimerización de actina, los motores moleculares y las adhesiones focales (FAs) en el frente celular durante la migración.

**Palabras clave:** mecanobiología, simulación computacional, elementos finitos, mecanosensor, migración celular, citoesqueleto, redes de actina, motores moleculares, polimerización, lamelipodio.

# ABSTRACT

Cell migration is a complex process, orchestrated by biological and chemical factors, and by the microstructure and extracellular matrix (ECM) mechanical properties among others. It is essential for tissue development in multicellular organisms, and as human beings, it accompanies us throughout life, from conception to death. It plays a major role during embryonic development, defining organ formation (morphogenesis) and being crucial in all the regenerative processes such as skin renewal, inflammatory response or wound healing. However, it is also involved in several pathological processes e.g. metastasis, mental retardation, osteoporosis or vascular diseases. Therefore, understanding the fundamental mechanisms controling cell migration is vitally important to effectively treat different pathologies and to make progress in organ transplantation and tissue development. Thus, the main scope of this Thesis is the development of mathematical models at different scales and focused on different aspects of cell migration so that specific phenomena can be better understood, serving as a guide for the development of new experiments. All the models and analysis contained in this thesis are focused on single cells, firstly due to the complexity and marked differences with respect to collective cell migration, and secondly owing to the importance of individual migration in important processes such as metastatic tumor cell migration. In addition, since three-dimensional environments are physiologically more relevant, 3D approaches have been considered in most of the models here developed to better mimic *in vivo* conditions.

Firstly, single cell migration of a cell embedded in a three-dimensional matrix was studied, regulating its velocity and polarization through mechanical clues. For this purpose, a finite element (FE) based *mechanosensing* model was developed, analyzing cell behavior according to different ECM rigidities and boundary conditions at the cell scale. As work advanced, results from the model together with recent findings from literature strengthened the idea that *mechanosensing* plays a critical role in cell motility driving processes. For this reason, a deeper understanting of this mechanism was needed, resulting in the development of a specific and more detailed model (at the intracellular scale).

Hence, the cytoskeletal structure response to mechanical stimuli has been explored using a discrete particle-based Brownian dynamics model. This model was used to simulate the formation of actin networks (through actin polymerization) cross-linked with proteins (ACPs) and molecular motors. Specifically, the active role of molecular motors

and their role as mechanosensors were studied, so that the results of the intracellular scale approach allowed the validation of the previous model main assumptions. As a consequence, the mechanical hypothesis were revised and a temporal dependence was incorporated, obtaining a new continuum model able to predict macroscopic cell responses based on microstructural components behavior. In other words, this simplification allowed introducing the emergent macroscopic response obtained from the active behavior of the microstructure, saving large amounts of computational time and permitting simulations at higher time and length scales.

Next, the new hypotheses were incorporated into a probabilistic, FE-voxel-based cell-scale migration model, permitting simultaneously the study of macro-scale factors (velocities, trajectories) and cell-scale ones (polarization, adhesion area, cell stress, ECM displacements etc.). Additionally this model includes the effect of fluid-chemical stimuli, which was also analyzed by means of FE-simulations.

With all this, the developed models still lacked a detailed description of important processes involved in cell migration such as membrane protrusion, actin polymerization or focal adhesion (FA) formation. As a result, a continuum model was designed to study the lamellipodium dynamics and the major role of actin polymerization and focal adhesions (FA) at the cell front during cell migration.

# AGRADECIMIENTOS

Quisiera comenzar expresando un profundo agradecimiento a mis directores de Tesis Roger y Manu, no sólo por su apoyo en el ámbito científico sino también por su cercanía y amistad personal. Sin su supervisión este trabajo no habría sido posible.

No me olvido de Mariángeles, quien me acogió por primera vez y me guió durante los primeros pasos en el mundo de la investigación.

A todo el departamento en general, por su ayuda desinteresada y por compartir mi obse… afición por el pádel. Por supuesto a Joan, Antonio y Alberto por el soporte informático. Ciertamente todas las simulaciones contenidas en este libro serían inconcebibles sin la ayuda del cluster. *Signal~9* y *segmentation fault* serán los nombres de mis próximas mascotas.

Especial mención merecen Belen, Clara, Dieguito, Fares, Myriam, Noelia, Sara, Sergio y Pablo, mis amigos y compañeros de batalla. Juntos hemos vivido grandes momentos dentro y fuera de la sala. Espero compartir muchos más.

A mi *pandilla* de oscenses, porque aunque todavía siguen preguntando de qué va mi trabajo seguimos unidos después de tantos años.

A mi abuela, primos, tíos y toda mi familia. No todos están hoy aquí pero no pasa un día sin que me acuerde de los ausentes. A vosotros, y especialmente a ellos, dedico esta Tesis.

A la nueva incorporación, Enriquín, que pronto podrá leer ya estas líneas.

A mis padres, porque todo lo que soy hoy os lo debo a vosotros. Por no haberme fallado ni una vez en 28 años. Por vuestro apoyo incondicional. Esta Tesis es también vuestra.

No podría cerrar los agradecimientos sin nombrar a Iria, mi Constante. Porque esto no ha hecho más que empezar. Simplemente gracias por ser como eres y hacerme feliz.

# ACKNOWLEDGEMENTS

I would like to deeply thank you Roger, not only for your wisdom and guidance during my PhD, but also for your kindness and friendship. This thesis wouldn't have been possible without you. Also thanks to you, Ben. I will miss those programming sessions.

To Taeyoon, my coding guide and *"master"*.

To Tamara, Bill, Vivek, Ioannis, Sebastien, Andrish, Alfonso, Andrea, Nick, Ingo, Navid, Vera, Richard, Janine, Julian, Lena, Kai… we shared short but good times. I hope we keep in touch and wish you all the best.

# CONTENTS-INDICE

# LIST OF FIGURES

## MAIN CHAPTERS

**APPENDIX A**

**APPENDIX B**



**APPENDIX C**

# LIST OF TABLES

# Multiscale computational modeling of single cell migration in 3D

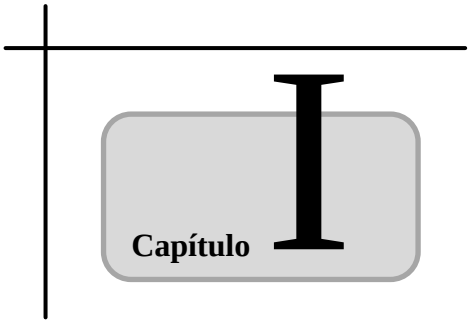


# RESUMEN

De acuerdo con la normativa vigente para la obtención del doctorado europeo (art. 15 RD 99/2011), se incluye en este capítulo inicial un resumen en castellano de los aspectos principales de la presente Tesis, entre los que se detallan: las motivaciones y objetivos principales, la organización de la misma, las conclusiones y el desarrollo futuro. Así mismo se presentan las contribuciones científicas aportadas durante el período de realización de la Tesis.

**Contenido**

# I.1. Motivación

La principal motivación de esta Tesis es el desarrollo de una metodología de simulación numérica para el modelado de la migración celular que ayude a comprender su papel en procesos patológicos críticos como la regeneración de heridas o la metástasis del cáncer. El término "modelo" significa que algunas características cualitativas o cuantitativas del proceso real que se pretende simular son abstraídas, idealizadas y simplificadas para ser descritas matemáticamente. Esta abstracción, sin embargo, necesita validación experimental. Aunque los experimentos de cultivo celular convencionales son útiles para investigar ciertas funciones biológicas, los recientes avances en técnicas de microcultivo han abierto el camino de la nueva generación de ensayos *in vitro*. Los dispositivos de microfluídica están ganando popularidad debido a su capacidad única de controlar espacial y temporalmente factores biofísicos y bioquímicos en un cultivo. Estos sistemas se pueden usar para el estudio *in vitro* de numerosos fenómenos como la angiogénesis, el cultivo de tejido orgánico o la migración de células tumorales, además de permitir la obtención de imágenes de alta calidad en tiempo real.

Por tanto, el objetivo de este trabajo es la investigación de cómo las condiciones del entorno extracelular guían la migración de la misma, cuantificando los efectos de la rigidez, el fluido intersticial o gradientes químicos, combinando el uso de dispositivos de microfluídica con el modelado computacional. Un conocimiento más completo de estos mecanismos podría ayudar en el desarrollo de técnicas de terapia y diagnóstico, reduciendo así la experimentación animal.

Esta Tesis, cuenta con una Beca FPI para el desarrollo de la misma (BES-2010-029927). Además, el trabajo ha formado parte del Proyecto Nacional titulado: "Modelado del efecto de la mecánica celular en la migración celular", financiado por el Ministerio de Ciencia e Innovación (DPI 2009-14115-CO3-01). Este proyecto se ha renovado y extendido al también Proyecto Nacional: "Modelado multiescala para la simulación predictiva de la migración celular en 3D: el papel de la interacción célula-matriz", financiado actualmente por el Ministerio de Economía y Competitividad (DPI2012-38090-C03-01).

Finalmente, en este contexto, esta Tesis se desarrolla como parte del proyecto europeo INSILICO-CELL-*Predictive modelling and simulation in mechano-chemo-biology: a computer multi-approach* (European Union Starting Grant / ERC-2012-StG - Proposal 306571), cuyo propósito fundamental es el estudio de las interacciones célula-célula y célula-matriz, así como la microfabricación de tejidos *in vitro* con tres

aplicaciones principales: regeneración de heridas, angiogénesis y remodelación ósea. Para conseguir esto, se propone un retroalimentación contínua entre diseño experimental y modelado computacional.

A continuación se describe brevemente la importancia del estudio de la migración celular así como el estado del arte de la experimentación y modelado de procesos relacionados.

### I.1.1. Migración celular

La migración celular ha ido ganando un gran protagonismo en los últimos años debido a su papel fundamental en varios procesos fisiológicos o patológicos de importancia como la morfogénesis, la respuesta inflamatoria, la regeneración de heridas o la metástasis del cáncer (Lauffenburger and Horwitz, 1996). De hecho, los problemas de salud pública relacionados con la migración son una fuente de preocupación creciente a nivel mundial. Por ejemplo, las heridas infectadas no solo se recuperan más lentamente sino que impiden el injerto de tejido sano y pueden provocar sepsis (síndrome de respuesta inflamatoria sistémica)(Atiyeh et al., 2005). Las heridas crónicas contribuyen a la morbidez e incluso a la muerte. Otro ejemplo bien conocido es el cáncer, una de las principales causas de muerte en el mundo. En 2008, 7.6 millones de personas murieron de cáncer (13% del total), una cifra que se prevé crezca hasta los 13.1 millones de muertes en 2030 (www.who.int). La comprensión de porqué las células cancerígenas se desplazan desde la masa tumoral inicial al sistema circulatorio, de cómo los leucocitos migran a las áreas afectadas en procesos de inflamación, o los mecanismos que dirigen a los fibroblastos y a las células endoteliales para regenerar una herida, es clave para el desarrollo de terapias, la efectividad del transplante de órganos o la fabricación de tejidos artificiales.

A lo largo de la última década, se han hecho enormes progresos en cuanto al entendimiento de procesos y mecanismos implicados en la migración celular, incluyendo la formación de estructuras polares, la regulación de procesos dinámicos como la polimerización de actina o microtúbulos, y la regulación espacial y temporal de la señalización celular (Ridley et al., 2003). La manera en que las células migran y responden a un micro-entorno 3D es un proceso multiescala que resulta de la integración de los efectos producidos por las propiedades de la matriz extracellular en los componentes de la célula a través del citoesqueleto. Este proceso de integración depende

de multiples factores: mecánicos, químicos y biológicos entre otros (Cukierman et al., 2002, Even-Ram and Yamada, 2005, Zaman et al., 2006). Por ejemplo, la influencia de la deformación de un sustrato (*Tensotaxis*), su rigidez y topografía (*Durotaxis*) han sido ampliamente investigadas (Beloussov et al., 2000, Lo et al., 2000, Saez et al., 2007, Baker et al., 2009, Hakkinen et al., 2011), mostrando que las células tienden a migrar hacia zonas de la matriz con mayores deformaciones o de mayor rigidez, donde las adhesiones focales son más estables y permiten la generación de mayores esfuerzos (Lo et al., 2000, Cukierman et al., 2001, Schwarz and Bischofs, 2005). Las células también responden a gradientes químicos (*Chemotaxis*) en el tejido o fluido circundantes (Rappel et al., 2002, Zhelev et al., 2004), moviéndose hacia la fuente o alejándose de ella según la sustancia. Además, las células individuales de una monocapa tienden a orientarse en la dirección local de máxima tensión normal transmitida a través de múltiples uniones célula-célula (*Plithotaxis*)(Trepat and Fredberg, 2011). Gradientes de potencial eléctrico (*Galvanotaxis*), condiciones del fluido o gradientes de concentración de ligandos (*Haptotaxis*) son guías adicionales de la migración celular actualmente bajo intenso estudio (Zhao et al., 2002, Curtze et al., 2004, Li et al., 2005, Hofmann et al., 2006, Polacheck et al., 2011). Entender la migración como un proceso integrado requiere la consideración de múltiples estructuras formadas a su vez por numerosos elementos que interaccionan y se coordinan entre sí espacial y temporalmente. Sólo cuando esta integración sea completamente comprendida y tenida en cuenta, la alteración genética o la utilización de fármacos podrán ser realmente eficaces, con el consecuente impacto en los tratamientos de enfermedades conocidos hasta ahora.

## I.1.2. Experimentación

Gracias al desarrollo de nuevas técnicas y tecnologías, la experimentación sobre migración celular se ha acelerado notablemente en los últimos años. Aún así, el aislamiento de los efectos producidos por un estímulo concreto *in vivo* todavía presenta numerosas dificultades. A consecuencia de ello, los ensayos *in vitro* han emergido como potentes herramientas para el estudio de la movilidad celular, permitiendo examinar factores específicos implicados en la migración. Debido a la vital importancia del cáncer, estos ensayos *in vitro* se utilizan de manera extendida para intentar entender los mecanísmos que conducen el movimiento de las células tumorales (normalmente

estímulos mecánicos y químicos) con el objetivo de mejorar la eficacia de las terapias que se utilizan actualmente.

El micro-entorno de un tumor está normalmente formado por una red dinámica de proteínas extracelulares bañadas en fluido intersticial así como grupos de células asociadas que incluyen fibroblastos, células endoteliales o derivadas de la médula osea (revisado en (Joyce and Pollard, 2009)). Estas células conectivas remodelan la matriz generando señales mecánicas y químicas que reciben las células tumorales. Debido a la naturaleza dinámica y a la variedad de componentes que conforman este micro-entorno, la investigación de estímulos individuales es realmente compleja y requiere que las propiedades mecánicas y químicas puedan ser adaptadas con precisión y repetibilidad. Los ensayos *in vitro* proporcionan dicho control y están específicamente preparados para el estudio de factores particulares de interés. A continuación se muestra como ejemplo una breve clasificación de los diferentes métodos experimentales utilizados en la actualidad (Polacheck et al., 2012):

(i) **Ensayos de micropipeta:** un micro-manipulador se usa para inyectar soluciones químicas en los alrededores de la célula o para inyectar factores de crecimiento. Los gradientes generados, sin embargo, son transitorios y difíciles de cuantificar (Soon et al., 2005).

(ii) **Cámaras de Boyden (o Transwell):** una membrana rígida y porosa se coloca entre dos cámaras de cultivo. Las células se colocan en suspension en la cámara superior y migran a través del filtro en respuesta a un gradiente químico generado por la diferencia de concentraciones entre los medios superior e inferior (Boyden, 1962).

(iii) **Micropatrones:** las células se cultivan sobre patrones de diferente geometría, tamaño y tipo de superficie en sustratos 1D, 2D y 3D. Estos ensayos ofrecen escalabilidad y la posibilidad de cultivar grandes poblaciones de células. Sin embargo, no suelen incluir flujo y la aplicación de estímulos mecánicos o químicos localizados no es generalmente posible (von Philipsborn et al., 2006).

(iv) **Ensayos de durotaxis:** las células se cultivan sobre sustratos planos de rigidez variable donde la respuesta celular (fuerzas de tracción, area de adhesion y dirección de migración) se monitoriza a lo largo del tiempo (Lo et al., 2000).

(v) **Ensayos de regeneración de heridas:** la migración colectiva de células se puede estudiar generando espacios vacíos (heridas) en una capa de células, donde las dinámicas de cierre (velocidad, morfología, etc) pueden ser monitorizadas. Estos ensayos están típicamente limitados a sustratos 2D con condiciones uniformes, aunque diferentes gradientes podrían ser creados mediante técnicas de microfabricación (Simpson et al., 2008).

(vi) **Ensayos en matrices 3D:** los biomateriales de última generación permiten la creación de entornos 3D con características físicas y químicas modificables y controlables. Las células se cultivan en un medio 3D y migran dependiendo de la arquitectura, la rigidez, el tamaño de los poros, la concentración de ligandos etc. (Sabeh et al., 2009).

(vii) **Microfluidica:** avances recientes en tecnologías de fabricación han hecho posible la creación de microdispositivos que permiten el control del micro-entorno celular. Con estos aparatos, es muy sencillo establecer campos eléctricos, gradientes químicos y diferentes condiciones de flujo intersticial que pueden ser controlados y ajustados libremente en los diferentes microcanales que conforman el dispositivo (Chung et al., 2010, Polacheck et al., 2011).

En resumen, los ensayos con micropipeta, cámaras de Boyden y dispositivos de microfluídica permiten el control de gradiantes bioquímicos. Los ensayos de durotaxis, matrices 3D y nuevamente los dispositivos de microfluídica, facilitan el control de las características biofísicas como la rigidez de la matriz o el flujo intersticial. Por otro lado, los ensayos de regeneración de heridas y micropatrones permiten el control de las distancias intercelulares, mientras que sólo estos últimos ofrecen un control sobre la topografía del sustrato.

## I.1.3. Modelado de la migración celular

Existe una cantidad inmensa de trabajos computacionales y modelos matemáticos en relación con aspectos específicos o generales de la migración celular. De hecho, la importancia que ha demostrado en numerosas enfermedades y procesos patológicos ha supuesto una gran inversión, provocando que un gran número de matemáticos, ingenieros

y físicos hayan redireccionado sus investigaciones al campo de la biofísica celular. Como resultado, los detalles y la sofisticación de los modelos de migración han aumentado notablemente. Sin embargo, a pesar de que cada modelo ofrece características únicas, se pueden clasificar en tres grandes grupos dependiendo del principal área de interes: modelos de protrusión celular, modelos de adhesión y retracción, modelos de la célula completa. A continuación se describen brevemente los principios físicos básicos sobre los que se basa cada grupo, así como sus posibilidades e interacciones con otros modelos. En cualquier caso, diferentes publicaciones revisan ésta y otras posibles clasificaciones, ofreciendo una visión más amplia y balanceada del estado del arte de modelos biofísicos (Flaherty et al., 2007, Carlsson and Sept, 2008, Rangarajan and Zaman, 2008, Mogilner, 2009).

**Modelos de protrusión celular**

La protrusión es probablemente el fenómeno más estudiado y mejor comprendido de todas las fases de la migración celular. Como se ha dicho anteriormente, el evento clave de la migración basada en actina es la polimerización de filamentos contra la membrana celular. Muchos trabajos matemáticos se han centrado en este tema, aunque pueden distinguirse según si consideran un único o múltiples filamentos de actina o si usan una aproximación contínua (Carlsson and Sept, 2008).

Los modelos de un único filamento pueden identificar mecanismos plausibles para la generación de esfuerzos, prediciendo la fuerza de saturación y estableciendo una relación de fuerza-velocidad. Normalmente consideran el crecimiento del filamento por difusión de monómeros de actina. Fluctuaciones Brownianas de la membrana y del extremo del filamento crean huecos que son rellenados por nuevos monómeros. De hecho, si la concentración de monómeros es suficientemente alta, su incorporación impide que la membrana vuelva a su posición original, un proceso conocido como “rueda Browniana” (Brownian-ratchet) (Peskin et al., 1993). Estos tipos de modelos han sido extendidos para incluir conexiones entre los extremos de los filamentos y la membrana, lo cual puede establecer nuevos mecanismos en la generación de fuerzas afectando a la relación de fuerza-velocidad (Dickinson and Purich, 2002, Zhu and Carlsson, 2006).

Los modelos de múltiples filamentos tratan la polimerización simultánea de muchos filamentos, incluyendo las interacciones entre ellos y con las proteínas de entrecruzamiento. La propulsión de patógenos intracelulares y la protrusión del lamelipodio y los filopodios celulares han sido los problemas que mayor atención han

recibido en este tipo de modelos. Por ejemplo, los filopodios y los entramados de actina empujando contra la membrana (Atilgan et al., 2005, Atilgan et al., 2006) o el movimiento de obstáculos debido al crecimiento de una red de actina (Carlsson, 2001) han sido estudiados con modelos que incluyen procesos a nivel molecular como el crecimiento de los filamentos de actina en los extremos positivos y la depolimerización en los negativos, la formación de ramas, su ruptura etc. Aproximaciones incluso más detalladas tienen en cuenta las interacciones de la actina con los obstáculos que se encuentra o la variación espacial de la concentración de la misma (Alberts and Odell, 2004).

Los modelos continuos describen el entramado de actina utilizando parámetros más simples como la concentración o el número de filamentos en contacto con la membrana. Estos métodos permiten predecir comportamientos de sistemas mucho más grandes y en escalas de tiempo mayores, a costa de tratar los eventos moleculares a partir de un comportamiento general promedio. Igual que en los modelos de múltiples filamentos, las aproximaciones contínuas se suelen centrar en la protrusión del lamelipodio o los filopodios celulares (Mogilner and Edelstein-Keshet, 2002, Dawes et al., 2006) así como la propulsión intracelular de patógenos (Gerbal et al., 2000, Mogilner and Oster, 2003). Sus predicciones incluyen las propiedades del dominio de actina como su grosor, su concentración, la relación fuerza-velocidad, la velocidad de protrusión durante la expansión del lamelipodio, las propiedades elásticas y difusivas de la membrana o la distribución de las longitudes de los filamentos y sus orientaciones, todas las cuales son observables experimentalmente.

**Modelos de adhesión-retracción**

A pesar del mayor dinamismo de los eventos que ocurren en el frente de avance celular, los mecanismos involucrados en la formación de adhesiones con el sustrato y la retracción de las zonas traseras son igualmente importantes. Aunque algunos tipos de células utilizan otros tipos de retracción, la retracción basada en miosina es la más común. De hecho la miosina II ha sido incluida en numerosos modelos como la causa principal de retracción y contracción celular (Ahmadi et al., 2005, Kruse et al., 2005). En cualquier caso, las fibras de estrés y los módulos contráctiles no pueden producir movimiento o esfuerzos sin una unión mecánica que los transmita al sustrato. Por tanto, la formación de adhesiones focales y la interacción célula-matriz han sido objeto de modelos, unos bajo la

premisa de que las fuerzas aplicadas sobre los filamentos tienen un efecto directo en la polimerización (Shemesh et al., 2005) y otros teniendo en cuenta la interacción entre las fibras de estrés y las integrinas (Novak et al., 2004).

**Modelos de célula completa**

Considerando el cuerpo celular completo existe una variedad de modelos tan amplia como los tipos posibles de célula. Estos modelos consideran normalmente fenómenos dinámicos y mecánicos incluyendo procesos explícitos a escala molecular como la polimerización de actina, o menos concretos como la desestabilización de adhesiones focales debida a fuerzas. Igualmente, la mecánica celular se puede tratar explícitamente o considerarse de forma fenomenológica. Los métodos pueden ser continuos (Gracheva and Othmer, 2004), discretos (Dokukina and Gracheva, 2010) o basados en elementos finitos (Bottino et al., 2002) entre otros. Además, diferentes niveles de detalle son incluidos en cada modelo, con escalas de tiempo y longitud muy diferentes entre ellos. Muchas de estas aproximaciones han estado comúnmente centradas en migración 2D, no sólo por simplicidad sino por la falta de datos de alta calidad en movimientos 3D. Sin embargo, el número de modelos 3D ha estado creciendo gradualmente, aunque con aproximaciones muy diversas. Algunas de ellas predicen la migración de células individuales (Zaman et al., 2005, Borau et al., 2011, Schluter et al., 2012) mientras otras simulan comportamientos colectivos (Ouaknin and Bar-Yoseph, 2009, Arciero et al., 2011). Según sus hipótesis principales se pueden clasificar en: modelos basados en fuerzas, modelos estocásticos, modelos de esferoides celulares, y estudios de Monte Carlo. En los primeros, la dinámica de migración se basa en el balance de fuerzas entre la parte trasera y delantera de la célula, así como en las fuerzas de protrusión y la fuerza de arrastre que se opone al movimiento debido a la viscosidad de la matriz (Zaman et al., 2005). El handicap de estos modelos es que sólo predicen la migración de células individuales y no tienen en cuenta cambios en la forma de la célula o en las propiedades de la matriz debido a la degradación. Por otro lado, los modelos estocásticos (o de caminos persistentes aleatorios) son capaces de predecir el movimiento de poblaciones (Parkhurst and Saltzman, 1992), pero no incluyen efectos dinámicos como las fuerzas de tracción o de arrastre, ni incorporan las propiedades del sustrato. Los modelos de multiesferoides celulares, se basan principalmente en gradientes de presión producidos por la proliferación y muerte de células (Pettet et al., 2001). Combinando movimientos aleatorios, presión y actividad química de los agregados celulares, estos modelos son

adecuados para el estudio de tumores, aunque no incluyen otros estímulos mecánicos importantes como la densidad, rigidez o porosidad de la matriz. Finalmente, los modelos de Monte Carlo que utilizan entramados cuadrados y un conjunto de reglas simples, permiten simulaciones muy rápidas, haciéndolos apropiados para el estudio de patrones migratorios a largo plazo (Zaman, 2007, Zaman et al., 2007). Su mayor problema es la naturaleza cualitativa de los parámetros estudiados como la polarización celular o los efectos mecánicos de la matriz.

## I.2. Objetivos y metodología

Basados en los argumentos expuestos hasta ahora, el objetivo de esta Tesis es el desarrollo de modelos númericos y computacionales para simular diversos aspectos de la migración como las interacciones célula-matriz o la respuesta mécanica de la célula en función de las condiciones del entorno. Con este propósito, a lo largo de la Tesis se han utilizado aproximaciones continuas, discretas y/o basadas en elementos finitos. El trabajo principal y los objetivos parciales se describen a continuación:

- Estudiar el efecto de factores mecánicos (rigidez del sustrato, geometría y condiciones de contorno) en la migración celular en matrices 3D. Esto implica el desarrollo de un modelo de elementos finitos macroscópico basado en el fenómeno mecanosensor que incluya las fases principales del ciclo migratorio.
- Explorar la estructura interna del citoesqueleto celular y su respuesta a la rigidez de la matriz extracelular. Se ha utilizado un modelo computacional de partículas basado en dinámica Browniana para polimerizar una red de actina tridimensional entrecruzada con proteínas. Además, se han incluido motores moleculares para analizar su comportamiento dinámico y su papel como elementos mecanosensores. A su vez, los resultados a escala micro se han utilizado para validar las hipótesis del modelo mecanosensor.
- Incorporar los hallazgos obtenidos con el modelo intracelular en el modelo macroscópico. La estabilización temporal de la red de actina provocada por el bloqueo gradual de los motores moleculares se introduce en el modelo mecanosensor a través de una función de regulación continua que reproduce la saturación de las fuerzas generadas por el sistema de actina-miosina.

- Estudiar las condiciones fluído-químicas a las que está sujeta una célula en un medio poroso, simulando para ello un sistema de microfluídica utilizando elementos finitos.
- Mejorar la comprensión de la respuesta celular a diversos factores simultáneos. Con este propósito, se ha desarrollado un modelo probabilístico de *voxels* basado en elementos finitos para simular la migración de una célula individual dependiendo de estímulos mecánicos y fluido-químicos.
- Analizar el comportamiento dinámico del lamelipodio celular, incluyendo el papel que juegan la Vinculina, los motores moleculares y las adhesiones focales en las funciones exploratorias de la célula, desarrollando para ello un modelo de diferencias finitas.

## I.3. Organización de la Tesis

La Tesis se estructura en siete capítulos y tres apéndices. Aunque los contenidos de cada capítulo son tratados individualmente, gran parte del material está interrelacionado y por lo tanto se requiere la consideración del trabajo en conjunto para apreciar el cuadro completo. Más específicamente la estructura de la Tesis se resume a:

**Capítulo I (actual):** contiene un resumen de la Tesis escrito en castellano que incluye los objetivos de la misma, la organización del documento, las conclusiones generales, las contribuciones científicas y las posibles líneas futuras.

**Capítulo 1:** es el capítulo equivalente al actual (en inglés) y sirve como introducción incluyendo el estado del arte, motivaciones, objetivos y organización de la tesis.

**Capítulo 2:** inicialmente presenta el fenómeno mecanosensor así como los modelos existentes que relacionan este proceso con la movilidad celular. Después describe un modelo de migración celular individual en 3D en el que se supone que el mecanismo mecanosensor es el principal regulador del movimiento direccional. A continuación se detallan las principales hipótesis, las fases consideradas (mecanosensora, de orientación del citoesqueleto y de migración) y los métodos numéricos utilizados. Finalmente se comparan los resultados obtenidos con experimentos de la bibliografía y se somete el modelo a un análisis de sensibilidad para comprender mejor su comportamiento.

**Capítulo 3:** introduce el papel dinámico del citoesqueleto celular en los procesos migratorios y describe la importancia de los motores moleculares en las redes de actina como elementos mecanosensores. Seguidamente, describe un modelo computacional de partículas basado en dinámica Browniana, detallando los métodos utilizados para la formación de las redes, la paralelización del problema y las condiciones de contorno consideradas. Para concluir se comparan los resultados computacionales con experimentos recientes.

**Capítulo 4:** está dedicado enteramente a la revisión de las hipótesis del modelo mecanosensor desarrollado en el Capítulo 2, introduciendo en la respuesta celular una dependencia temporal basada en los resultados obtenidos en el modelo de partículas descrito en el Capítulo 3. Esta nueva aproximación se utiliza para simular experimentos relacionados con la detección de la rigidez del sustrato, incluyendo cambios bruscos en la misma y la saturación de fuerzas en el equilibrio. Este capítulo incluye también un análisis de sensibilidad y describe la posibilidad de extensión del modelo teórico a geometrías 3D más complejas.

**Capítulo 5:** reúne las hipótesis consideradas hasta ahora y las incluye en un nuevo modelo de migración a escala celular. Este capítulo enfatiza la importancia de los múltiples estímulos que aparecen en entornos 3D y describe un modelo probabilístico basado en *voxels* y elementos finitos que simula la respuesta celular dependiendo de diversos factores como la rigidez de la matriz extracelular, la tensión, el flujo o las condiciones químicas. Primero presenta la simulación con elementos finitos de un dispositivo de microfluídica real. Después se evalúa el comportamiento de las funciones de probabilidad que determinan el comportamiento celular. Finalmente el capítulo resume las implicaciones del modelo y sus posibles aplicaciones.

**Capítulo 6:** describe el papel crítico de los componentes dinámicos del lamelipodio durante los ciclos de protrusión-retracción de la membrana celular. El capítulo comienza reseñando los últimos descubrimientos de las estructuras que conforman el frente celular así como los modelos existentes en relación al tema. A continuación, se presenta un modelo basado en diferencias finitas utilizado para validar experimentos de cualquier fenómeno involucrado en el lamelipodio en general, y de los efectos de la Vinculina en el flujo retrógrado de actina en particular.

**Capítulo 7:** cierra la Tesis con un resumen de todo el trabajo realizado incluyendo las conclusiones más relevantes de cada capítulo. Adicionalmente, presenta una lista con las contribuciones originales conseguidas (publicaciones y congresos) y propone una serie de líneas futuras para la continuación del trabajo.

## I.4. Resumen

El principal objetivo de la tesis es el desarrollo de modelos numéricos computacionales que permitan una mejor comprensión de los mecanismos que controlan la migración celular. Con este propósito, se han usado diversas aproximaciones contínuas, discretas o basadas en elementos finitos. Por ejemplo, para estudiar el efecto de los factores mecánicos (rigidez del sustrato, geometría y condiciones de contorno) sobre la migración en matrices tridimensionales, se ha desarrollado un modelo de migración de elementos finitos basado en el mecanismo mecanosensor incluyendo las fases principales del ciclo migratorio. Este modelo, descrito en el Capítulo 2, es capaz de simular el movimiento preferencial de una célula individual bajo diferentes condiciones mecánicas, prediciendo velocidades y patrones de migración similares a los obtenidos experimentalmente. En esta aproximación, el comportamiento mecánico de todo el cuerpo celular se simplifica a dos muelles en paralelo con un actuador en serie (equivalente a un tercer muelle precomprimido), lo cual implica un aumento de la fuerza ejercida por la célula conforme aumenta la rigidez del sustrato hasta alcanzar la saturación. Además, utilizando un balance de fuerzas junto con la hipótesis de que la fricción de la matriz aumenta con la rigidez (debido a mayores densidades del material), se captura el comportamiento bifásico de la velocidad migratoria. El modelo se ha utilizado también para simular un experimento concreto en el que una micro-aguja se introduce en el sustrato en los alrededores de la célula tirando o empujando hacia ella, modificando el estado tensional y, por tanto, provocando que la célula migre y se reoriente de una forma determinada. Las simulaciones sugieren que la célula en realidad no siente directamente las fuerzas, sino la tracción o compresión espacial de las zonas que la rodean causadas por cargas externas. Por tanto, si la micro-aguja estira el sustrato, las fuerzas contráctiles de la célula se oponen a las de la aguja, sintiendo una mayor rigidez en esa dirección y tendiendo a reorientarse y moverse ella. En cambio, si la micro-aguja empuja, la compresión de la célula ocurre en el mismo sentido que la de la aguja y por tanto siente menor rigidez y

tiende a huir de la aguja. El análisis de sensibilidad de los parámetros del modelo, sugiere que la rigidez de la actina es uno de los principales factores a la hora de determinar la respuesta celular. En una estructura más compleja como el cuerpo real de la célula, este papel corresponde a la organización del citoesqueleto. De hecho, se ha observado experimentalmente cómo algunas estructuras celulares (adhesiones focales, fibras de estrés, anillos de actina etc.) reaccionan a determinados cambios en las condiciones del entorno, adaptando por tanto el citoesqueleto a la nueva situación. Para entender mejor estos mecanismos, se requiere de aproximaciones más detalladas que modelen el citoesqueleto celular teniendo en cuenta sus principales componentes, lo que da paso al siguiente modelo descrito en el Capítulo 3.

Para explorar el papel de la estructura interna del citoesqueleto y su comportamiento dependiendo de la rigidez extracelular, se ha utilizado un modelo computacional de partículas basado en dinámica Browniana para polimerizar una red de actina 3D entrecruzada con proteínas, la cual ha sido sometida a diferentes simulaciones para comprobar sus propiedades contráctiles. Sólamente incluyendo la dinámica de los motores moleculares y las proteinas de entrecruzamiento, las redes de actina muestran comportamientos macroscópicos similares a observaciones experimentales, indicando que las propiedades microscópicas de los componentes individuales son las que gobiernan la respuesta global de la red completa. De hecho, se ha encontrado que los motores moleculares juegan un papel central como mecanosensores, demostrando que, además de otros factores complejos como la señalización bioquímica, la mecánica simple es uno de los posibles mecanismos determinantes en el fenómeno mecanosensor. Confirmando evidencias experimentales, el modelo predice que la tensión celular es proporcional a la rigidez del sustrato para matrices blandas y se satura para sustratos más rígidos. La existencia de esta transición puede explicarse mediante los mecanismos que provocan que los motores moleculares disminuyen su velocidad o se detengan por completo: (i) ausencia de puntos de unión libres con los filamentos de actina, (ii) saturación por fuerzas elevadas, (iii) llegada al extremo del filamento de actina. Se ha demostrado aquí que sólo una pequeña fracción de motores llega a los extremos de los filamentos para todo el rango de rigideces de sustrato estudiado, ejerciendo por tanto poca influencia en el fenómeno de saturación. Por otro lado, el bloqueo por ausencia de puntos de unión es especialmente importante en rigideces bajas, debido principalmente al aumento de densidad y aglomeramiento de estructuras que se produce en sustratos demasiado blandos donde las deformaciones son apreciables. Para sustratros rígidos, sin embargo, las deformaciones

son más bajas y los motores se bloquean rápidamente debido a las altas tensiones a los que se ven sometidos. Por tanto, para altas rigideces el mecanismo predominante es la saturación por fuerzas mientras que para bajas rigideces es la ausencia de puntos de unión libres, siendo esta transición el mecanismo que controla el mecanismo mecanosensor celular. De hecho, este mecanismo se ha confirmado con simulaciones adicionales variando la longitud de los filamentos de actina así como su concentración. En resumen, este trabajo predice uno de los posibles mecanismos con los que las células modulan sus propiedades y responden a su entorno mediante la contracción del citoesqueleto. Aunque el modelo se basa en procesos a nivel molecular, el comportamiento macroscópico de redes activas de actina concuerda bien con observaciones experimentales y sirve de validación para las hipótesis del modelo mecanosensor previo. Además, el modelo de partículas puede ser utilizado para el estudio de gran variedad de fenómenos relacionados con la actina como la rigidización/ablandamiento del citoesqueleto (*stiffening/softening*), la fluidización de las redes o la formación de anillos durante la citokinesis entre otros. Sin embargo, aunque el modelado detallado facilita análisis muy específicos y precisos, también conlleva un coste computacional elevado. Por ejemplo, una sola simulación de un pequeño dominio y utilizando 8 CPUs en paralelo puede llegar a durar varias semanas, un tiempo demasiado grande para estudiar la migración de una célula ya que la simulación tardaría más que el experimento real. Por tanto, una ley fenomenológica capaz de reproducir las características macroscópicas del citoesqueleto se hace necesaria.

Para incorporar los resultados obtenidos en las simulaciones micro-escala (intracelulares) en las hipótesis macro-escala (a nivel celular), la estabilización temporal de la red de actina producida por el bloqueo de motores moleculares se ha introducido en el modelo mecanosensor mediante una función regulatoria contínua que reproduce el incremento de fuerza y su posterior saturación. Esta suposición, descrita en el Capítulo 4, ha permitido realizar simulaciones de segundos de duración en vez de semanas, haciendo la aproximación viable para su incorporación en modelos de elementos finitos con mayores escalas de longitud y tiempo. A pesar de su simplicidad, el modelo es capaz de simular múltiples condiciones mecanosensoras y sus predicciones presentan una buena correspondencia con experimentos y con los resultados computacionales del modelo de partículas de redes de actina. Como anteriormente, esto sugiere que aunque la señalización intracelular u otros fenómenos químicos complejos juegan un papel importante, el proceso mecanosensor depende directamente de la mecánica. Igual que en el modelo descrito en el Capítulo 2, el cuerpo completo de la célula se representa con dos

muelles en paralelo y un actuador en serie, esta vez con una contracción dependiente del tiempo. En otras palabras, este actuador es equivalente a un muelle precomprimido cuya longitud de equilibrio se va acercando a cero mediante una función temporal. Esta configuración tri-muelle, permite distinguir entre la respuesta activa y pasiva de la célula. Mecánicamente, la adición de la rigidez de la actina en serie con el actuador de miosina permite capturar la linealidad de la fuerza celular con la rigidez del sustrato para sustratos blandos y su saturación para sustratos más rígidos. Además, los valores relativos entre la rigidez de actina y los componentes pasivos del citoesqueleto regulan el comportamiento de la célula bajo diferentes condiciones, jugando la rigidez de la actina un papel predominante especialmente en sustratos duros. Por otro lado, esta separación entre componentes activos y pasivos del citoesqueleto permite la simulación de fenómenos más complejos que los afectan por separado, como por ejemplo la rigidización de las fibras de estrés, la ruptura de la red por depolimerización, el corte de filamentos mediante proteínas especializadas etc. Finalmente, se ha analizado la respuesta mecánica de la célula ante cambios bruscos en la rigidez del sustrato, encontrando que la reacción celular ocurre instantáneamente e indicando por tanto que la adaptación del citoesqueleto es en este caso un proceso puramente mecánico, como sugieren los experimentos y de acuerdo con las hipótesis del modelo. La precisión de los resultados obtenidos sugieren que una aproximación 1D es suficiente para modelar al menos el simple ensayo experimental propuesto, sin embargo, la implementación de esta teoría en 3D y en combinación con modelos de migración puede suponer un avance para el desarrollo futuro de modelos con aplicaciones en regeneración de heridas, ingeniería de tejidos o metástasis del cáncer. De hecho, ya que la migración celular requiere la integración de múltiples procesos, este tipo de modelos deberían incluir efectos adicionales a los puramente mecánicos, como por ejemplo las condiciones químicas o de flujo intersticial.

Con esto en mente, se ha desarrollado un modelo fenomenológico probabilista basado en *voxels* y elementos finitos para simular la migración 3D de una célula individual. A través de una serie de funciones de probabilidad y combinando diferente software, el modelo es capaz de predecir la migración teniendo en cuenta diferentes factores entre los que se encuentran: las propiedades mecánicas de la matriz extracelular, gradientes químicos, flujo y condiciones de contorno. Para estudiar las condiciones fluído-químicas que rodean la célula en un medio poroso, se ha simulado mediante elementos finitos un dispositivo de microfluídica completo. Después, los resultados de este análisis se han extraído e interpolado a una malla más fina compuesta de *voxels*,

donde finalmente se han computado el análisis mecánico y la migración. Como ya se ha comentado anteriormente, mientras que las aproximaciones basadas en partículas son útiles para análisis en detalle, leyes fenomenólogicas más generales son necesarias para el estudio de mayores escalas de longitud y tiempo. Discretizando tanto la matriz extracelular como el cuerpo de la célula mediante *voxels*, y considerando que cada *voxel*-célula se comporta siguiendo el modelo mecanosensor descrito en capítulos anteriores, el modelo es capaz de predecir aspectos macroscópicos de la migración como trayectorias, velocidades, áreas de adhesión, relación de aspecto de la célula, tensiones celulares etc, para escalas temporales del orden de horas. Además, definiendo el comportamiento individual de cada uno de los componentes de la célula (*voxels*) mediante las funciones de probabilidad, el comportamiento general emerge naturalmente. Estas funciones permiten el control de los pesos relativos de cada factor estudiado (mecánica, química y flujo), así como la adición de nuevos factores en el futuro. La migración se ha estudiado tanto en matrices extracelulares contínuas como porosas, produciendo estas últimas comportamientos más complejos debido a la geometría de los poros. Aunque la utilización de matrices contínuas puede ser suficiente para predecir tendencias generales, la consideración de la guía por contacto o la presión hidrostática debida al estrechamiento de la célula al pasar por poros reducidos, deberían ser tenidos en cuenta para una simulación 3D realista del movimiento celular. En pocas palabras, se ha establecido una metodología para la comprobación y el diseño de experimentos, siendo particularmente útil para la simulación de los novedosos sistemas de microfluídica y el estudio de diversas funciones biológicas como la migración celular, la angiogénesis o la formación de tejidos. Además, la forma modular en la que se ha concebido el modelo, permite una adaptación y actualización contínua según la investigación aporta nuevos descubrimientos o elucida los mecanismos celulares envueltos en la migración.

Los modelos y aproximaciones utilizados en esta Tesis se han centrado fundamentalmente en la respuesta celular a estímulos exteriores, sin embargo, las condiciones internas son igualmente importantes para determinar la actividad celular. Por ejemplo, la migración y los movimientos exploratorios del frente celular se producen en ciclos de protrusión y retracción de la membrana, provocados por el empuje de la polimerización de actina. A su vez, esto produce un flujo retrógrado de actina que condiciona la formación y maduración de adhesiones focales, las cuales unen el citoesqueleto celular con el sustrato y determinan las interacciones célula-matriz. Por tanto, una aproximación contínua ha sido desarrollada para modelar el comportamiento

dinámico del lamelipodio celular y el papel de la vinculina como "embrague" o "elemento de fricción" del flujo de actina. Basando las hipótesis principales en observaciones experimentales y utilizando parámetros con significado físico, el modelo es capaz de predecir comportamientos generales como los ciclos de protrusión/retracción o activación periódica de la miosina, o efectos más específicos como la reducción de velocidad de la membrana y el incremento del periodo de retracción cuando se inhibe la polimerización de actina, o el aumento de duración de la fase de contracción cuando la actividad de la miosina se reduce. Aparte de la reproducción de resultados experimentales, el modelo sirve para predecir comportamientos todavía no comprobados, y en consecuencia para diseñar nuevos experimentos. Por ejemplo, las hipótesis iniciales del modelo no eran capaces de reproducir al mismo tiempo un engrosamiento del lamelipodio y un incremento en las velocidades de la membrana y del flujo de actina cuando la vinculina es desactivada, sugiriendo que otros factores, además de la fricción de las adhesiones focales, podrían alterarse en estas condiciones. Asumiendo que la velocidad de polimerización aumenta mientras que la cantidad total de actina permanece constante, ha permitido reproducir los comportamientos observados en células sin vinculina. Esta hipótesis se apoya además en otros experimentos donde se han encontrado concentraciones más bajas de faloidina o cortactina (proteínas que se unen a la actina) en células sin vinculina. El modelo utiliza una aproximación 1D basado en diferencias finitas donde el lamelipodio se discretiza tanto en longitud como en tiempo. De esta manera, el coste computacional es notablemente bajo, permitiendo simulaciones rápidas (del orden de minutos) a expensas de la pérdida de detalle o el uso de valores promediados. En cualquier caso, su simplicidad facilita su incorporación en modelos más complejos. Por ejemplo, la combinación de la presente aproximación con métodos basados en partículas o en elementos finitos (donde cada partícula o elemento se comporte según las ecuaciones del modelo) permitiría simulaciones 3D muy detalladas con costes computacionales razonables. Además se han desarrollado diferentes algoritmos basados en el principio de convolución de matrices y correlación de funciones para medir y analizar experimentos propios. Con estos códigos, se han estudiado las velocidades de la membrana y el flujo de actina, su correlación, la periodicidad de las contracciones y el desfase entre los movimientos de la actina y la membrana. Los resultados han confirmado las tendencias generales observadas en experimentos previos y han proporcionado nuevos hallazgos relacionados con la periodicidad de los ciclos exploratorios, así como del desfase de velocidades entre membrana y actina. De hecho, las células sin vinculina presentan un

aumento en la velocidad de protrusión y un flujo de actina mucho más rápido comparado con el resto de casos. Tanto las células de control (WT) como las células con vinculina pre-activada (PA) tienen los flujos de actina más lentos, mientras que las células mutadas con vinculina deficiente, con el dominio de unión a la actina desactivado (dAB, PAdAB), presentan velocidades de flujo intermedias, sugiriendo que la interacción actina-vinculina es de hecho crítica para determinar la velocidad del flujo retrógrado y por tanto el comportamiento del lamelipodio. La baja variabilidad de los periodos, unida a la observación de que la disminución de la fricción produce lamelipodios más largos y velocidades de actina más altas, respalda la idea de que el periodo de las contracciones es proporcional a la longitud del lamelipodio e inversamente proporcional a la velocidad del flujo. Un alto porcentaje de las células analizadas (73%) han mostrado desfases negativos (entre 0 y -90º) entre las curvas de velocidad de la actina y la membrana, lo cual significa que, en general, los movimientos de la membrana siguen a los de la actina. Ya que ésto no ha sido demostrado antes en ningún trabajo científico, más experimentos con éstos y otros tipos de células deberían realizarse para confirmarlo.

## I.5. Conclusiones

Las principales conclusiones de esta Tesis se pueden resumir como sigue:

- Modelado del mecanismo mecanosensor y la migración celular en 3D
    1. Uno de los principales mecanismos que dirigen el movimiento celular es el fenómeno mecanosensor. Los estímulos mecánicos como la rigidez de la matriz o las condiciones de contorno, pueden ser por sí sólos capaces de dirigir la migración celular.
    2. El comportamiento mecanosensor del cuerpo celular completo se puede simplificar a dos muelles en paralelo, uno de ellos en serie con un actuador contráctil (equivalente a un tercer muelle pre-comprimido). Este esquema tan simple implica un incremento de la tracción de la célula con la rigidez de la matriz extracelular hasta que satura.
    3. La rigidez de la actina es uno de los principales parámetros controlando la respuesta celular. En un entramado mucho más complejo como el citoesqueleto, principalmente compuesto de filamentos de actina, la

organización y adaptación de su estructura determina el comportamiento de la célula. Para comprender mejor estos mecanismos, se requiere un modelado más detallado de las redes de actina teniendo en cuenta sus principales componentes (proteínas de entrecruzamiento y motores moleculares).

4. Las células se contraen para evaluar las propiedades mecánicas de su entorno. Las simulaciones sugieren que la célula en realidad no siente directamente las fuerzas externas, si no el estado de deformación espacial que sufre el sustrato al que está anclada.

- Modelado de redes dinámicas de actina entrecruzadas con proteínas
  1. Al menos dos componentes son necesarios para simular una red de actina: filamentos de actina y proteínas de entrecruzamiento. Simplemente incluyendo el comportamiento dinámico de estas proteínas así como de los motores moleculares, las redes de actina simuladas exhiben comportamientos macroscópicos similares a los observados experimentalmente, indicando que las propiedades microscópicas de cada componente individual determinan la respuesta global de la red.
  2. Los motores moleculares juegan un papel central como mecanosensores. De entre todos los factores estudiados, aquellos afectando la dinámica de los motores son los que más han influenciado la respuesta de la red.
  3. La tensión ejercida por la célula es proporcional a la rigidez de la matriz extracelular en sustratos blandos y constante (se satura) para altas rigideces. La existencia de esta transición puede explicarse mediante los mecanismos que producen el bloqueo de los motores moleculares, constituyendo por lo tanto un posible mecanismo mecanosensor: (i) todos los puntos de anclaje (unión del motor con la actina) de los alrededores están ocupados por otros motores o proteínas, (ii) las fuerzas soportadas son demasiado altas, (iii) se ha llegado al extremo del filamento de actina.
  4. Los modelos de partículas son especialmente útiles para estudios detallados de cualquier tipo de fenómeno relacionado con las redes de actina como el mecanismo mecanosensor, u otros como el fenómeno de rigidización /reblandecimiento del citoesqueleto, la fluidificación de su estructura o la formación de anillos de actina entre otros. Sin embargo, estos modelos conllevan altos costes computacionales incluso utilizando técnicas de

paralelización, haciéndolos inadecuados para simulaciones completas del citoesqueleto.

- Respuesta temporal del proceso mecanosensor
    1. La dependencia temporal es esencial para capturar comportamientos de célula reales. Introduciendo esta dependencia por medio de una variable interna que representa la evolución del bloqueo de motores es suficiente para reproducir resultados observados experimentalmente, permitiendo simulaciones que duran segundos en lugar de semanas, haciendo por tanto la aproximación adecuada para su incorporación en modelos de elementos finitos con mayores dimensiones y escalas temporales. En cualquier caso, salvo en condiciones muy específicas (y no biológicas) como cambios súbitos de la rigidez extracelular, la respuesta mecanosensora de las células a largo plazo está gobernada únicamente por el equilibrio mecánico.
    2. El bloqueo de motores aumenta exponencialmente hasta que satura, con un tiempo de relajación independiente de la rigidez del sustrato. Aunque experimentalmente se ha encontrado que la relajación es dependiente de la rigidez a pequeñas escalas de tiempo, el modelo ha confirmado que esta dependencia es despreciable a largo plazo.
    3. El comportamiento mecanosensor del cuerpo completo de la célula se puede representar mediante dos muelles en paralelo y un actuador en serie con uno de los muelles. A diferencia de lo expuesto anteriormente, este actuador es equivalente a un muelle pre-comprimido, cuya longitud de equilibrio es llevada a cero mediante una función de relajación.
    4. Esta configuración tri-muelle permite distinguir entre las respuestas activas y pasivas de la célula. Al añadir la rigidez de la actina en serie con el actuador, es posible capturar la linealidad de la fuerza celular con respecto a la rigidez del sustrato para bajas rigideces y su saturación para altas. Además, el ratio entre la rigidez activa y pasiva permite regular la respuesta celular bajo diferentes condiciones mecánicas, jugando la rigidez de la actina un papel fundamental especialmente en sustratos rígidos y permitiendo la simulación de procesos más complejos como rupturas en la red del citoesqueleto o la rigidización por formación de fibras de estrés.

5. Se ha demostrado experimentalmente que la reacción celular ante cambios bruscos de la rigidez del sustrato se produce casi instantáneamente, confirmando que la adaptación del citoesqueleto es un proceso puramente mecánico como sugiere el modelo.

- Simulación de la migración en función de múltiples estímulos
  1. El establecimiento de leyes fenomenológicas es necesario para el estudio de mayores escalas espacio-temporales. Al discretizar tanto la célula como el sustrato mediante *voxels* y considerar que cada *voxel* celular se comporta siguiendo el modelo mecanosensor descrito previamente, el modelo de migración es capaz de predecir, en escalas temporales del orden de horas, aspectos macroscópicos del movimiento celular como trayectorias, velocidades, área de adhesión, relación de aspecto, tensiones etc.
  2. Al definir el comportamiento individual de cada *voxel* celular a través de funciones de probabilidad, el comportamiento macroscópico emerge de manera natural.
  3. La consideración o no del volumen de una sóla célula en la simulación de un microdispositivo completo no afecta a los resultados globales. Por tanto, salvo que se modelen grandes poblaciones celulares, el cuerpo de la célula se puede despreciar y la solución del estado estacionario se puede considerar constante durante las simulaciones de migración, permitiendo desacoplar el cálculo mecánico y ahorrando coste computacional. Aun así, debido a la normalmente irregular geometría de las células reales, los efectos del flujo y la concentración química a lo largo de la superficie celular deberían ser tenidos en cuenta para una consideración completa de dichos factores.
  4. Comparado con una aproximación contínua, la geometría de una matriz porosa afecta a la migración, guiando a la célula a través de los poros y modificando el proceso mecanosensor. Aunque una matriz contínua es suficiente para capturar tendencias migratorias generals, la consideración de factores como la guía por contacto o la presión hidrostática sería necesaria para obtener simulaciones realistas de migraciones 3D.

- Simulación del lamelipodio y el efecto de las adhesiones focales
    1. Una aproximación 1D es adecuada para simular el lamelipodio celular y estudiar el papel de la vinculina como "embrague" del flujo retrógrado de actina. De hecho, un modelo simple es suficiente para predecir comportamientos generales como los ciclos de protrusión/retracción de la membrana, la activación periódica de la miosina o los efectos cuando la polimerización de actina o la actividad de los motores moleculares son alterados mediante agentes químicos.
    2. La convolución de matrices y la correlación de funciones son herramientas matemáticas de gran potencial que pueden ser aplicadas para la medida y el análisis de experimentos mediante tratamiento de imágenes.
    3. Desactivar la vinculina en una célula altera las condiciones de fricción y polimerización en el lamelipodio. Asumiendo que la polimerización aumenta pero manteniendo una cantidad total de actina, el modelo es capaz de predecir los efectos en las células deficitarias de vinculina (Vcl-KO) observados experimentalmente.
    4. Desactivar la vinculina provoca un incremento sustancial en la velocidad del flujo de actina. Las células de control (WT) así como las células con vinculina pre-activada (PA) presentan flujos más lentos mientras que las células con vinculina cuyo dominio de unión con la actina está desactivado (dAB, PAdAB) muestran velocidades intermedias, sugiriendo que la interacción actina-vinculina es el determinante fundamental del flujo retrógrado.
    5. La disminución de la fricción produce lamelipodios más largos y mayores velocidades de flujo, mientras que la periodicidad de las contracciones no se ve afectada. Por tanto, este periodo puede ser considerado proporcional a la longitud del lamelipodio e inversamente proporcional a la velocidad de la actina.
    6. En general, teniendo en cuenta las hipótesis utilizadas en el cálculo, el desfase negativo entre las curvas de velocidad de la actina y la membrana demuestra que los movimientos de la membrana siguen a los de la actina. Ya que este fenómeno concreto no ha sido mostrado previamente en ningún trabajo científico, más experimentos son necesarios para confirmarlo.

## I.6. Contribuciones científicas

A continuación se describen brevemente las principales contribuciones originales de esta Tesis:

- Formulación de un modelo de migración individual en 3D basado en *el* mecanismo mecanosensor, es decir, dependiente de las condiciones mecánicas de la matriz extracelular y de las cargas externas.
- Simulaciones númericas de elementos finitos para determinar patrones migratorios, fuerzas y velocidades para diferences condiciones de contorno y fuerzas externas.
- Adaptación de un modelo computacional de partículas basado en dinámica Browniana para estudiar el fenómeno mecanosensor en una red de actina entrecruzada con proteínas.
- Extensión del modelo mecanosensor para incluir la respuesta temporal basada en los resultados del modelo de partículas.
- Análisis de la influencia de los parámetros mecánicos y estudio de la respuesta del sistema ante cambios bruscos de la rigidez del sustrato.
- Desarrollo de un modelo fenomenológico probabilístico basado en *voxels* y elementos finitos para el estudio de la migración celular en 3D bajo diferentes condiciones de contorno y la actuación de múltiples factores externos: mecánicos y fluído-químicos.
- Simulaciones de elementos finitos en 3D de un dispositivo de microfluídica para determinar el flujo y el gradiente químico a través de un material poroso.
- Formulación de un modelo continuo para describir el comportamiento del lamelipodio y estudiar la influencia de las adhesiones focales en el flujo retrógrado de actina.
- Adaptación de una herramienta para medir el flujo de actina y el movimiento de la membrana a partir de microscopía de fluorescencia (*Fluorescent Speckle Microscopy*).
- Desarrollo de una herramienta para analizar la periodicidad de los ciclos de protrusión/retracción de la membrana y su correlación con la velocidad de la actina.

- Análisis del efecto de diferentes sustancias químicas que inhiben o incrementan la polimerización de actina, la actividad de la miosina o la fuerza de las adhesiones focales.

### I.6.1. Publicaciones

A continuación se enumeran las publicaciones realizadas durante el desarrollo de la presente Tesis en revistas internacionales.

1. **BORAU, C.**, KAMM, R.D. & GARCÍA-AZNAR, J.M. 2011. Mechano-sensing and cell migration: a 3D model approach. *Physical Biology*, 8, 066008.
2. **BORAU, C.**, KIM, T., BIDONE, T., GARCIA-AZNAR, J.M. & KAMM, R.D. 2012. Dynamic mechanisms of cell rigidity sensing: insights from a computational model of actomyosin networks. *PLoS One*, 7, e49174.
3. **BORAU, C.**, GARCIA-AZNAR, J.M. & KAMM, R.D. 2013. A time-dependent phenomenological model for cell mechano-sensing. *(Enviado)*
4. **BORAU, C.**, POLACHECK, W.J., GARCIA-AZNAR, J.M. & KAMM, R.D. 2013. Probabilistic voxel-FE model for single cell motility in 3D *(En proceso)*
5. **BORAU, C.**, THIEVESSEN, I., GARCIA-AZNAR, J.M. & FABRY, B. 2013. Modeling lamellipodium dynamics and effects of vinculin on rearward actin flow. *(En proceso)*.

### I.6.2. Contribuciones a congresos

El trabajo desarrollado durante la tesis ha sido expuesto en diferentes congresos de ámbito nacional e internacional. Los más relevantes son:

1. **BORAU, C**., DOWEIDAR, M.H., GARCÍA-AZNAR, J.M., Mechanosensing and Cell Migration: 3D modeling. *XXVIII Congreso Anual de la Sociedad Española de Ingeniería Biomédica (CASEIB)*, Madrid (Spain) 2010.
2. GARCÍA-AZNAR, J.M., **BORAU, C**., KAMM, R. D., Three-Dimensional modelling of cell migration due to active mechanosensing. *TERMIS-EU*, Galway (Ireland), 2010.

3. GARCÍA-AZNAR, J.M., **BORAU, C**., KAMM, R. D., Modeling of cell migration and mechano-sensing in 3D. *17th Congress of the European Society of Biomechanics (ESB)*, Edinburgh (UK), 2010
4. **BORAU, C.**, KAMM, R. D., KIM, T, GARCÍA-AZNAR, J.M., Exploring Rigidity Sensing and Acto-myosin based Contractility: a 3-D Actin Network Computational Model. *4th European Cell Mechanics Meeting (CellMech).* Amsterdam (Netherlands) 2011.
5. GARCÍA-AZNAR, J.M., **BORAU, C.**, KAMM, R. D., Modelling mechanosensing in cell-material interaction: implications for tissue engineering. *TERMIS-EU Annual Meeting*, Granada (Spain), 2011.
6. **BORAU, C.**, KAMM, R. D., KIM, T, GARCÍA-AZNAR, J.M., Computational Model of 3-D Cross-linked Actin Networks: mechanosensing behaviour of cells. *II International Conference on Particle-based Methods. Fundamentals and Applications (PARTICLES)*. Barcelona (Spain), 2011.
7. GARCÍA-AZNAR, J.M., **BORAU, C.**, KIM, T, KAMM, R. D., Computational Model of 3-D Cross-linked Actin Networks: Mechanosensing Behaviour of Cells. *II International conference on particle based methods Fundamentals and applications (PARTICLES)*, Barcelona (Spain), 2011.
8. GARCÍA-AZNAR, J.M., **BORAU, C.**, KAMM, R. D., Models of cell migration: implications for tissue engineering. *II International Conference on Tissue Engineering (ICTE)*, Lisbon (Portugal), 2011.
9. **BORAU, C.**, KAMM, R. D., KIM, T, GARCÍA-AZNAR, J.M., Acto-myosin system Contraction: computational study of 3D actin networks and their response to extracellular matrix stiffness. *I Reunión del Capítulo Nacional Español de la Sociedad Europea de Biomecánica (ESB-Cap Esp)*, Zaragoza (Spain), 2011.
10. KAMM, R. D., **BORAU, C.**, KIM, T, GARCÍA-AZNAR, J.M., Computational insights into cytoskeletal rheology. *Biophysical Society Meeting*, Baltimore, MD, (USA), March, 2011.
11. KAMM, R. D., **BORAU, C.**, KIM, T, GARCÍA-AZNAR, J.M., Computational models of the cytoskeleton and a look forward to simulation of mechanotransduction. *Microscale Modeling in Biomechanics and Mechanobiology*, Ericeira (Portugal), 2011.

12. KAMM, R. D., **BORAU, C.**, KIM, T, GARCÍA-AZNAR, J.M., A Computational, Brownian Dynamics Simulation of Cytoskeletal Mechanics, *The 1st KIAS Conference on Subcellular Dynamics*, Seoul (Korea), 2011.
13. KAMM, R. D., **BORAU, C.**, KIM, T, GARCÍA-AZNAR, J.M., The unique biomechanical properties of the cell: Insights from computational modeling. *Nanyang Technological University*, 2011.
14. **BORAU, C.**, KAMM, R. D., KIM, T, GARCÍA-AZNAR, J.M., Cell cytoskeleton dynamics: mechanosensing properties. *I3A -Jornada de jóvenes investigadores*, Zaragoza (Spain), 2012.
15. GARCÍA-AZNAR, J.M., **BORAU, C.**, KIM, T, KAMM, R. D., Mechanosensing: from a discrete to a continuum approach. *8th European Solid Mechanics Conference*, Graz (Austria), 2012.
16. **BORAU, C.**, KAMM, R. D., GARCÍA-AZNAR, J.M., Computational model of 3D single cell migration: a mechano-chemical approach. *18th Congress of the European Society of Biomechanics (ESB)*, Lisbon (Portugal), 2012.
17. KAMM, R. D., **BORAU, C.**, KIM, T, GARCÍA-AZNAR, J.M., Biomechanical properties of the cell: Insights from computational modeling. *Society of Physical Regulation and Biomolecular Modeling*, San Juan (Puerto Rico), 2012.
18. KAMM, R. D., **BORAU, C.**, KIM, T, GARCÍA-AZNAR, J.M., The unique biomechanical properties of the cell: Insights from computational modeling. *Worcester Polytechnic Institute (WPI)*, Worcester, MA (USA), 2012.
19. KAMM, R. D., **BORAU, C.**, KIM, T, GARCÍA-AZNAR, J.M., The unique biomechanical properties of the cell: Insights from computational modeling. *International Federation for Medical & Biological Engineering (IFMBE)*, Beijing (China), 2012.
20. GARCÍA-AZNAR, J.M., **BORAU, C.**, BIDONE, T., KIM, T, KAMM, R. D., Modeling 3D actin networks: dynamics of cell mechanosensing. *III International Conference on Particle-based Methods Fundamentals and Applications*, Stuttgart (Germany), 2012
21. **BORAU, C.**, THIEVESSEN, I. GARCÍA-AZNAR, J.M., FABRY, B., Lamellipodium dynamics and rearward actin flow depend on vinculin. *19th Congress of the European Society of Biomechanics (ESB)*, Patras (Greece), 2013. (Candidato a los premios de la ESB para estudiantes)

## I.7. Desarrollo futuro

La variedad de modelos presentados en esta Tesis es sólo una pequeña contribución a la comprensión del comportamiento celular en el proceso de migración. Los resultados y conclusiones obtenidas durante este trabajo provocan a su vez nuevas preguntas y abren posibles líneas de investigación futuras. Las más importantes se describen a continuación:

- Extensión de los modelos de migración individual para simular poblaciones celulares

  Los modelos presentados en los Capítulos 2 y 5 son útiles para aislar los efectos específicos de ciertos parámetros y de su influencia en la migración celular individual. Sin embargo, las interacciones célula-célula dan lugar a complejos cambios en la estructura y procesos de tejidos pluricelulares, como por ejemplo la regeneración de la piel o la vascularización. Por tanto, la incorporación de tales interacciones entre distintas células extendería enormemente el potencial de los modelos. Aunque algunos aspectos técnicos deberían ser revisados, los modelos actuales están, de hecho, preparados para la inclusión de múltiples células.

- Estudio de diferentes estructuras de actina relevantes para el comportamiento celular

  Extisten numerosas estructuras formadas en su mayor parte por actina implicadas en diferentes procesos celulares que podrían ser estudiadas con el modelo de partículas de dinámica Browniana descrito en el Capítulo 3. Por ejemplo las fibras de estrés (compuestas por filamentos de actina entrecruzados de forma paralela con proteínas y motores de miosina) son cruciales para distribuir las fuerzas celulares a lo largo del citoesqueleto, y juegan un papel fundamental en la contracción celular o la morfogénesis entre otros procesos. Los anillos de actina que aparecen en la citoquinesis (la división del citoplasma durante la proliferación celular) podrían también ser simulados con el citado modelo. En estos anillos, la miosina constriñe la membrana de la célula hasta que ocurre la escisión. Fenómenos como la hidrólisis de ATP o estructuras adicionales como los microtúbulos deberían ser incorporadas para analizar debidamente este proceso. Igualmente se podrían estudiar los arcos de actina que se forman en el frente de la

célula y que sirven de elementos estructurales donde se forman y maduran las adhesiones focales, que a su vez forman una base firme sobre la cual polimeriza la actina y empuja la membrana en movimientos exploratorios de protrusión. Combinando el modelo de partículas con las hipótesis teóricas descritas en el Capítulo 6, permitiría un análisis muy detallado del comportamiento del lamelipodio y sus componentes.

- Desarrollo de las interacciones célula-matriz

  Las interacciones célula-matriz se producen a través de receptores transmembrana (integrinas) y adhesiones focales, actuando como transductores de señales y presentando comportamientos muy complejos y dinámicos. Su simulación en detalle no se ha considerado a lo largo de esta Tesis. Por ejemplo, en el modelo de migración descrito en el Capítulo 5, se considera que la totalidad de la superficie celular se adhiere al sustrato y por tanto todo los *voxels* del perímetro ejercen fuerzas de contracción. En realidad, sólo algunas partes de las células se adhieren firmemente al sustrato y sólo algunas de ellas forman adhesiones focales capaces de ejercer fuerzas apreciables. Por tanto, un modelo detallado de la formación y maduración de adhesiones focales sería interesante para comprender realmente su papel en la migración celular. Además, mecanismos como la polimerización de actina o la presión hidrostática interna, especialmente importantes en materiales porosos y con poros pequeños, tampoco han sido incluidas en los modelos de esta Tesis, lo cual sería necesario para un modelado completo y realista de migración en 3D.

- Distinguir las diferentes partes de la célula

  En las simulaciones 3D de los Capítulos 3 y 5, se han diferenciado a grandes rasgos tres partes de la célula: núcleo, citoplasma y córtex. De una forma muy simplificada, se han considerado diferencias como el nivel de tensión máxima o la ausencia de componente contráctil en el núcleo (modelado como un material pasivo). Aunque esto se ha hecho así inicialmente para no complicar innecesariamente el modelo, los códigos han quedado preparados para su posterior desarrollo. Por ejemplo, la rigidez de la actina podría relacionarse con la polimerización de actina (o la densidad de actina) obtenida en experimentos. La concentración de proteínas de entrecruzamiento podría también determinar la

rigidez de la estructura, afectando por tanto al comportamiento local y global de la célula. Del mismo modo, la concentración de miosina influiría en la capacidad de contracción de cada zona, y la distribución de adhesiones focales determinaría si esa fuerza se transmite al sustrato o se disipa en los elementos pasivos del citoesqueleto.

- Uso de geometrías reales de célula y matriz

  Las aproximaciones mediantes *voxels* son útiles para el estudio de tendencias generales permitiendo grandes escalas de tiempo y longitud, sin embargo, importantes detalles pueden perderse debido a las simplificaciones. Por ejemplo, la curvatura de la membrana puede activar la polimerización de actina en zonas específicas, dirigiendo el avance de filopodios u otras estructuras exploratorias y regulando la tensión que produce el flujo retrógrado (de retroceso) de actina en el lamelipodio. Un modelo que utilice elementos finitos de superficie podría combinar las ventajas del cálculo matricial (fiable y rápido) preservando los detalles de geometrías irregulares.

- Incluir la formación y maduración de adhesiones focales en el modelo del lamelipodio.

  Mientras que las aproximaciones contínuas permiten rápidas simulaciones para investigar comportamientos generales, el modelado en detalle se hace necesario para analizar fenómenos complejos como la formación y maduración de adhesiones focales durante los ciclos de protrusión/retracción del lamelipodio. Este proceso es crítico para la migración, ya que las adhesiones maduras forman una base firme en el borde de la lamela, lo cual frena el flujo de actina y permite la protrusión de la membrana a la vez que transmite fuerzas al sustrato. Por tanto, la incorporación explícita de la formación de adhesiones dependiendo de la velocidad o concentración de la actina, la rigidez del sustrato u otros parámetros como la concentración de diferentes proteínas proporcionaría resultados mucho más precisos.

- Combinar el modelo continuo con métodos de partículas o elementos finitos.

El principal inconveniente de la aproximación 1D para describir el comportamiento del lamelipodio, es la falta de detalles y el uso de variables promediadas. Sin embargo, su simplicidad facilita su incorporación en modelos de partículas o elementos finitos, lo que permitiría simulaciones complejas en 3D con costes computacionales razonables. Por tanto, un modelo incorporando mecanosensibilidad cuyas propiedades mecánicas dependiesen de parámetros dinámicos como la concentración de adhesiones focales, la polimerización de actina o la activación de miosina, presentaría ciertamente una detallada y muy interesante aproximación que permitiría el estudio simultáneo de efectos a escala micro y macro en una sóla simulación.

Chapter 1

# INTRODUCTION

A brief summary of the current knowledge on experiments and simulations of cell migration is presented in this Chapter. Specifically, the role of cell migration on a wide variety of critical processes, current experimental technologies used in migration-related research and common approaches for mathematical and computational modeling are addressed here. Next, the motivation and main objectives of this Thesis, as well as a description of its structure are presented.

**Contents**

## 1.1. Background

Cell motility has gained increasing prominence during the past years due to its major role in several physiological and pathological processes, e.g., morphogenesis, the inflammatory response, wound healing or tumor metastasis (Lauffenburger and Horwitz, 1996). Public health problems are a growing concern worldwide. For instance, infected wounds not only heal more slowly, but prevent adequate skin grafting and may lead to sepsis (Atiyeh et al., 2005). Chronic wounds contribute to morbidity, and occasionally to mortality. As another example, Cancer is a leading cause of death, accounting for 7.6 million deaths (13% of total) in 2008, which are projected to continue rising, with an estimated 13.1 million deaths in 2030 (www.who.int). Understanding why tumor cells migrate from the initial tumor mass into the circulatory system, how leukocytes immigrate into areas of insult in inflammation processes or the reasons driving fibroblasts and vascular endothelial cells during wound healing holds the promise of effective therapeutic approaches for treating disease, cellular transplantation, and the preparation of artificial tissues.

Over the past few years, immense progress has been made in understanding cell migration, including the establishment of polar structures, the regulation of the dynamic processes of actin and microtubule polymerization, and the regulation of spatial and temporal signal transduction (Ridley et al., 2003). The way cells migrate and respond to their 3D micro-environment is a multiscale process that results from the integrated effect of the properties of the tissue extracellular matrix (ECM) and the sub-cellular constituents of the cell, mediated by the cytoskeleton (CSK). This integration process depends on multiple mechanical, chemical and biological factors (Cukierman et al., 2002, Even-Ram and Yamada, 2005, Zaman et al., 2006)(Figure 1.1). For instance, the influences of ECM prestrain (*Tensotaxis*), stiffness and topography (*Durotaxis*) have been widely investigated (Beloussov et al., 2000, Lo et al., 2000, Saez et al., 2007, Baker et al., 2009, Hakkinen et al., 2011), showing that cells prefer to migrate toward more strained or stiffer zones of the ECM, where the focal adhesions are more stable allowing to exert higher forces (Lo et al., 2000, Cukierman et al., 2001, Schwarz and Bischofs, 2005). Cells also respond to spatial chemical gradients (*Chemotaxis*) in the surrounding fluid or tissue (Rappel et al., 2002, Zhelev et al., 2004), moving towards or away from the source of chemical variation. In addition, individual cells within a monolayer tend to migrate along the local orientation of the maximal normal stress, transmited across many cell-cell

junctions (*Plithotaxis*)(Trepat and Fredberg, 2011). Potential gradients (*Galvanotaxis*), fluid conditions and ligand adhesion gradients (*Haptotaxis*) are additional clues for cell migration guidance currently under study (Zhao et al., 2002, Curtze et al., 2004, Li et al., 2005, Hofmann et al., 2006, Polacheck et al., 2011). Understanding cell migration as an integrated process requires an appreciation of multicomponent structures and assemblies, physically coordinated both spatially and temporally. Only when understood as an integrated system will its alteration via genetic, pharmacologic or materials-based interventions acquire a truly rational basis.

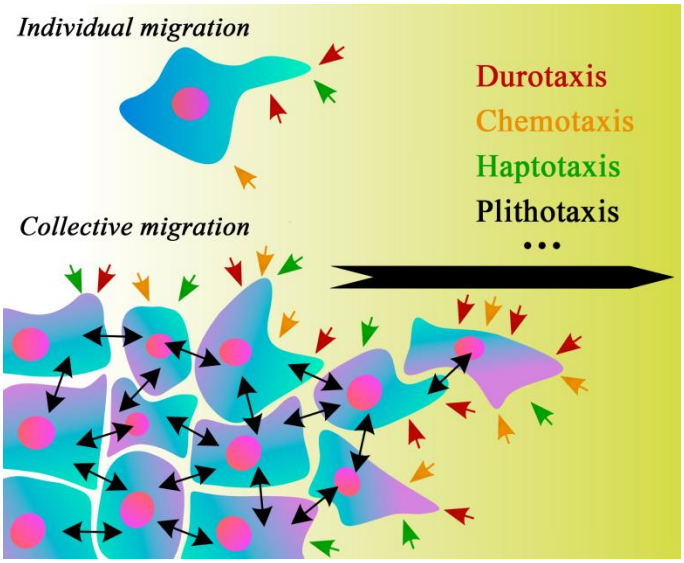


**Figure 1.1:** Factors influencing cell migration.
Individual and collective cell migration depends on multiple mechanical, chemical and biological factors, actively responding to the surrounding environment.

### 1.1.1. The migration cycle

Cell migration can be generally conceptualized as a cyclic process (Lauffenburger and Horwitz, 1996, Ridley et al., 2003). The initial response of a cell to a migration-promoting agent is to polarize and extend protrusions. Several proteins such as myosin II are involved in the generation of polarity, organizing the CSK and restricting protrusions to the cell front (Figure 1.2A). These protrusions can take several forms, from spike-like filopodia to large, broad lamellipodia. They are usually driven by actin polymerization, and are stabilized by adhering to the extracellular matrix (ECM) or adjacent cells via transmembrane receptors linked to the actin CSK (Figure 1.2B). These adhesions serve as

traction sites for migration as the cell moves forward over them, and they are disassembled at the cell rear, allowing it to detach and contract (Figure 1.2C). Note that although this picture is common among different cell types, the specific details may differ to a large extent. For example, slow-moving cells such as fibroblasts clearly show these steps in contrast with fast-moving cells such as neutrophils, where the observation of the different phases is not as obvious. In addition, cell's migratory behavior strongly depends on its environment, being the main cause of discrepancies between *in vivo* and *in vitro* cultures.

### 1.1.2. Numbers matter: collective versus single cell migration

As just stated, cell migration is commonly understood as the movement of individual cells that undergo polarized extension-contraction cycles coupled with adhesion to and deadhesion from the surrounding substrate. However, at least one additional major principle is relevant to cell translocation in or on tissues: the movement of cell groups, sheets, or strands consisting of multiple cells that are mobile yet simultaneously connected by cell-cell junctions (Friedl et al., 2004)(Figure 1.1). Collective cell dynamics give rise to complex changes in multicellular tissue structures, including epithelial regeneration, the sprouting of vessels and ducts in angiogenesis and branching morphogenesis, and the deregulated invasion of cell masses during cancer progression and consecutive tissue destruction (Ilina and Friedl, 2009). In this way, collective cell migration shares similarities but also important differences to individually migrating cells. For instance, similarly to single-cell migration, collective cell movement results from actin polymerization and contractility coupled to cell polarity, however in the latter case, cells remain coupled by cell-cell junctions at the leading edge as well as in lateral regions and inside the moving cell group.

Therefore, collective cell migration differs from single-cell migration in the simultaneous coordinated polarization of (often many) cells at the leading edge of the cell group; the translocation of cells through physical coupling and drag force; the activity of actin-rich lamellae in multiple cells along or underneath the cell collective; the secondary remodelling of the extracellular matrix along the migration track, leading to the formation of a basement membrane or the widening of a 3D track (macropatterning) to encompass an increasing volume of the cell mass; and the coordinated retraction of multiple cells at the rear end of the group (Friedl and Gilmour, 2009).

### 1.1.3. Microenvironment: 2D versus 3D migration

Mechanisms regulating cell motility have been extensively studied in 2D. Studies of cell migration in 3D cell culture systems and *in vivo* have revealed several differences when compared with cell migration flat surfaces, including their morphology and mechanical and signaling control (Friedl et al., 2012). Furthermore, 3D research has been rapidly growing as it entails a better representation of the microenvironmental conditions in living tissues. In fact, the desire to look within living organisms has led to the development of advanced technologies for real-time *in vivo* imaging. Nevertheless, *in vitro* models are still indispensable to isolate and define specific contributions of single factors to the overall process.

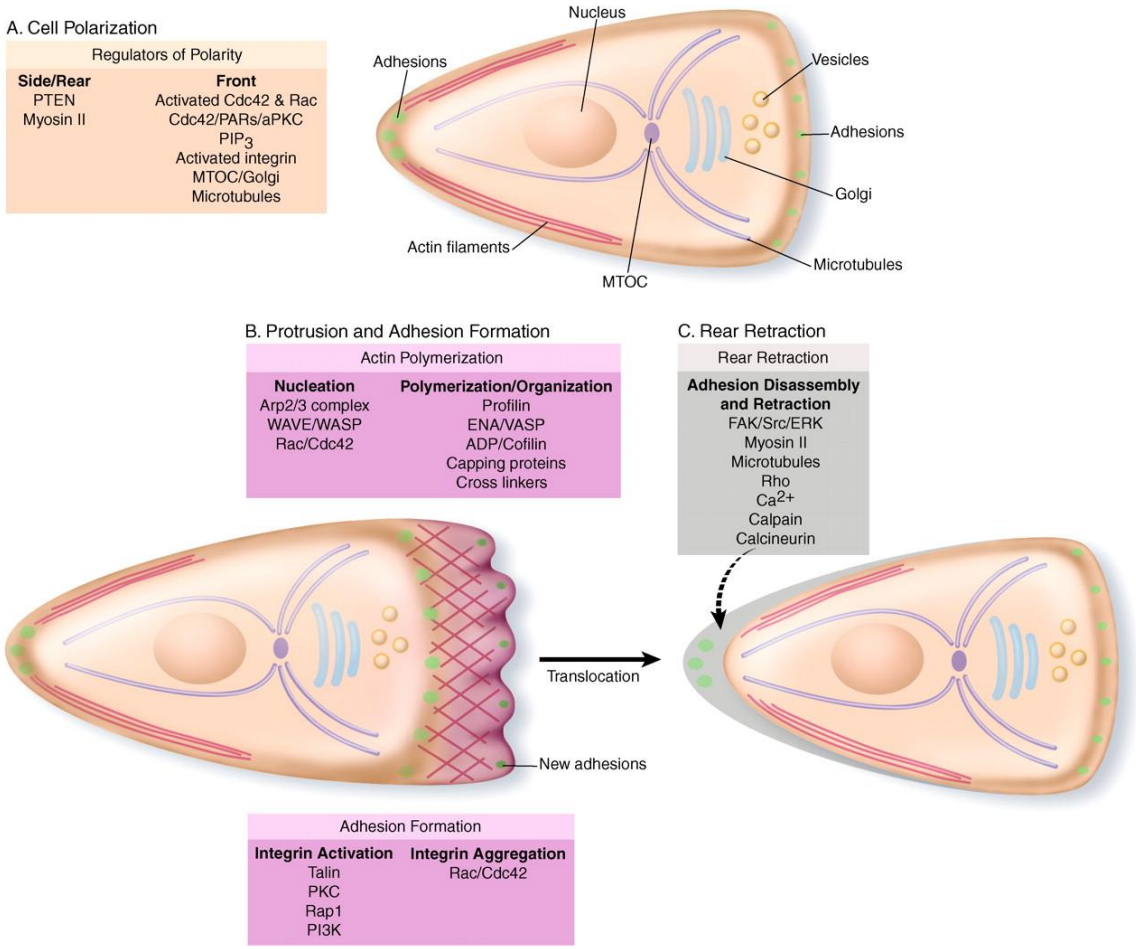


**Figure 1.2:** The migration cycle. With the permission of Ridley et al., 2003
Scheme showing the main steps of cell migration: A) Cell polarization B) Protrusion and adhesion formation. C) Rear retraction.

Three are the major types of ECM through which cells migrate *in vivo* (Even-Ram and Yamada, 2005): tightly packed basement membrane (Figure 1.3A), dense connective tissue (Figure 1.3B) and loose connective tissue (Figure 1.3C). To mimic these environments, the most commonly ECMs used *in vitro* are: collagen gels, cell-derived matrix (CDM) from fibroblasts, fibrin gels and basement membrane extract (BME or Matrigel) (Hakkinen et al., 2011). All of them are useful for exploring differences in cell morphology, signaling, adhesions and motility, which vary even for the same type of ECM depending on specific properties or whether the cells are plated on top or inside. For instance, ligand concentration on 2D surfaces is often low, whereas 3D ECMs usually contain tighltly packed clusters of ligands. In addition, cells on 2D substrates present marked lamellipodia and filopodia activity at the leading edge, mainly used for exploratory functions. In 3D, however, the more elongated and very thin morphology of cells entails that some structures can appear less obvious. For instance, focal adhesions are strong and clearly visible at the leading edge in flattened cells on 2D substrates, whereas cells in 3D exhibit adhesions all over their surface.

Signalling is also affected by dimensionality: higher Rac activity is associated with spontaneous changes of cell migration direction on 2D surfaces (Pankov et al., 2005), much less persistent than cells in 3D ECMs. Furthermore, changes in substrate compliance may alter the distribution of integrins and several related signaling molecules (Katsumi et al., 2005).

In sum, matrix organization, composition and biological activity likely modulate both normal and pathological cell migration and invasion. 3D ECM models together with advanced imaging techniques are contributing to an increasing understanding of physiological and pathological motility processes. Some of these systems permit to isolate and study the contribution of single components to the migration process; however, it is necessary to keep in mind that oversimplification of complex microenvironments in terms of structure, content and cellular interactions may lead to unreliable observations, thus reducing the relevance of the analysis.

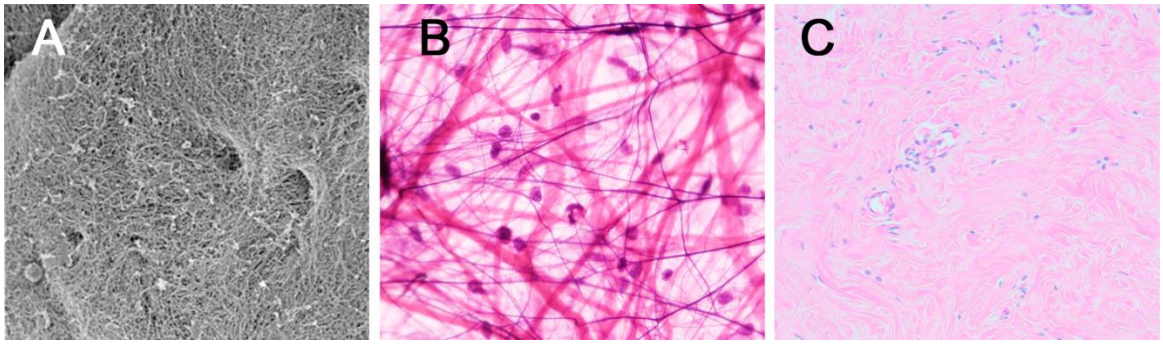


**Figure 1.3:** Major types of *in vivo* ECM. Adapted from Even-Ram and Yamada, 2005 A) Dense collagen meshwork of the basement membrane visualized by scanning electron microscopy. B) Loose areolar connective tissue of mesentery showing collagen fibers, elastic fibers and fibroblasts. C) Irregular dense connective tissue of nipple skin with irregularly oriented densely packed collagen fibers.

### 1.1.4. Distinct modes of 3D cell migration

How different cell types employ different mechanisms to efficiently move through structurally and chemically diverse 3D environments is not well understood. Despite the evidence that migrating cells express various proteases that are able to degrade ECM components, it is unclear whether 3D migration absolutely depends on proteolytic events. In fact, recent studies of cancer cell migration in 3D environments showed that metastatic cells can switch between adhesion-dependent mesenchymal (elongated) and adhesion-independent amoeboid (rounded) cell motility, driven by actin polymerization and actomyosin contraction, respectively (Wolf et al., 2003, Lammermann and Sixt, 2009). Currently, blebbing is the only known alternative to actin driven protrusion. Membrane blebs are actin filament-free cellular extensions, generated after cortex rupture or actin-membrane breakage by intracellular hydrostatic pressure. This pressure inflates the membrane until a new actin cortex is reassembled allowing the cycle to restart (Charras and Paluch, 2008). In addition, lobopodia (large blunt cylindrical protrusions) was recently found to be the predominant protrusion type of mesenchymal cells migrating in physiological 3D environments (Petrie et al., 2012), presenting features of both blebs and lamellipods. Interestingly, they also found that in 3D environments with nonlinear elastic features, lamellipodial locomotion dominates, whereas in a regimen showing linear elasticity, fibroblasts rather use lobopodia. Nevertheless, how cells show stable functional polarity, distinguish ECM elasticity or which features feed back on the extracellular environment to switch between migration modes are still open questions.

### 1.1.5. Experimental research

Experimental works on the cell migration field have grown enormously during the past decades, largely thanks to the development of new technologies and techniques which have accelerated even more the process. Nevertheless, isolating the effects of individual stimulus on cell migration *in vivo* still presents important difficulties. As a result, *in vitro* models have emerged as powerful tools for investigating cell motility, permitting to examine in detail specific factors guiding cell migration. Due to the vital importance of cancer, these *in vitro* assays are commonly used to understand the mechanisms driving tumor cell migration (usually chemical and mechanical clues) and aim to improve the efficacy of cancer therapy.

The tumor microenvironment is comprised of a dynamic network of ECM proteins bathed in interstitial fluid and a host of associated cells including endothelial cells, fibroblasts, bone marrow-derived and infiltrating immune cells (reviewed in (Joyce and Pollard, 2009)). These stromal cells remodel the ECM and provide mechanical and chemical signals to the tumor cells. Due to the dynamic nature and the variety of components comprissing the tumor microenvironment, the investigation of the effect of individual stimuli on migration requires that the mechanical and chemical properties can be tuned precisely with reproducibility. *In vitro* assays provide such control and are well suited for dissecting the signaling pathways that govern cell migration in response to a specific factor of interest. In particular, different experimental methods to assay tumor cell migration *in vitro* are shown in Figure 1.4. A further description of these methods can be found in (Polacheck et al., 2012). As a brief summary, they can be classified in

(viii) **Micropipette assays:** a micromanipulator-controlled pipette is used in the vicinity of the cell to inject a chemoattractant solution into the culture medium to establish a growth-factor gradient. These chemokine gradients, however, are transient and difficult to quantify (Soon et al., 2005).

(ix) **Boyden (or Transwell) chambers:** a stiff porous membrane is incorporated between two cell culture chambers. Cells are seeded in suspension in the top chamber and migrate through the filter in response to a chemokine gradient, which is established by the different culture medium concentrations in the top and bottom chambers (Boyden, 1962).

(x) **Micropatterning:** cells are seeded on patterns of different geometry, size and surface coatings in 1D, 2D and 3D substrates. These assays offer scalability and the capability to culture large cell numbers, however, as they don't usually include fluid flow, the application of localized mechanical stimuli or chemical gradients is generally not possible (von Philipsborn et al., 2006).

(xi) **Durotaxis assays:** cells are seeded on 2D substrates of variable stiffness where cell responses (traction forces, spread area, and migration direction) are monitored (Lo et al., 2000).

(xii) **Wound healing assays:** collective cell migration can be studied by generating an area without cells (wound) in a cellular monolayer, where dynamics of wound closure are monitored. These assays are tipically limited to 2D substrates with uniform conditions, although stimulus gradients can be created using modified microfabrication techniques (Simpson et al., 2008).

(xiii) **3D ECM assays:** novel biomaterials enable the creation of 3D environments with tunable chemical and physical parameters of the ECM. Cells are seeded inside the 3D medium and migrate depending on the ECM architecture, stiffness, pore size, and ligand concentration (Sabeh et al., 2009).

(xiv) **Microfluidics:** recent advances in fabrication technology have made it possible to create novel microdevices that allow a precise control of the cellular microenvironment. With these assays it is facile to stablish electrical fields, cytokine gradients or interstitial flow, which can be tuned by adjusting the potential, chemokine concentration or hydrostatic pressure at the different microchannels (Chung et al., 2010, Polacheck et al., 2011).

In short, Micropipette, Boyden chamber and microfluidics assays enable control of biochemical gradients whereas Durotaxis, 3D ECM and microfluidics assays enable control of biophysical forces (ECM stiffness and interstitial flow). Wound healing and micropatterning assay enable control of intercellular distances, whereas only micropatterning assays enable control of substrate topography.

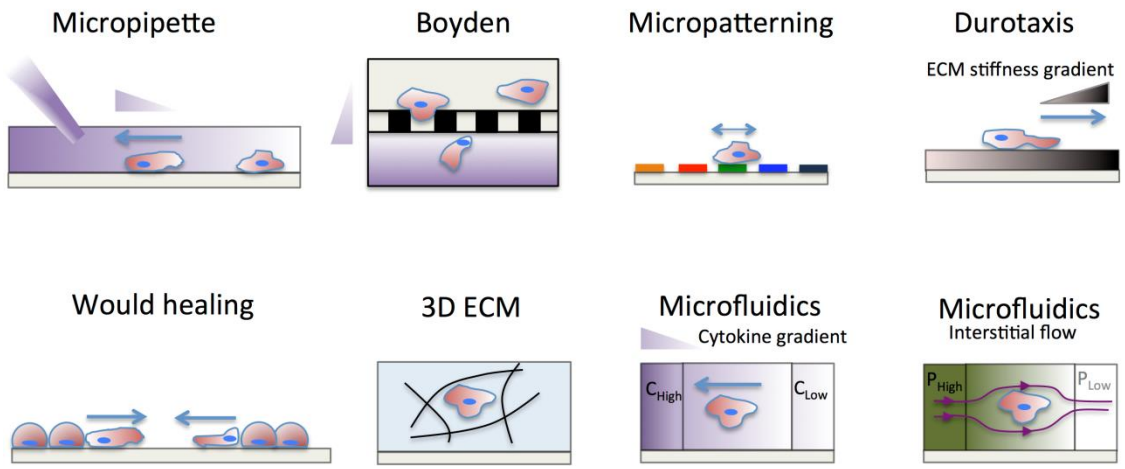


**Figure 1.4:** Experimental methods. With the permission of Polacheck et al., 2012 Experimental methods for investigating factors that influence tumor cell migration. Triangles indicate growth-factor (purple) and ECM stiffness (black) gradients. Blue arrows indicate direction of tumor cell migration, and pressure gradients are indicated by the shades of green.

## 1.1.6. Cell migration modeling

There exist a vast amount of computational or mathematical models involving specific or general aspects of cell migration. The importance that cell migration has demonstrated in many pathological processes and diseases has caused great investment and a growing influx of mathematicians, engineers, and physicists into the field of cellular biophysics. As a result, the details and sophistication of migration models has grown concomitantly, however, and despite each model is oftenly unique, they can be classified into three principal types depending on the main area of interest: cell protrusion, cell adhesion and retraction, whole-cell models. Here, a brief summary explaining their physical basis, capabilities, and relationship to other models is presented. Nevertheless, several reviews cover this and other classifications providing a wider and more balanced picture (Flaherty et al., 2007, Carlsson and Sept, 2008, Rangarajan and Zaman, 2008, Mogilner, 2009).

### 1.1.6.1. Protrusion models

Protrusion is probably the most studied and best understood of all locomotion steps. As described before, the key event underlying actin-based cell migration is the generation of force by the polymerization of actin filaments against the cell membrane. Many mathematical works have focused on this issue and they can usually be distinguished

depending on whether they consider a single actin filament, multiple filaments or they use a continuum approach (Carlsson and Sept, 2008).

Single-filament growth models can identify plausible mechanisms for force generation, predicting the stall force and establishing a force-velocity relationship. Usually, they consider filament growth to occur by passive monomer diffusion. Brownian fluctuations of the membrane or filament tip make room for new monomer addition. If the free-monomer concentration is high enough, the addition of these new monomers prevent the membrane from returning to its previous position, a process commonly known as "Brownian-ratchet" (Peskin et al., 1993). These types of models have been extended to include attachments between the filament tip and the membrane which can stablish what additional mechanisms may be active in force generation and evaluate the effects on the force-velocity relation (Dickinson and Purich, 2002, Zhu and Carlsson, 2006).

Multiple-filament models treat the simultaneous polymerization of many actin filaments, including filament-filament interactions and actin-binding proteins. Propulsion of intracellular pathogens, lamellipodial and filopodial protrusion have been the problems receiving the most attention with this kind of models. For instance, filopodia and branched actin networks growing against a membrane (Atilgan et al., 2005, Atilgan et al., 2006) or obstacle propelling by the growth of an actin network (Carlsson, 2001) have been studied with models including molecular-level processes such as barbed-end growth, pointed end depolymerization, branch formation, debranching, barbed-end capping, and barbed-end uncapping. Even more detailed approaches taking into account filament–obstacle attachments or spatial variation of actin concentration have been used to study this phenomena (Alberts and Odell, 2004).

Continuum models describe the actin gel using coarse-grained properties such as the actin concentration or the number of filaments in contact with the membrane. These methods allow predictions for larger systems over longer times at the cost of treating molecular-level events in an averaged fashion. Alike the multiple-filament models, continuum approaches have focused on lamellipodial and filopodial protrusion (Mogilner and Edelstein-Keshet, 2002, Dawes et al., 2006) as well as intracellular pathogen propulsion (Gerbal et al., 2000, Mogilner and Oster, 2003). Their predictions comprise the properties of the actin gel such as its thickness and spatial density distribution, the force–velocity relation for pathogen propulsion, the protrusion velocity for lamellipodial extension, the elastic and diffusion properties of the membrane, and the distributions of filament lengths and orientations, all of which are experimentally observable.

#### 1.1.6.2. Adhesion and retraction models

In spite of the more dynamic events occurring at the leading edge of motile cells, mechanisms involved in formation of adhesions to the substrate and retraction of the rear are equally important. Although some types of cells use non-myosin-based retraction, Myosin II has been generally implicated in retraction of the trailing edge of cells as well as breaking or removal of focal adhesions, and it has been included in several modeling works as the main cause of cell contractility (Ahmadi et al., 2005, Kruse et al., 2005). Furthermore, contractile bundles or stress fibers cannot provide work or movement without a mechanism for adhering to the underlying substrate. Therefore, the formation of focal adhesions and the mechanical cell-environment interactions have been modeled in detail with the underlying premise that forces applied to a filament have a direct effect on its polymerization (Shemesh et al., 2005) and also taking into account the interaction between the stress fibers and the integrins (Novak et al., 2004).

#### 1.1.6.3. Whole-cell models

Considering the whole cell, there exist a variety of migration models as large as the number of cell types. These models usually consider dynamical and/or mechanical phenomena including explicit molecular-scale processes such as the polymerization of actin, or less specific physical based ones such as the change in stability of a focal adhesion due to force. Similarly, cell mechanics may be treated explicitly or may be included in a phenomenological manner. Methods differ from continuum (Gracheva and Othmer, 2004) to discrete (Dokukina and Gracheva, 2010) approaches as well as finite element calculations (Bottino et al., 2002). In addition, different levels of detail are described, with time and length-scales varying significantly. Many of these studies have usually focused on 2D migration, not only for simplicity but due to the lack of high quality data of cell movement in 3D. Nevertheless, the number of 3D migration models has been gradually increasing, although focused on different aspects of cell motility. Some of them predict individual cell migration (Zaman et al., 2005, Borau et al., 2011, Schluter et al., 2012) while others simulate collective behavior (Ouaknin and Bar-Yoseph, 2009, Arciero et al., 2011). According to their main assumptions they can be grouped in: force based dynamics models, stochastic models, multi-cell spheroid migration and Monte Carlo studies. In the former ones, migration dynamics is accounted for by the traction forces at both the front and rear end of the cell and forces due to viscous drag and

cell protrusion into the ECM (Zaman et al., 2005). Imbalances of these forces produce cell migration. The drawback of these models is that they only predict migration of single cells, not taking into account changes in cell shape or ECM properties due to degradation. On the other hand, stochastic models of persistent random walks are able to predict population behavior (Parkhurst and Saltzman, 1992), however, they do not include dynamic effects such as traction or drag, neither incorporating the ECM properties. Multi-cell spheroid migration models are mainly based on pressure gradients produced by proliferation and death of cells (Pettet et al., 2001). Combining random walks, pressure and chemotactic activity of cell aggregates make them suitable to study tumours, but fail to take into account mechanical cues such as ECM density, porosity or stiffness. Finally, Monte Carlo models using square lattices and a set of simple rules allow faster simulations thus providing long-term migration patterns (Zaman, 2007, Zaman et al., 2007). The main handicap is the qualitative nature of the studied parameters such as cell-matrix interface, cell polarization or ECM mechanical effects.

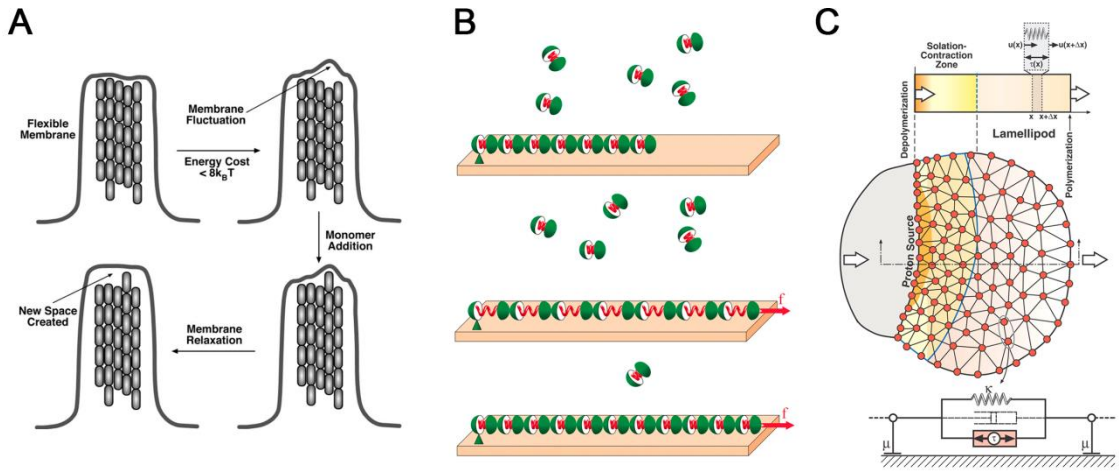


**Figure 1.5:** Examples of migration models.
A) Protrusion model of filopodia growth by Atilgan et al. 2006. B) Adhesion-retraction model of focal-adhesion mechanosensitivity by Shemesh et al. 2005 C) Whole-cell model of nematode crawling by Bottino et al. 2002.

## 1.2. Motivation, aim and scope

### 1.2.1. Motivations

The main motivation of this Thesis is to advance towards a numerical methodology for modeling cell migration, helping to understand its major role in pathological processes such as wound healing or tumour metastasis. The term "model" means that some qualitative and quantitative characteristics of the process in a living system are abstracted, idealized, and described mathematically, rather than the system itself. This abstraction, however, needs experimental validation. Although conventional cell and tissue culture experiments are useful to investigate certain biological functions, the recent advances in microculture techniques have opened the way to the next generation of *in vitro* culture studies. Microfluidic devices are gaining popularity due to their unique capability to spatially and temporally control biophysical and biochemical factors in culture. These microfluidic culture systems can be applied to a wide variety of *in vitro* studies such as angiogenesis, cultures of organ function or tumor cell migration, and allow for high quality, time-lapse imaging (Chung et al., 2010, Chung et al., 2012).

Therefore, the aim of this work is the assessment and investigation of how environmental conditions drive cell behaviour, quantifying the effects of gel stiffness, interstitial fluid flow and chemotacting gradients by the combination of microdevices and computer modeling. A further understanding of these mechanisms could provide new insights in the development of therapies and diagnosis techniques, reducing animal experiments.

In this context, this Thesis is involved in the project INSILICO-CELL-*Predictive modelling and simulation in mechano-chemo-biology: a computer multi-approach* (European Union Starting Grant / ERC-2012-StG - Proposal 306571) whose main purpose is the research of cell-cell and cell-environment interactions and the micro-fabrication of tissues *in vitro* with three main applications: wound healing, angiogenesis and bone regeneration. To achieve this, an iterative feedback between experimental design and computational modeling is proposed (Figure 1.6).

Initially this research was involved in the National Project entitled "*Modeling how mechanics influences cell migration*" and supported by the Spanish Ministry of Science and Innovation (DPI 2009-14115-CO3-01). This project was renewed and extended to the National Project "*Multiscale modeling for predictive simulation of 3D cell migration:*

*role of cell-matrix interactions*" and it is currently supported by the Spanish Ministry of Economy and Competitiveness (DPI2012-38090-C03-01). Additionally, this work is funded with the FPI grant (BES-2010-029927).

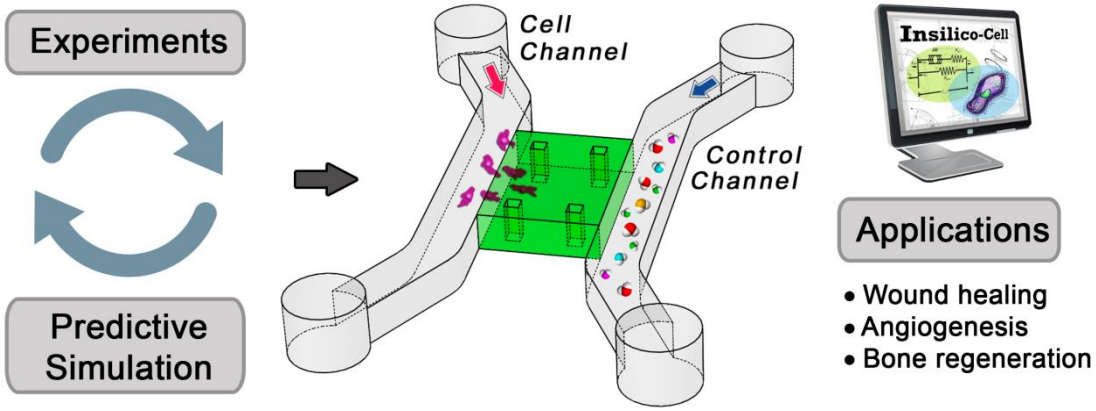


**Figure 1.6:** Experimentation-Modeling feedback.
The project INSILICO-CELL-*Predictive modelling and simulation in mechano-chemo-biology: a computer multi-approach* (European Union Starting Grant / ERC-2012-StG - Proposal 306571) proposes the combination of experiments and simulations to predict cell behavior in 3D environments.

## 1.2.2. Objectives

Based on the arguments above, the objective of this Thesis is the development of numerical and computational models to simulate several aspects of cell migration such as cell-matrix interactions or cell mechanical response depending on environmental conditions. With this purpose, continuum, discrete and finite element-based approaches are used. The main work and partial objectives are itemized below:

- To study the effect of mechanical factors (substrate stiffness, geometry and boundary conditions) on cell migration within a 3D ECM. This implies the development of a finite element (FE) single cell migration macro-model based on *mechanosensing* and including the major phases of the migratory cycle.
- To explore the internal structure of cell CSK and its response to ECM stiffness. A Brownian-dynamics particle-based computational model is used to polymerize a 3D cross-linked actin network. Molecular motors are included to analyse their active behavior and their role as *mechanosensors*. The results at the micro scale are used to validate the assumptions from the *mechanosensing* model.

- To incorporate the findings at the micro-scale (intracellular) into the macro-scale (cell) model hypothesis. The temporal network stabilization caused by motor stalling is introduced into the *mechanosensing* model by means of a continuum regulatory function, reproducing the force build-up and saturation.
- To study the fluid-chemical conditions surrounding a cell embedded in a porous medium, simulating a real micro-fluidic device using a FE approach.
- To improve the understanding of cell response depending on environment conditions. With this purpose, a probabilistic voxel FE model for single cell motility is developed, including mechanical and fluid-chemical stimulus from previous simulations.
- To analyze lamellipodium dynamics and the role of vinculin, molecular motors and focal adhesions in cell migration and exploratory functions. A finite-difference method is used for the simulations.

## 1.3. Outline

This Thesis is organized into seven chapters and three appendices. Although the contents of each chapter are treated rather distinctly, much of the material, by its very nature, is interrelated and requires the consideration of the overall picture. More specifically the Thesis is structured as follows:

**Chapter I** comprises a Thesis summary written in Spanish.

**Chapter 1 (the present one):** serves as an introduction, including the state of the art, goals and motivations and Thesis organization.

**Chapter 2** presents a brief overview of the *mechanosensing* phenomenon as well as the existing models relating this process with cell motility. Next, a 3D single cell migration model, in which it is hypothesized that *mechanosensing* is the main regulator of the directional movement, is described. Subsequently, the main assumptions as well as the steps considered (*mechanosensing*, CSK orientation and migration) are detailed, and the numerical implementation using a FE approach is depicted. Finally, the results validation and a parameter sensitivity analysis are presented.

**Chapter 3** introduces the role of cell cytoskeleton dynamics in migratory processes and describes the importance of molecular motors in cross-linked actin networks and their *mechanosensitive* properties. Following, a Brownian-dynamics computational model is presented. First, the formation of an actin network cross-linked with proteins and molecular motors is explained, as well as the parallelization of the codes to reduce computational costs. Secondly, the actin-actin, actin-protein and actin-boundary interactions are detailed. Finally, the obtained results are discussed and compared with experiments.

**Chapter 4** is entirely dedicated to revise the assumptions of the *mechanosensing* model described in Chapter 2, introducing a temporal dependence of the cell response based on the results obtained by the Brownian-dynamics model detailed in Chapter 3. This new approach is used to simulate recent experimetns of cell *mechanosensing* involving sudden changes in substrate compliance and force saturation with time and stiffness. A parameter sensitivity analysis is also included, as well as a brief discussion of the model extension to more complex 3D geometries.

**Chapter 5** summarizes the hypothesis considered so far, including them into a new migration model at the cell scale. This chapter emphasizes the importance of multiple stimuli in 3D environments and describes a probabilistic voxel FE model that addresses the cell response to several input factors, specifically: ECM stiffness, cell stress, fluid flow and chemical conditions. First, a microfluidic device simulation using FE is presented. Secondly, the probability functions, and thus the cell behavior, are tested under different environment conditions (ECM stiffness, chemical gradients, flow direction etc.). Finally the implications and possible developments of the model are discussed.

**Chapter 6** describes the key role of lamellipodium dynamics during cell-edge protrusion and retraction cycles. This chapter introduces the latest findings in experimental research as well as the most relevant modeling works regarding this issue. Next, a finite-different model is developed to validate lamellipodium-related phenomena experiments (in general) and vinculin effects on actin rearward flow experiments (specifically). Results are discussed, as well as the possible integration of the model in higher-scale approaches. Additionally, some mathematical techniques used to extract biological data from experiments are briefly reported.

**Chapter 7** concludes with a summary of the main achievements of the Thesis and the most relevant conclusions from previous chapters. In addition, the original contributions of the work are reviewed and future research lines are proposed.

**Appendix A** comprises some algorithms and numerical methods used in this Thesis which are not fully described in the corresponding chapters.

**Appendix B** describes a sensitivity analysis performed to computationally obtain the kinetic properties of a minifilament depending on the number of myosin heads. This study permits to adjust the behavior of the molecular motors used in Chapter 3, representing myosin II, with respect to the experimental kinetics measured for myosin V.

**Appendix C** includes some additional validations of the migration model described in Chapter 5 such as probability randomness or parameter sensitivity analysis. Furthermore, some assumptions of the microfluidic simulation are tested with detailed simulations at the cell scale.

Chapter 2

# COUPLING MECHANOSENSING AND CELL MIGRATION: A 3D MODEL APPROACH

This chapter describes a 3D single cell migration model assuming *mechanosensing* as the leading mechanism driving cell motility. The model formulation and main hypothesis are presented, as well as its numerical implementation using FEM. In spite of the simplifications and limitations of this approach, the outputs are in agreement with recent literature, finding that substrate stiffness, boundary conditions and external forces, regulate specific and distinct cell movements. In addition the model lays the foundation for the development of this Thesis, and its main features and results are gathered in (Borau et al., 2011).

**Contents**

## 2.1. Introduction

As it has been shown so far, cell motility is generally guided by environmental signals or cues from the surrounding microenvironment (Even-Ram and Yamada, 2005, Ehrbar et al., 2011). These cues reflect the physical–chemical nature of the ECM and its binding to transmembrane receptors, allowing cells to probe the mechanical properties of their environment and react in a specific way (Ingber, 2010). This ability of cells to sense ECM stiffness or pre-strain enables them to regulate their mechanical response and, therefore, its characterization is crucial for understanding their directional migration. It has become clear, in the last few years, that cells sense their surroundings by extending lamellipodia and filopodia that attach to the substrate, then exerting contractile forces in order to explore the mechanical properties of their environment (Discher et al., 2005). These active forces are generated by myosin motors and are transmitted to the ECM by means of transmembrane proteins (integrins) that often cluster to form focal adhesions (Bershadsky et al., 2003, Yang and Zaman, 2007, Yang and Zaman, 2010). The influence of the stiffness and topography of the ECM is critical to this process, and has been thoroughly investigated (Lo et al., 2000, Engler et al., 2004a, Yeung et al., 2005, Saez et al., 2007, Ghibaudo et al., 2008, Baker et al., 2009, Janmey et al., 2009, Mitrossilis et al., 2009, Sanz-Herrera et al., 2009, Ehrbar et al., 2011, Harunaga and Yamada, 2011, Trichet et al., 2012, Ghassemi et al., 2012).

One important finding is that cells prefer to migrate to the stiffer part of the ECM or substrate (Lo et al., 2000, Cukierman et al., 2001, Bischofs and Schwarz, 2003, Schwarz and Bischofs, 2005). Focal adhesions are more stable and contraction forces increase on stiffer substrates (Lo et al., 2000, Ghibaudo et al., 2008, Mitrossilis et al., 2009, Cukierman et al., 2001, Trichet et al., 2012, Ghassemi et al., 2012). However, whether cells are able to sense stress or strain is still unclear (Freyman et al., 2002, Saez et al., 2005, De et al., 2008). Furthermore, the application of external stress/strain on the cell also stimulates focal adhesion formation and subsequent strengthening (Riveline et al., 2001, Kaverina et al., 2002) and therefore, this stress can trigger molecular reorganization and CSK adaptation.

Cell migration studies have primarily focused on migration on 2D substrates. These studies have helped to elucidate the mechanisms by which cells migrate, interact with the substrate or change their speed. However, when completely surrounded by the ECM, cells experience a different environment and some factors that were not present in 2D appear,

such as the role of volume exclusion (Simpson et al., 2010) and relevant differences in cell morphology, adhesions and signaling (Fraley et al., 2010, Hakkinen et al., 2011).

Therefore, to fully understand how cells migrate *in vivo*, it is necessary to study the movement of cells in 3D environments. In recognition of this need, experimental 3D cell movement studies (Friedl and Brocker, 2000, Cukierman et al., 2002, Vickerman et al., 2008, Chung et al., 2012) and modeling efforts (Zaman et al., 2005, Harjanto and Zaman, 2010, Groh and Wagner, 2011) have been growing in number in the recent past. In fact, although most models for cell migration have been developed for 2D conditions, more recently, 3D models have appeared.

Among the possible classifications described in the previous chapter, all of these models may be generally grouped as either continuum or discrete approaches. On one hand, most continuum models are based on reaction diffusion equations for cells and diffusive chemicals (Manoussaki, 2003, Moreo et al., 2008, Häcker, 2011). In general terms, these continuum approaches have the following limitations: they are valid only when there are weak cell-cell interactions and they underestimate volume exclusion effects that are present in 3D (Simpson et al., 2010). On the other hand, discrete models have also been developed. These are of two main types: lattice models and interaction-force based models. The former ones can be subdivided into two approaches: cellular automata models (Chopard et al., 2010) and cellular Potts models (Chen et al., 2007, Merks and Koolwijk, 2009). Their main limitations are that they do not include the role of cell mechanical properties and they are mainly phenomenologically based approaches, requiring many nonphysical parameters to be determined from experiments. Finally, the so-called force-based dynamics method (Zaman et al., 2005) normally uses single cells as basic units, each of which is characterized by its location and orientation, its state of stress and the active forces it can exert in response to the local microenvironment. Knowing this for each cell, the velocity of each individual cell can be evaluated through the equilibrium of forces. Normally, the differences among models are based on the consideration of different kinds of forces that define this equilibrium. Using this approach, a mathematical model for cell movement in multicellular systems has been developed (Palsson, 2001), incorporating viscoelastic properties of cells to simulate 3D cell movement during aggregation and the slug stage of Dictyostelium discoideum, embryogenesis, limb formation and wound healing. Three main forces are considered in this work: passive, active and a viscous drag force. The active force is due to a chemotactic signal and the passive force takes into account the elastic interactions

between neighboring cells. Other force-based dynamics approaches (Zaman et al., 2005, Harjanto and Zaman, 2010) have been used to model the movement of individual cells in 3D, considering a more realistic cell–matrix interaction and taking into account the receptor–ligand adhesivity. A recent study on single-cell migration in 3D has been presented, based on this approach (Groh and Wagner, 2011), where chemotaxis as well as contact guidance are considered to regulate cellular movement. Although all these models take into account many different effects through the forces that regulate cell migration, none of them have incorporated *mechanosensing*. This mechanism is associated with the active contractile forces that cells exert on their surroundings in order to probe the mechanical environment (Discher et al., 2005, Sen et al., 2009).

This chapter describes a 3D single cell migration model in which *mechanosensing* is the main regulator of the directional movement. The main mechanically relevant components of the cell are taken into account, as well as the contraction forces exerted on the ECM/substrate and the major phases in cell migration. These phases are grouped in: (i) *mechanosensing* through cell contractility, (ii) cell polarization/adaptation that can influence directional cell motility by means of the formation of the leading and trailing cell edges and (iii) the cell movement in 3D. With these assumptions, the model qualitatively predicts some features such as cell movement tendencies, traction forces and cell speeds in several substrates with different stiffnesses and under different mechanical constraints. The premise of this work is that a better understanding of all these features provides new possibilities to guide and regulate tissue regeneration, and is therefore useful for the design of new biomaterial scaffolds aiming at optimizing mechanical conditions to control cell migration for tissue engineering applications or medical device designs.

## 2.2. Model formulation

The model mainly focuses on the mechanical interaction of an individual cell with the ECM/substrate. The migration of a single cell is computed to isolate the mechanical inputs from other possible intercellular interactions. Chemical or other factors are not taken into account, thereby, the cell movement is only regulated by the mechanical properties of the matrix and the cell–matrix interactions. As previously described, when a cell migrates, complex-coupled and cyclic mechanisms are activated regulating its movement, which includes polarization, protrusion and adhesion, contraction of the cell

body and retraction of the rear. The cell embedded within the gel extends filopodia and/or lamellipodia possibly to sense the surrounding mechanical conditions. Contractile forces are exerted to evaluate the substrate stiffness, and consequently the substrate (and the cell) are stressed and strained (Buxboim et al., 2010). According to this, the cell's CSK adapts, and the cell becomes directionally polarized. More focal adhesions develop at the front than at the rear. Detachment of rear adhesions leads to the imbalance of traction forces that they can support, subsequently resulting in the contraction and forward movement of the cell. In this model these mechanisms are simplified into three fundamental ones: *mechanosensing*, CSK adaptation and cell movement. Although they occur simultaneously, for simplicity, they are considered here independent but interrelated mechanisms. In fact, these three different mechanisms are coupled assuming that all of them are regulated by the contraction stress exerted by the cell on the ECM/substrate during the *mechanosensing* phase.

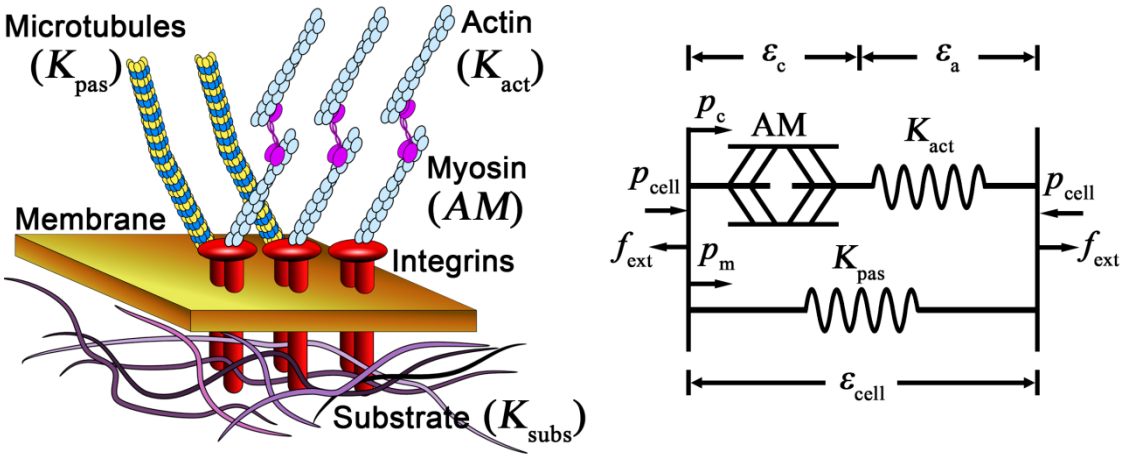


**Figure 2.1:** Schematic diagram of cell mechanical components.
Actin bundles are modeled as spring ($K_{act}$) in series with the acto-myosin (AM) contractile system. These components act in parallel with the passive elements of the cell cytoskeleton ($K_{pas}$).

### 2.2.1. Mechanosensing mechanism

The CSK is a dynamic structure that maintains cell shape (Wang et al., 2001), protects it and plays an important role in different processes such as cell division (Heng and Koh, 2010), intracellular transport (Damania et al., 2010) or cell locomotion (Burnette et al., 2011). The behavior of this structure is complex and various approaches have been

adopted to model its interesting rheological (Astrom et al., 2008, Astrom et al., 2009, Kim et al., 2009a, Kim et al., 2009b, Kim et al., 2011) and contractile properties (Deshpande et al., 2006, McGarry et al., 2009, Borau et al., 2012). In this work, and based on a previous approach (Moreo et al., 2008), a simplified model is proposed. The cell body is represented using a spring-like structure with a contractile actuator (Figure 2.1). The cellular elements responsible for the cell mechanics behavior considered here are the actin bundles ($K_{act}$), the actomyosin contractile apparatus (*AM*) and the passive mechanical stiffness of the rest of the cell whose main contribution comes from the cytoskeleton microfilaments and the membrane ($K_{pas}$). The CSK is linked with the ECM/substrate through focal adhesions and transmembrane integrins that are assumed perfectly rigid.

The stress effectively transmitted by the cell to the ECM ($p_{cell}$) depends on the cell strain ($\varepsilon_{cell}$). This strain can be decomposed into two parts: the strain in the actin bundles ($\varepsilon_a$) and the strain in the contractile *AM* system ($\varepsilon_c$). Therefore:

$$\varepsilon_{cell} = \varepsilon_c + \varepsilon_a \tag{2.1}$$

and since the actin bundles are modeled as a spring with a stiffness $K_{act}$, $\varepsilon_a$ can be expressed as:

$$\varepsilon_a = \frac{p_c}{K_{act}} \tag{2.2}$$

The stress that the cell effectively transmits to the ECM/substrate corresponds to the sum of the contribution of the active actin–myosin component and the stress absorbed by the passive elements ($p_c$ and $p_m$ respectively):

$$p_{cell}(\varepsilon_{cell}) = p_c + p_m = p_c(\varepsilon_c) + K_{pas}\varepsilon_{cell} \tag{2.3}$$

The active stress contribution of the actin–myosin motors ($p_c$) is related to the extension/contraction (overlap) between the actin–myosin filaments ($\varepsilon_c$)(Rassier et al., 1999). Here, according to the classical Huxley's law (Huxley, 1957), the following form is assumed:

$$p_c(\varepsilon_c)=\begin{cases}0 & \varepsilon_c<\varepsilon_{min}\\ \dfrac{p_{max}}{-\varepsilon_{min}}\left(\varepsilon_c-\varepsilon_{min}\right) & \varepsilon_{min}<\varepsilon_c<0\\ \dfrac{p_{max}}{\varepsilon_{max}}\left(\varepsilon_{max}-\varepsilon_c\right) & 0<\varepsilon_c<\varepsilon_{max}\\ 0 & \varepsilon_{max}<\varepsilon_c\end{cases} \tag{2.4}$$

Hence, four different zones can be distinguished as a function of the value of ($\varepsilon_c$) as shown in Figure 2.2A. Without external loads, the mechanical equilibrium is governed by the *AM* contractile system that contracts the cell body (Zone 2: $\varepsilon_{min}<\varepsilon_c<0$) and causes tension on the cell surroundings. Under too high external compression (Zone 1: $\varepsilon_c<\varepsilon_{min}$ ), the *AM* contractile system is not able to exert contraction. However, when there are external loads causing cell extension (Zones 3 and 4), cell contraction is compensated decreasing the *AM* contractile action until reaching $\varepsilon_{max}$ where its force contribution equals 0.

In summary, combining equations (2.1), (2.2), (2.3) and (2.4), equation (2.3) can be rewritten and the magnitude of $p_{cell}$ can be expressed as follows:

$$p_{cell}(\varepsilon_{cell})=\begin{cases}K_{pas}\varepsilon_{cell} & \varepsilon_{cell}<\varepsilon_{min}\\ \dfrac{K_{act}p_{max}}{K_{act}\varepsilon_{min}-p_{max}}\left(\varepsilon_{min}-\varepsilon_{cell}\right)+K_{pas}\varepsilon_{cell} & \varepsilon_{min}<\varepsilon_{cell}<p_{max}/K_{act}\\ \dfrac{K_{act}p_{max}}{K_{act}\varepsilon_{max}-p_{max}}\left(\varepsilon_{max}-\varepsilon_{cell}\right)+K_{pas}\varepsilon_{cell} & p_{max}/K_{act}<\varepsilon_{cell}<\varepsilon_{max}\\ K_{pas}\varepsilon_{cell} & \varepsilon_{max}<\varepsilon_{cell}\end{cases} \tag{2.5}$$

which is plotted in Figure 2.2B together with $p_c(\varepsilon_{cell})$.

Although the description thus far has been in terms of a scalar stress, it is now extended to three dimensions using $p_{cell}$ to compute an effective stress tensor $\boldsymbol{\sigma}_{cell}$. It is assumed that the cell occupies a spherical space, with constant shape and volume. However, the cell is exerting anisotropic forces on its immediate surroundings depending on the temporal evolution of the CSK polarization. Considering this *mechanosensing* model, the total cell stress tensor $\boldsymbol{\sigma}_{cell}$ is a function of the total cell strain tensor $\boldsymbol{\varepsilon}_{cell}$ and

consists of two terms related to the orientation of the CSK. One term is isotropic and dependent on the volumetric strain ($\theta_{cell}$)(trace of the cell strain tensor $\boldsymbol{\varepsilon}_{cell}$) considering that the cell body contracts in all directions. The other is anisotropic depending on the direction of the CSK polarization ($\mathbf{d}_{pol}$), and the longitudinal deformation in the polarization direction ($\varepsilon_{cell} = \mathbf{d}_{pol}^{T} \cdot \boldsymbol{\varepsilon}_{cell} \cdot \mathbf{d}_{pol}$). Hence, the following expression defines the stress behavior of the cell:

$$\boldsymbol{\sigma}_{cell} = p_{cell}(\varepsilon_{cell})\mathbf{d}_{pol} \otimes \mathbf{d}_{pol} + p_{cell}(\theta_{cell})\mathbf{I} \tag{2.6}$$

where $\mathbf{I}$ is the identity second-order tensor and $\mathbf{d}_{pol}$ is the direction of polarization of the CSK which is described in the following subsection.

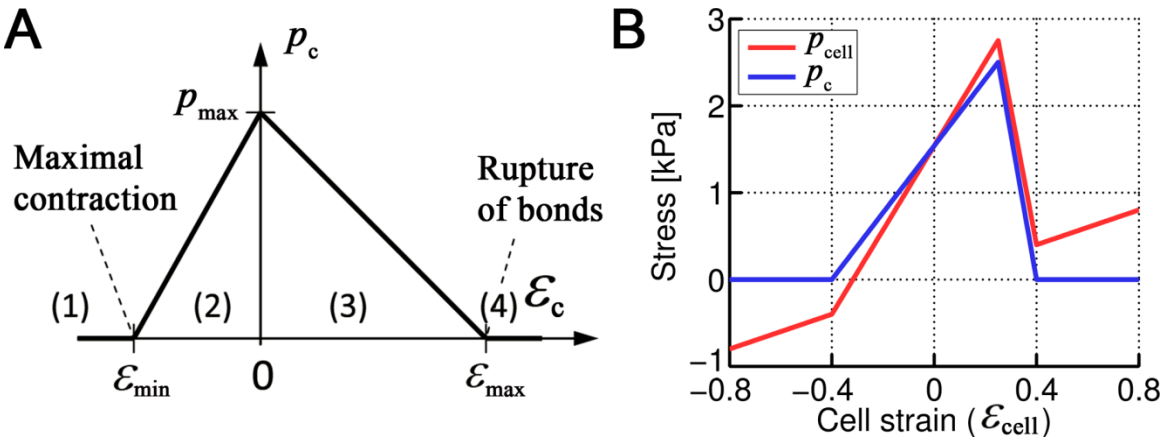


**Figure 2.2:** Acto-myosin contraction dependence.
A) Function of $p_c(\varepsilon_c)$. Zone 1: passive behavior, external loads compress the cell. Zone 2: contraction, the cell exerts contractive forces to sense its surroundings. Zone 3: tension, the cell is being stretched by external loads but still contracts itself against those forces. Zone 4: passive behavior, external loads stretch the cell. B) Dependence of $p_c$ and $p_{cell}$ on $\varepsilon_{cell}$ corresponding to equation (2.5) and for the parameters collected in Table 2-1.

The global mechanical equilibrium has to be fulfilled in the cell body and in the substrate, which is modeled as a linear elastic solid to a first approximation. The ECM or substrate stress tensor ($\boldsymbol{\sigma}_{subs}$) must be in equilibrium with the external forces applied ($\mathbf{f}_{ext}$) e.g. a needle inserted in the matrix exerting pulling or pushing forces:

$$\begin{aligned} \nabla(\boldsymbol{\sigma}_{cell}) &= 0 \quad \text{in} \quad \Omega_{cell} \\ \nabla(\boldsymbol{\sigma}_{subs}) &= \mathbf{f}_{ext} \quad \text{in} \quad \Omega_{subs} \end{aligned} \tag{2.7}$$

To solve these mechanical equilibrium equations, the finite element method (FEM) is used, as detailed in next sections.

## 2.2.2. CSK adaptation

Here, it is hypothesized that the *mechanosensing* mechanism permits the cell to detect the principal directions ($\mathbf{d}_\varepsilon$) of the cell strain tensor $\boldsymbol{\varepsilon}_{\text{cell}}$, and that the CSK is reoriented according to them. Initially, the cell is assumed to be an isotropic and homogeneous body embedded in the ECM. Consistent with previous experimental observations (Schwarz and Bischofs, 2005), the active actin-myosin fibers are assume to develop preferentially parallel to the direction of lower principal strain or higher principal stress. Hence, the cell is assumed to align gradually with the closer principal strain direction (see Figure 2.3A) as follows:

$$\Delta\mathbf{d}_{\text{pol}} = \frac{d\mathbf{d}_{\text{pol}}}{dt}\Delta t = \kappa\left(\mathbf{d}^i_{\text{pol}} \times \left(\mathbf{d}_\varepsilon \times \mathbf{d}^i_{\text{pol}}\right)\right)\Delta t \tag{2.8}$$

where the index *i* denotes the time step and $\mathbf{d}_\varepsilon$ is the principal strain direction, which forms the lower angle ($\alpha$) with the previous polarization direction $\mathbf{d}^i_{\text{pol}}$. The symbol $\kappa$ is the constant of reorientation ($\text{min}^{-1}$) and determines how fast the vectors align. Once this direction is defined, it is updated:

$$\mathbf{d}^{i+1}_{\text{pol}} = \mathbf{d}^i_{\text{pol}} + \Delta\mathbf{d}_{\text{pol}} \tag{2.9}$$

Note that at the end of each time step, $\mathbf{d}^{i+1}_{\text{pol}}$ is normalized, becoming the unitary vector $\mathbf{d}^i_{\text{pol}}$ for the next time step.

The rate of reorientation ($\kappa$) is assumed to be 1/30 $\text{min}^{-1}$, which means that when $\mathbf{d}_\varepsilon$ and $\mathbf{d}_{\text{pol}}$ are perpendicular, the cell is able to orientate its CSK $\pi/4$ degrees in a single time step to align with $\mathbf{d}_\varepsilon$. It has been observed in experiments (Wang et al., 2000, Hayakawa et al., 2001, Yoshigi et al., 2005) that cells remodel their cytoskeleton on a timescale of tens of minutes to hours. This timescale has been also used in other modeling works (De et al., 2007).

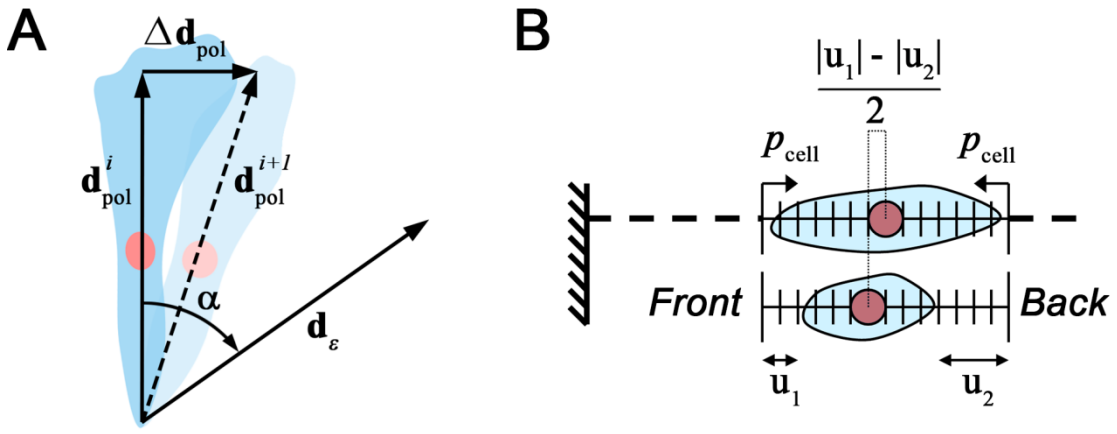


**Figure 2.3:** CSK reorientation and definition of cell's front/back.
A) Scheme of the direction of polarization of the current time step ($\mathbf{d}_{pol}^{i}$) rotating toward the nearest principal strain direction ($\mathbf{d}_{\varepsilon}$). B) One-dimensional representation of the cell's front/back definition following a centroid-displacement criterion.

### 2.2.3. Migration

The last mechanism to be modeled is the cell movement as dictated by an equilibrium of forces on the cell centroid (Zaman et al., 2005). It is important to clarify that this mechanism is considered here totally distinct from the *mechanosensing* one, although they are obviously interdependent. Thus, the stress equilibrium (equation (2.7)) is not affected by the subsequent formulation, since in this model, migration occurs sequentially following *mechanosensing* and CSK remodeling. Nevertheless, it is assumed that they are related through $p_{cell}(\varepsilon_{cell})$. Focusing on the equilibrium of forces for each single cell, three distinct types of independent forces acting on the cell are considered, defining cell movement according to:

$$\mathbf{F}_{tot} = \mathbf{F}_{prot} + \mathbf{F}_{drag} + \mathbf{F}_{trac} = \mathbf{0} \tag{2.10}$$

The protrusive force, $\mathbf{F}_{prot}$, is needed to extend membrane processes and is independent of myosin motors. It arises from actin polymerization and cell–matrix interactions and introduces stochastic behavior to the model. It is calculated as a vector with random direction with magnitude proportional to $p_{cell}(\varepsilon_{cell})$. This implies that the direction of cell migration is always random in the absence of any effect of chemotaxis, haptotaxis or durotaxis.

The second force, $\mathbf{F}_{\text{drag}}$, represents the resistance to movement, which is proportional to the cell speed ($\mathbf{v}_{\text{cell}}$):

$$\mathbf{F}_{\text{drag}} = \eta \mathbf{v}_{\text{cell}} \tag{2.11}$$

where $\eta$ is an effective viscosity that reflects the sum of all dissipation effects including viscous friction as well as the energy dissipated by the rupture of bonds under tension. Based on the approach proposed in (Dokukina and Gracheva, 2010), this viscosity coefficient is assumed as a linearly increasing function of the substrate stiffness ($K_{\text{subs}}$), where $c_{\text{vis}}$ (μm min) is its slope. This function was slightly modified from that used in (Dokukina and Gracheva, 2010), incorporating a minimum value of viscosity $\eta_0$ (μN min μm$^{-1}$) (see Table 2-1):

$$\eta = \eta_0 + c_{\text{vis}} K_{\text{subs}} \tag{2.12}$$

The third force, $\mathbf{F}_{\text{trac}}$, is the traction force exerted by the cell in order to move. It has two contributions, the traction force at the front part of the cell ($\mathbf{F}_{\text{trac}}^{\text{F}}$) and the traction force at the rear ($\mathbf{F}_{\text{trac}}^{\text{B}}$). The definition of the front and the rear parts of the cell is assumed to be intrinsic to the *mechanosensing* mechanism presented here. When the cell contracts its body, its centroid displaces toward the more constrained side following the imposed boundary conditions or the stiffness variations, establishing in this way the 'front' (Figure 2.3B). Since focal adhesions tend to exhibit higher density at the front, the rear adhesions experience more stress per bond and tend to detach. Even though this behavior is highly dynamic, it is assumed for simplicity that there is a constant difference in strength between the front and back receptors. To reflect this, similar to (Zaman et al., 2005), a dimensionless 'adhesivity' ($\beta$) at the front and back parts of the cell is introduced. In addition, this term is assumed proportional to the ratio of cell receptors ($n_{\text{F}}, n_{\text{B}}$), the ligand concentrations ($[L_{\text{F}}], [L_{\text{B}}]$) and the binding constants for the binding of integrins of the cell to the ligands in the ECM ($k_{\text{F}}, k_{\text{B}}$):

$$\begin{aligned} \beta_{\text{F}} &= k_{\text{F}} n_{\text{F}} [L_{\text{F}}] \\ \beta_{\text{B}} &= k_{\text{B}} n_{\text{B}} [L_{\text{B}}] \end{aligned} \tag{2.13}$$

In the current model, it is assumed that as the cell polarizes and adaptates, integrins are distributed asymmetrically on the cell surface ($n_F > n_B$). During migration, the majority of integrins shift to the leading edge of the cell (Lauffenburger and Horwitz, 1996, Harjanto and Zaman, 2010), so it is considered here that 95% of the total number of receptors are localized at the front. Also for simplicity, it is assumed that $k_F = k_B$ and $[L_F] = [L_B]$, considering that the ligand density is spatially uniform throughout the matrix, at least initially. It is important to note that matrix metalloproteinases produced by migrating cells can alter the ligand density in the extracellular matrix. Furthermore, cells can also synthesize new matrix components with associated adhesion receptor ligands and can cause deformations in the matrix due to cell contraction. The dynamics of these processes may be important for modulation of migration through the matrix, but in this first version of the model their effects have not been included. Under these assumptions, the traction force magnitude, depends upon the cell stress $p_{cell}$ and the area over which it is applied ($a_a$). Cells transmit mechanical forces to the ECM through focal adhesions, which dynamically assemble and disassemble during cell migration. However, both the composition and the morphology of focal adhesions change during cell migration but the mechanism is complex and still poorly understood. Establishing a constant parameter to simulate the contact area is a first approach to this problem. Therefore, $a_a$ was fitted to obtain contractile forces and cell speeds similar to those observed in experiments performed with fibroblasts (Zaman et al., 2005, Hakkinen et al., 2011). With all this, traction forces are exerted in the direction of polarization ($\mathbf{d}_{pol}$) and can be expressed as:

$$\begin{aligned} F_{trac}^{F} &= \beta_F p_{cell} a_a \mathbf{d}_{pol} \\ F_{trac}^{B} &= \beta_B p_{cell} a_a \mathbf{d}_{pol} \end{aligned} \tag{2.14}$$

The resultant traction force ($\mathbf{F}_{trac}$) is the difference of the traction forces at the front and the rear:

$$\mathbf{F}_{trac} = \mathbf{F}_{trac}^{F} - \mathbf{F}_{trac}^{B} = (\beta_F - \beta_B)\, p_{cell} a_a \mathbf{d}_{pol} \tag{2.15}$$

Cell speed can be therefore calculated from equations (2.10) and (2.11) and the new cell position can be determined:

$$\mathbf{v}_{cell} = \left(\mathbf{F}_{prot} + (\beta_F - \beta_B)\, p_{cell} a_a \mathbf{d}_{pol}\right)\eta^{-1} \tag{2.16}$$

## 2.3. Numerical implementation

This model has been implemented using three distinct, sequential processes at each time step (*mechanosensing*, polarization and migration), following the loop shown in Figure 2.4. This simplified analysis in three different computations aims to replicate the most relevant mechanisms used by individual cells to migrate. As initial conditions it is assumed that both the substrate and the cell are completely unloaded; thus, the displacement, strain and stress fields are zero in the whole domain. Also, it is considered that the cell is not polarized and its initial position is specified. In addition, at the beginning of each step of analysis, the stress/strain fields are assumed to be zero in both the cell body and the substrate. At the end of each time step, the location and the polarization of the cell are updated.

Now these three analyses that define one time step are briefly described. First, the *mechanosensing* analysis provides a calculation of the strain field in the ECM and the cell strain due to the cell contraction. To solve this mechanical problem, the FEM is used through a commercial software package (Simulia- ABAQUS FEA 6.10) including user subroutines to incorporate the active behavior of the cell. Specifically the UEL subroutine is utilized to define the features of cell and ECM elements. For the implementation, the cell body is modeled as a single hexahedron element. This simplification highly facilitates the computation of the mechanical problem since it allows using regular hexahedrons (element type: C3D8) for both ECM and cell (20×20×20 μm shape). To start the simulation, the cell is initially placed in a specific element and exerts contraction forces to sense its surroundings (equation (2.6)). In this first step, the contraction is isotropic as the cell is not yet polarized. The element is compressed in all directions and its neighbors are under tension. These forces produce displacements, strains ($\boldsymbol{\varepsilon}_{\text{cell}}$ and $\boldsymbol{\varepsilon}_{\text{subs}}$) and stresses ($\boldsymbol{\sigma}_{\text{cell}}$ and $\boldsymbol{\sigma}_{\text{subs}}$) on the cell and the substrate, respectively.

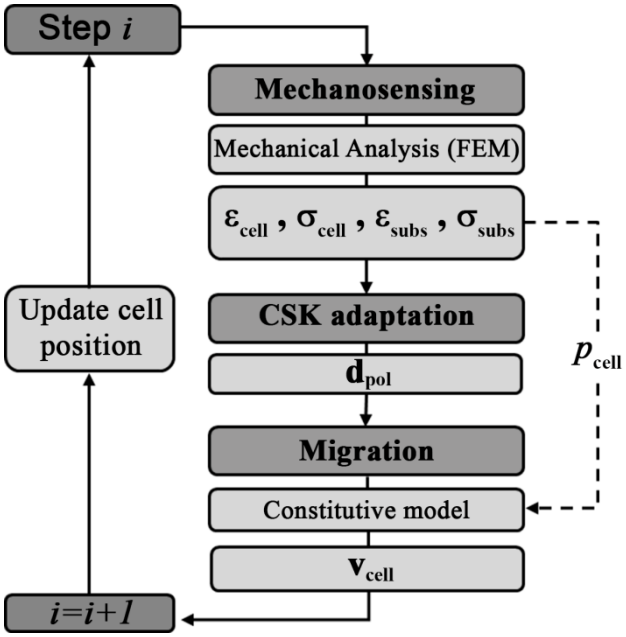


**Figure 2.4:** Computational algorithm. First the cell exerts contraction forces on the ECM in order to sense its surroundings (*mechanosensing*). The stress and strain produced in the ECM regulate the cell polarization (CSK adaptation). After that, the traction forces exerted to move are computed to determine the cell speed (migration). When a new position is computed, this loop is repeated.

The second analysis corresponds to the cell polarization or CSK adaptation. It consists of an algorithm to evaluate the orientation of the cell body. Through the nodal displacements and using linear shape functions, the tensor $\boldsymbol{\varepsilon}_{cell}$ and its principal directions ($\mathbf{d}_{\varepsilon}$) are evaluated, as well as $p_{cell}$ and all the related variables. For simplification it is aasumed that the cell reorients in each step with one of the principal strain directions. In the first step, $\mathbf{d}_{pol}$ is still undefined, so initially the direction of minimum contraction ($\mathbf{d}_{\varepsilon 1}$), and therefore maximum $p_{cell}$, is selected. In successive steps, the direction is not always the first one, but closer to the polarization direction as was previously described. This means that the cell tends to migrate in the direction in which it is already oriented; however, this does not imply that the cell moves in a unidirectional manner since it slowly reorients to migrate toward preferred zones. Thirdly, after sensing and reorientation, migration is computed taking into account the equilibrium of forces (equation (2.10)), evaluating cell speed from equation (2.16) and updating the new position of the cell. Although a regular mesh was used to compute the simulations, a general algorithm to find the cell inside the ECM was developed. This code, described in Appendix A, is capable of finding the cell centroid inside irregular elements as long as they are hexahedrons and have 8 nodes. Hence, the model is prepared to run also in complex geometries. In all the examples, the total time analyzed is 9 h with a time increment of 30 min.

| Symbol | Variable | Value | Reference |
|---|---|---|---|
| $K_{pas}$ | Passive cell stiffness | 0.001 [MPa] | (Schafer and Radmacher, 2005) |
| $K_{act}$ | Actin stiffness | 0.01 [MPa] | (Schafer and Radmacher, 2005) |
| $\varepsilon_{min}$ | Minimum strain (maximum overlap) | -0.4 | (Moreo et al., 2008) § |
| $\varepsilon_{max}$ | Maximum strain (minimum overlap) | 0.4 | (Moreo et al., 2008) § |
| $p_{max}$ | Maximum stress exerted by the *AM* system | 2.5 [kPa] | (Maskarinec et al., 2009) |
| $\kappa$ | Reorientation rate | 0.0333 [$min^{-1}$] | * |
| $K_{subs}$ | Substrate stiffness | 0.001-0.5 [MPa] | (Dokukina and Gracheva, 2010) |
| $c_{vis}$ | Viscosity slope | 0.4 [µm min] | (Dokukina and Gracheva, 2010) § |
| $\eta_0$ | Viscosity constant | 0.07 [µN min $µm^{-1}$] | (Dokukina and Gracheva, 2010) § |
| $k_F, k_B$ | Binding constant at the cell's front/back | $10^8$ [$M^{-1}$] | (Zaman et al., 2005, Harjanto and Zaman, 2010) |
| $n_F, n_B$ | Ratio of receptors at the cell's front/back | 0.95, 0.05 | (Schmidt et al., 1993, Harjanto and Zaman, 2010) |
| $[L_F], [L_B]$ | Lingand density at the cell's front/back | $10^{-8}$ [$M^{-1}$] | (Harjanto and Zaman, 2010) |
| $a_a$ | Effective area of traction | 55 [$µm^2$] | * |
| $\Delta t$ | Time increment | 30 [min] | (Zaman et al., 2005) |
| $E_1, E_2$ | Young's modulus of the substrate | 0.001, 0.04 [MPa] | (Dokukina and Gracheva, 2010) |
| $\nu$ | Poisson's ratio of the substrate | 0.3 | (Bischofs and Schwarz, 2003, Schwarz and Bischofs, 2005) |

**Table 2-1:** Major parameters used in the model
* Estimated parameters
§ Parameters derived from the referenced manuscript

## 2.4. Model outputs

This section starts describing the model response for different sets of parameters (sensitivity analysis) and follows with a sample of migration calculation with fixed parameters and different boundary conditions. Finally, a simulation including external loads is briefly discussed.

### 2.4.1. Parameter sensitivity

The model has the capability of capturing a wide variety of behaviors by appropriate selection of the model parameters. A sensitivity analysis is performed in order to illustrate some types of behavior that can be produced and also to better understand the relative importance of the major parameters. All the reference values used in all the simulations are in Table 2-1.

The actin stiffness ( $K_{act}$ ) is a critical factor which determines the magnitude of the forces ( $p_{cell}$ ) exerted during *mechanosensing*. By virtue of the model construction, it also determines the magnitude of traction forces and therefore the velocity. It is interesting to note that the dependence of cell speed on substrate stiffness is bi-modal, having a peak at substrate stiffness of about 20–30 kPa (Figure 2.5A). Traction forces increase with substrate stiffness until saturationand decrease for lower values of $K_{act}$ (Figure 2.5B). Consequently, low values of $K_{act}$ lead to slower cell motion over the entire range of substrate stiffness in comparison with the reference value (Figure 2.5A). The reason is that increasing the value of $K_{act}$ leads to lower *AM* overlap, reducing contraction and causing higher forces with the same substrate stiffness. Therefore cell speed increases accordingly. Interestingly, the value of $K_{pas}$, although also important, plays a significant role only when its value is similar to the substrate stiffness (data not shown).

As described in equation (2.12), the viscosity is assumed to increase linearly with substrate stiffness, and its value strongly affects cell behavior. In fact, viscosity saturates, but it happens outside the rigidity range of this study (Saez et al., 2005). The speed is very sensitive to the value of $\eta_0$ for the range of stiffness tested, since it defines the minimum viscosity in softer substrates. If this factor is decreased, the cell can reach higher velocities in compliant substrates (Figure 2.5C). In addition, the velocity peak is displaced so that maximum speeds are achieved in softer substrates compared to the control case. Consequently, increasing $\eta_0$ produces opposite effects. Nevertheless, the slope $c_{vis}$ also significatively affects the velocity, more markedly at high stiffness. This effect is due to the saturation of forces in stiffer substrates. As can be deduced from equation (2.16), if the viscosity keeps increasing with stiffness while the force ( $p_{cell}$ ) remains mostly unchanged the cell speed tends to decrease, to lower values the faster the

viscosity increases (higher $c_{vis}$). Hence, if this factor is decreased, the velocity increases and the point of maximum speed is displaced to a higher substrate stiffness (Figure 2.5D).

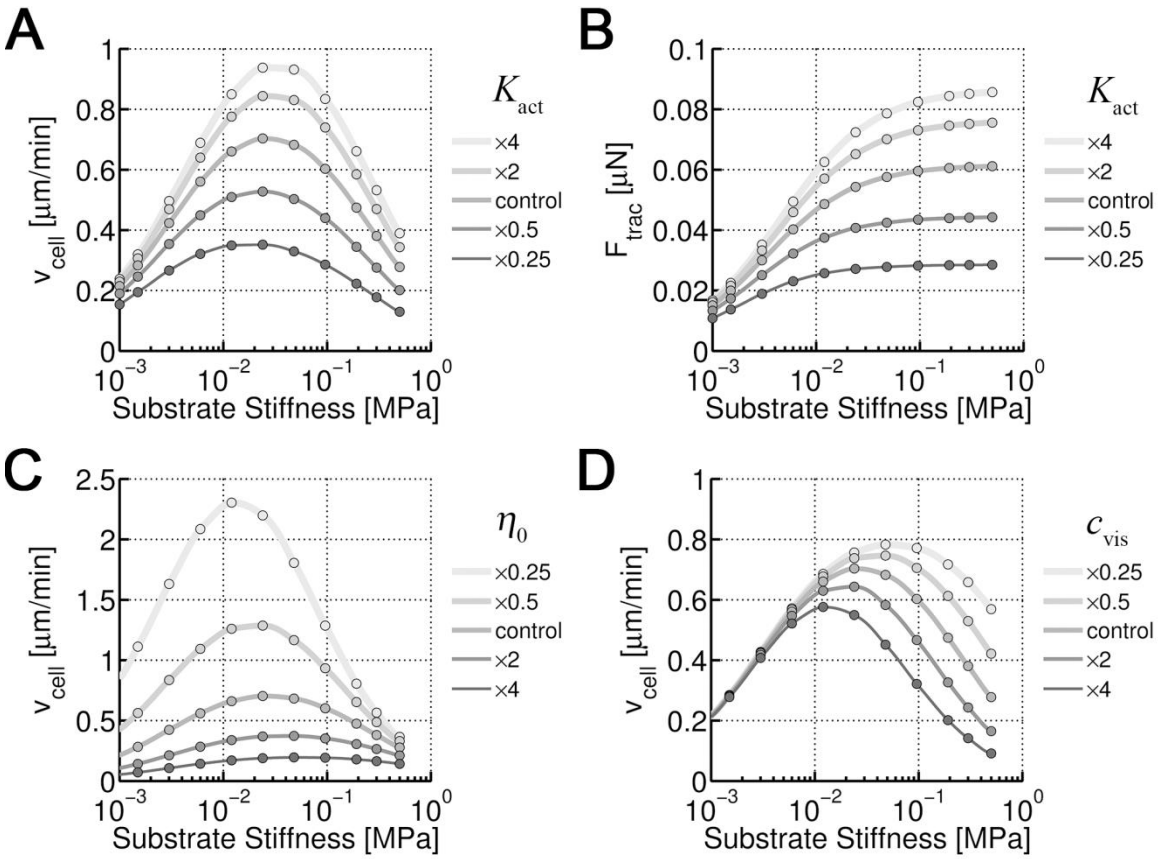


**Figure 2.5:** Parameter sensitivity analysis
A) Cell speed ($v_{trac}$) and B) traction force ($F_{trac}$) depending on substrate stiffness for several values of actin stiffness ($K_{act}$). C) Cell speed depending on substrate stiffness for different values of minimum viscosity ($\eta_0$) and D) viscosity slope ($c_{vis}$).

## 2.4.2. Sample of calculation

A 3D ECM is simulated, which consists of a rectangular cuboid of the following dimensions: 1400 × 700 × 700 µm, with two different rigidities ($E_2 = 0.04$ MPa, $E_1 = 0.001$ MPa) under different boundary conditions listed below for each of the three examples analyzed here (Figure 2.6).

*Case 1*: The stiffer side is constrained (fixed nodes on the left surface) and the softer side is free of external loads (on the right surface). The remaining four surfaces are also free of external loads.

*Case 2*: Both sides are constrained (fixed nodes on left and right surfaces). The remaining four surfaces are free of external loads.

*Case 3*: The stiffer side is free of loads (on the left surface), whereas the softer side is constrained (fixed nodes on the right surface). The remaining four surfaces are also free of external loads.

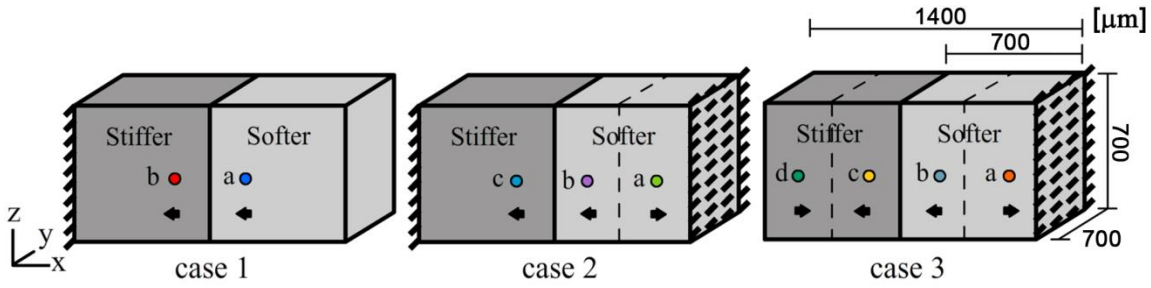


**Figure 2.6:** Simulated cases.
The size of the computational domain is 1400 × 700×700 μm. Black arrows represent the direction of migration. Dotted lines represent zones where a change in the migration direction is observed. Circles in each case represent schematically the initial cell position for each subcase.

A regular mesh of 85750 hexahedron elements (C3D8) is used. Simulated time is 9 h, whereas the computational time is 30 min. Although only some results corresponding to different initial positions in each case are shown (subcases), many simulations have been performed, finding similar and consistent patterns. At least ten repetitions per subcase were tested. The computed trajectories of migration were all different due to the stochastic behavior; however, the general trend was consistent for each subcase. Hence, for clarity, only one of the examples for each subcase is plotted in Figure 2.7. As the boundary conditions change along the x-axis, the principal results are discussed focusing on migration in the x-direction. Note that all the subcases are referred as *c-casenumber-letter*.

In the first case, no matter where the cell is initially placed, either in the softer side (c1a) or the stiffer side (c1b), since it always moves toward the constrained side, which also has the highest Young's modulus ( $E_2$ ). The cell never migrates from the stiffer side to the softer one (Figure 2.7). Note that the randomness seen in the trajectories causes the cell to deviate from a straight line, and move out of the x–y plane. These computational results are consistent with experiments (Lo et al., 2000), where they found that cells tend to move from a soft substrate to a stiffer one, but not in the opposite direction.

In the second case, as the soft side is also constrained, there exists a zone (dotted line in the figures) where the cell changes its migration direction. A cell placed close enough to the soft side constraint (c2a) moves toward that boundary. In other cases (cells placed further from the boundary), the tendency is to move toward the left constraint, whether the cell is initially on the softer (c2b) or stiffer side (c2c) (Figure 2.7).

In the third example, three zones can be distinguished (separated by dotted lines). From right to left, a cell placed in the right zone, near the constraint (c3a), migrates directly toward it as in the previous case. A cell placed in the intermediate zone, either on the softer side (c3b) or the stiffer side (c3c), moves to the left. If the cell reaches the left zone (c3c), it stops its advance and moves backward. Once again in the intermediate zone, the cell migrates to the left, crosses to the left zone and moves backward, repeating this process randomly, but indefinitely. Thus, in a zone with no differences in mechanical properties and in the absence of other stimuli (such as chemistry, flow, cell–cell interactions) random cell migration would predominate (Petrie et al., 2009). The cell would migrate randomly within that zone but would not deviate far. In the same way, a cell initially placed in the left zone (c3d) moves away from the free side to the interior of the ECM, but once it crosses to the intermediate zone, it reverses and randomly migrates as in the previous subcase, becoming trapped around this interface. This change in the cell's migration pattern always occurs at similar x-coordinates, but at different y- and z-coordinates due to the randomness of the cellmovement (Figure 2.7).

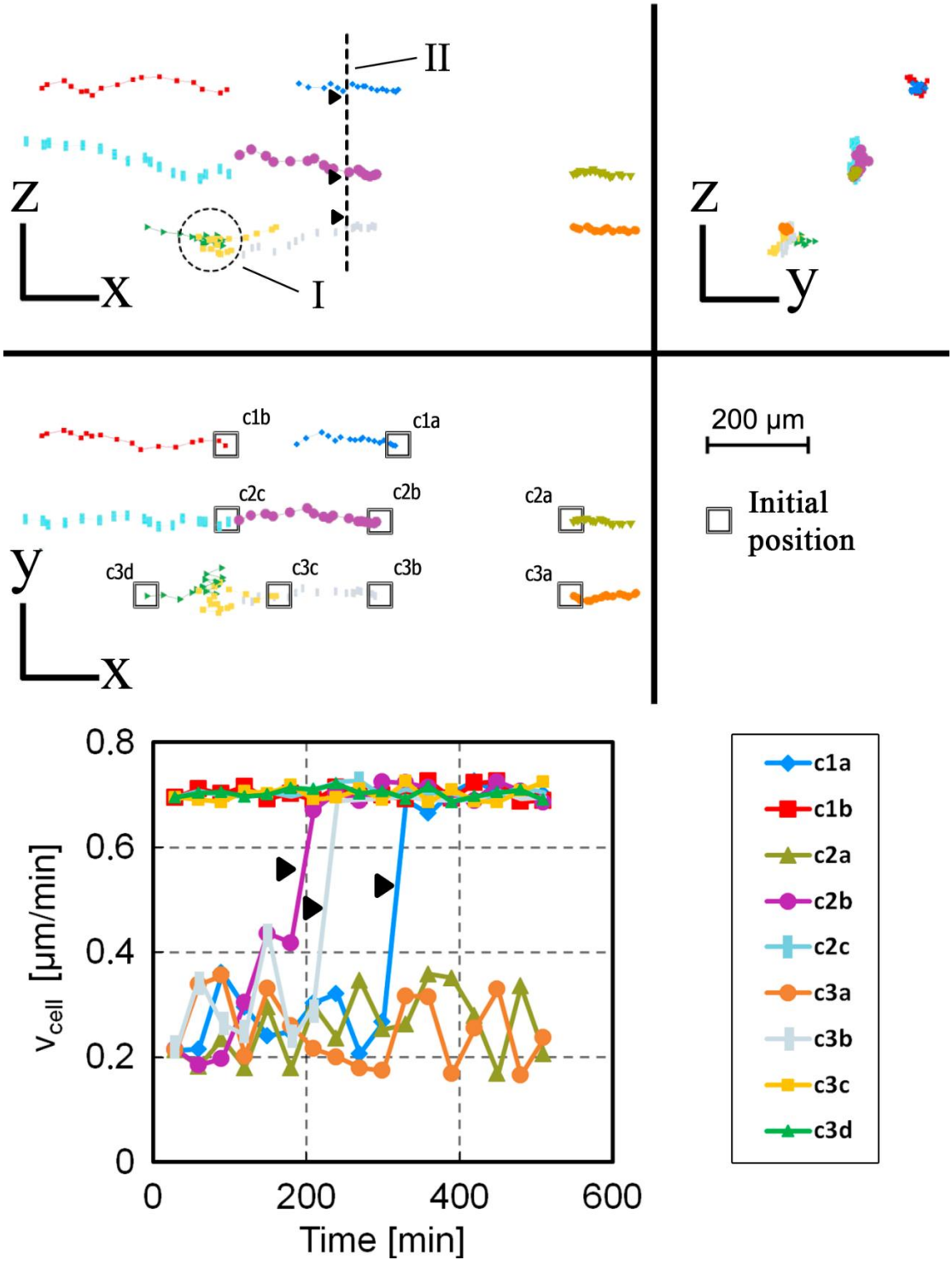


**Figure 2.7:** Migration trajectories and cell speeds.
Computed trajectories projected on y–z (top right), x–y (bottom left) and x–z (top left) planes. The initial position of each case is highlighted with a square and the corresponding label. I indicates a zone where cells become trapped due to specific mechanical conditions. II denotes the interface separating the regions of different stiffnesses. Note that in all simulations, the cell starts at the same y–z point, but are plotted displaced to identify clearly the different cases. Black arrows refer to cells crossing the interface denoted by II.

### 2.4.2.1. Traction forces and cell speed

The model predicts that traction forces increase with higher substrate stiffness until saturation (Figure 2.5B), which has previously been reported in experiments (Mitrossilis et al., 2009, Webster et al., 2011, Trichet et al., 2012, Ghassemi et al., 2012). It also predicts a biphasic dependence of cell migration speed on substrate compliance, as reported in (Peyton and Putnam, 2005) and modeled in (Dokukina and Gracheva, 2010). In all the analyzed examples, the cell exerts higher forces while moving in the stiffer substrate. When a cell moving in the softer substrate approaches and crosses an interface where Young's modulus changes (as happens in c1a, c2b and c3b), the traction force increases abruptly. When the new value is reached, it remains nearly constant as the cell migrates further into the stiffer zone. Traction forces are about 0.015 μN on the more compliant side (0.001 MPa) and 0.055 μN on the stiffer one (0.04 MPa) which correspond with speeds of 0.21 μm $min^{-1}$ and 0.67 μm $min^{-1}$, respectively (Figure 2.7 bottom). The work developed in (Lo et al., 2000) in a 2D substrate with different rigidities shows good agreement with the values of traction forces and cell speeds in the range of their study. They measured a maximum traction stress of 1.09 ± 0.34 kPa and a maximum cell speed of 0.54 ± 0.13 μm $min^{-1}$ for a 0.03 MPa substrate stiffness. The corresponding computational values in the present model are 0.662 kPa and 0.67 μm $min^{-1}$, respectively. Similar speed ranges were found in (Peyton and Putnam, 2005) with a maximal of 0.72 ± 0.06 μm $min^{-1}$ for 0.021 MPa substrate stiffness. In addition, they suggested that optimal stiffness for maximum migration is shifted depending on the concentration of the ECM protein covalently attached to the substrate. However, it is necessary to keep in mind that 2D and 3D speeds are being compared. The recent literature (Fraley et al., 2010, Hakkinen et al., 2011) demonstrates the low correlation between 2D and 3D motility, suggesting that 2D studies are poor predictors of 3D speeds. Nevertheless, they found 3D cell speeds similar to those obtained in this model (specifically 0.3–0.8 μm $min^{-1}$ in (Fraley et al., 2010) and 0.2–0.7 μm $min^{-1}$ in (Hakkinen et al., 2011).

A direct quantitative comparison of cell speeds is difficult, due to the significant variability observed in the experiments as a function of the cell type, substrate composition or morphology. In fact, in (Hakkinen et al., 2011) they studied the cell behavior in four different ECMs (cell-derived matrix, matrigel, collagen, fibrin) and they concluded that considering the molecular composition of the matrix is crucial for a 3D

cell migration study. Similar conclusions can also be found (Harley et al., 2008, Peyton et al., 2011, Ehrbar et al., 2011), which studied the influence of geometrical and mechanical properties of the microenvironment on 3D migration. Interestingly, in spite of different conditions and cell types, similar ranges (comparable with the model results) of cell speeds were found (~0.1–0.26 μm $min^{-1}$ in (Harley et al., 2008), ~0.1–0.8 μm $min^{-1}$ in (Peyton et al., 2011) and ~0.2–1.0 μm $min^{-1}$ in (Ehrbar et al., 2011)).

## 2.4.3. External forces

All the previous results correspond to isolated cells under different mechanical conditions, focusing on the boundary conditions and the elasticity of the ECM. Some additional simulations were performed aiming to understand the effect of applying external loads on specific locations inside the matrix surrounding a single cell. In particular, relevant in this respect is the work of (Lo et al., 2000), where they demonstrated that inserting a micro-needle near the cell and stretching/pushing it, can modify its behavior and even change completely its migration direction.

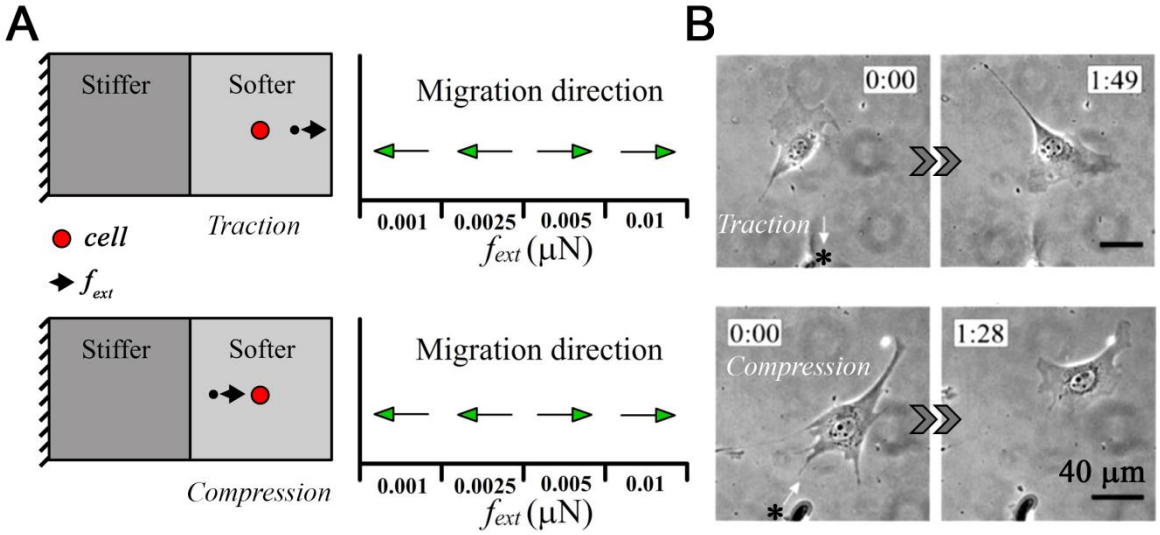


**Figure 2.8:** External forces modulate migration direction.
A) Left: scheme corresponding to case 1, showing the relative position of a micro-needle and the direction of the applied force. Right: migration direction depending on traction/compression magnitude. B) Experiment from *Lo et al.* showing the change in cell polarization and migration in response to a pulling/ pushing micro-needle. Image adapted from (*Lo et al., 2000*).

In order to test the model under external forces, the insertion of a micro-needle was simulated by means of the application of one local external force applied at a distance of

40 μm from the cell, which was maintained constant throughout the simulation. The conditions of the substrate were exactly the same as those used in the case 1 (specifically c1a, as shown in Figure 2.8A). It was found that with a sufficient level of applied force, the micro-needle was able, as shown by (Lo et al., 2000), to change the polarization and the direction of the cell movement (Figure 2.8B). In the simulated case, in normal conditions, the cell tends to migrate toward the stiffer substrate (left). When the stretching (or pushing) force exceeds a certain threshold value (specifically 0.005 μN), the cell changes its migration trend. Interestingly, stretching and pushing values were equivalent. In addition, as could be expected, similar results were obtained varying the distance between the cell and the microneedle, where further distances are equivalent to lower forces. Nevertheless, further research is needed on this issue, being a key point for instance in cell-cell interaction phenomena.

## 2.5. Discussion and conclusions

Although cell migration phenomena involve many different and complex mechanisms, here, a simplified model capable of simulating the preferential movement of an individual cell in 3D under different mechanical conditions is presented. This simplification is based on the hypothesis that *mechanosensing* is one of the main regulatory mechanisms to direct cell movement. In fact, three relevant phenomena are considered: *mechanosensing*, CSK remodeling and migration, and their corresponding equations are solved separately and sequentially (since the *mechanosensing* defines the CSK remodeling and both define the migration). First, during *mechanosensing*, the stress equilibrium between the cell, substrate and external forces is satisfied. Depending on the mechanical properties and boundary conditions, different strain/displacement fields and values of forces exerted by the cell on the ECM/substrate ( $p_{\text{cell}}$ ) are obtained in each step. With these data, the CSK remodels and reorients, updating the internal variable that describes the preferential orientation of the cell ( $\mathbf{d}_{\text{pol}}$ ). Once the values of $p_{\text{cell}}$ and $\mathbf{d}_{\text{pol}}$ are obtained, the traction forces are evaluated, and by satisfying the equilibrium of forces acting on the cell, its speed is computed.

Consistent with this model is the observation that traction forces increase with substrate stiffness (Mitrossilis et al., 2009, Webster et al., 2011, Trichet et al., 2012,

Ghassemi et al., 2012). Without external loads, the cell strain is always negative (contractile) since the *AM* system is always active to reduce the dimensions of the cell. Therefore, stiffer substrates lead to lower values of strain (closer to zero), higher values of $p_{\text{cell}}$ and consequently to higher values of the traction exerted ($\mathbf{F}_{\text{trac}}$). In the presented cases, cell speed is higher in the stiffer substrate. However, the elastic modulus of the stiffer side ($E_2$) was selected to reach maximum velocitieswith the reference values used in the model. Using a higher value of stiffness would lead to lower speeds, which could be even lower than in the softer substrate due to the increase in viscosity and the saturation of forces (Figure 2.5A,B). Of course, a stiffer matrix would also tend to be more difficult to enzymatically degrade and may have different transport properties and density of adhesive ligand, all of which could influence the migration speed. It is important to note here that the presented calculations only examine mechanical effects, thereby down-playing other additional factors.

Recent experimental works (Fraley et al., 2010, Hakkinen et al., 2011) have quantitatively demonstrated the main differences between 2D and 3D cell migration. The lack of correlation between 2D and 3D motility suggests that focal adhesion proteins may regulate motility in a matrix in a manner fundamentally different from that in planar cell motility. Nevertheless, 2D studies are still useful and, in some respects, comparable to 3D (directionality, number of adhesions, axial ratio and even adhesion area (Hakkinen et al., 2011)). Here, some of the model results and predictions are compared with the experimental data on 2D developed in (Lo et al., 2000). These experiments consist of 2D substrates with two different rigidities, where some isolated cells (only interacting with the ECM) are embedded. Their findings indicate that cells placed in the softer part of the substrate tend to migrate toward the stiffer part and cross the interface which separates the substrates, whereas cells placed in the stiffer zone do not cross this interface. This suggests, as proposed here, that cells are capable of sensing the mechanical properties of their surroundings and tend to move toward stiffer substrates. As the only forces acting on the substrate are those exerted by the cell itself, its movement is governed by the local mechanical environment, the boundary conditions and the mechanical properties of the ECM. In fact, it has been investigated in recent experiments (Harley et al., 2008, Fraley et al., 2010, Peyton et al., 2011, Ehrbar et al., 2011, Hakkinen et al., 2011) how microarchitecture, local mechanical properties and molecular composition influence cell migration behavior. The main assumption of the model is that the cell aligns with the

direction of principal strain and moves according to the relative displacements between the cell body and its centroid, which depend on imposed boundary conditions and local changes in substrate stiffness. The recent literature suggests that elasticity, boundary conditions and perhaps embedded fibers can modulate the apparent elasticity of matrices that cells are likely to sense (Buxboim et al., 2010). In all the shown cases, cell migration follows this criterion, in agreement with those experimental observations (Figure 2.7). For example in the second case, there are two zones with an interface located in the middle of the softer side, where the local displacement field is modified due to the right constraint. When a cell is located near that constraint, the cell senses it and moves to the right, whereas if located further away, it moves to the left, where Young's modulus is higher ( $E_2$ ) and there is also a constraint. Note how in the third case, where the stiffer side (left) is free of constraints, a third zone appears. The substrate displacement field obtained by the *mechanosensing* analysis, reaches a minimum in the middle of the stiffer substrate. As a result, the opposing gradients of displacements cause a cell to move randomly around this location. This happens when the cell reaches a zone in the substrate with similar mechanical conditions in all directions. With no differences in local mechanical properties (and absence of other stimuli such as chemistry, flow, cell–cell interactions, etc), the cell would not be able to decide where to move and random migration would be predominant (Petrie et al., 2009).

The magnitude of cell speed for the reference values of parameters used in the model ranges from 0.2 to 0.7μm $min^{-1}$, showing good agreement with experimental data (Lo et al., 2000, Peyton and Putnam, 2005, Harley et al., 2008, Fraley et al., 2010, Peyton et al., 2011, Ehrbar et al., 2011, Hakkinen et al., 2011). The wide range of parameters used in the model, allows adapting it to different conditions and/or experiments, taking into account the limitations discussed below. The model is also used to study the case in (Lo et al., 2000), where local forces are applied in the cell surroundings to understand their role on the preferential movements of single cells. A blunted micro-needle is introduced in the substrate near the cell and moves toward or away from the cell to modify the local state of stress in the ECM. Experiments show that the cell moves toward the pulling forces, and away from the pushing forces. As it has been shown in the results section, the model is able to predict this effect and helps to explain it. If the microneedle pulls, the compressive forces of the cell oppose the needle forces. Hence, the local displacement field changes in a way that the cell senses the forces induced by the needle

as if they were a constraint, and therefore the cell's CSK polarizes to move toward the needle. However, if the micro-needle pushes, the compression forces of the cell follow the same direction as those of the micro-needle. This causes the cell to sense lower rigidity in the direction of the micro-needle, even though Young's modulus is the same in all directions. Hence, the cell reorients and moves away from the needle. The distance and the magnitude of the applied forces determine the local mechanical environment and, therefore, regulate whether or not the cell changes its behavior.

Nevertheless, it is important to keep in mind that cell migration in 3D is a complex process where multiple phenomena are involved. Cell type, molecular composition, morphology and microarchitecture of the ECM/substrate each contribute to determine the migration behavior and, therefore, some simplifications are necessary. Next, some of the simplifications assumed in this model are briefly described in order to understand their implications to the main conclusions. First, this work has focused on the modeling of *mechanosensing* as the main regulatory mechanism of cell migration. Clearly other mechanisms, such as chemistry (Harjanto and Zaman, 2010), biochemical gradients (Roussos et al., 2011) or fluid flow (Polacheck et al., 2011), all influence individual cell migration in 3D. However, the consideration of these mechanisms does not affect the results obtained in the present numerical studies, which are only focused on analyzing the effect of different mechanical conditions in the absence of these other effects. The addition of these effects is left as future work toward a more comprehensive model under different environmental conditions. Second, when one cell migrates in 3D, the matrix is degraded due to the action of proteases released by the cell (Wang and McNiven, 2012), while at the same time, the cell produces and secretes new matrix, remodeling and altering the structure and stiffness of the matrix around it (Groh and Wagner, 2011). As a first approximation, these phenomena have not been considered. In addition, mechano-biological phenomena associated with the evolution of the area of adhesion between the cell and matrix have not been simulated (McGarry et al., 2009) and the change of cell shape as a consequence of its deformation was not considered. For simplicity, the cell is considered occupying a spherical volume and such sphere is modeled as a regular hexahedron, whose shape and size do not change with time. Cell shape and other factors (such as cell stress or ECM/substrate stiffness) could affect the reorientation rate ($\kappa$) of the CSK, but this parameter was considered constant in the simulations for simplicity. Finally, the work have been focused on the modeling of biased migration of single cells in

3D; however, when cell populations migrate collectively, much more complex events are involved, such as cell–cell interactions (Palsson, 2001, Buxboim et al., 2010).

Therefore, the model presented here is only one step in the challenging task of modeling 3D cell migration. So far, and despite the simplifications assumed, it is able to predict different 3D migration patterns of single cells as a function of the local mechanical environment defined by the mechanical properties of the ECM, the boundary conditions and the application of local external forces. As such, the present model attempts to understand the role of different mechanical conditions in 3D cell migration, being a potential tool for instance for the development of biomaterial scaffolds for different applications in tissue engineering and biomedical research.

Chapter 3

# MODELING CYTOSKELETON DYNAMICS: RIGIDITY-SENSING OF ACTIN NETWORKS

In this chapter the dynamic behavior of a cross-linked actin network surrounded by an elastic medium are investigated using an agent-based computational model. The *mechanosensing* role of molecular motors and cytoskeleton reorganization is thus studied by systematically varying the surrounding stiffness. The formation of the network as well as the mechanical and dynamic properties of its components are detailed. As a result, this work elucidates one possible mechanism by which cells can modulate their properties and respond to the surrounding environment via cytoskeleton contractility. Although the model is based on molecular-level processes, macroscopic behaviors of the active cross-linked actin networks agree well with the response of cells probed in experimental quantitative studies. This work is gathered in (Borau et al., 2012).

**Contents**

## 3.1. Introduction

It is clear at this stage that cells modulate their properties and activities in response to the surrounding environment, via morphological rearrangements driven by cytoskeletal contractility and reorganization (Figure 3.1). Various quantitative studies using gels with tuned elasticity have provided insights into the understanding of how cells respond to matrix stiffness (Lo et al., 2000, Ruegg et al., 2002, Discher et al., 2005, Zaman et al., 2006). On soft substrates, cells generate low forces with randomly aligned actin filaments, leading to a weak response with wrinkles or strains of the substrates. By contrast, stiff substrates result in extensive cell spreading and enhance contractility with numerous stress fibers. Other experimental results collectively suggested that on stiff substrates, cells tend to deform intracellular structures rather than the substrate as seen in myosin/actin striations (Engler et al., 2004a, Engler et al., 2004b, Munevar et al., 2004, Richert et al., 2004).

Several mechanisms governing such *mechanosensing* of cells have been proposed in experimental studies, and multiple mechanisms likely exist involving different intracellular structures. For example, a large number of *mechanosensing* molecular motifs that vary conformation over a range of mechanical forces transduce mechanical signals into biochemical ones (Silver and Siperko, 2003, Martinac, 2004, Kung, 2005). It has also been believed that actomyosin contractility contributes to cell *mechanosensing* (Mitrossilis et al., 2009, Ren et al., 2009, Trichet et al., 2012, Ghassemi et al., 2012)(Figure 3.1A). For example, non-muscle myosins were shown to be crucial for stem cells to sense matrix elasticity (Engler et al., 2006). Local forces acting on both integrin-mediated (Saez et al., 2005, Ghibaudo et al., 2008) and cadherin-mediated adhesions exhibit a similar relationship with stiffness (Ganz et al., 2006, Ladoux et al., 2010).

Different phenomenological laws have been proposed to explain the substrate-dependent *mechanosensing*. For example, a simple "two-spring model" predicted that stiffer environments lead to stronger traction forces (Schwarz et al., 2006). A "three-spring model" was proposed later to explain the stiffness-dependent orientation of stress fibers in adherent cells (Zemel et al., 2010b). To elucidate interactions of molecular motors with adhesion complexes in the *mechanosensing* process, a different theoretical model based on active matter theory was proposed (Marcq et al., 2011). It demonstrated that for short timescales ($t << 100$ s), mechano-chemical transduction from the motors plays a dominant role since the adhesion complexes are unlikely to have enough time to

recruit associated proteins. Concurrently, numerous computational models have been developed to elucidate the mechanisms of *mechanosensing*. For instance, they showed that actin networks can adjust to mechanical environments by modulating cross-links within the networks (Astrom et al., 2008), and also suggested a mechanism for stiffness-sensing of cells adhered to a compliant surface mediated by actin filament alignment in the direction of force application (Walcott and Sun, 2010).

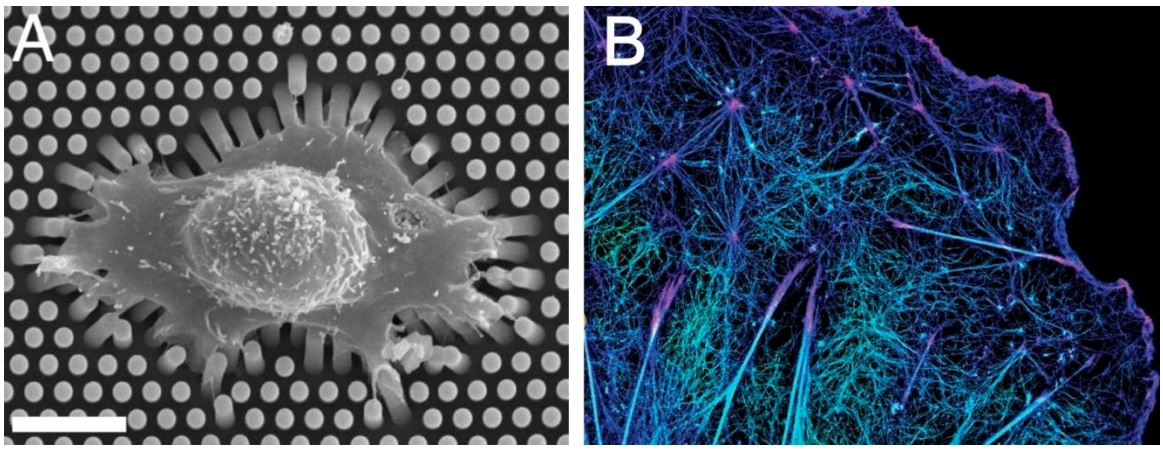


**Figure 3.1:** Fibroblast on a micropilar substrate and actin layers of a cell.
A) Scanning electron micrograph image of a REF52 fibroblast on a micropillar substrate. (Scale bar, 15 μm.)(*Trichet et al., 2012*). B) Ventral actin layer forming a web-like structure (*Xu et al., 2012*).

Taken together, these recent experimental, theoretical, and computational efforts have led to new insights about the structural reorganization of the cytoskeleton as well as the effects of extracellular stiffness on cell behaviors. However, little is known about the roles of actomyosin contractility in *mechanosensing* on timescales of hundreds of seconds, which are biologically relevant. In this work, using a Brownian dynamics computational model (Kim et al., 2009a, Kim et al., 2009b), it is investigated the large-scale contractile responses of an actomyosin network on timescales of hundreds of seconds, during which protein recruitment and responses from molecular motifs can occur, to elucidate one actomyosin-driven rigidity-sensing mechanism that functions under diverse conditions. Specifically, the effects of external elasticity on cytoskeletal contractility and network morphology are evaluated by systematically varying model parameters, e.g. the concentration and kinetics of motors. These simulations successfully reproduce some of the large-scale *mechanosensing* responses of cells such as active contractility and force generation, in good agreement with recent experimental observations (Mitrossilis et al., 2009, Mitrossilis et al., 2010, Webster et al., 2011).

Merely by modeling actin and myosin activity in the absence of proteins related to adhesion complexes, both equilibrium and dynamic behaviors are predicted, indicating that actomyosin machinery can function as a stand-alone mechanism for the *mechanosensing* of cells.

## 3.2. Model features

A previous agent-based Brownian Dynamics model (Kim et al., 2009b) is used to simulate active cross-linked actin networks as systems that generate force as well as sense surrounding mechanical conditions. In this approach, actin filaments, actin cross-linking proteins (ACPs), and molecular motors and their local interactions are explicitly taken into account. To facilitate understanding of the results predicted in this study, its main features are briefly presented.

### 3.2.1. Formation of an active actin network

Before going into the modeling details, it is useful to introduce how real actin networks are formed and how nature regulates polymerization dynamics.

Actin exists as a globular monomer (G-actin) and as a filamentous polymer (F-actin), which is in fact a string of G-actin subunits. Although the filament is often described as a single helix of monomers, it can also be thought of as consisting of two protofilaments, held together by lateral contacts, which wind around each other as two parallel strands of a helix, with a twist repeating every 37 nm (Alberts et al., 2008).

The polymerization of actin filaments proceeds in three sequential phases: lag nucleation, elongation and steady state. In the first phase, G-actin aggregates slowly into short, unstable oligomers. These oligomers can act as a seed or nucleus, which in the second phase rapidly elongate into a filament by the addition of monomers onto both ends. All the subunits within the filament have the same orientation, giving it a structural polarity and making the two ends of the polymer different. The kinetic rate constants for association and dissociation ($k_{on}$ and $k_{on}$ respectively) are much greater at one end than at the other. The more dynamic end, where both growth and shrinkage are fast, is called the plus (barbed) end and the other end is called minus (pointed) end. Furthermore, as a consequence of the nucleotide hydrolysis that accompanies polymer formation, the critical concentration of free monomers at each end changes ($C_c^+ < C_c^-$). Thus, polymerization and growing proceed until the third phase, where the concentration of free

monomer reaches a value above $C_c^+$ but below $C_c^-$. At this steady state, called treadmilling, the subunits undergo a net assembly at the plus end and a net disassembly at the minus end at an identical rate. There is a net flux of subunits through the polymer, but it maintains constant length.

In this work, active actin networks with motors are generated in a similar fashion to previous studies (Kim et al., 2009b). G-actins, passive ACPs, and motors are assembled into a network via reversible reactions in a 3D cubical domain with periodic boundary conditions in all directions. ACPs and motors can exist in three states: monomeric (free), inactive (partially bound), and active (bound to two filaments) states. Note that following the initial formation of the network, monomeric ACPs and motors are implicitly considered via their local concentration and second-order reaction equations. After concentrations of G-actin, ACPs, and motors reach a dynamic steady state, residual G-actins are deleted with actin assembly/disassembly deactivated for simplicity.

A geometrically identical network is used in all simulations to isolate the effects of the stiffness of the surrounding medium and other parameters. To vary the concentration of motors, they are removed from networks or added as monomers at the beginning. The average filament length ($\langle L_f \rangle$) is ~2 μm, actin concentration, $C_A$, is 12 μM, density of ACPs, $R_{ACP}$ ($=C_{ACP}/C_A$), is 0.01, and the initial width of the cubical domain is 5.0 μm. Density of motors, $R_M$ ($=C_M/C_A$), is 0.02 unless specified.

### 3.2.2. Parallelization

The number of particles involved in the simulations is relatively high (tens of thousands), however, what makes the codes computationaly heavy is the huge amount of time increments (tens of millions) needed. This is due to the small time scale (of the order of nanoseconds, see Table 3-1) at which the dynamic processes such as binding or unbinding occur and the desire of simulating long periods of time (hundreds of seconds). Thus, a parallelized approach is compulsory.

Parallel computing operates in the principle that large problems can be divided into smaller ones, which are then solved concurrently. It is, indeed, a powerful tool which permits to face requirements otherwise unthinkable with current technology. Multiple-instruction multiple-data systems (MIMD) are those in which a collection of autonomous processors operate on their own data streams. The most commonly used method of programming in MIMD systems is message passing. The processes coordinate their

activities by explicitly sending and receiving messages. For the computation of the model, the Message Passing Interface (MPI) is used. Note that it is not a new programming language, but a collection of functions, macros, or a library that can be used in C programs. It assumes that all the processes are statically allocated, i.e., the number of processes (p) is set at the beginning of the execution and do not change during the calculation. Each process is assigned a unique integer rank (0, 1, … , *p*-1) where rank 0 acts usually as "master process" gathering and managing the data from other processes. This approach is called single-program, multiple data (SPDM) (Pacheco, 1997).

In the upcoming calculations, long-range interaction forces are not present. Thus, the most convenient parallelization strategy is spatial subdivision with load balancing, that is to say, maintaining a similar load in each CPU (Rapaport, 2002). Therefore the initial domain is divided in *p* equal-sized parts (Figure 3.2), each of them corresponding to a different process. Each CPU performs computations for the particles belonging to its subdomain. However, it is important to notice, that all the information of particles located within a region in adjacent subdomains must be transferred for synchronization and calculation of forces. This is called the *overlapping region*, and its size strongly affects the computational cost, since the time required for data communication directly depends on this factor. Regarding to the load balancing, the size of each subdomain (and therefore the number of particles belonging to it) is uploaded periodically to maintain, as long as possible, a similar number of calculations in each CPU.

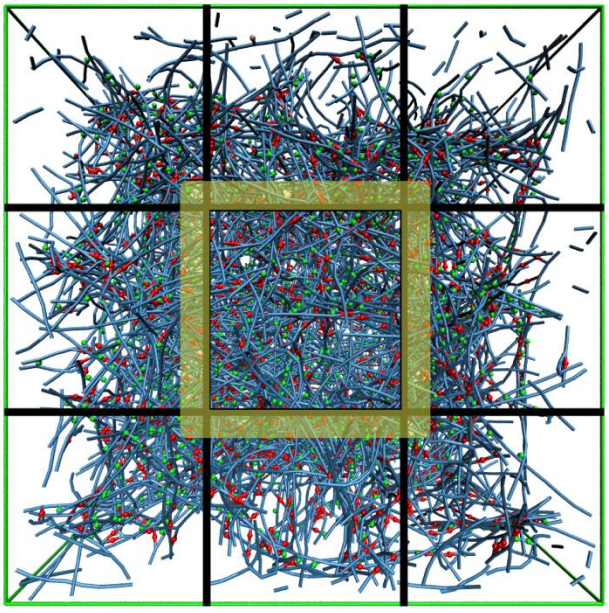

**Figure 3.2:** Parallelization scheme. The network is divided in *p* equal-sized parts (black lines) each of them corresponding to a different CPU. The overlapping region (yellow shade) transfers the information of contained particles between subdomains for syncronization. Size of subdomains is uploaded periodically to balance the loads of the CPUs.

### 3.2.3. Mechanics of actin filaments, ACPs and motors

Actin filaments comprise cylindrical segments of length 140 nm ($r_{0,\mathrm{A}}$), and both the ACPs and motors are represented by two arms parallel to each other spanning between cross-linked actin filaments a distance of 70 nm ($2\times r_{0,\mathrm{ACP}}$) and 140 nm ($2\times r_{0,\mathrm{M}}$), respectively. Motions of the network components are governed by the Langevin equation:

$$m\frac{d\mathbf{r}^2}{dt^2}=\mathbf{F}-\zeta\frac{d\mathbf{r}}{dt}+\mathbf{F}^{\mathrm{B}} \tag{3.1}$$

where $m$ is the mass of each element (actin, ACP, or motor), $\mathbf{r}$ is the element's location, $\zeta$ is the friction coefficient, $t$ is time, $\mathbf{F}^{\mathrm{B}}$ is a thermal force satisfying the fluctuation-dissipation theorem, and $\mathbf{F}$ is a net deterministic force including extension, bending, and repulsive forces. Since inertia of all elements is negligible on the length and time scales of interest, positions of the elements are updated using the Euler integration scheme:

$$\mathbf{r}\left(t+\Delta t\right)=\mathbf{r}\left(t\right)+\frac{1}{\zeta}\left(\mathbf{F}+\mathbf{F}^{\mathrm{B}}\right)\Delta t \tag{3.2}$$

where $\Delta t$ is a time step.

Extension and bending of the cylindrical segments constituting actin filaments, ACPs, and motors are computed using simple quadratic potentials, denoted by subscripts "s" and "b" respectively:

$$U_{\mathrm{s}}\left(r\right)=\frac{1}{2}\kappa_{\mathrm{s}}\left(r-r_0\right)^2 \tag{3.3}$$

$$U_{\mathrm{b}}\left(\theta\right)=\frac{1}{2}\kappa_{\mathrm{b}}\left(\theta-\theta_0\right)^2 \tag{3.4}$$

where $r$ is bond length, $\kappa_{\mathrm{s}}$ is extensional stiffness, $\theta$ is bending angle, $\kappa_{\mathrm{b}}$ is bending stiffness, and the subscript 0 denotes an equilibrium (zero-force) value. As in previous studies (Kim et al., 2009b), bending stiffnesses are introduced to restrict actin filament bending ($\kappa_{\mathrm{b,A}}$), keep the two arms of ACP ($\kappa_{\mathrm{b,ACP1}}$) or motor ($\kappa_{\mathrm{b,M1}}$) parallel, and maintain the right angle between the axis of a filament and the arm of ACP ($\kappa_{\mathrm{b,ACP2}}$) or motor ($\kappa_{\mathrm{b,M2}}$). Specific values of the geometrical and mechanical parameters are listed in Table 3-1. In addition, the repulsive force is responsible for volume-exclusion effects by

which actin filaments cannot pass through each other, which is calculated by the following harmonic potential, $U_{\mathrm{r}}$, depending on the minimum distance, $r_{12}$, between two cylindrical segments (Kim et al., 2009b):

$$U_{\mathrm{r}}(r_{12}) = \begin{cases} \frac{1}{2}\kappa_{\mathrm{r}}\left(r_{12} - r_{\mathrm{c}}\right)^2 & \text{if} \quad r_{12} < r_{\mathrm{c}} \\ 0 & \text{if} \quad r_{12} \geq r_{\mathrm{c}} \end{cases} \tag{3.5}$$

where $\kappa_{\mathrm{r}}$ is the strength of repulsive effects, and $r_{\mathrm{c}}$ is the diameter of cylindrical segments. Then, the repulsive force is distributed to the two ends of the actin segment based on the relative location on the segment where $r_{12}$ is measured.

### 3.2.4. Dynamic behaviors of ACPs and motors

Each motor in the simulation is assumed to correspond to a single myosin minifilament consisting of multiple myosin II molecules. Motors in the active state walk along actin filaments toward a barbed end at a rate, $k_{\mathrm{w}}$ [$\mathrm{s}^{-1}$], depending on the extensional force acting on the arm, $\vec{F}_{\mathrm{s}} = \nabla U_{\mathrm{s}}$:

$$k_{\mathrm{w}}\left(\vec{F}_{\mathrm{s}}\right) = \begin{cases} \dfrac{3.6\times10^{-8} / r_{0,\mathrm{A}}}{d_{\mathrm{w},1}\exp\left[\dfrac{\left(\vec{F}_{\mathrm{s}}\cdot\vec{t}\right)\lambda_{\mathrm{w},1}}{k_{\mathrm{B}}T}\right] + d_{\mathrm{w},2} + d_{\mathrm{w},3}\exp\left[\dfrac{\left(\vec{F}_{\mathrm{s}}\cdot\vec{t}\right)\lambda_{\mathrm{w},2}}{k_{\mathrm{B}}T}\right]} & \text{if } r \geq r_{0,\mathrm{M}} \text{ and } \vec{F}_{\mathrm{s}}\cdot\vec{t} \geq 0 \\ \dfrac{3.6\times10^{-8} / r_{0,\mathrm{A}}}{d_{\mathrm{w},1} + d_{\mathrm{w},2} + d_{\mathrm{w},3}} & \text{else} \end{cases} \tag{3.6}$$

where $d_{\mathrm{w}}$'s and $\lambda_{\mathrm{w}}$'s are time constants and mechanical sensitivities for walking of motors (Table 3-1), respectively, and $\vec{t}$ is a unit vector locally tangent to an actin segment in the direction of a pointed end. Although motors in this study mimic a myosin minifilament consisting of numerous myosin II molecules, equation (3.6) and the values of $d_{\mathrm{w}}$'s and $\lambda_{\mathrm{w}}$'s are adopted from a single-molecule experiment examining myosin V under 1 mM ATP. The intention was to model generalized motor activity, and myosin V was chosen because it has been extensively characterized. In fact, the load-dependent walking rate of the minifilament (myosin II) is still qualitatively similar to that of myosin V, justifying the use of equation (3.6) for roughly mimicking myosin minifilament behavior. Nevertheless, a specific study of minifilament kinetics depending on the number of myosin heads was performed (Appendix B) concluding that, after adjustment,

myosin V and II behaviors are computationally similar. As seen in that equation, only tension ($r > r_{0,\mathrm{M}}$) directed to a pointed end ($\vec{F}_{\mathrm{s}} \cdot \vec{t} \geq 0$) affects $k_{\mathrm{w}}$, resulting in a stall force, ~4 pN, beyond which motors cease walking.

In addition, as in (Kim et al., 2011), ACPs and motors are able to unbind in a force-dependent manner following Bell's equation:

$$k_{\mathrm{u}}\left(\vec{F}_{\mathrm{s}}\right) = \begin{cases} k_{\mathrm{u}}^{0} \exp\left(\dfrac{\lambda_{\mathrm{u}} \left|\vec{F}_{\mathrm{s}}\right|}{k_{\mathrm{B}}T}\right) & \text{if } r \geq r_0 \\ k_{\mathrm{u}}^{0} & \text{if } r < r_0 \end{cases} \tag{3.7}$$

where $k_{\mathrm{u}}^{0}$ is the zero-force unbinding rate coefficient for ACPs ($k_{\mathrm{u,ACP}}^{0}$) or motors ($k_{\mathrm{u,M}}^{0}$), and $\lambda_{\mathrm{u}}$ is the mechanical sensitivity for unbinding of ACPs ($\lambda_{\mathrm{u,ACP}}$) or motors ($\lambda_{\mathrm{u,M}}$) (Table 3-1). Note that although unbinding of motors is also one of the phases of walking, these two events are considered separable for systematic analysis. If the arm of motors reaches the barbed end of a filament by walking, it remains there until it unbinds.

### 3.2.5. Boundary conditions of the 3D computational domain

After obtaining the network, actin filaments crossing the domain boundaries are severed and permanently clamped with periodic boundary conditions deactivated in all directions. During the measurement of strain and stress, the boundaries also act as sticky surfaces to take the binding between actin filaments and membrane into account; if either end of an actin filament is located within 30 nm of a boundary, the end is irreversibly clamped.

Normal stress ($\sigma$) on each boundary is the sum of normal forces exerted by actin filaments clamped on the boundary, divided by actual area. $\sigma$ is used to compute movement of the boundaries in simulation; assuming that the domain is surrounded by an elastic medium with identical Young's modulus, $E$, on all boundaries. Each boundary (assumed planar) experiencing $\sigma$ is displaced a distance corresponding to a strain $\sigma / E$.

Simulations begin with zero stress on all boundaries and proceed over time for 200 s. At this point, the network reaches a steady state stress in most cases, which is here defined to be the plateau stress. However, in a few cases, stress continues to slowly rise even after 200 s.

## 3.3. Results

Here, the role of molecular motors as rigidity sensors is investigated and the contractile (normal) stress and strain of actomyosin networks tethered to 3D cubical domains is predicted. These are examined as a function of the various kinetic parameters and concentrations of motors as well as different elasticity of the surrounding medium.

### 3.3.1. Network morphology and stress evolution depend on substrate stiffness

The initial network (Figure 3.3A) starts from a zero stress condition. Due to motor activity, and depending on substrate stiffness ($E$), the network shrinks to different extents at different rates. Lower $E$ leads to shrunk and concentrated networks with highly bent actin filaments (Figure 3.3B and Figure 3.4-left). On the other hand, higher $E$ prevents the domain contraction, forming heterogeneous networks with highly stretched filaments (Figure 3.3B and and Figure 3.4-right). These differences in network morphology have been reported in experiments where they found, for different cell types, that F-actin networks tend to be denser and less organized on more compliant substrates (Bordeleau et al., 2012, Blakney et al., 2012).

Stress ($\sigma$) in all cases rapidly increases at the beginning although the rate of increase gradually falls, rising at a much slower rate by ~200 s in most cases (Figure 2A). Recognizing that stress continues to rise after this time, but constrained by computational resources from extending the calculations further, the value of stress at 200 s is used as a reference, and it is denoted as the "plateau stress", $\sigma_p$. For $E < 3$ kPa, $\sigma_p$ is proportional to $E$ but becomes relatively constant for $E \geq 3$ kPa, which corresponds well to literature (Lo et al., 2000, Mitrossilis et al., 2009, Mitrossilis et al., 2010, Saez et al., 2005) (Figure 3.5B). The maximum of $\sigma_p$ is ~420 Pa. The initial slope of stress, $\dot{\sigma}_0$ , measured at $t <$ 10 s increases swiftly for $E < 3$ kPa and slower for $E > 3$ kPa (Figure 3.5D).

The initial strain rate, $\dot{\varepsilon}_0$ ($= \dot{\sigma}_0 / E$), decreases with greater $E$ (Figure 3.5C); since contraction is associated with energy expenditure to overcome the internal friction and the rupture of cross-links, cells contracting against softer substrates will experience larger energy dissipation, leading to the slower rise in stress. The "plateau strain", $\varepsilon_p$ (strain at plateau stress), decreases with greater $E$ falling below 0.05 for $E > 10$ kPa (Figure 3.5E).

$\sigma_p$ and $\varepsilon_p$ with various $E$ show a first zone where $\sigma_p$ rapidly changes, followed by a period of slower increase, which agrees well with (Rassier et al., 1999).

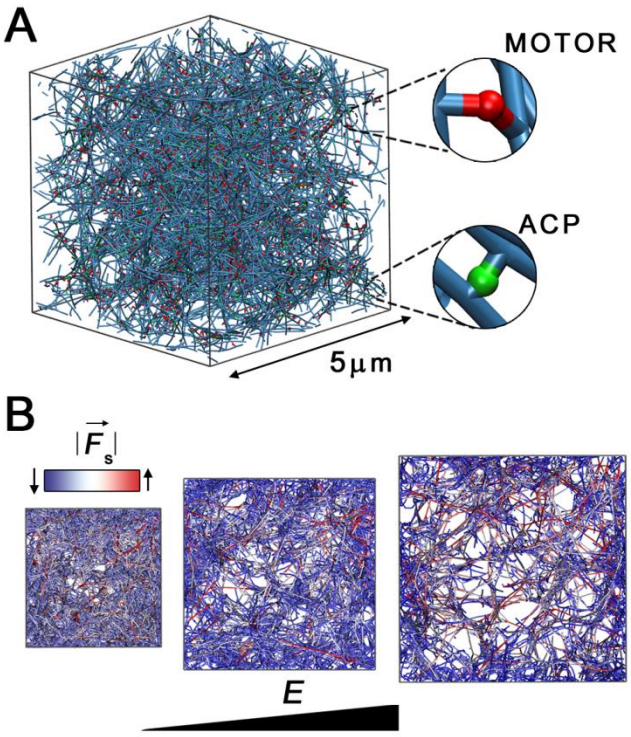


**Figure 3.3:** Initial 3D network and cross-sections.
A) The initial network is generated using a polymerization model and consists of actin filaments (cyan) cross-linked by ACPs (green) and molecular motors (red). Details of motors and ACPs are magnified.
B) Cross-sections of the network at $t$ = 200 s for three different values of $E$ showing morphology and the magnitudes of extensional forces ($|\vec{F}_s|$). Softer substrates lead to a condensed network, whereas stiffer substrates contract very little, resulting in a heterogeneous network with tensed filaments.

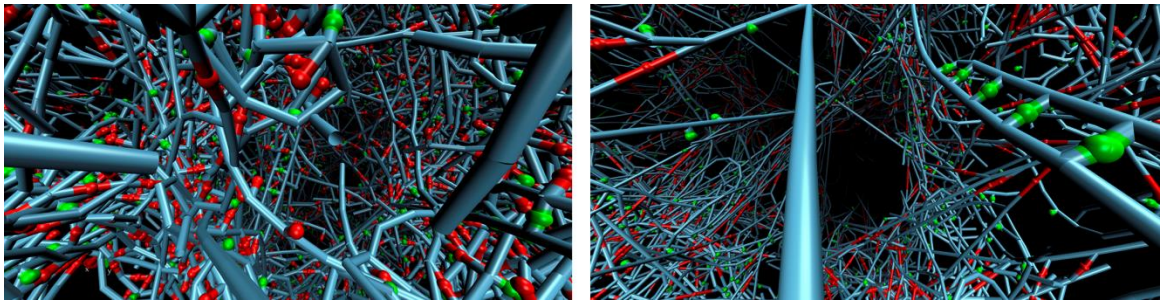

**Figure 3.4:** Different network organization.
Inner view of a network surrounded by a compliant substrate (left) and a stiff one (right). Softer substrates lead to packed and more homogeneous network organization compared with stiffer ones which bring heterogeneous formations with long straight filaments crossing the network.

The mechanical power was also measured, $P = \sigma_0 \dot{\varepsilon}_0 V$ where $\sigma_0$ is initial stress corresponding to $\dot{\varepsilon}_0$, and $V$ is the instantaneous volume of the domain. $P$ exhibits a bimodal dependence on $\sigma_0$, having a peak at $E$ ~ 0.6 kPa (Figure 3.5F). At this peak, the network exerts 40% of the maximum $\sigma_0$ with intermediate $\dot{\varepsilon}_0$ (~0.015 $s^{-1}$), compared to cases with other $E$.

### 3.3.2. Network stiffness tracks the generated stress

It has been recently found that cell stiffness tracks substrate stiffness over a range of stiffnesses before reaching a constant value (Tee et al., 2011). The steady-state stiffness of networks was measured at each $E$. Network stiffness ($E_n$) was found to be proportional to (and nearly equal to) $\sigma_p$ over the entire range of $E$, but proportional to $E$ only up to a value of $E \sim 3$ kPa (Figure 3.5B). This tendency is consistent with the direct proportionality between prestress and *G*' (or *K*') of passive actin networks observed in experiments (Gardel et al., 2006).

It is worth it to note that in order to measure the stiffness of networks, differential sinusoidal normal displacement of amplitude 280 nm was applied to the networks and the responding stress was calculated. For the purpose of this calculation, all the motor and actin cross-linking dynamics was deactivated to probe the instantaneous network stiffness, avoiding any progressive time-dependent changes in the network. Under these conditions, the networks exhibited a predominantly elastic response as indicated by the small phase delay between the applied strain and the responding stress (Figure 3.6). The network stiffness was then calculated by dividing the amplitude of stress by that of strain.

### 3.3.3. Effects of motor concentration

Motor density is varied by adjusting the initial concentration of motors in the network, $R_M$. In all cases, $\sigma$ increases with $E$ and then exhibits a much slower rate of increase at high $E$ (Figure 3A), but compared to the control case ($R_M$ = 0.02), the tendency is less clear in the other cases, especially for low $R_M$ where the dependence between $\sigma_p$ and $E$ weakens. For low $R_M$ (< 0.02), $\sigma_p$ tends to be higher with greater $R_M$, in good agreement with literature (Dou et al., 2007, Kovacs et al., 2004, Mitrossilis et al., 2009). With a maximum at $R_M$ = 0.02 for most $E$, $\sigma_p$ drops for higher $R_M$. High contractile activity of the network enhances the rate of stress generation. Thus, $\dot{\sigma}_0$ and $\dot{\varepsilon}$ increase for all values of $E$ until $R_M$ reaches the optimal level explained above (Figure 3.7B and C).

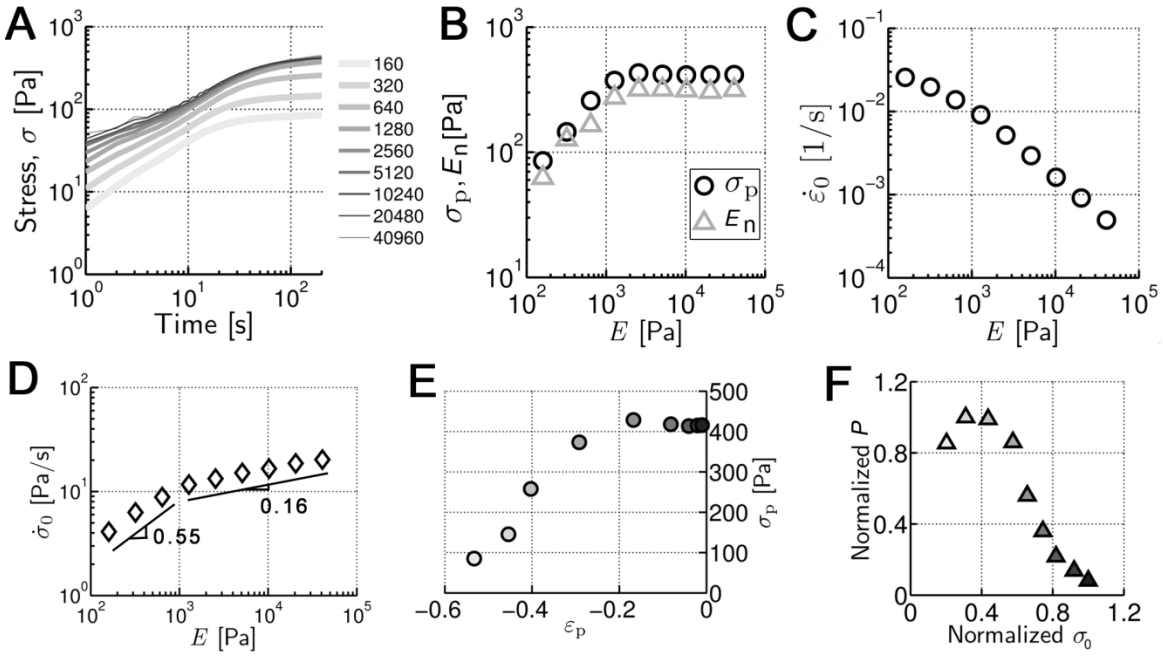


**Figure 3.5:** Effects of substrate stiffness on network stress and strain.
A) Time evolution of $\sigma$ at different $E$. Numbers in the legend indicate the values for $E$. $\sigma$ increases rapidly at first but reaches a nearly constant plateau value ($\sigma_p$) at ~200 s regardless of $E$. B) $\sigma_p$ (circles) and network stiffness ($E_n$, triangles) as functions of $E$. $\sigma_p$ monotonically increases for $E < 3$ kPa but saturates for $E > 3$ kPa. The network stiffness shows the same tendency as $\sigma_p$ for all $E$. C) Contraction speed ($\dot{\varepsilon}_0$) as function of $E$. The network contracts rapidly with low $E$ but more slowly as $E$ increases. D) Initial rate of stress increase ($\dot{\sigma}_0$) with different $E$. $\dot{\sigma}_0$ increases following $\sim E^{0.55}$ for $E$ < 1 kPa and $\sim E^{0.16}$ for $E$ > 1 kPa. E) $\sigma_p$ and corresponding strain ($\varepsilon_p$) at various $E$. Higher $|\varepsilon_p|$ corresponds to lower $\sigma_p$. For high $E$, $\varepsilon_p$ asymptotically approaches 0. F) A relation between normalized power ($P$) and initial stress ($\sigma_0$). $P$ becomes maximal at $E$ ~ 0.6 kPa, generating 40% of the maximum $\sigma_0$ and intermediate $\dot{\varepsilon}_0$ of ~0.015 $s^{-1}$. Each color within the symbols in E and F indicates the value of $E$ in A with the same line color.

### 3.3.4. Effects of unbinding and walking behaviors of motors

Motor unbinding is explored by varying the zero-force unbinding rate ($k_{u,M}^0$) and the processivity ($\lambda_{u,M}$). On the other hand, motor walking is studied by varying the sensitivity ($\lambda_w$) which is equivalent to variation of the stall force.

Although higher $k_{u,M}^0$ results in more frequent unbinding, it does not necessarily lead to lower $\sigma_p$ since unbinding can also help stalled motors due to blocking effects to bind to other binding sites so that they can keep walking. However, too frequent

unbinding prevents motors from remaining attached to filaments for enough time to generate large stress. The early phase of $\sigma$ evolution is practically unaffected by changes in $k^0_{u,M}$ while the later phase is strongly influenced; $\dot{\sigma}_0$, $\dot{\varepsilon}_0$ and $P$ are relatively conserved, whereas $\sigma_p$ tends to decrease with higher $k^0_{u,M}$ (Figure 3.8A-D). These are likely to account for the complicated effects of $k^0_{u,M}$.

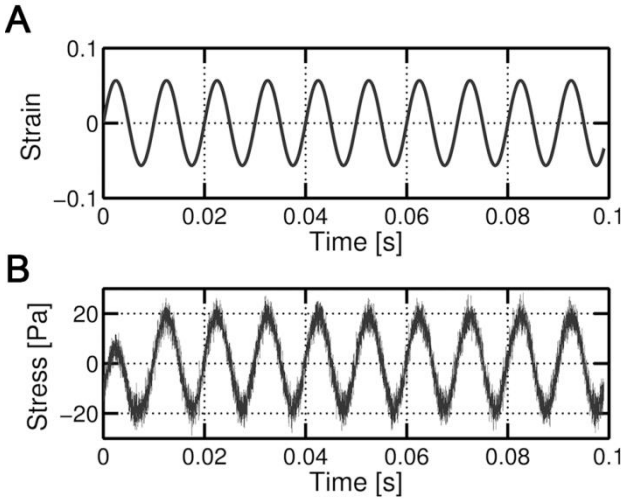


**Figure 3.6:** Meassurement of network stiffness.
A) Sinusoidal normal strain applied to networks to measure the steady-state stiffness of networks ($E_n$), corresponding to an amplitude of 280 nm.
B) Stress in response to the applied strain. These show examples of stress and strain for a control case with $E$ = 40960 Pa.

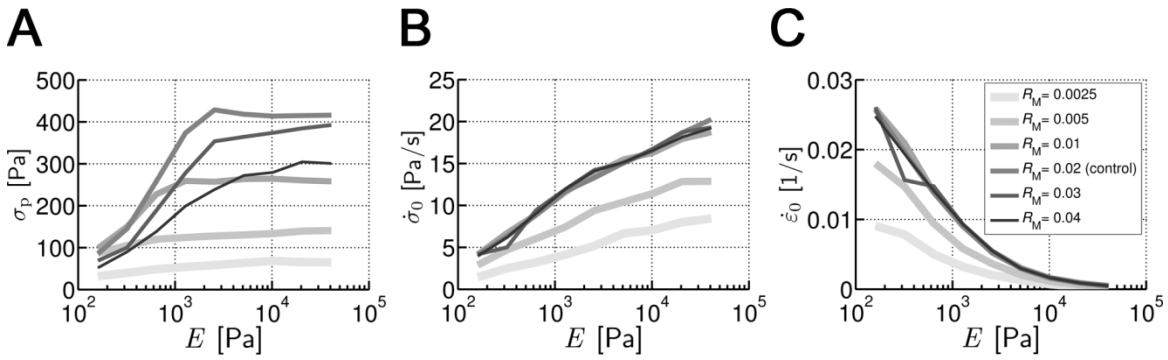


**Figure 3.7:** Influences of motor concentration.
A) $\sigma_p(E)$ with various $R_M$. With low $R_M$, the tendency of an increase followed by a plateau is less clear. $\sigma_p$ is maximal for all $E$ at either $R_M$ = 0.01 or 0.02. B) $\dot{\sigma}_0(E)$ and C) $\dot{\varepsilon}_0(E)$. Both $\dot{\sigma}_0$ and $\dot{\varepsilon}_0$ increase with greater $E$ and are higher for greater $R_M$ until saturation at $R_M \geq 0.02$. The legend in C is also applicable to A and B.

By contrast, the effects of $\lambda_{u,M}$ and are much clearer; $\sigma_p$, $\dot{\sigma}_0$, and $\dot{\varepsilon}_0$ tend to be all higher for lower $\lambda_{u,M}$ (Figure 3.9A-C) and $\lambda_w$ (Figure 3.9D-F). Note that $\lambda_w$ refers to both $\lambda_{w,1}$ and $\lambda_{w,2}$, and their values are varied simultaneously. In response to variations of $\lambda_{u,M}$, the typical tendency of $\sigma(E)$ is conserved in most cases except that with

$\lambda_{u,M} = 7 \times \lambda_{u,M}^{*}$ where the dependence on $E$ is noticeable only at low $E$ since motors can bear very small forces (Figure 3.9A). Therefore, $\dot{\sigma}_0$ and $\dot{\varepsilon}_0$ deviate from the control case only for high values of $\lambda_{u,M}$ (Figure 3.9B and C). Interestingly, $P(\sigma_0)$ and $\dot{\varepsilon}_0(\sigma_0)$ after normalization are collapsed into a unique curve (Figure 3.10A and C). Regarding motor walking, $\lambda_w$ determines the stall force at which the walking rate of motor approaches nearly zero (equation (3.6)). Lower values of $\lambda_w$ lead to higher stall forces, so the motors can overcome the applied forces and thus walk longer distances. Multiplying $\lambda_w$ by 0.1 increases $\sigma_p$ nearly three times compared to the control case (Figure 3.9D). Besides, due to higher $\dot{\sigma}_0$, the domain shrinks more notably (Figure 3.9E and F). Again, $P(\sigma_0)$ and $\dot{\varepsilon}_0(\sigma_0)$ collapse well into a single curve after normalization (Figure 3.10B and D).

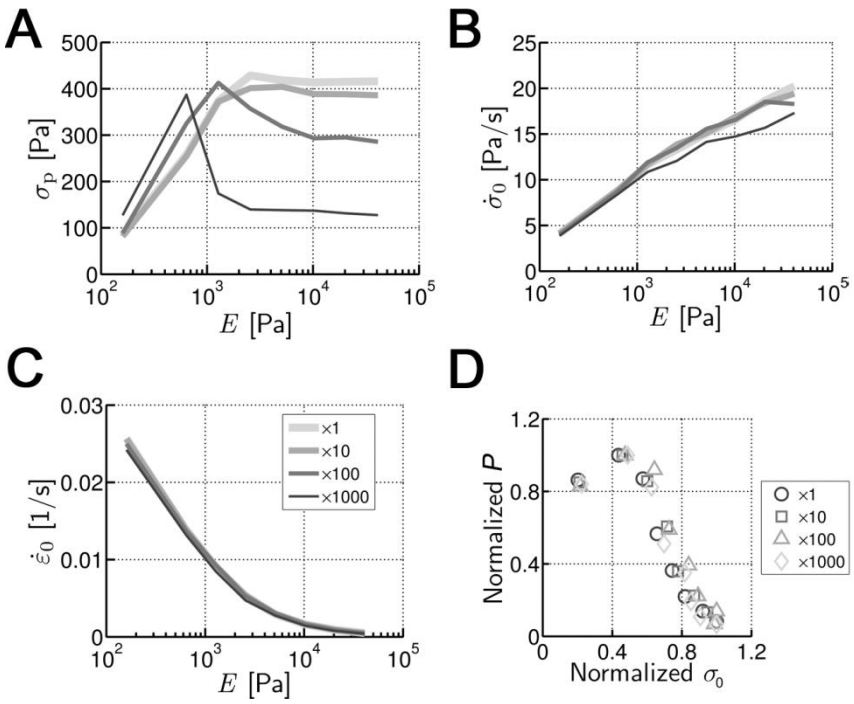


**Figure 3.8:** Influences of zero-force unbinding rate of motors.
Effects of $k_{u,M}^{0}$ $(= n \times k_{u,M}^{0*})$ on A) $\sigma_p(E)$, B) $\dot{\sigma}_0(E)$, C) $\dot{\varepsilon}_0(E)$, and (D) $P(\sigma_0)$. Numbers in the legends represent *n*, and A, B and C share the same legend. The early phase of stress evolution is virtually unaffected by changes in $k_{u,M}^{0}$ while the later phase is strongly influenced. This means that $\dot{\sigma}_0$ , $\dot{\varepsilon}_0$ and *P* are relatively conserved (B-D), whereas $\sigma_p$ tends to decrease with higher $k_{u,M}^{0}$ (A), demonstrating that motor unbinding plays a role only in determining the level of stress that can be attained under steady-state conditions once stress has developed. There also appears to be an optimal stiffness (at least for high $k_{u,M}^{0}$) at which plateau stress reaches a maximum.

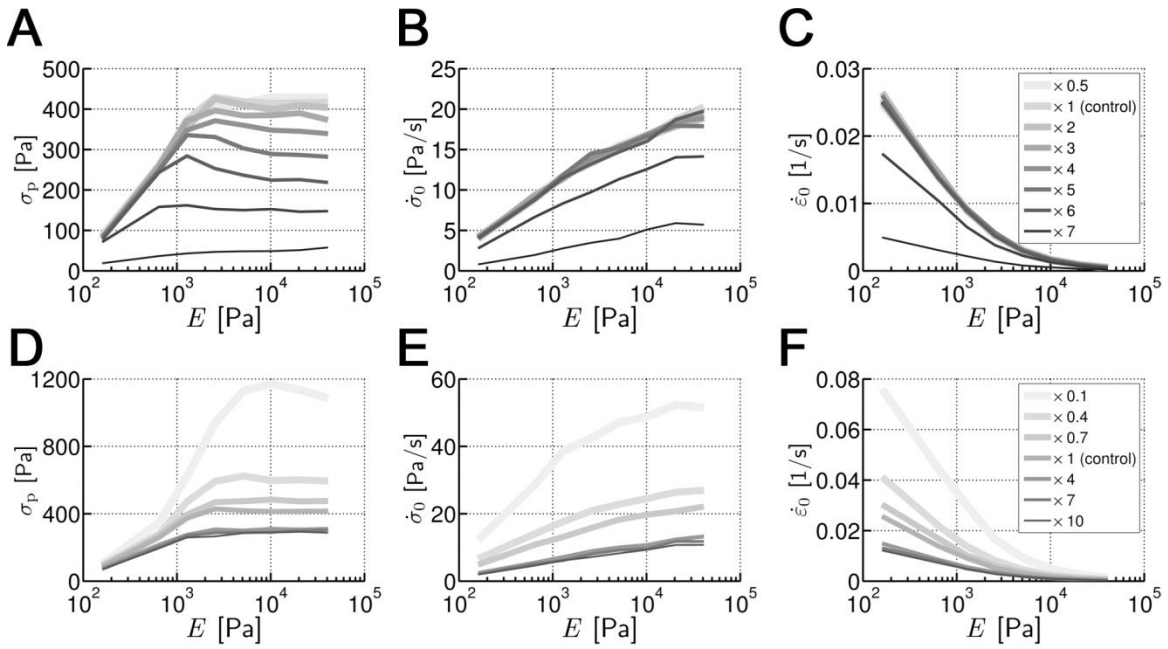


**Figure 3.9:** Effects of mechanical sensitivity of motor unbinding and walking.
A-C) Influence of the mechanical sensitivity of motor unbinding ($\lambda_{u,M} = n \times \lambda^*_{u,M}$) and D-F) motor walking ($\lambda_{w,M} = n \times \lambda^*_{w,M}$) on A, D) $\sigma_p(E)$, B, E) $\dot{\sigma}_0(E)$, and C, F) $\dot{\varepsilon}_0(E)$. "*" denotes reference values (Table 3-1), and numbers in the legends indicate *n*. Note that A and B share a legend with C, and D and E share a legend with F. $\sigma_p$ tends to be higher with lower $\lambda_{u,M}$ and $\lambda_w$ which correspond to more processive and stronger motors, respectively.

## 3.4. Discussion

Cells are capable of adapting their properties through a variety of mechanisms. In this study, the role of molecular motors as rigidity sensors is investigated. In addition, it is proposed how these motors can induce such precise *mechanosensing*. Despite the oversimplifications and assumptions made in the described system which only includes the dynamics of motors and ACPs, the simulated actin network exhibits macroscopic contractile behaviors remarkably similar to several experiments (Mitrossilis et al., 2009, Mitrossilis et al., 2010, Webster et al., 2011), further indicating that microscopic properties of individual constituents govern the network responses, and that motors play a central role in *mechanosensing*. However, this does not negate the significance of other factors such as actin dynamics and structures, biochemical signaling, and adhesions dynamics in the cell's response and adaptation to mechanical cues. Rather, it is demonstrated here that actomyosin machinery can be one of several possible mechanisms for cell rigidity-sensing phenomena. Nevertheless, a wide range of parametric spaces was

explored in order to study how different parameters of the model influence cell adaptation, finding that those parameters affecting the kinetics of motors are the most critical for cellular adaptation to substrate stiffness.

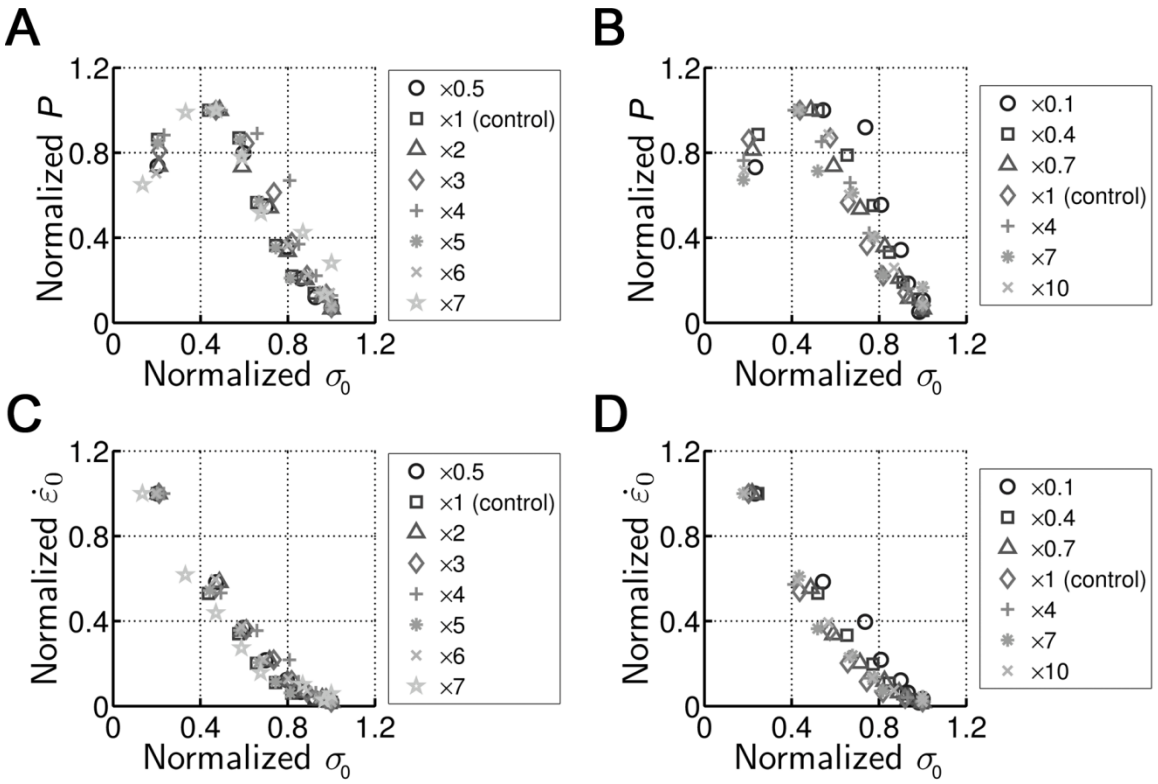


**Figure 3.10:** Influences of mechanical sensitivity of motor unbinging and walking. A, C) motor unbinding ($\lambda_{\mathrm{u,M}} = n \times \lambda_{\mathrm{u,M}}^{*}$) and B, D) motor walking ($\lambda_{\mathrm{w,M}} = n \times \lambda_{\mathrm{w,M}}^{*}$). Numbers in the legends indicate *n*. A shares a legend with C (unbinding); and B shares a legend with D (walking). A, B) and C, D) show normalized *P* and $\dot{\varepsilon}_0$ vs normalized $\sigma_0$, respectively. Regardless of *n*, the curves collapse well after normalization. *P* exhibits a biphasic behavior with a peak at ~40% of $\sigma_0$. On the other hand, $\dot{\varepsilon}_0$ decreases with increasing $\sigma_0$, approaching zero for higher loads.

Diverse contractile large-scale characteristics were probed by evaluating network morphology, plateau stress ($\sigma_{\mathrm{p}}$), the initial increasing rate of stress ($\dot{\sigma}_0$), the initial rate of strain ($\dot{\varepsilon}_0$), and mechanical power (*P*) over a wide range of parameters – the stiffness of the surrounding environment ($E$), the concentration ($R_{\mathrm{M}}$) and the dynamics of motors ($k_{\mathrm{u,M}}^{0}$, $\lambda_{\mathrm{u,M}}$ and $\lambda_{\mathrm{w}}$). It was observed that softer substrates lead to shrunken and dense networks, whereas stiffer ones result in heterogeneous networks with minimal domain contraction (Figure 3.3B and Figure 3.4). Overall, the qualitative pattern of stress evolution is quite consistent with multiple recent experimental works (Mitrossilis et al.,

2009, Mitrossilis et al., 2010, Trichet et al., 2012); $\sigma$ increases with time rapidly at first but reaches $\sigma_p$ in most cases before 200 s (Figure 3.5A). In addition, it was found that $\sigma_p$ is roughly proportional to $E$ for $E < 3$ kPa and becomes relatively constant for $E > 3$ kPa (Figure 3.5B). The existence of a transition to a slower rate of stress increase can be explained by the mechanisms that cause the motors to slow or stall: (i) all of the next binding sites in a barbed-end direction are already occupied (blocking), (ii) reaching the motor stall force, or (iii) reaching the barbed end of an actin filament. Figure 3.11A demonstrates that only a small fraction of motors reach the barbed end of a filament for all $E$, so this would have little direct influence on $\sigma_p$. Blocking, on the other hand, is observed over the entire range of $E$, but is especially prevalent at lower $E$. This is due to the greater distance that motors need to walk before reaching their maximum force, combined with the tendency for all constituents (filaments, motors, and ACPs) to increase in density under large negative strains. For stiffer substrates, material strains are smaller and motors walk shorter distances before attaining the stall force. For $E > 3$ kPa, $\sigma$ can reach $\sigma_p$ determined by the stall force that motors can exert maximally while at lower $E$, $\sigma_p$ is limited by the blocking effect which progressively decreases as $E$ increases (Figure 3.11B). This transition from blocking at low $E$ to limitation due to motor stall force at high $E$ constitutes a mechanism by which cells can sense substrate stiffness. Forces transmitted along the cytoskeleton and across adhesion complexes will vary according to the generated stress, leading to varying degrees of conformational change in these stress-bearing proteins. Since conformation determines biochemical activity, factors such as exposing cryptic binding sites, changes in binding affinity, or phosphorylation, for example, will modulate signaling activity and therefore, cell function.

This mechanism is further confirmed by effects of $C_A$ on $\sigma_p$ (Figure 3.12A). At $E$ = 2560 Pa, $C_A$ was varied maintaining $C_M$ at 0.24 μM, meaning that $R_M$ decreases with higher $C_A$. Note that $C_M$ = 0.24 μM is equivalent to $R_M$ = 0.02 in the control case with $C_A$ = 12 μM. $\sigma_p$ is proportional to $C_A$ even with the same number of motors (Figure 3.12A). More actins can provide the motors with greater space to walk, leading to fewer stalling events by blocking but more frequent stalling by applied forces (Figure 3.12B). In addition, the effects of average filament length ($\langle L_f \rangle$) demonstrate the mechanism. It was found that networks attain stress roughly proportional to the cube of $\langle L_f \rangle$ (Figure 3.12C).

With shorter filaments, more motors reach the barbed ends while with longer filaments, motors are more likely to stall by attaining their maximum level of force generation (Figure 3.12D). Interestingly, the percentage of blocking events remains relatively constant, independent of $\langle L_f \rangle$. The increase in the number of motors exerting maximum stall forces results in higher $\sigma_p$, consistent with the mechanism above.

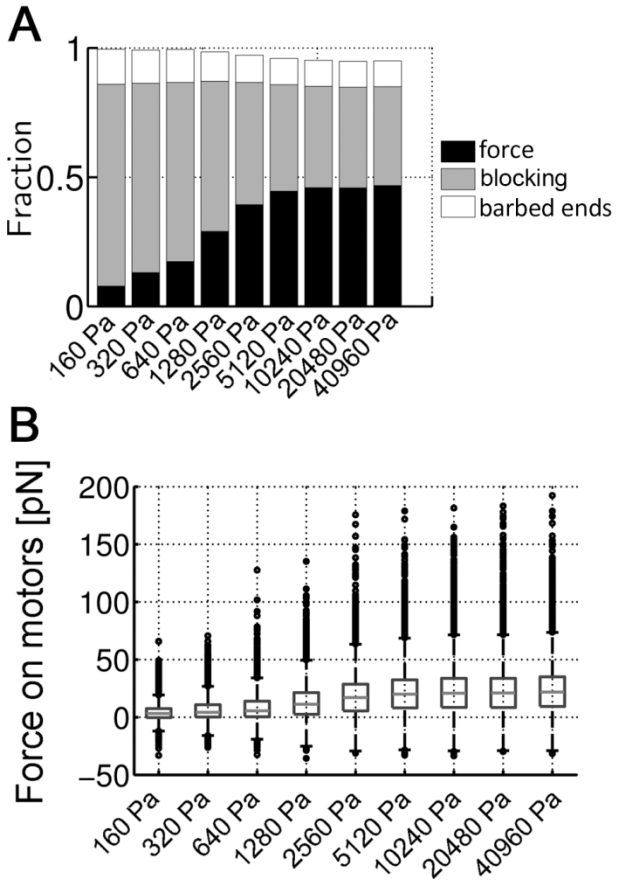


**Figure 3.11:** Mechanisms limiting network contraction.
A) Fraction of motors stalled at steady state ($t$ = 200 s) due to three different reasons as a function of $E$: high applied forces (black), lack of binding sites (blocking, gray), or arrival at barbed ends of filaments (white). The blocking effect is a major cause of motor stalling at all $E$. Percentage of motors stalled by applied loads increases with $E$ for $E < 3$ kPa and becomes independent of $E$ for $E > 3$ kPa. Since the number of barbed ends in the domain is constant, the corresponding fraction is largely independent of $E$.
B) Statistical distribution of forces acting on motors at $t$ = 200 s. The median slightly increases with $E$, whereas the upper quartile clearly increases at higher $E$.

Several recent studies suggested that the proportionality between $\sigma_p$ and $E$ could be correlated with $\dot{\sigma}_0$ (Mitrossilis et al., 2009, Mitrossilis et al., 2010, Webster et al., 2011), which is consistent with the observation that $\dot{\sigma}_0$ increases swiftly for $E < 3$ kPa but slows down for $E > 3$ kPa (Figure 3.5D). From a biological point of view, cells are polarized and migrate in the direction of higher stiffness inducing the faster increase of traction force (Bischofs and Schwarz, 2003, Lo et al., 2000, Pelham and Wang, 1997, Schwarz and Bischofs, 2005, Zemel et al., 2010a). The rise of $\dot{\sigma}_0$ with increasing $E$ is in the same order of magnitude of the experimental findings (Mitrossilis et al., 2009,

Mitrossilis et al., 2010, Webster et al., 2011). Although the time required to reach $\sigma_p$ is somewhat different between ~200 s in these simulations and ~600 s in experimental studies, it is common that the time needed to reach $\sigma_p$ is relatively independent of $E$ in both, as found in (Mitrossilis et al., 2009) (Figure 3.5A). The inverse proportionality between $\varepsilon_p$ and $E$ (Figure 3.5E), consistent with experiments (Rassier et al., 1999), supports that cells on stiff substrates tend to rearrange intracellular structures rather than deforming the substrate, as in (Engler et al., 2004b, Munevar et al., 2004, Engler et al., 2004a, Richert et al., 2004). Numerical results of $\dot{\varepsilon}_0$ depending on $E$ (Figure 2C) and of $P(\sigma_0)$ (Figure 3.5F), show that the emergent behavior of the network follows Hill's equation for muscle contraction (Hill, 1938). The $\dot{\varepsilon}_0(\sigma_0)$ curve was fit (Figure 3.13) with the relation $(\sigma_0 + a)(\varepsilon_0 + b) = c$ where $a$ = 10.0 Pa, $b$ = 0.0103 $s^{-1}$, and $c$ = 1.0023 Pa/s. In experiments using various types of muscle cells (McMahon, 1985) and myoblasts cells (Mitrossilis et al., 2009), introducing a shape factor $r = a/F_{max} = b/V_{max} \approx 0.25$ normalized the data. For the control case, it was obtained $r_1 = a/\sigma_{0,max} \approx 0.12$ and $r_2 = b/\dot{\varepsilon}_{0,max} \approx 0.4$. The values of these factors were found to be regulated by parameters, such as $k^0_{u,M}$, $\lambda_{u,M}$ and $\lambda_w$ although normalizing the data leads to similar curves (Figure 3.10A-D).

Further insights were provided regarding the effects of motor concentration ($R_M$). It was observed $\sigma_p$ attains a maximum at $R_M$ = 0.02 (Figure 3A). This could be attributed to the limited binding sites for motors on actin filaments in the simulations. However, note that $R_M$ in this model corresponds to the concentration of multimerized myosin II structures in cells rather than that of individual molecules. Therefore, $R_M$ = 0.02 is actually a very high density of large motor structures, and thus cells are likely to have such an optimal $R$ due to blocking effects between the large aggregates of myosins. A refined model including multiple myosin heads per motor and multiple binding sites per actin segment would help to clarify this issue.

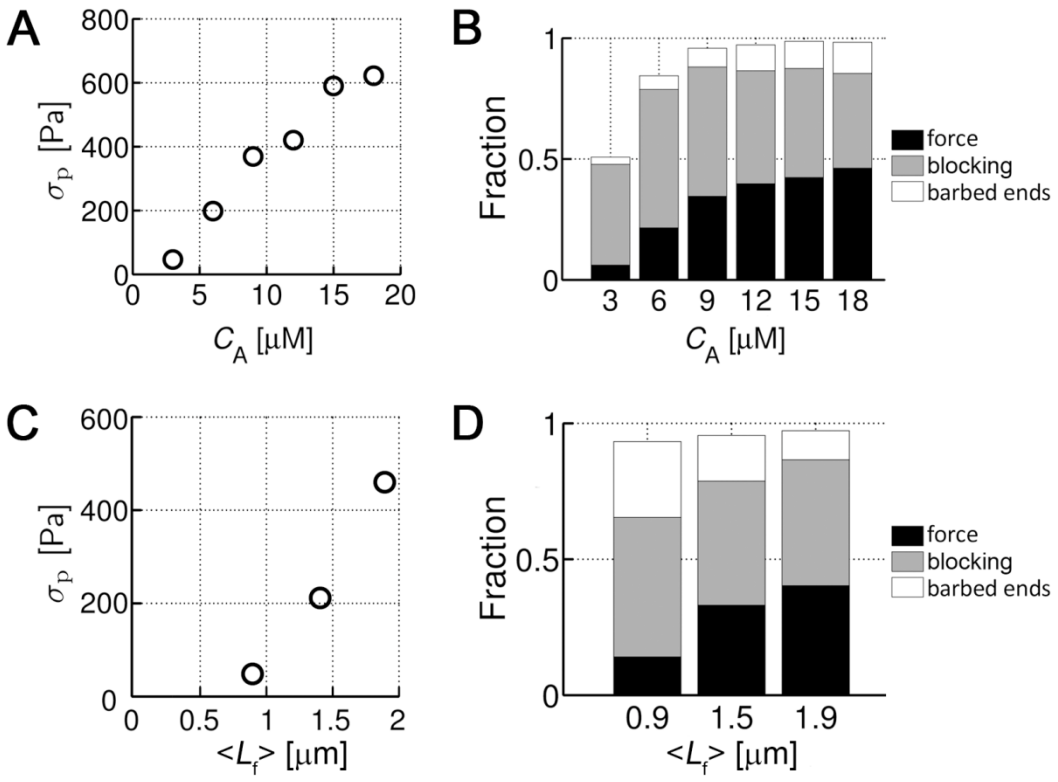


**Figure 3.12:** Effects of actin concentration and actin filament length.
A) $\sigma_p$ monotonically increases with $C_A$. In these simulations, $R_{ACP}$ is constant at 0.01, but $R_M$ decreases with higher $C_A$ since $C_M$ is fixed at 0.24 μM, corresponding to the constant number of motors. B) Fraction of motors stalled due to: (i) high applied forces (black), (ii) blocking (gray), or (iii) arrival at barbed ends of filaments (white) at steady state as a function of $C_A$. At low $C_A$, ~50% of motors are not stalled since many of them lie in the inactive state due to lack of network percolation. As $C_A$ increases, motors are more likely to be stalled due to high forces as opposed to blocking. C) $\sigma_p$ increases dramatically as $\langle L_f \rangle$ is increased. D) Fraction of motors stalled as a function of $\langle L_f \rangle$. Legend is shared with B. As $\langle L_f \rangle$ increases, more motors are stalled due to attaining their maximum force while fewer motors are stalled due to arrival at barbed ends. The number of motors stalled due to blocking remains nearly constant regardless of $\langle L_f \rangle$.

Considering the variable extent of multimerization of myosin II molecules into a minifilament or thick filament, the effects of the zero-force rate of motor unbinding ($k_{u,M}^0$) were evaluated (Figure 3.8) and the mechanical sensitivity for unbinding ($\lambda_{u,M}$) and walking ($\lambda_w$) on network contraction. Motors with high $\lambda_{u,M}$ more readily unbind, and those with high $\lambda_w$ are more likely to be stalled at small forces. $\sigma_p$, $\dot{\sigma}_0$ and $\dot{\varepsilon}_0$ are higher for lower $\lambda_{u,M}$ (Figure 3.9A-C) or for lower $\lambda_w$ (Figure 3.9D-F) although the

overall trend of the curves is conserved well in both cases. By contrast, with high $k_{u,M}^{0}$, $\sigma_p$ is substantially reduced while $\dot{\sigma}_0$ and $\dot{\varepsilon}_0$ are not affected (Figure 3.8A-C).

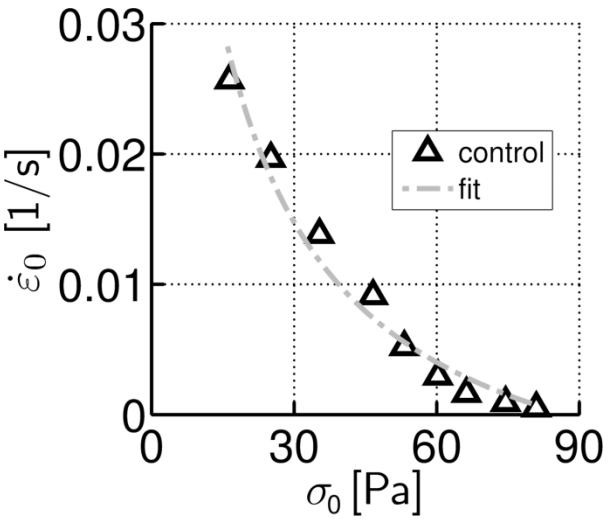


**Figure 3.13:** Control case reduced to Hill's equation.
The network shrinks faster for softer substrates, developing less stress while slower shrinkage leads to higher stress. Values for the constants *a*, *b*, and *c* in Hill's equation $(\sigma_0 + a)(\varepsilon_0 + b) = c$ are 10.0 Pa, 0.0103 $s^{-1}$, and 1.0023 Pa/s respectively. Note that $\dot{\varepsilon}_0$ and $\sigma_0$ were measured at $t$ = 10 s.

In summary, this work elucidated one mechanism by which cells can modulate their properties and respond to the surrounding environment via cytoskeleton contractility, using an agent-based computational model. Although the model is based on molecular-level processes, macroscopic behaviors of the active cross-linked actin networks agree well with the response of cells probed in experimental quantitative studies (Zaman et al., 2006, Discher et al., 2005, Lo et al., 2000, Ruegg et al., 2002). It was found that the biphasic relation between substrate stiffness and the level of generated forces (Engler et al., 2004b, Munevar et al., 2004, Engler et al., 2004a, Richert et al., 2004) is attributable to a transition from stalling due to steric hindrance or "blocking" in soft substrates to that due to stall forces in stiff substrates. In addition, the results showed that in response to increases in substrate stiffness, the contraction rate of cells increases while the corresponding contraction velocity decreases, also consistent with experiments (Webster et al., 2011). All of these suggest that actomyosin contractility is one plausible stand-alone mechanism capable of contributing directly to cell mechano-sensing (Mitrossilis et al., 2009), consistent with various experimental findings that myosins are crucial for cells to sense surrounding matrix elasticity (Engler et al., 2006, Trichet et al., 2012), and that cell responses to rigidity of the external matrix reflect adaptation of the actomyosin machinery to load following Hill's relation (Mitrossilis et al., 2009).

| Variable | Symbol | Value |
|---|---|---|
| Diameter of cylindrical actin segments | $r_c$ | $7.0\times10^{-9}$ [m] (0.05) |
| Length of cylindrical actin segments | $r_{0,A}$ | $1.4\times10^{-7}$ [m] (1.0) |
| Time step | $\Delta t$ | $2.3\times10^{-8}$ [s] ($1.0\times10^{-5}$) |
| Strength of repulsive force | $\kappa_r$ | $4.2\times10^{-4}$ [N/m] (2,000) |
| Extensional stiffness of actin | $\kappa_{s,A}$ | $4.2\times10^{-3}$ [N/m] (20,000) |
| Bending stiffness of actin | $\kappa_{b,A}$ | $2.64\times10^{-19}$ [N m] (63.75) |
| Number of actins per segment | $N_c$ | 20 |
| Length of a single arm of ACP | $r_{0,ACP}$ | $3.5\times10^{-8}$ [m] (0.25) |
| Extensional stiffness of ACP | $\kappa_{s,ACP}$ | $4.3\times10^{-4}$ [N/m] (2,000) |
| Bending stiffness 1 of ACP | $\kappa_{b,ACP1}$ | $1.04\times10^{-18}$ [N/m] (250) |
| Bending stiffness 2 of ACP | $\kappa_{b,ACP2}$ | $4.142\times10^{-18}$ [N m] (1,000) |
| Length of a single arm of motor | $r_{0,M}$ | $7.0\times10^{-8}$ [m] (0.5) |
| Extensional stiffness of motor | $\kappa_{s,M}$ | $4.23\times10^{-4}$ [N/m] ] (2,000) |
| Bending stiffness 1 of motor | $\kappa_{b,M1}$ | $1.04\times10^{-18}$ [N/m] (250) |
| Bending stiffness 2 of motor | $\kappa_{b,M2}$ | $4.142\times10^{-20}$ [N m] (10) |
| Substrate stiffness | $E$ | 0.16 - 40.96 [kPa] |
| Concentration of actin | $C_A$ | $1.2\times10^{-5}$ [M] |
| Ratio of $C_{ACP}$ to $C_A$ | $R_{ACP}$ | 0.01 |
| Ratio of $C_M$ to $C_A$ | $R_M$ | 0.02 (unless specified) |
| Zero-force unbinding rate coefficient of ACP | $k^0_{u,ACP}$ | 0.115 [$s^{-1}$][a] |
| Sensitivity of ACP unbinding | $\lambda_{u,ACP}$ | $1.04\times10^{-10}$ [m][a] |
| Zero-force unbinding rate coefficient of motor | $k^{0*}_{u,M}$ | $2\times10^{-5}$ [$s^{-1}$][b§] |
| Sensitivity of motor unbinding | $\lambda^*_{u,M}$ | $2.6\times10^{-10}$ [m][b§] |
| Sensitivity 1 of motor walking | $\lambda^*_{w,1}$ | $1.3\times10^{-8}$ [m][c] |
| Sensitivity 2 of motor walking | $\lambda^*_{w,2}$ | $2.2\times10^{-9}$ [m][c] |
| Time constant 1 of motor walking | $d_{w,1}$ | $1.1\times10^{-3}$ [s][c] |
| Time constant 2 of motor walking | $d_{w,2}$ | $8.0\times10^{-2}$ [s][c] |
| Time constant 3 of motor walking | $d_{w,3}$ | $5.9\times10^{-3}$ [s][c] |

**Table 3-1:** Main parameters used in the simulations
Numbers in parentheses are corresponding dimensionless values as defined in the text. "*" on symbols indicates reference values of parameters studied in the sensitivity analysis. [a](Ferrer et al., 2008), [b](Guo and Guilford, 2006), [c](Uemura et al., 2004).
Values marked by "§" are adopted from given literature with adjustment based on assumption that motors in this study consist of many myosin II molecules.

Chapter 4

# TIME DEPENDENT MECHANOSENSING

This chapter revises the assumptions of the *mechanosensing* model described in Chapter 2, introducing a temporal dependence of the cell response based on experimental findings from literature and the results predicted by the Brownian-dynamics model detailed in Chapter 3. This new approach, which is initially simplified to 1D, is used to simulate recent experiments of cell *mechanosensing* involving sudden changes in substrate compliance and force saturation with time and stiffness. Finally, the model is extended and applied to different 3D geometries simulating the same experiments and the results are compared to the previous simplified approach.

**Contents**

## 4.1. Introduction

Currently, there exists much interest in characterizing the mechanical properties of living cells as a material (Kasza et al., 2007). In particular, cells behave completely different when supporting loads (passive) than when exerting forces (active) (Kollmannsberger and Fabry, 2011, Ronan et al., 2012, Ujihara et al., 2012). As stated in previous chapters, cells are constantly pulling on the extracellular matrix (ECM) in order to evaluate the mechanical environment and accordingly respond, adjusting their properties. This mechanism that cells use to sense rigidity has been attributed to two main contributions: cytoskeleton contractility and adhesion complexes (Discher et al., 2005). However, recent experimental works have shown the predominant role of cell contractility. In fact, some of these experiments (Mitrossilis et al., 2009, Mitrossilis et al., 2010, Fouchard et al., 2011) suggest that contractility at cell scale due to acto-myosin response to load is the main hypothesis to understand rigidity sensing mechanism. Others, however, have presented strong evidences that the rigidity-sensing mechanism in cell migration is not only locally driven by focal adhesion growth, but also mediated by a larger-scale mechanism originating in the cytoskeleton (Trichet et al., 2012).

Many different experimental (Kobayashi and Sokabe, 2010, Trichet et al., 2012, Ghassemi et al., 2012) and computational works (McGarry et al., 2009, Zemel et al., 2010b, Vernerey and Farsad, 2011) have been developed in order to characterize the mechanical active response of cells under different rigidity conditions of the extracellular environment. In particular, novel experiments using uni-axial loading conditions with a precise control of the mechanical properties of the extracellular environment have been rising. In this sense, Mitrossilis et al (Mitrossilis et al., 2009) have recently developed a single cell traction force experiment with a custom-made parallel microplate setup. In this study, the authors adhere single cells to two parallel glass microplates coated with fibronectin. One plate was rigid, whereas the other was flexible and used as a nano-Newton force sensor (i.e., a spring of calibrated stiffness). A computer-controlled detection of the flexible plate deflection allowed quantifying real-time single cell traction forces. Therefore, using this setup they were able to measure the cell response as a function of the plate rigidity. In a first phase, the forces increased at different rates, depending on the plate stiffness. After approximately 10 minutes, the forces saturated reaching a plateau. This plateau force was observed to depend upon the stiffness of the flexible plate as long as the stiffness is less than 60nN/μm. However, at higher stiffness

values, the plateau force achieved a maximum value of ≈300 nN that was independent of the stiffness.

Moreover, using this measurement system is facile to induce a step change in the extracellular stiffness in order to evaluate the viscoelastic response of cell contraction to this change. In fact, recently, several authors carried out this experiment, concluding that contracting cells are able to adapt to the stiffness step change on a short timescale of 10's of seconds, showing practically an instantaneous response (Mitrossilis et al., 2010, Crow et al., 2012).

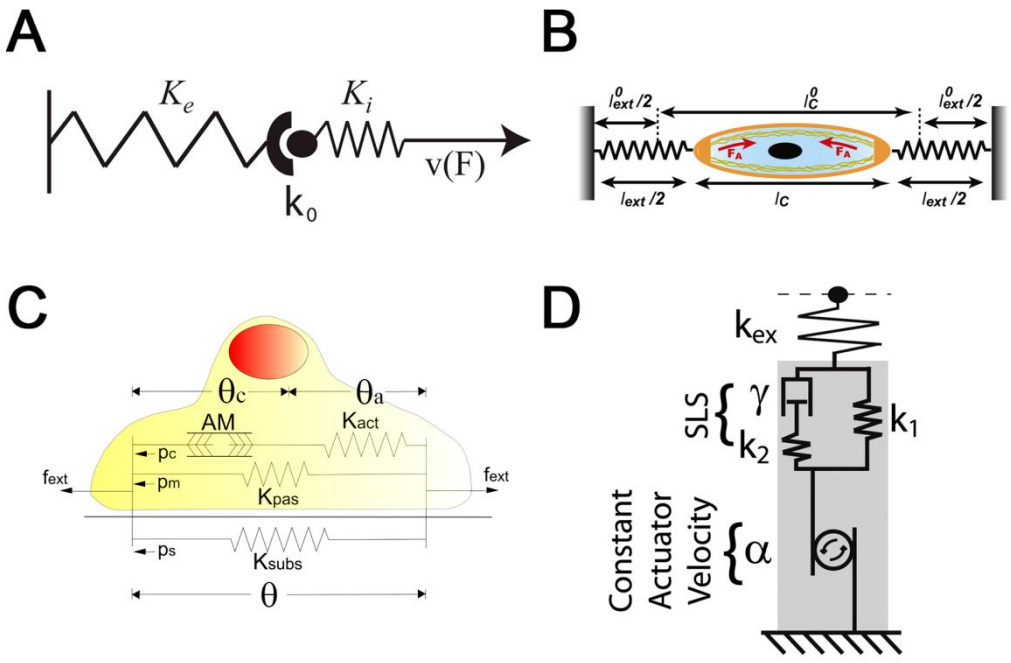


**Figure 4.1:** Mechanical models to describe the contractile cell response.
A) the two-spring approach (Schwarz et al., 2006), B) active matter theory (Marcq et al., 2011), C) the three-spring approach (Moreo et al., 2008) and D) the three-spring and a dashpot approach (Crow et al., 2012).

Collectively, these experiments constitute a set of benchmark data that can be used to validate the predictive potential of models to simulate mechanosensing. The first computational model developed to simulate the mechanosensory role of cells was proposed by Schwarz et al (Schwarz et al., 2006) and was based on a two-spring approach (Figure 4.1A). This model is able to predict saturation force phenomena, although the plateau force is independent of extracellular stiffness. Different "three-spring" approaches have been also proposed to model mechanosensing phenomenon (Figure 4.1B). In particular, Moreo et al. (Moreo et al., 2008) presented a three-spring model with a linear stiffness-dependent actuator, which was capable of predicting cell contractility in

response to changes in extracellular matrix stiffness (Figure 4.1C). In fact, this is the model used and described in Chapter 2 of this Thesis. However, the mechanical approach is static, whereas real cell contractility is time-dependent as has been extensively exhibited experimentally (Mitrossilis et al., 2009). To overcome this limitation several authors have proposed a different theoretical model based on active matter theory (Zemel et al., 2010b, Marcq et al., 2011). Indeed, Zemel et al (Zemel et al., 2010b) established a new model in order to understand the stiffness-dependent orientation of stress fibers in adherent cells. Marcq et al (Marcq et al., 2011) focused their modeling work on the analysis of the temporal cell response to substrate rigidity, but, they did not study the response of their model to sudden changes in substrate rigidity. Recently, Foucard and Vernerey (Foucard and Vernerey, 2012) investigated the viscoelastic behavior of stress fibers, but their primarily addressed the dependence of stress fiber elasticity on stretching frequency. Deshpande et al. combined mechanics with time-dependent chemical signaling (Deshpande et al., 2006) in order to predict the role of focal adhesions and stress fiber concentration in the development of force by cells. Finally, Crow and co-workers (Crow et al., 2012) proposed a three-spring model including a dashpot and an independent actuator contracting at a constant velocity (Figure 4.1D), although their approach was focused on capturing the instantaneous cell response rather than the long term behavior. Notably, with this scheme the authors were able to adjust a mechanical law to successfully simulate step changes induced in the extracellular rigidity; however, their model is not able to predict temporal saturation of forces under different stiffness. Therefore, to fully predict this benchmark of experiments, a novel one-dimensional constitutive law for cell contractility and force generation, capable of reproducing some important features of cell response to extracellular stiffness is proposed in this chapter.

## 4.2. Constitutive law

In this work, the *mechanosensing* model described in Chapter 2 (initially proposed by (Moreo et al., 2008)) is extended to include rate-dependent effects. The system is similar as in the previous work, consisting on two parallel springs representing the stiffness of the passive mechanical components of the cell and the actin filaments which are, furthermore, in series with the myosin motor contractile system (Figure 4.2). This approach was purely mechanical and static, so that the contractile system exerted a specific force depending on the cell strain, and thus depending on the substrate stiffness. However, the time-force

evolution, which plays a critical role in cell *mechanosensing*, was not taken into account. These rate-dependent or viscous effects have already been included into other models by means of the addition of dashpots, e.g. in the three-spring approach, however, they are not able to simulate all cell responses associated with changes in the extracellular rigidity. Hence, a different approach is here presented incorporating an internal variable that takes into account the kinetics associated to cell molecular motors, in particular, the force saturation due to motor stalling.

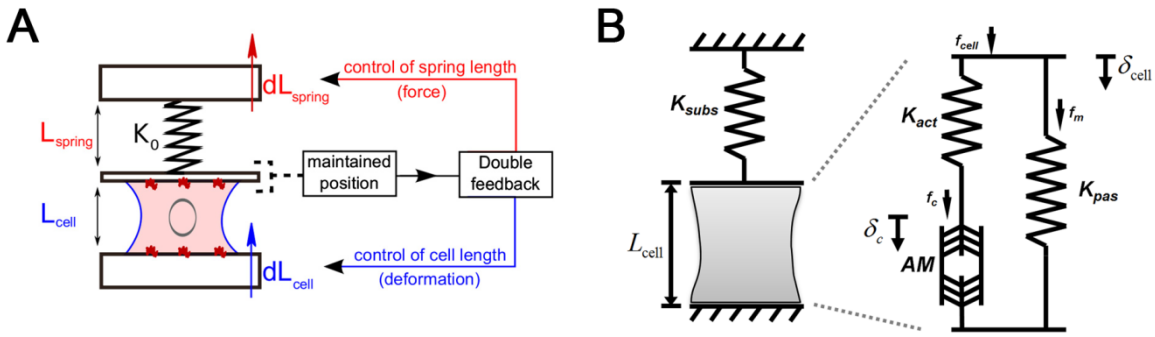


**Figure 4.2:** System schemes for measuring cell mechanosensing properties.
A) Experimental setup used by (Mitrossilis et al., 2009) to measure the effect of substrate rigidity on cell forces. They decouple probe elongation (i.e., force) from cell contraction using a double feedback loop which independently regulates spring and cell lengths to maintain cell-spring contact in a fixed position. In this way, the setup acts as if the cell was compressing a spring of stiffness $K_0\left(dL_{\text{spring}}/dL_{\text{cell}}\right)$, permitting the study of a wide range of rigidities with a single probe of stiffness $K_0$. B) Model scheme used in this work to investigate stiffness-dependent cell response. In similar fashion to the experimental setup, the substrate stiffness is represented by a single spring ($K_{\text{subs}}$). The cell body is modeled as two parallel springs, one of them in series with a contractile actuator. $K_{\text{pas}}$ represents the passive stiffness of different mechanical components of the cell (e.g. microtubules, membrane, cytoplasm), whereas $K_{\text{act}}$ stands for the rigidity of the actin filaments. The acto-myosin system (*AM*) is then placed in series, contracting the cell body by stretching the actin and compressing the passive components

### 4.2.1. Definition of internal variables

To simulate the cell, a one-dimensional mechanical device consisting of two springs and a linear stiffness-dependent actuator $f_{\text{c}}\left(\delta_{\text{c}}\right)$ is considered (Figure 4.2B). The active force of the contractile actuator simulates the force provided by the actin and myosin cross-bridges at the sarcomere level when shortening. In this scheme, the series element $K_{\text{act}}$

corresponds to the stiffness of the actin components and the parallel element $K_{\text{pas}}$ to the stiffness of different mechanical components of the cells, such as, the membrane, microtubules, cytoplasm and others. In addition, $K_{\text{subs}}$ corresponds to the extracellular or substrate stiffness that describes the rigidity associated to the deformed plate used in the mechanosensing experiments (Mitrossilis et al., 2009) presented above.

The temporal response of the cell is characterized by using an internal variable as follows: let [0,T] be the time interval of interest. Following the results from the previous chapter, the internal variable $\alpha$ is defined:

$$\alpha : [0,T] \to \mathbb{R}$$

and interpreted as the level of motor stalling, that is to say, the ratio of myosin molecules that are stalled, with $\alpha = 1$ meaning that the cell has reached equilibrium (Borau et al., 2012). Therefore, this ratio takes on various values corresponding to the range $0 \le \alpha(t) \le 1$.

From a phenomenological point of view, motor activation is regarded as an internal variable, which is characterized in terms of the history of the cell contraction displacements $\delta_{\text{cell}}(t)$.

## 4.2.2. Additive decomposition of the displacement field

The basic assumptions underlying the formulation of this phenomenological model of cell mechanosensing, lead to a set of local governing equations that can be summarized as follows.

From the model depicted in Figure 4.2, the compatibility equation in the displacement field can be derived:

$$\delta_{\text{cell}} + \delta_{\text{subs}} = 0 \tag{4.1}$$

It is assumed that the cell displacement or cell stretching can be decomposed into a contractile and an elastic part. In other words, the total displacement is the sum of the contraction of the acto-myosin system ($\delta_{\text{c}}$) and the extension of the actin filaments ($\delta_{\text{a}}$):

$$\delta_{\text{cell}} = \delta_a + \delta_c \tag{4.2}$$

### 4.2.3. Cell forces

The force that a cell exerts on the plate or the extracellular substrate ( $f_{\text{cell}}$ ) is defined through the stiffness of the substrate $K_{\text{subs}}$ and the variation of the cell height ( $\delta_{\text{cell}}$ ):

$$f_{\text{cell}} = K_{\text{subs}}\delta_{\text{subs}} = -K_{\text{subs}}\delta_{\text{cell}} \tag{4.3}$$

Now the governing equations for the model depicted in Figure 4.2 are derived from equilibrium, where the force that the cell exerts can be decomposed into the force exerted by the contractile system and the force borne by the passive matrix of the cell:

$$f_{\text{cell}} = f_c + f_m \tag{4.4}$$

where $f_{\text{m}}$ depends on the cell passive stiffness:

$$f_m = K_{\text{pas}}\delta_{\text{cell}} \tag{4.5}$$

Cell tension is generated by the myosin II molecular motors walking along the actin filaments. The force generated by the activity of myosin causes oppositely orientated actin filaments to slide relative to one another if they are free to move, or to experience tension if they are not. For simplicity, as described in Chapter 2, the following linear constitutive relationship is assumed, connecting the contractile acto-myosin force $f_{\text{c}}$ and the relative slippage distance between the actin filaments $\delta_{\text{c}}$, according to the classical Huxley's law:

$$f_c\left(\delta_c\right) = \begin{cases} f_{\max}\left(1-\dfrac{\delta_c}{\delta_1}\right) & \text{if} \quad \left(1-\dfrac{\delta_c}{\delta_1}\right) > 0 \\ 0 & \text{if} \quad \left(1-\dfrac{\delta_c}{\delta_1}\right) \le 0 \end{cases} \tag{4.6}$$

where $f_{\max}$ describes the zero-slippage force and $\delta_1$ is the maximum slippage distance. In the same way that Huxley (Huxley, 1957) defined a maximum cross-bridge extension to limit the number of attached motors, it is needed to establish a range where the dependence of acto-myosin force on slippage is valid. Hence, for slippages higher than this maximum distance ( $\delta_{\text{c}} \ge \delta_1$ ), the acto-myosin force ( $f_{\text{c}}$ ) drops to 0. At zero slippage ( $\delta_{\text{c}} = 0$ ), $f_{\text{c}}$ is maximum. With no further assumptions, the mechanical equilibrium is

independent of time, and $f_c$ takes a unique value for a given $\delta_c$,which in turn depends on the substrate stiffness, as will be shown below. To account for time-dependent phenomena, Huxley used cross-bridge attachment and detachment rates, as well as transport effects due to relative fiber motion. Here it is assumed that this time-dependent response is based on the stalling of myosin motors with time. Hence, equation (4.6) should be equivalent to the real constitutive equation when the system has reached steady state ($\alpha = 1$); that is to say, when all the motors are actively walking along the actin filaments exerting maximum force. Therefore (4.7) is naturally updated from the previous expression by introducing the fraction of active motors ($\alpha(t)$). In this way, although the linear relationship between $f_c$ and $\delta_c$ remains, the force that the acto-myosin actuator is able to exert increases with time, and accordingly with $\alpha$, as shown in Figure 4.3A. The force exerted by the motors and transmitted to the actin filaments can be then expressed as:

$$f_c(\delta_c,\alpha) = K_{\text{act}}\delta_a = \begin{cases} f_{\max}\left(\alpha(t) - \dfrac{\delta_c}{\delta_1}\right) & \text{if} \quad \left(\alpha(t) - \dfrac{\delta_c}{\delta_1}\right) > 0 \\ 0 & \text{if} \quad \left(\alpha(t) - \dfrac{\delta_c}{\delta_1}\right) \le 0 \end{cases} \tag{4.7}$$

Note that this expression renormalizes both the maximum contraction and maximum force that the *AM* system is able to do at each time instant (Figure 4.3A) and ensures the continuity of the time dependent response as discussed in the next section. This equation (4.7) aims to model the contractile activity due to the acto-myosin machinery, nevertheless, the expression could be generalized to incorporate also negative forces (cell pushing the matrix) due to other different mechanisms such as actin polymerization (Mogilner, 2009).

By equilibrium of forces, and combining equations (4.3) (4.4) (4.5) and (4.6), it can be found a direct relationship between the relative displacement of the actin filaments of the acto-myosin contractile system $\delta_c(t)$ and the ratio of active motors $\alpha(t)$ being dependent on extracellular rigidity:

$$\delta_c(t) = \frac{\left(K_{\text{act}} + K_{\text{pas}} + K_{\text{subs}}\right) f_{\max}\delta_1}{\left(K_{\text{act}} + K_{\text{pas}} + K_{\text{subs}}\right) f_{\max} - \left(K_{\text{pas}} + K_{\text{subs}}\right) K_{\text{act}}\delta_1}\alpha(t) \tag{4.8}$$

Using the same procedure, the force that a cell transmits to the substrate can be derived as a function of $\alpha(t)$ and $K_{\text{subs}}$:

$$f_{\text{cell}} = \alpha(t)\, f_{\max} \frac{\dfrac{K_{\text{subs}}}{K_{\text{act}}}}{\left(\dfrac{K_{\text{subs}}}{K_{\text{act}}} + \dfrac{K_{\text{pas}}}{K_{\text{act}}}\right)\left(1 - \dfrac{f_{\max}}{K_{\text{act}}\delta_1}\right) - \dfrac{f_{\max}}{K_{\text{act}}\delta_1}} \tag{4.9}$$

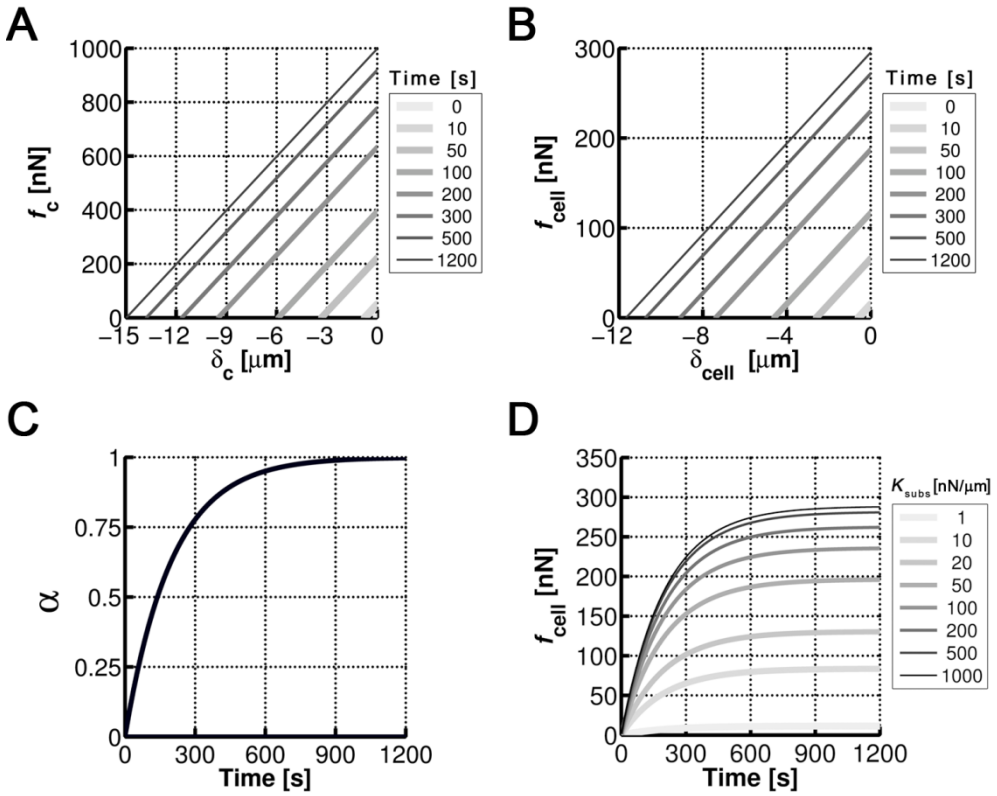


**Figure 4.3:** Model temporal response.
A) Force generated by the contractile system ( $f_c$ ) as a function of the relative slippage distance between the actin filaments ( $\delta_c$ ) at different times. Longer $\delta_c$ leads to lower forces. At a given slippage, the force increases with time. B) Force of the cell transmitted to the ECM as a function of cell contraction ( $\delta_{cell}$ ) at different times. Longer $\delta_{cell}$ lead to lower forces. At a given cell contraction, the force increases with time. C) Fraction of active motors vs. time. The activity of motors increases with time following an exponential law until saturation. D) Force evolution for different substrate stiffness. The force increases with time until saturation, at a faster rate for stiffer substrates.

### 4.2.4. Time-dependent response

As described in previous works, motors can walk, bind and unbind depending on the forces supported (Guo and Guilford, 2006), and during this process, they are able to

generate increasing contraction forces in the cell network. Eventually, a mechanical equilibrium is reached due to generalized stalling of the motors. These stalling events may occur for several reasons such as high forces, arrival at barbed ends or blocking due to lack of binding sites. These phenomena and their role in cell mechanosensing were previously explored in Chapter 3 of this Thesis (Borau et al., 2012). In that chapter, using a Brownian dynamics computational model, it was found that although the cause for motor stalling depends on the extracellular matrix (ECM) compliance, the number of stalled motors and the stalling evolution with time is practically independent of ECM stiffness. Other previous phenomenological models assumed the relaxation time to be a decreasing function of substrate rigidity (Marcq et al., 2011, Crow et al., 2012). However, this dependency was found to be significant only at very short times. In fact, Crow et al. (2012) showed experimentally that relaxation time ranges between 6.53 s (for null substrate stiffness) and 2.64 s (for infinity rigid substrates). Hence, for the long term response (~1000 s as used in Mitrossilis's experiments), a constant relaxation time gives similar results.

Here, a general and simplified regulatory rule is proposed to define the temporal evolution of motor stalling depending on the force transmitted through the actin filaments and independent of substrate rigidity, with the following explicit form:

$$\dot{\alpha} = \frac{g\left(f_c\right)}{\mu} \tag{4.10}$$

where $\mu$ [nN.s] is a viscosity coefficient and $g\left(f_c\right)$ is the regulatory function that controls this time evolution, defining the system approach to its maximum force:

$$g(f_c) = f_c^{\max} - f_c = f_{\max}\left(1-\frac{\delta_c}{\delta_1}\right) - f_{\max}\left(\alpha(t)-\frac{\delta_c}{\delta_1}\right) = f_{\max}\left(1-\alpha(t)\right) \tag{4.11}$$

Combining equations (4.10) and (4.11), and defining $\tau$ as the relaxation time, the evolution of motor stalling is obtained:

$$\dot{\alpha} = \frac{f_{\max}\left(1-\alpha\right)}{\mu} = \frac{\left(1-\alpha\right)}{\tau} \tag{4.12}$$

On physical grounds, $\alpha(t)=\alpha_0$ is assumed as initial condition ($t=0$) and integrating this equation, the expression that defines the evolution of $\alpha(t)$ can be written:

$$\alpha(t)=1+(\alpha_0-1)e^{\frac{-t}{\tau}} \tag{4.13}$$

Using the specific values of the different parameters indicated in Table 4-1, the temporal evolution of $\alpha$ and the forces generated by the contractile system ($f_c$) and those transmitted to the substrate ($f_{cell}$) are computed as a function of the relative slide and time, respectively (Figure 4.3A-D). Note that although the relaxation time ($\tau$) is substrate stiffness-independent, the rate of force build-up ($dF/dt$) is not, capturing the stiffness-dependent instantaneous cell response (as shown in next section):

$$\frac{dF}{dt}=\frac{(1-\alpha)}{\tau}f_{max}\frac{\frac{K_{subs}}{K_{act}}}{\left(\frac{K_{subs}}{K_{act}}+\frac{K_{pas}}{K_{act}}\right)\left(1-\frac{f_{max}}{K_{act}\delta_1}\right)-\frac{f_{max}}{K_{act}\delta_1}} \tag{4.14}$$

It is important to clarify that the regulatory function $g(f_c)$ is chosen for simplicity, because $\alpha$ can be given a physical meaning (motor stalling) and because it gives predictions in good agreement with experimental observations. Certainly $g(f_c)$ could be revised if $f_c$ was differently defined. In fact, its current definition (equation (4.7)) permits to renormalize both the slippage and the force exerted by the *AM* system so that its contraction varies in time even for a fixed value of substrate stiffness. Other definitions (e.g. $f_c=\alpha(t)f_{max}(1-\delta_c/\delta_1)$) could also be valid, but apart from the mathematical implications (shown later), the physical interpretation would differ. Figure 4.4 shows the differences between the current (left) and an alternative (right) definition of $f_c$.

The current main assumption is that $\alpha$ represents the fraction of stalled motors, that is, the ratio of molecular motors that are stalled (either by blocking due to lack of binding sites, high forces or arrival to barbed ends of actin filaments) whose temporal evolution was found to follow an exponential law in previous studies (Borau et al., 2012). In addition, these stalling events are related to network stability, so that stalled motors form stronger cross-links and transmit higher forces through the cytoskeleton network. In other

words, free motors tend to form dynamic links that may reorganize the network but contribute little to the overall contraction, whereas stalled motors stabilize the cross-links leading to a more organized structure able to contract and generate high forces. Therefore, this hypothesis implies that at $\alpha = 0$, the cytoskeleton network is still not fully formed, and the motors have not yet had much opportunity to contract ($\delta_c = 0$) and little or no force is generated ($f_c = 0$). However, when all the motors are stalled ($\alpha = 1$), the cell cytoskeleton has achieved its maximum ability to generate force at all values of $\delta_c$. Hence, when $\delta_c = 0$ and all of the motors have become stalled, the maximum force can be generated ($f_c = f_{max}$); when $\delta_c = \delta_1$ (that is, when no constrains impede contraction, $K_{subs} \sim 0$) all motors have reached their maximum contractile displacement, and the force generating capacity goes to zero ($f_c = 0$). In any case, $\alpha_0$ in equation (4.13) allows regulating the initial network state, although $\alpha_0 = 0$ was used in the simulations. On the other hand, the alternative definition of $f_c$ implies that the acto-myosin system is able to contract up to $\delta_1$ regardless of the number of motors that have stalled, which is not fully consistent with the assumption that represents the motor stalling evolution. For instance, $\alpha(t)$ is set to 0 (so that no motor stalls in the simulation) and a hypothetical actin network behaving as we propose is considered, the actin would permanently slide on the myosin motors, continuously remodeling the cytoskeleton network but not necessarily contracting the whole structure. In other words, if motors were not stalled (forming a more stable cross-linked network), they would tend to "walk", sliding on actin filaments rather than transmitting contraction through the network. Additionally, the alternative approach would lead to more complicated equations as shown below.

Recall the mathematical procedure described previously in this Chapter but starting from the alternative definition of $f_c = \alpha(t) f_{max} \left(1 - \delta_c^{alt} / \delta_1\right)$. The superscript "alt" is used to avoid confusion with previous equations:

With this new approach and again combining combining equations (4.3) (4.4) (4.5) and (4.6), the slippage ($\delta_c^{alt}$) dependence on $\alpha$ becomes:

$$\delta_c^{alt}(t) = \frac{\left(K_{act} + K_{pas} + K_{subs}\right) f_{max} \delta_1}{\left(K_{act} + K_{pas} + K_{subs}\right) \alpha(t) f_{max} - \left(K_{pas} + K_{subs}\right) K_{act} \delta_1} \alpha(t) \tag{4.15}$$

And therefore the cell force can be written as:

$$f_{\text{cell}} = \alpha(t)\, f_{\max} \frac{\dfrac{K_{\text{subs}}}{K_{\text{act}}}}{\left(\dfrac{K_{\text{subs}}}{K_{\text{act}}} + \dfrac{K_{\text{pas}}}{K_{\text{act}}}\right)\left(1 - \dfrac{\alpha(t)\, f_{\max}}{K_{\text{act}}\delta_1}\right) - \dfrac{\alpha(t)\, f_{\max}}{K_{\text{act}}\delta_1}} \tag{4.16}$$

Note the presence of $\alpha(t)$ in the denominators

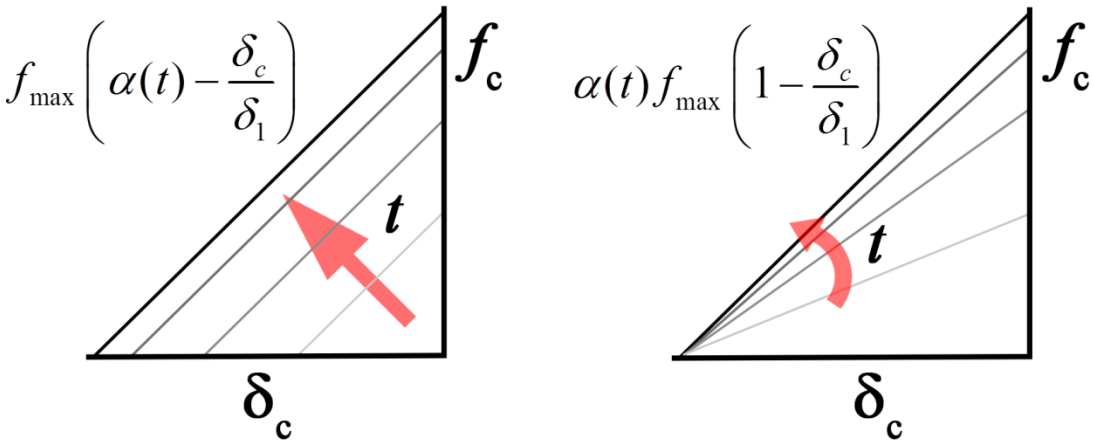


**Figure 4.4:** Renormalization of AM system contraction depending on the definition of the acto-myosin force.
The current approach (left) renormalizes both the maximum slippage and maximum force with time, whereas an alternative definition (right) only renormalizes the force with important mathematical implications.

In sum, this alternative definition of $f_c$ makes difficult to choose a regulatory rule ( $\dot{\alpha}$ ) with physical menaning (e.g. system approaching to its maximum force) which furthermore leads to a temporal response $\alpha(t)$ that fulfills the experimental data, also maintaining some physical meaning (e.g. motor stalling evolution).

## 4.3. Problem description and results

### 4.3.1. Simulated experimental assay

A single cell fixed between a rigid and a flexible plate is simulated in order to reproduce the experimental setup designed by Mitrossilis et al.(Mitrossilis et al., 2009) and used by different authors (Webster et al., 2011, Crow et al., 2012) to evaluate cell mechano-

sensing properties (Figure 4.2A). In this setup, the cell pulls on the two parallel plates while the plate deflection is measured. By using a double feedback loop which independently regulates spring and cell lengths to maintain cell-spring contact in a fixed position, they obtain the temporal cell response for different external rigidities.

A simplified one-dimensional problem is defined to understand contractility and force generation due to cell response under different extracellular rigidities (Figure 4.2B). Two main conditions are simulated. Firstly, the temporal evolution of cell contractility and force generation under a wide range of extracellular rigidity values are evaluated. Secondly, the cellular time-response under step-changes of the extracellular stiffness is computed.

### 4.3.2. Cell contraction and force generation under different extracellular stiffnesses

The temporal evolution of force generation, which depends on the extracellular rigidity, is shown in Figure 4.3D and Figure 4.5A. In the former, and according to equation (4.9), force develops following the evolution of motor activation. The maximum value achieved (the plateau force $f_p$) depends on the substrate stiffness ($K_{subs}$)(Figure 4.5B). Note that the model parameters were adjusted to obtain similar values to experimental data (Mitrossilis et al., 2009). At a given time, the force increases with stiffness, abruptly for low stiffness and smoothly for higher ones (Figure 4.5A). Qualitatively similar results were found experimentally, measuring the cell stress exerted on micropillars of different stiffness. (Trichet et al., 2012). Taking the force at $t$=1200 seconds as the plateau force and plotting it against substrate stiffness, it is found that for $K_{subs}$ < 100 nN/μm, $f_p$ rapidly increases with stiffness, saturating for higher rigidities, in good agreement with literature (Mitrossilis et al., 2009). In fact, both in the model and experiments, $f_p$ is proportional to $K_{subs}$ in compliant substrates ($\sim K_{subs}^{0.87}$ and $\sim K_{subs}^{0.94}$ respectively). In addition, other authors found an initially linear relationship ($\sim K_{subs}^{0.93}$) (Trichet et al., 2012), although their study only took into account substrate stiffness up to 80 nN/ μm (Figure 4.5B). The rate of force build-up ($dF/dt$, slope of the force curve) increases quickly and proportionally to the stiffness at first, and slows down as the force approaches the maximum plateau (~300 nN (Mitrossilis et al., 2009)). In relation with the

substrate stiffness and measuring $dF/dt$ in the first phase of contraction ($t$<100 s), the rate of force build-up strongly increases for compliant substrates and presents slight changes for stiffer ones (Figure 4.6A), similarly to recent experimental findings (Mitrossilis et al., 2009, Mitrossilis et al., 2010, Trichet et al., 2012). Note that in this last work (Trichet et al., 2012), as in the measurement of the plateau force, only the initial linear regime was observed since their study was focused on compliant substrates.

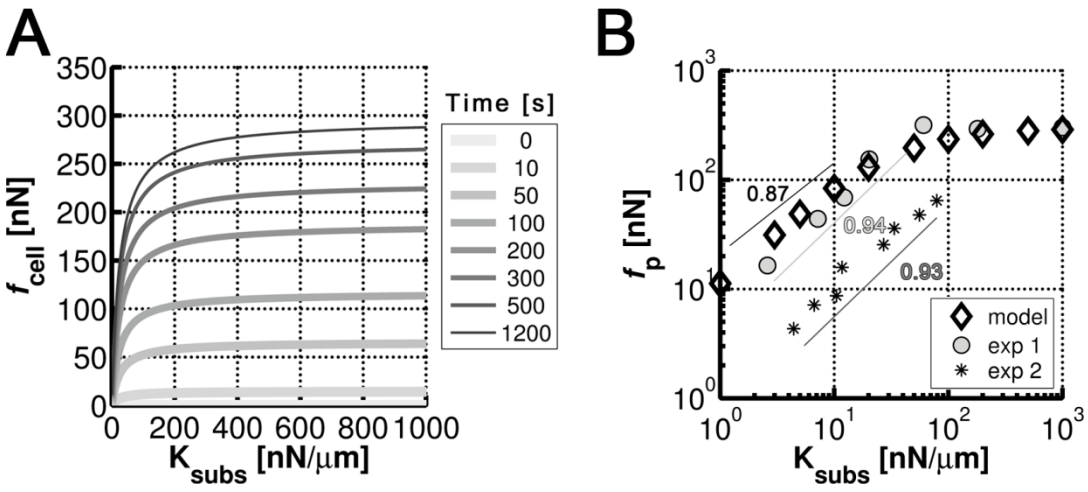


**Figure 4.5:** Cell force evolution and plateau values depending on substrate stiffness. A) Cell force as a function of substrate stiffness for different times. The force increases exponentially at low stiffness, and saturates (plateau force) for higher ones. The force increases with time for all the stiffness due to the growing motor activation. B) Saturation or plateau force ( $f_p$ ) as a function of substrate stiffness in log-log scale. $f_p$, in other words $f_{cell}$ measured at $t$=1200 s, increases proportionally to $K_{subs}$ ( $f_p \sim K_{subs}^{0.87}$ ) for softer substrates, in similar fashion to the experimental finding from (Mitrossilis et al. 2009) ( $f_p \sim K_{subs}^{0.94}$, exp 1 in the legend), and (Trichet et al. 2012) ( $f_p \sim K_{subs}^{0.93}$, exp 2), and saturates for stiffer ones as in (Mitrossilis et al. 2009).

The speed of shortening ($v_{cell}$) is easily derived from the rate of force build-up as $v_{cell} = (dF/dt)/K_{subs}$. The cell shortening is faster for compliant substrates, whereas stiffer substrates, which resist the contraction, lead to practically null velocities for $K_{subs}$ >1000 nN/μm (Figure 4.6B), qualitatively similar to the speed behavior found in (Mitrossilis et al. 2009). Mechanical power ($P$) is also computed, presenting a bi-phasic behaviour with the load and showing a peak at ~40% of the maximum generated force, following the classical behavior observed in muscles and recently found in myoblasts (Mitrossilis et al., 2009) due to acto-myosin contraction (Figure 4.6C).

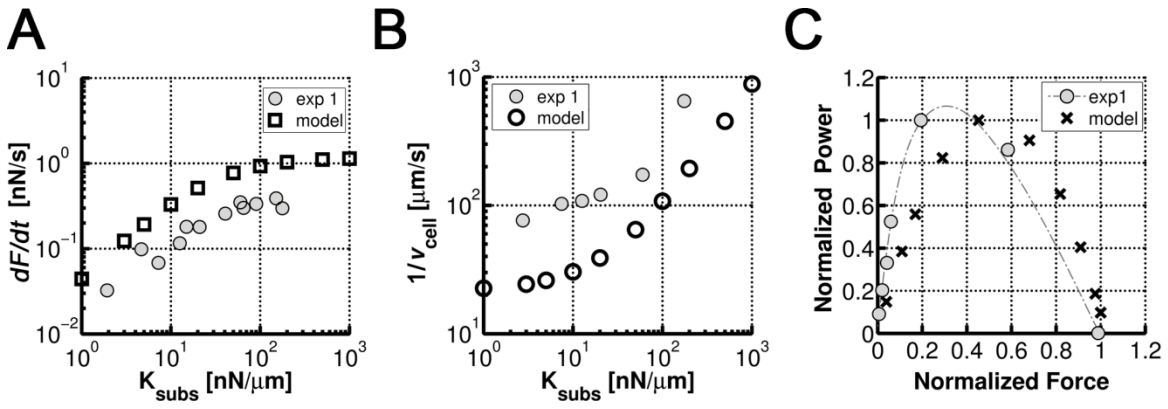


**Figure 4.6:** Rate of force build-up, speed of shortening and cell power.
A) Initial rate of force build-up ($dF/dt$) as a function of substrate stiffness. In the first phase of contraction ($t$ <100 s), the rate of force build-up strongly increases for compliant substrates and presents slight changes for stiffer ones as found by (Mitrossilis et al. 2009)(exp 1 in the legend). B) Inverse of cell speed of shortening ($v_{cell}$) as a function of substrate stiffness. The cell contracts faster for softer substrates, $v_{cell}$ approaching zero for $K_{subs}$ >1000 nN/μm. The curve behaves similarly to experiments (Mitrossilis et al. 2009) C) Normalized mechanical power vs. normalized force. $P$ presents a bi-phasic behaviour with the load, showing a peak at ~40% of the maximum generated force. These behaviors are qualitatively similar to those found by (Mitrossilis et al. 2009).

### 4.3.3. Simulating step changes in extracellular stiffness

In these simulations the cell response to step-changes in substrate stiffness is evaluated with a period of 20 seconds (Figure 4.7A top plot), following the experiments carried out by Crow et al. (Crow et al., 2012) and of 100 seconds (Figure 4.7B top plot), to study the long-term response and compare the results with Mitrossilis et al. data (Mitrossilis et al., 2010). Specifically, $K_{subs}$ is first varied from 10 to 100 nN/μm in a first case, and then from an extremely low value (~0) to an extremely high one (∞) with a period of 20 seconds (Figure 4.7A,B). In both cases, the force generated increases faster (higher slope) when the stiffness is higher (since $dF/dt$ increases with $K_{subs}$) (Figure 4.7A,B middle plots) in good agreement with the simulated experiments (Mitrossilis et al., 2010, Crow et al., 2012). The cell height, however, decreases faster for compliant substrates (Figure 4.7A,B bottom plots). The general trend is clearly seen in the cases with extreme values of substrate stiffness. When $K_{subs} \sim \infty$ the force increases very fast (Figure 4.7A middle plot), especially during the first seconds when the activation of motors is in its early phase, whereas the cell height remains constant (Figure 4.7B bottom plot). In contrast, when $K_{subs} \sim 0$, the rate of force build-up is near zero but cell height rapidly decreases (Figure 4.7B bottom plot). For higher periods of stiffness step change (Figure 4.7C), the

system behaves similarly but the effect of substrate stiffness on the cell force variation is less relevant as time increases due to the saturation of $\alpha$. The motor stalling determines the time at which the system reaches equilibrium, however, the force attained at that point depends on the load-history. For this reason, in the case with stiffness step variations from ~0 to ~∞ (Figure 4.7C), the plateau force after 500 seconds is below 200 nN, much lower than the value that would correspond to an infinitely rigid substrate (~ 300 nN). Logically the cell contraction is higher than in previous cases due to the long periods of low stiffness.

Certainly, the motor stalling could also depend on substrate stiffness due, for instance, to morphology changes of the intracellular network. This could affect the force evolution after each step change, however, it has been reported that although the reasons for motor stalling depend on external stiffness (higher percentage of motors get stalled by forces for stiffer substrates whereas higher percentage of motors get stalled by blocking phenomena if softer substrates), the temporal evolution of stalling remains practically unchanged (Borau et al., 2012).

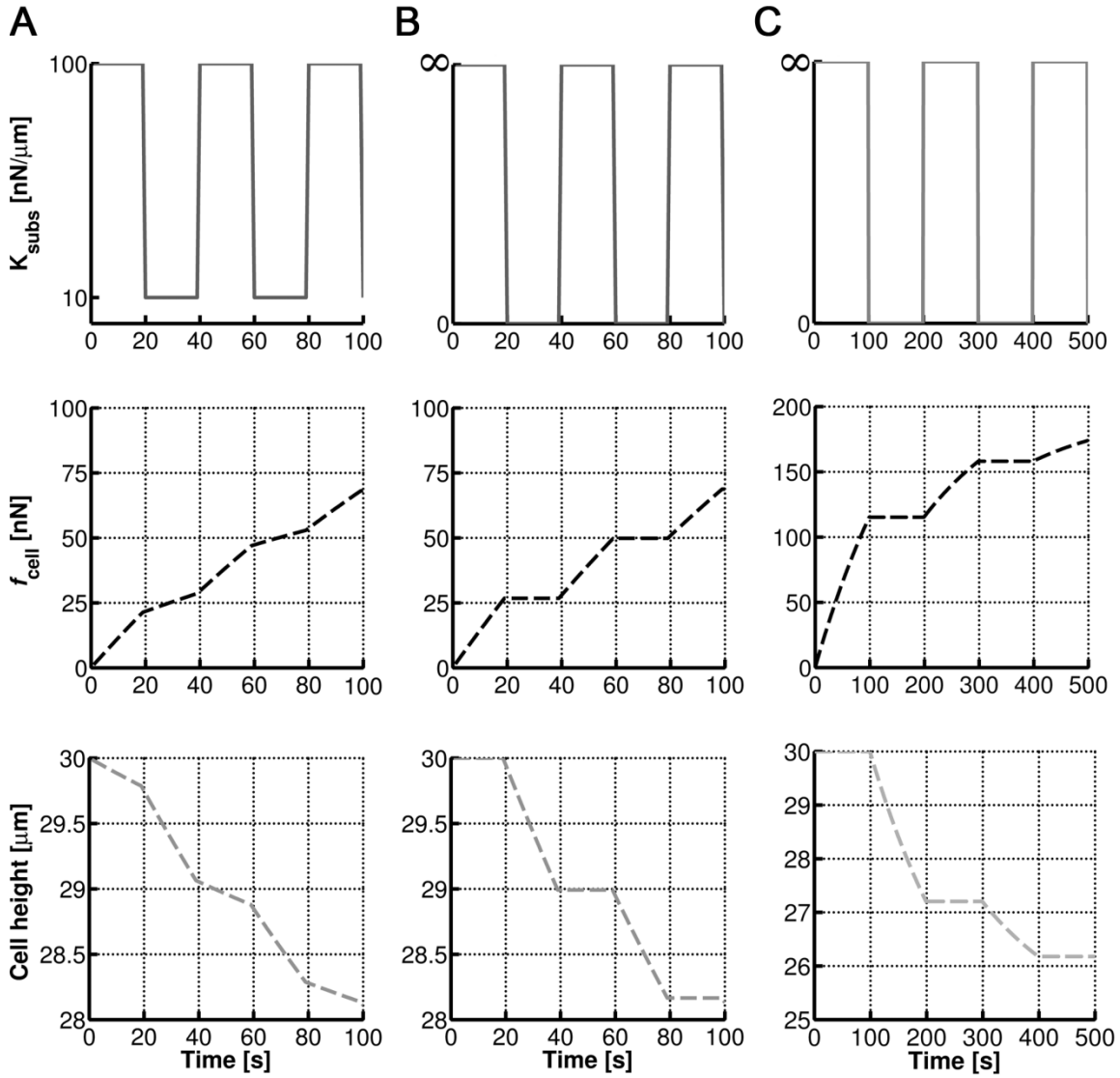


**Figure 4.7:** Cell response to step-changes in substrate stiffness.
A) The stiffness switches from 10 to 100 nN/μm with a period of 20 seconds. The force generated increases faster (higher slope) when the stiffness is higher. The cell height, however, decreases faster for low substrate stiffness. B) The stiffness switches from 0 to ∞ with a period of 20 seconds and C) 100 seconds. The force increases at maximum rate for a completely rigid substrate, whereas the cell height remains invariable. Nevertheless, for a completely compliant substrate, there is no force development and the cell body contracts at maximum speed.

## 4.4. Parameter sensitivity analysis

In order to find which parameters most strongly influence cell rigidity-sensing, a sensitivity analysis is performed. For this analysis, the substrate stiffness is held constant ($K_{subs}$ =100 nN/μm).

The definition of the internal variable that describes the motor stalling evolution ($\alpha$) is the key for all the time-dependent processes simulated in this model. Thus, a proper understanding of the effects of the involved parameters is needed. The global parameter controlling the time evolution of $\alpha$ is the relaxation time ($\tau$), which determines how fast the stalling events reach saturation and specifically the rising of force with time ($dF/dt$). Figure 4.8A shows how $\alpha$ plateaus faster for lower values of $\tau$. However, $\tau$ is not a free parameter, since it depends on $\mu$ and $f_{\max}$ ( equation (4.12)). While $\mu$ only affects $\alpha$, $f_{\max}$ affects the mechanical equilibrium, therefore altering the magnitude of the exerted forces ( $f_{\text{cell}}$ ). Figure 4.8B shows how the plateau force adjusts due to variations of $f_{\max}$, while the time-evolution remains unchanged. This happens because $\mu$ is varied in the same proportion as $f_{\max}$ thus leading to a constant relaxation time. If however, $f_{\max}$ is varied alone (Figure 4.8C), both the plateu force and the relaxation time are affected. High values of $f_{\max}$ lead to higher forces, which are, furthermore, attained faster. On the other hand, $\mu$ is a parameter only affecting time evolution (Figure 4.8D). Hence, changes in $\mu$ are equivalent to changes in $\tau$ (Figure 4.8A).

The purely mechanical components of the cell ( $K_{\text{pas}}$ , $K_{\text{act}}$ ) do play an important role in the mechanical equilibrium. The actin stiffness ( $K_{\text{act}}$ ) appears to be the more relevant component in the mechanical system. Therefore, changing its value, leads to substantial changes in the plateau force (Figure 4.9A). As shown in Figure 4.2, this component is in series with the *AM* system. Thus, increasing the actin stiffness leads to lower values of $\delta_{\text{c}}$ , which in turn increases the cell force (equations (4.4) and (4.6)). However, bigger changes of $K_{\text{pas}}$ are needed to be reflected in $f_{\text{cell}}$ (Figure 4.9B). Actually, these changes in the plateau force are only noticeable when $K_{\text{pas}}$ has similar or greater values than $K_{\text{act}}$. This is confirmed in Figure 4.9C, where both parameters are varied together obtaining similar results to Figure 4.9C, where only $K_{\text{act}}$ changes.

Moreover, the effects of the slippage distance parameter $\delta_1$ are explored. It is important to note that this parameter is independent of the cell length ( $L_{\text{c}}$ ). Hence, $L_{\text{c}}$ does not affect the results as long as $\delta_1$ remains constant. However, higher values of slippage, lead to higher forces and higher deformability of the cell as shown in Figure 4.10. Other authors have taken this value as infinity (Marcq et al., 2011), which is equivalent to consider a constant force of the *AM* system, independent of substrate

stiffness and other parameters. This allows capturing the force-stiffness linearity only for very compliant substrates, whereas the approach presented in this chapter is able to extend the linear regime to experimental ranges, as will be discussed subsequently.

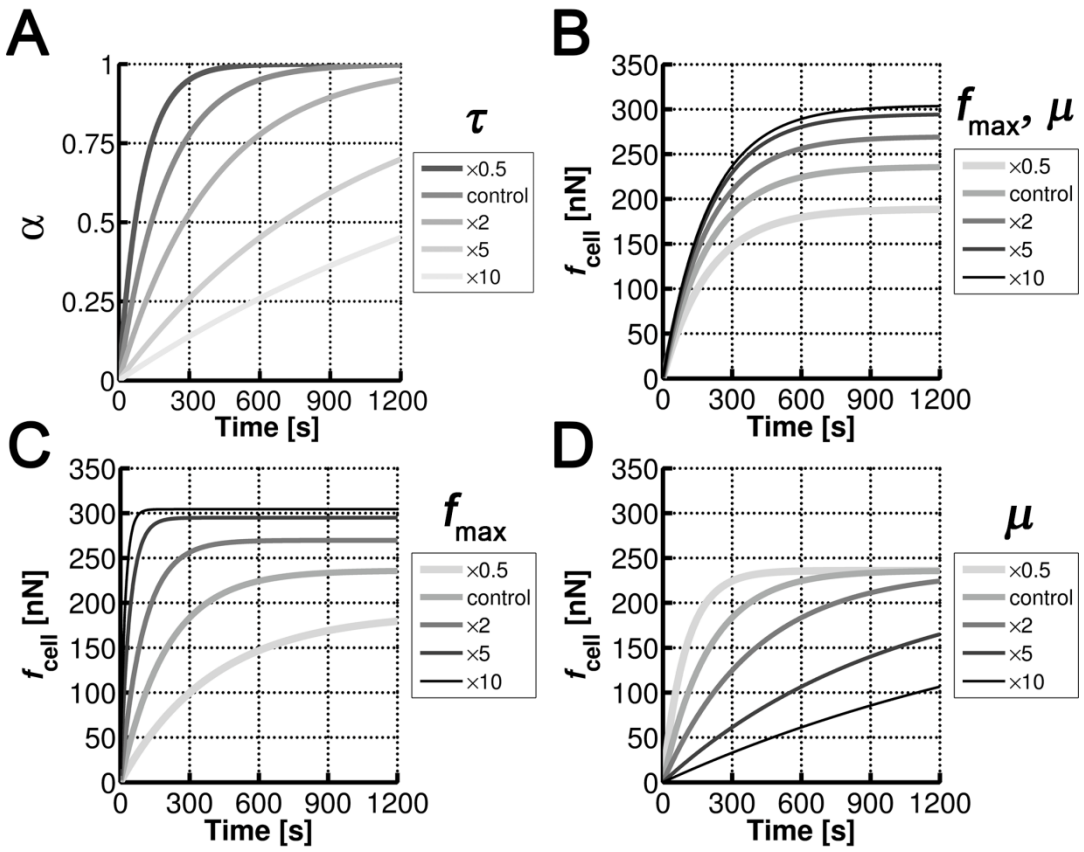


**Figure 4.8:** Sensitivity analysis of parameters involved in motor stalling evolution. A) Evolution of stalling depending on the relaxation time ($\tau$). For higher values of $\tau$, $\alpha$ needs more time to reach plateau. B) If $f_{max}$ and $\mu$ are varied together, the relaxation time ($\tau$) remains constant, whereas the magnitude of exerted forces changes. C) $f_{max}$ affects both the relaxation time and the mechanical equilibrium. Higher values of $f_{max}$ correspond with higher plateu forces attained faster. D) The viscosity coefficient only affects the time-evolution. Thus, changes in $\mu$ are equivalent to changes in the relaxation time.

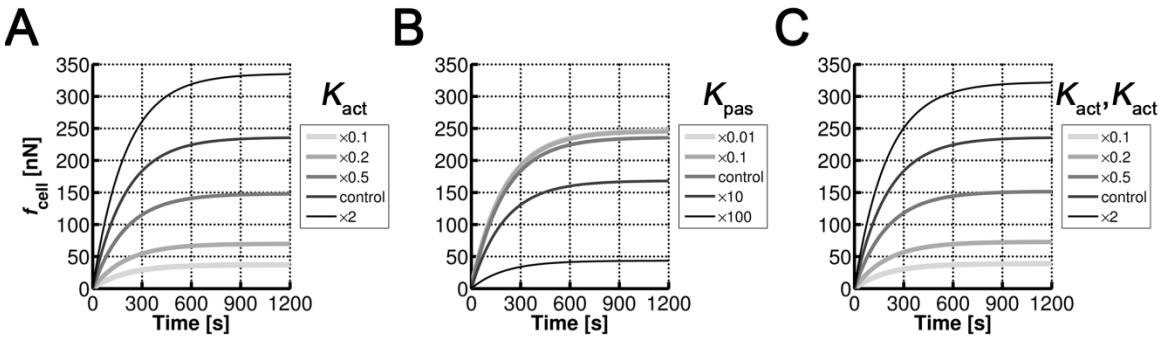


**Figure 4.9:** Sensitivity analysis of the cell force evolution depending on actin and passive stiffness.
A) Changes in $K_{act}$ lead to important changes in the plateau force. High values of actin stiffness decrease the contraction of the *AM* system, thus producing higher forces. B) Variations of the cell passive stiffness affect the force generation only when the values of $K_{pas}$ are similar or greater than the values of $K_{act}$. C) By varying both $K_{act}$ and $K_{pas}$ at the same time, the changes in force generation are similar to those obtained when varying only $K_{act}$, confirming that the actin stiffness is the predominant mechanical parameter.

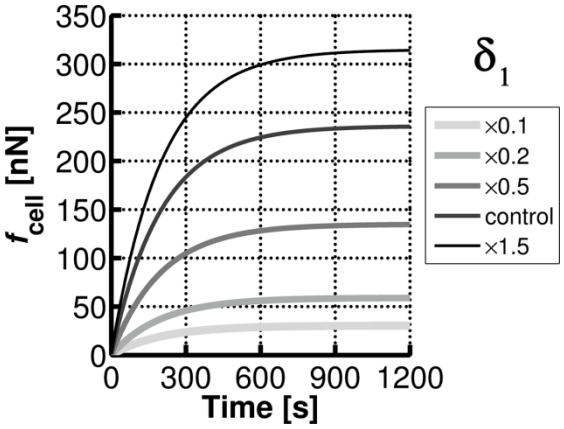


**Figure 4.10:** Effects of maximum slippage distance.
Curves corresponding to $K_{subs}$=100 nN/μm. Higher values of $\delta_1$ enhance system contractility, leading to higher exerted forces.

## 4.5. Extension to 3D problems

So far, the 1D approach of the *mechanosensing* model has demonstrated its ability to reproduce experimental data and its potential in cell motility models. However, in vivo cell response involves many complex mechanisms such as internal pressure, evolving adhesion area, steric effects, curvature and other factors that become relevant in 3D. In this section, following the simulations previously described and using a experimental set similar to the one proposed by (Mitrossilis et al., 2009), the cell contractile response is computed using a 3D approach.

### 4.5.1. Geometry and model adaptation

The experimental system is more accurately modeled using flat surfaces (shell elements) representing the microplates and an initially ellipsoidal cell in contact with both surfaces (Figure 4.11). This system permits plate deflection and the cell elongation in x,y directions when vertically contracting (in z). For that, the *mechanosensing* model was slightly modified. In fact, the AM system-actin branch was simplified and substituted by a thermal expansion element. As stated before, eliminating $K_{act}$ implies some limitations such as the non-linear response of force with respect to $K_{subs}$ for high stiffness, however, this simplification presents important computational advantages for future development.

Since ABAQUS allows coupled mechanical-temperature analysis, the active and passive components of the cell can be modeled and computed in parallel. The active branch can be defined using subroutines, so that the system contraction is controled and made dependent on any desired factor defined in the simulation (e.g. time, strain, stress, actin concentration, motor concentration, degree of cross-linking etc.). In turn, the passive components can be simulated using the material behaviors included on ABAQUS libraries, which describe and model complicated features such as hiperelasticity, poroelasticity, viscoelasticity etc. In this way, the potential of the model increases substantially, allowing testing and combination of complex behaviors by taking advantage of the already inbuilt materials.

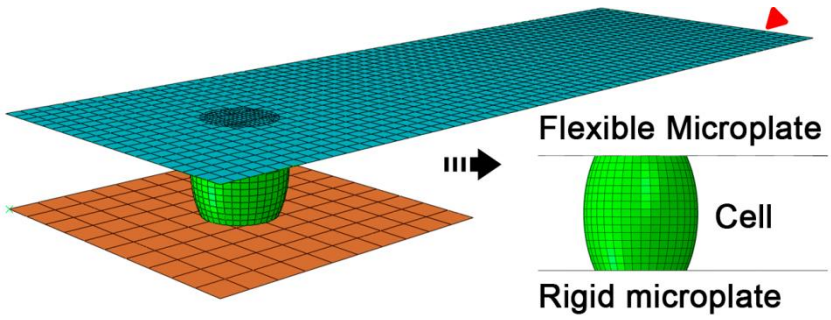


**Figure 4.11:** Experimental setup simulation in 3D.
Cell is represented by an ellipsoidal body placed between a rigid plate (brown) and a flexible one (blue), whose displacements are constrained in one of its edges (red arrow).

### 4.5.2. Material definition and boundary conditions

As a first approximation, for the current calculations the passive components of the cell were simulated with a linear elastic material of Young's modulus $E = 1$ kPa and poisson ratio $\nu = 0.45$. The AM system behavior producing contractile forces, however, was simulated as an anisotropic contraction due to temperature ($\Delta T = 1$) in the vertical direction and expansion in the horizontal one ($\Delta\varepsilon_x^{th} = \Delta\varepsilon_y^{th} = -\Delta\varepsilon_z^{th} = 0.4$) so that the contraction in z-direction is equivalent to the previous 1D scheme. By making the expansion coefficients depending on the motor stalling function ($\alpha$), the temporal response is easily incorporated. This roughly mimics the complicated dynamics that may lead to the dramatic change in cell's aspect ratio such as internal pressure, actin polymerization, formation and maturation of new FA's or CSK reorganization. Nevertheless, this simple approach was enough to reproduce the temporal increase of cell area adhered to the microplates in this specific experiment, serving as the basis for future simulations of actual cell's geometries embedded in 3D media.

The setup was computed using FEM with the following constrains and boundary conditions:

- Top surface is modeled with Shell elements (S4), with contrained nodal displacements at its right side. Its stiffness is varied in the simulations in order to reproduce the experiments developed by (Mitrossilis et al., 2009) .
- Bottom surface is considered a rigid body with null displacements. No friction with the cell surface is taken into account.
- Cell body is meshed using hetrahedral elements (C3D8) and contracts following the temperature-*mechanosensing* coupled model. Cell's bottom surface slides over the bottom plate with restricted z-dispacement. On the other hand, cell's top surface sticks with the top plate in z-direction and slides in x and y.

### 4.5.3. Results

As reported in experiments the cell contracts in the vertical direction while spreading horizontally (Figure 4.12). Introducing the expansion coefficients as a function of motor stalling ($\alpha$), leads to the desired time-contraction dependence. Additionally, the vertical forces exerted on the top microplate were measured at the steady state ($\alpha = 1$) for

different plate rigidities. As expected, higher plate stiffnes lead to lower deflections but higher forces until saturation (Figure 4.13).

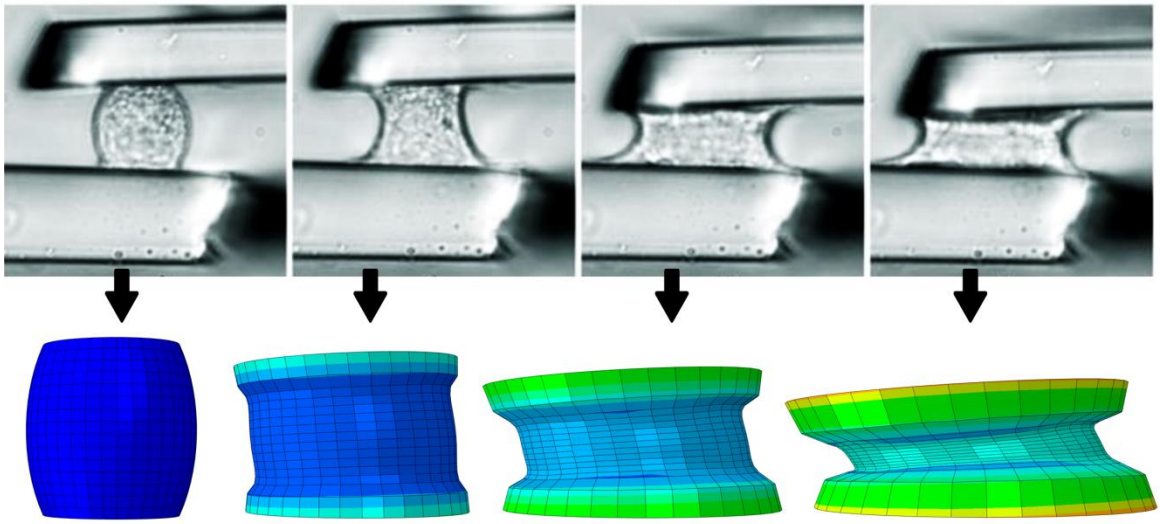

**Figure 4.12:** Cell contraction between two microplates.
Top panels show the experiment developed by *Mitrossilis et al. 2009*. Bottom panels show the simulations, where cell contraction evolves following the motor stalling function ($\alpha$). Colouring indicates higher stresses at the cell adhesion surfaces.

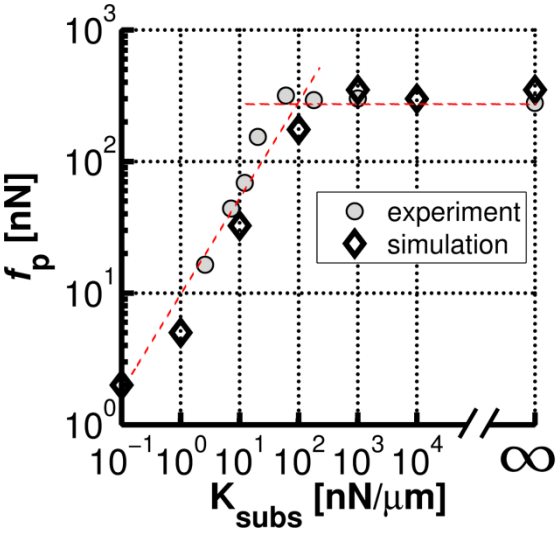


**Figure 4.13:** Saturation force vs. substrate stiffness.
As shown experimentally by *Mitrossilis et al. 2009*, the plateau force magnitude linearly increases for compliant substrates and saturates for high stiffness. The expression $K = F/\delta$ was used to convert $E$ [Pa] to $K_{subs}$ [nN/μm], where $F$ is the vertical force and $\delta$ the plate deflection.

## 4.6. Discussion

To adhere and migrate, cells generate forces through the cytoskeleton that are transmitted to the surrounding matrix. The ways that cells exert these forces are dependent on the properties of the surrounding extracellular matrix, being rigidity one of the most studied features due to its implications in numerous aspects of cell behavior and function (Zemel et al., 2011). Indeed, Zemel et al. have reviewed theoretical and experimental studies of the physical consequences of cellular forces, generated by acto-myosin contractility, including its role in cell morphology, stress-fiber formation and alignment and the elastic properties of cells. Apart from the various specific force generating or responsive functions that cells perform (e.g., wound healing, remodeling of the extracellular matrix or muscle contraction), cells also apply forces as a generic means of sensing and responding to the mechanical nature of their environment. This mechanosensing mechanism has been hypothesized in theoretical and computational models to explain cell organization (Bischofs and Schwarz, 2003), collective (Moreo et al., 2008), and individual 2D (Trichet et al., 2012) cell migration and 3D cell migration (Borau et al., 2011). These and other mechanisms have been proposed from a molecular point of view, as a portion of one cell (Soares e Silva et al., 2011, Borau et al., 2012, Yamaoka et al., 2012, Wang and Wolynes, 2012), to macroscopic constitutive laws of the whole cell (Moreo et al., 2008, Crow et al., 2012) or from purely mechanical models to multiphysics models (Besser and Schwarz, 2010, Taber et al., 2011). In this work, a macroscopic phenomenological one-dimensional constitutive law is proposed to model cell rigidity sensing based on a purely mechanistic approach. Despite its simplicity, the model is able to successfully simulate multiple rigidity-sensing conditions and its results are in good correspondence with experiments. Three main features distinguish the present model from previous ones: macroscopic force generation, time dependent response and a one-dimensional structure approach.

Firstly, a three-spring configuration with a length-actuator (linearly dependent on the relative displacement) is used. Further simplifications of this system produce a similar mechanical response as in the work from (Marcq et al., 2011), but diminish the predictive potential of the model in some aspects as discussed below. In fact, in the absence of external loads such as localized forces or pre-stressed substrates, $\alpha(t)-\delta_c/\delta_1$ is always $\geq 0$ in equation (4.7). Thus, the second condition in that equation would not be required to reproduce the experiments here presented, and the whole construct could be simplified to

a single pre-stressed spring whose equilibrium length is brought to zero through a decay clock ($\alpha$). However, this three-spring configuration allows distinguishing between active and passive responses of the cell. For example, introducing equation (4.13) in equation (4.9) leads to a cell force evolution qualitatively similar to that proposed by (Marcq et al., 2011), although important differences can be identified. Mechanistically, the addition of the series spring ($K_{\text{act}}$) with the acto-myosin actuator, as well as the dependence of $f_{\text{c}}$ with $\delta_{\text{c}}$, captures the linearity of $f_{\text{cell}}$ with respect to substrate stiffness ($K_{\text{subs}}$) for compliant substrates, and its saturation for higher rigidities. In Marcq's model, where a constant contractile force is applied in parallel with the cell stiffness, the linearity of the transmitted (traction) force is only obtained when substrate stiffness is much lower than cell stiffness ($k_{\text{ext}}<<k_{\text{C}}$ using his notation). In the model here presented, however, this linearity extends up to 100 nN/μm as found in experiments (Mitrossilis et al. 2009). This occurs due to the combination of the $K_{\text{act}}$ spring with a force indirectly depending on stiffness ($f_{\text{c}}$). If this force was considered constant (as in Marcq's model and equivalent to $\delta_1 \to \infty$), the effect of the $K_{\text{act}}$ spring would be cancelled and equation (4.9) would be simplified to $f_{\text{cell}} = \alpha(t)\, f_{\max}\left(K_{\text{subs}} / \left(K_{\text{subs}} + K_{\text{pas}}\right)\right)$, thus presenting the aforementioned limitations. In addition, relative values of $K_{\text{act}}$ and $K_{\text{pas}}$ are not arbitrary (Schafer and Radmacher, 2005, Lim et al., 2006) and their independent role can be evaluated as shown in Figure 4.9. In fact, the relation between both values is really relevant, regulating the cell response under different mechanical conditions. This approach may allow in the future simulating more complex phenomena such as stress-fiber rigidization, network disruption etc.

Secondly, time-dependent response has been normally considered due to the viscoelasticity of the membrane or to some cytoskeleton components and have been modeled by means of the addition of dashpots (Crow et al., 2012). However, these models are not able to predict simultaneously two distinct experimental phenomena: immediate cell response to rigidity step changes and cell saturation for high rigidities of the substrate. It is required then to model additional effects, such as the dynamics of myosin motors which introduce, furthermore, a physical meaning to the time-dependent response. This fact is in concordance with the hypothesis of active matter theory proposed by several authors (Marcq et al., 2011, Zemel et al., 2010b) and has been also tested with a particle-based Brownian dynamics computational model (Borau et al., 2012). In fact, in

that model, molecular motors are proposed as one possible mechanism of cell mechanosensing and their dynamics are found to be crucial for the time-dependent force evolution. Other models, however, rather than a mechanical phenomenon, attribute the temporal response to a chemical decaying signal (eg. concentration of $Ca^{2+}$) that triggers actin polymerization or myosin phosphorylation (Deshpande et al., 2006), obtaining similar trends for force evolution and saturation depending on substrate stiffness. The model here presented incorporates, through the internal variable $\alpha$, the motor stalling time-evolution, assuming a single decay law. Saturation is achieved when most of the motors become stalled, not being able of exerting higher forces. Similar relaxation laws have been proposed by other authors (Crow et al., 2012, Marcq et al., 2011), although these other works assume relaxation time to be a decreasing function of substrate rigidity. However, this dependence was found to be not significant for long term responses (e.g. $\tau$ only varied from 6.53 s. to 2.64 s for zero and infinite substrate rigidities respectively (Crow et al., 2012)). Based on these experimental results and the computational work presented in previous chapter (Borau et al., 2012), the relaxation time was assumed to be independent of substrate stiffness, ensuring the continuity of the motor stalling function ( $\alpha$ ).Despite this simplification, the model is able to achieve good predictions of force evolution and saturation, quantitatively similar to those found by (Mitrossilis et al., 2009, Mitrossilis et al., 2010) and qualitatively comparable to those found by (Crow et al., 2012, Trichet et al., 2012). In fact, although the relaxation time is independent of $K_{\text{subs}}$, the rate of force build-up ( $dF/dt$ ) is not (equation (4.14)), permitting to capture the stiffness-dependent instantaneous cell response. As in these experiments, the force develops and saturates at ~300 nN after 1200 seconds (Figure 4.3D). In addition, plateau force barely changes for substrate stiffness higher than 100 nN/μm (Figure 4.5B) (Mitrossilis et al., 2009). In this model force evolution is mainly exponential according to the motor stalling function ( $\alpha$ ) which is in agreement with previous computational results (Borau et al., 2012), however, in experiments (Mitrossilis et al., 2009) this evolution presents a biphasic behavior with a linear initial regime of about 600 seconds, followed by a saturation phase. This difference suggests that although myosin motor dynamics may be important, there likely exist other mechanisms, such as bio-chemical signals, that may also regulate rigidity sensing. Nevertheless, the model is able to capture some time-dependent cell responses such as the rate of force build-up ( $dF/dt$ ) and the contraction speed ( $v_{\text{cell}}$ ) (Figure 4.6A,B) observed in the experiments developed by (Mitrossilis et al.,

2009, Mitrossilis et al., 2010, Trichet et al., 2012). Due to the distinct evolution pattern discussed above, the values of these variables differ from experiments, although they are in the same order of magnitude: maximum $dF/dt$ ~1 nN/s in the model compared with ~0.4 nN/s in the experiments, and maximum $v_{cell}$ ~0.045 μm/s (~22 s/μm) compared with ~0.015 μm/s (~70 s/μm)(Mitrossilis et al., 2009) (Figure 4.6A,B). Interestingly, mechanical power ($P$) presents a biphasic behavior attaining a peak at ~40% of the maximum load both in the model and experimentally (Figure 4.6C) (Mitrossilis et al., 2009). In addition, the model was tested against periodic step changes in substrate stiffness. Specifically, stiffness was varied from 10 to 100 nN/μm and from ~0 to ~∞, and a period of 20 seconds in a total of 100 seconds (Figure 4.7A,B top plot) was used, following the experiments carried out by Crow et al. (Crow et al., 2012, Webster et al., 2011) and a period of 100 seconds in a total of 500 seconds (Figure 4.7C top plot), to study longer time response as Mitrossilis et al. (Mitrossilis et al., 2010). Due to the evolution of motor stalling, for shorter times the response is mainly linear, and the stiffness step changes lead to periodic stretches which switch the slope of force build-up. On the other hand, for longer period and simulated time, the effect of substrate stiffness is less relevant as time advances due to the saturation of $\alpha$. The motor stalling determines the time at which the force exerted by the cell reaches equilibrium, however, this force depends on the load-history. For this reason, when periodically varying the substrate stiffness from ~0 to ~∞ (Figure 4.7C) every 100 seconds during 500 seconds, the plateau force is below 200 nN, much lower than the value that would correspond to an infinitely rigid substrate (~ 300 nN). This, again, strengths the idea that there might exist additional mechanisms that permit to keep cell response mainly linear even for the long-term, but reaching plateau afterwards. Note that this could be reproduced with the model by using a high value of $\tau$ (to obtain linear-like response for longer times) together with some kind of limiting mechanism that didn't allow the system to increase the force beyond a specific limit (the plateau force). Up till now, the reasons for this cell behavior are still unknown, so further experiments would be needed to investigate such mechanisms.

Thirdly, the proposed model focuses only on a 1D approach, when the series of experiments simulated are mainly 2D or even 3D (Mitrossilis et al., 2009, Crow et al., 2012, Mitrossilis et al., 2010). Although the experiments focused on the vertical response, cells spread horizontally during contraction, changing from a convex to a concave curvature in the borders and increasing the contact area and changing the load

distribution. Obviously, in vivo cell response involves many other factors and complex mechanisms, however, the accuracy obtained in the numerical results suggests that a one-dimensional approach is adequate to model this problem, at least for the simple scheme proposed in the experiments. Nevertheless, the extension of the model to the third dimension has been briefly introduced, being ready for future development.

Certainly, this model is a first and simple approximation to predict macroscopic active behaviour of the cell as a whole and, although additional effects could be easily incorporated (such as large strains, cytoskeletal remodeling or coupled mechano-chemical analysis), it could serve as a potential guide for experiments which could furthermore be used to test the model. In addition, this model can be suitable to simulate cell migration, since it is hypothesized that cells tend to sense the rigidity of the ECM to regulate their migration direction. In fact, a non-time dependent version of this model was previously used to simulate cell migration in 3D, as described in Chapter 2 (Borau et al., 2011). Hence, the implementation of this theory in combination with models of cell migration would provide a strong impetus for the development of future models with applications in wound healing, tissue engineering and cancer metastasis.

| **Variable** | **Symbol** | **Value** | **Units** | **References** |
|---|---|---|---|---|
| Actin stiffness | $K_{act}$ | 28 | [nN/μm] | (Schafer and Radmacher, 2005, Lim et al., 2006) |
| Passive CSK stiffness | $K_{pas}$ | 5.6 | [nN/μm] | (Schafer and Radmacher, 2005, Lim et al., 2006) |
| Substrate stiffness | $K_{subs}$ | 1-1000 | [nN/μm] | (Mitrossilis et al., 2009, Mitrossilis et al., 2010) |
| Maximum slippage distance | $\delta_1$ | -15 | [μm] | * |
| Zero-slippage force | $f_{max}$ | 1000 | [nN] | (Mitrossilis et al., 2009, Mitrossilis et al., 2010) |
| Cell length | $L_{c,0}$ | 30 | [μm] | (Crow et al., 2012) |
| Viscosity coefficient | $\mu$ | $2e^5$ | [nN.s] | * |
| Relaxation time | $\tau$ | 200 | [s] | * |

**Table 4-1:** Parameter list. *Adjusted parameters

Chapter 5

# MODELING 3D MIGRATION AT THE CELL SCALE: A PROBABILISTIC APPROACH

This chapter summarizes all the approaches considered so far, including them into a new migration model at the cell scale, emphasizing the importance of multiple stimuli in 3D environments. A probabilistic voxel-based FE model that addresses the cell response to several input factors is described in detail. Specifically, ECM stiffness, cell stress, fluid flow and chemical conditions are taken into account through probability functions. To consider *chemotaxis* and flow through a porous medium, a microfluidic device is simulated using FE. On the other hand, the mechanical problem is also computed using FE, but on a smaller domain. Finally, the cell behavior (speeds, migration trajectories, directionality, spread area, aspect ratio etc.) is tested under different environment conditions (ECM stiffness, chemical gradients, flow direction etc.). Moreover, some supporting simulations are included in Appendix C.

**Contents**

## 5.1. Introduction

It has become clear throughout this Thesis that the ECM properties, the CSK constituents and their interactions regulate cell response in a multiscale process. As previously discussed, this integration depends on multiple mechanical, chemical and biological factors (Cukierman et al., 2002, Even-Ram and Yamada, 2005, Zaman et al., 2006), that have been widely investigated (Zhelev et al., 2004, Polacheck et al., 2011, Hakkinen et al., 2011). In fact, over the past few years, cell migration understanding has increased enormously, largely thanks to the active interaction between experiments, mathematical and computational modeling (Rangarajan and Zaman, 2008). Due to cell motility complexity, models are taking a leading role in future developments, permitting researches to run complex biophysical and biochemical scenarios without the difficulties, time and resource consumption inherent to *in vitro* investigations. Most of these studies have focused on 2D migration, sometimes due to the lack of high quality data of cell movement in 3D. This deficiency is, however, becoming increasingly overridden especially by recent advances in microfluidic technologies which allow high resolution imaging and provide enormous flexibility in controlling the critical biochemical and biomechanical factors that influence cell behavior (Chung et al., 2010, Chung et al., 2012). Therefore, the number of 3D migration models has been increasing, focused on individual (Zaman et al., 2005, Borau et al., 2011, Schluter et al., 2012) or collective cell migration (Ouaknin and Bar-Yoseph, 2009, Arciero et al., 2011). In spite of the large number of approaches used, they can be classified in few categories as described in the introduction chapter of this Thesis. In this Chapter, a probabilistic FE 3D migration model for individual cells is developed, presenting features from several of the previous mentioned categories such as force balance, random effects and environmental factors dependence. This model allows quantitative and qualitative comparison with experimental data, as well as studying the influence of multiple external stimuli (namely ECM stiffness, chemistry, flow and boundary conditions) estimating important features of cell migration such as: velocities, trajectories, cell shape and aspect ratio, cell stress, ECM displacements etc. Furthermore, the model is conceived in a modular form, so that it can be constantly updated and redefined as research provides new insight into cell behavior.

## 5.2. Model description

It has been shown that multiple combined factors drive cell migration through 3D ECMs, which properties influence the cell-matrix interactions and determine cell movements and orientation. This model focuses in three of these factors: fluid flow, chemistry and mechanical conditions. First, flow and chemical conditions of a real 3D microfluidic device (Polacheck et al., 2011) are simulated obtaining pressure distribution, chemical gradients and stream lines through a collagen (porous matrix). Then, since the distance magnitudes that a single cell is able to migrate in a few hours (simulated time) are much shorter than the microdevice size, a central region of the gel is selected to compute the mechanical analysis. The macroscale conditions evaluated at the cell surface influence its behavior, changing its morphology and thus determining the migration. With this in mind, several approaches could have been valid to model cell motility in 3D or other related phenomena, such as the classical FEM (Wong and Tang, 2011) or the more specific surface finite element method (SFEM)(Elliott et al., 2012). However, for simplicity and due to the advantages of lattice-based models, a FE approximation using voxels was chosen for the simulations as described below.

## 5.3. Numerical implementation

This work describes a probabilistic voxel-FE model for 3D migration at the cell-scale level. For this purpose, the ECM as well as the embedded cell are discretized with voxels, each of them corresponding with the component of a three-dimensional mathematical matrix of data (***M***) which contains relevant information for the simulation. For instance, ***M*** stores the centroid of each voxel or whether a specific component corresponds to ECM or cell, therefore determining its mechanical properties. A thorough description of the stored variables and how ***M*** is updated to compute the cell migration is given in the next sections. At this point it is useful to present the iterative scheme (Figure 5.1) which can be described as follows: (i) mechanical, chemical and flow conditions are collected from the corresponding FE analysis. These data serve as input for (ii) the cell-dynamics functions which determine the probability of whether an ECM-type voxel becomes a cell-type voxel or vice versa. (iii) A random-number generator checks the probability corresponding to each voxel so the cell shape is updated. Note that only ECM voxels in contact with the cell may become cell, and that only voxels of the cell surface may

become ECM. It is also important to clarify, that the cell-voxel distribution (cell shape) is essential for the mechanical analysis since the cell forces are the only ones taken into account. Hence, the mechanical problem is computed at each step, whereas the fluid chemical analysis is computed only once at the beginning. This choice saves computational time and it is justified by the fact that the cell volume is much smaller than the problem domain (collagen). Therefore, assuming steady state at the microdevice, it is considered that the cell shape does not affect the fluid-chemical analysis carried out in the first step. Nevertheless, to test this simplification, a specific fluid-chemical simulation with a random cell shape embedded in a porous matrix was performed. The results confirmed that its effects on the stationary solution are negligible (Appendix C, Section C.5). Hence, the fluid-chemical conditions are considered constant through the simulation.

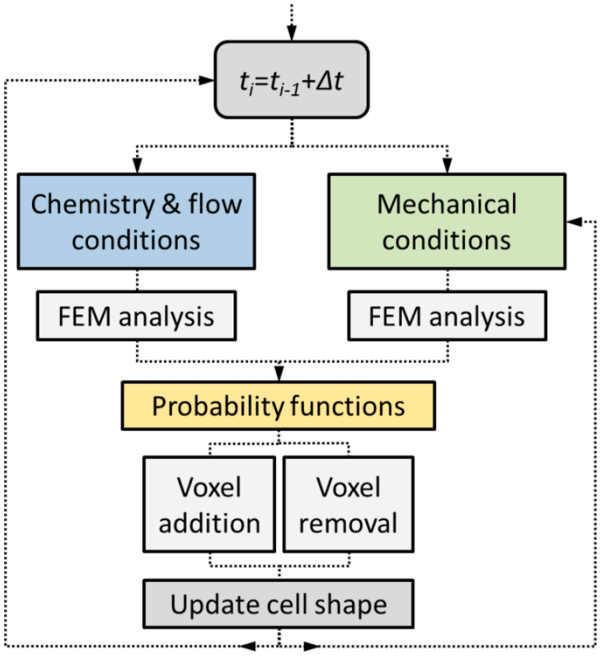


**Figure 5.1:** Scheme of the iterative loop. At each temporal step the fluid chemical and mechanical conditions determine the probability of adding/deleting voxels to/from the cell. At the end of the step, the cell shape is updated. Note that to save computational time, chemistry and flow conditions are considered constant through the simulation, performing the corresponding FE analysis only once at the beginning and not at each time step

### 5.3.1. Macroscopic FE Analysis: evaluation of the environment stimuli

So far the general iteration scheme has been described, but not how the fluid chemical and mechanical problems are solved. As explained below, these problems are computed separately although interacting via changes in cell shape and position which depend, through the probability functions, on several environmental input factors as described in next section.

### 5.3.1.1. Modeling chemotaxis and flow through a porous medium

A complete 3D microfluidic device is simulated, which geometry and boundary conditions are taken from a recent experiment (Polacheck et al., 2011). This device consists of two channels separated by a region containing single cells suspended in collagen I gel (Figure 5.2 left). Applying a hydrostatic pressure gradient across the gel region a consistent flow field is generated. In addition, different chemical concentrations are established up and downstream, generating a linear chemical gradient, which, although difficult to obtain experimentally, is useful in the simulations to test the model. Finite element software (COMSOL Multiphysics) is used to compute the flow through collagen and the transport of diluted species:

$$\frac{\partial c}{\partial t} + \mathbf{u}\nabla c = \nabla\left(D\nabla c\right) + R \tag{5.1}$$

where $c$ is the concentration of the diluted species, $D$ is the diffusion coefficient, $R$ is a production or consumption rate expression (0 in the simulations) and $\mathbf{u}$ is the solvent velocity field.

The flow in porous media is governed by a combination of the continuity equation and momentum balance equation, which together form the Brinkman equations:

$$\frac{\partial}{\partial t}(e_{\mathrm{p}}\rho) + \nabla\cdot(\rho\mathbf{u}) = Q_{\mathrm{br}} \tag{5.2}$$

$$\frac{\rho}{e_{\mathrm{p}}}\left(\frac{\partial \mathbf{u}}{\partial t} + \left(\mathbf{u}\cdot\nabla\right)\frac{\mathbf{u}}{e_{\mathrm{p}}}\right) = -\nabla P + \nabla\cdot\left(\frac{\mu}{e_{\mathrm{p}}}\left(\nabla\mathbf{u} + \left(\nabla\mathbf{u}\right)^{T}\right) - \frac{2}{3}\frac{\mu}{e_{\mathrm{p}}}\left(\nabla\mathbf{u}\right)\mathbf{I}\right) - \left(Q_{\mathrm{br}} + \frac{\mu}{\kappa}\right)\mathbf{u} + \mathbf{F} \tag{5.3}$$

In these equations, $\mu$ denotes the dynamic viscosity of the fluid, $\mathbf{u}$ is the velocity vector, $\rho$ is the density of the fluid, $P$ is the pressure, $e_{\mathrm{p}}$ is the porosity, $\kappa$ is the permeability of the porous medium, and $Q_{\mathrm{br}}$ is a mass source or mass sink. Influence of gravity and other volume forces can be accounted for via the force term $\mathbf{F}$, although they are neglected, as well as the inertial term $\left(\mathbf{u}\cdot\nabla\right)\mathbf{u}/e_{\mathrm{p}}$, in the current simulations. Values of these main parameters are listed in Table 5-1.

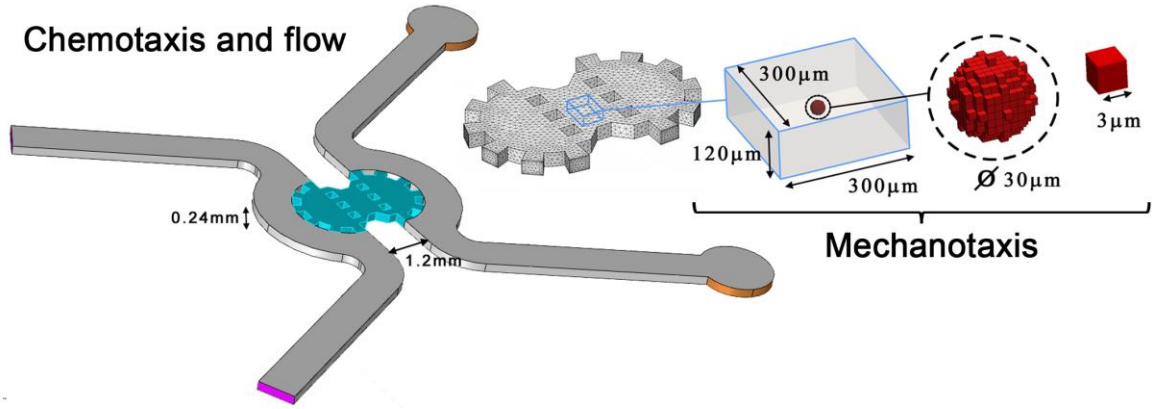


**Figure 5.2:** Geometry of the microfluidic device and details of domain and cell mesh. Left: two channels (gray) are separated by collagen I gel (cyan). Pressure and chemical gradients are established between inlet (purple) and outlet (orange) boundaries. A box-like domain (right) is taken from the central part of the gel to simulate the mechanical analysis and the cell migration. This domain is discretized with voxels of 3 µm, some of them considered cell-voxels and forming an initially spherical shape of about 30 µm of diameter embedded in the ECM to perform the mechanical and migration simulation.

Since the purpose of this work is to study the migration of a single cell, which volume is negligible in comparison with the whole microdevice domain, the steady state simulation is performed only once, not considering the embedded cell body. Then the results from a central box-like region are extracted to compute the mechanical analysis and the cell migration (Figure 5.2 right). Hence, the chemical concentration and flow direction at each point of the box-like domain remain unalterable regardless cell position in the subsequent steps of the migration simulation. As pointed before, the effect of a 3D body embedded in the centre of the gel is analyzed to support this assumption, finding that its influence was practically null except at points very close to the body surface (Appendix C, Section C.5).

#### 5.3.1.2. Modeling mechanotaxis

The steady-state solution from small box-like domain the fluid simulation is extracted and interpolated into an organized mesh and stored in ***M***. Specifically the domain is discretized with voxels of 3 µm, some of them assigned to model cell behavior (from now called cell-voxels) and forming an initially spherical-like shape embedded in the ECM (Figure 5.2 right). For simplicity, the ECM is considered linear elastic, whereas cell-voxels have their own mechanical properties.

In similar fashion to the scheme presented in Chapter 2, the *mechanosensing* behavior of each cell-voxel is simplified to two springs representing the actin stiffness

($K_{act}$) nd the passive components ($K_{pas}$) of the cytoskeleton, and an active actuator representing the myosin machinery (*AM*), each of them assumed to independently act in the x,y,z directions (Figure 5.3). The stress exerted by this actuator depends upon the sliding between actin filaments and myosin arms ($\varepsilon_c$) which is limited by a maximum contraction parameter ($\varepsilon_{min}$). This sliding depends in turn on the cell strain ($\varepsilon_{cell}$) and therefore on the ECM stiffness. Hence, cell stress transmitted to the matrix by each voxel in each direction "*i*" can be expressed as a function of cell strain:

$$\sigma^i_{cell} = \begin{cases} K_{pas}\varepsilon^i_{cell} & \varepsilon^i_{cell} < \varepsilon_{min} \\ \dfrac{K_{act}\sigma_{max}}{K_{act}\varepsilon_{min} - \sigma_{max}}\left(\varepsilon_{min} - \varepsilon^i_{cell}\right) + K_{pas}\varepsilon^i_{cell} & \varepsilon_{min} < \varepsilon^i_{cell} < \left(\sigma_{max}/K_{act}\right) \\ \dfrac{K_{act}\sigma_{max}}{K_{act}\varepsilon_{max} - \sigma_{max}}\left(\varepsilon_{max} - \varepsilon^i_{cell}\right) + K_{pas}\varepsilon^i_{cell} & \left(\sigma_{max}/K_{act}\right) < \varepsilon^i_{cell} < \varepsilon_{max} \\ K_{pas}\varepsilon^i_{cell} & \varepsilon_{max} < \varepsilon^i_{cell} \end{cases} \quad (5.4)$$

The main difference with respect to the approach used in Chapter 2 is that the polarization term is not explicitly included in the stress tensor (which is now isotropic), since the polarization direction emerges from the cell morphology, as shown later. Also note that in the probability functions (explained in next section) only one value of stress is used, in particular the volumetric stress of each voxel ($\sigma_v = \left(\sigma^x_{cell} + \sigma^y_{cell} + \sigma^z_{cell}\right)/3$). In the present model, three different zones of the cell body are considered: cortex, cytoplasm and nucleus (Figure 5.3 right). In a first approach, the only difference between the cortex zone and the cytoplasm is the exertion of higher stress, therefore assigning higher $\sigma_{max}$ to the cortex-voxels (2.5 kPa compared with 1.5 kPa at the cytoplasm). On the other hand, the nucleus presents no contractile behavior, so only its passive resistance ($K_{pas}$) is considered (acto-myosin actuator and actin branch are therefore disabled in the corresponding voxels). All these parameters are listed in Table 5-1.

The mechanical problem is computed at each step, taking into account the redistribution of voxels belonging to each zone of the cell or to the ECM. To solve that, a user-subroutine of the software ABAQUS together with a MATLAB script are employed. Once the FE subroutine computes the mechanical equilibrium at each step, the script comes into action to compute the probabilities of voxel addition/removal according with

the mechanical, flow and chemical conditions. In this process, the cell shape is updated as well as all the necessary variables of ***M***. This data act as an input for the FE subroutine in the next step, repeating the process until the end of the simulation. Note that the mechanical analysis only corresponds to the cell-matrix interactions, and not to the flow-ECM or flow-cell interactions which are not considered in this first approach.

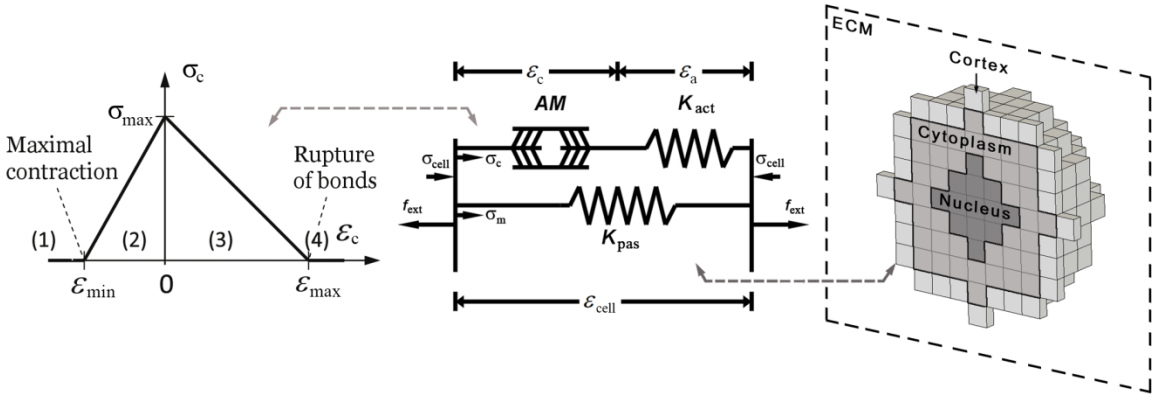


**Figure 5.3:** Mechanosensing scheme for 3D and different cell parts.
Cell material is modeled as in Chapter 2, using two springs in parallel representing the actin stiffness ($K_{act}$) and the passive components ($K_{pas}$) of the cytoskeleton, in series with an active actuator representing the myosin machinery (*AM*) Left plot shows the stress exerted by the AM as a function of the sliding between actin filaments and myosin arms ($\varepsilon_c$). Cell-voxels (right) are divided in three zones: cortex (light gray), cytoplasm (medium gray) and nucleus (dark gray). The nucleus plays only a passive role and is modeled as an elastic material. The cortex and cytoplasm, however, present a contractile behavior depending on ECM stiffness, following the *mechanosensing* model.

## 5.3.2. External stimuli and cell dynamics determine cell migration

In this model, four different factors are considered to account for the mechanical, chemical and flow conditions surrounding the cell and driving cell migration. Namely these factors are: cell stress magnitude, maximum stress direction, chemical concentration at the ECM and flow direction. The volumetric cell stress ($\sigma_v$) due to cell contraction is computed at each voxel following the previous *mechanosensing* model (Borau et al., 2011). Here, the maximum stress direction ($\mathbf{d}_{\Delta\sigma}$) is defined as the direction in the cell body where the cell is exerting maximum stress. In other words, it is the direction joining the cell centroid (computed geometrically) with the element of maximum stress (Figure 5.4). The chemical concentration ($C_c$) is a scalar field coming from the fluid chemical analysis, having each voxel an associated value. Similarly, $\mathbf{d}_f$ stores the flow direction corresponding to each voxel of the ECM. To define the addition/removal of voxels

depending on the stimuli, these factors are introduced into the cell-dynamics or probability functions as follows:

$$p_* = p_*^0 + p_*^{\max}\left(1 - e^{-k_*^0\left(\lambda_*^\sigma F_*^\sigma + \lambda_*^{\Delta\sigma} F_*^{\Delta\sigma} + \lambda_*^C F^C + \lambda_*^F F_*^F\right)dt}\right) \tag{5.5}$$

where * represents addition (+) or removal (-) of voxels. $p^0$ and $p^{\max}$ are the minimum/maximum values bounding the probability. $k^0$ is a temporal rate affecting all the factors and *dt* is the time step. In addition $\lambda$'s are sensitivity constants permitting to control the weight of each factor (*F*). All these parameters are pre-adjusted and are held constant during the simulation. Their values are listed in Table 5-2. On the other hand, *F*'s are variable parameters describing the environment conditions, different for each voxel and depending on the aforementioned stimuli. Each *F* ranges from 0 to 1 and they are described in the subsequent sections. A sensitivity analysis of the cell-dynamics functions was performed to study the influence of each separate factor (Appendix C, Section C.4).

| **Symbol** | **Variable** | **Value** |
|---|---|---|
| $\Delta P$ | Pressure gradient at the microdevice | 40 [Pa] |
| $D$ | Diffusivity constant | $10^{-9}$ [$m^2/s$][a] |
| $\kappa$ | Gel permeability | $10^{-13}$ [$m^2$][a] |
| $\mu$ | Fluid viscosity | $10^3$ [Pa.s][a] |
| $\rho$ | Fluid density | $10^3$ [$kg/m^3$][a] |
| $\Delta C$ | Chemical gradient | 1 [$mol/m^3$] |
| $K_{pas}$ | Passive resistance of cell cytoskeleton | 1 [kPa][b] |
| $K_{act}$ | Actin stiffness | 10 [kPa][b] |
| $\varepsilon_{max}$ , $\varepsilon_{min}$ | Maximum/minimum cell strain | -0.4,0.4[b] |
| $\sigma_{max}^{cort}$ | Maximum stress of the acto-myosin (AM) system at the cortex zone | 2.5 [kPa][b] |
| $\sigma_{max}^{cyto}$ | Maximum stress of the acto-myosin (AM) system at the cytoplasm | 1.5 [kPa] |

**Table 5-1:** Parameters for the fluid-chemical and mechanical analysis
[a](Polacheck et al., 2011), [b](Borau et al., 2011)

| Symbol | Variable | Value |
|---|---|---|
| $p_+^0$, $p_-^0$ | Minimum probabilities of voxel addition/removal | 0.1, 0.1 |
| $p_+^{max}$, $p_-^{max}$ | Maximum probabilities of voxel addition/removal | 0.8, 0.4 |
| $k_+^0$, $k_-^0$ | Addition/removal rate | 0.4, 0.4[$min^{-1}$] |
| $\lambda_+^\sigma$, $\lambda_-^\sigma$ | Sensitivity constants of addition/removal regarding cell stress magnitude | 0.0035, 0.0035 |
| $\lambda_+^{\Delta\sigma}$, $\lambda_-^{\Delta\sigma}$ | Sensitivity constants of addition/removal regarding cell stress gradient | 0.004, 0.004 |
| $\lambda_+^C$, $\lambda_-^C$ | Sensitivity constants of addition/removal regarding chemical concentration | 0.3, 0.3 |
| $\lambda_+^F$, $\lambda_-^F$ | Sensitivity constants of addition/removal regarding flow direction | 0.004, 0.004 |
| *dt* | Time step | 5 [min] |

**Table 5-2:** Constant parameters of the probability functions

#### 5.3.2.1. Cell stress

The parameter representing the cell stress magnitude ($F^\sigma$) measures the stress born in a specific voxel compared with the maximum possible cell stress ($\sigma_{max}$)(equation (5.5)), which value comes intrinsically from the *mechanosensing* model. The probabilities of adding/removing voxels, increase with the stress to reflect that cells embedded in stiffer substrates exert higher forces and move at faster speeds (Lo et al., 2000, Friedl and Brocker, 2000, Cukierman et al., 2002, Hakkinen et al., 2011). This parameter also takes into account the voxel orientation. When adding a voxel, $\theta$ represents the angle between the direction of the possible new voxel (relative to the current voxel) and the direction of the voxel with maximum cell stress. In contrast, when removing a voxel, $\theta$ stands for the angle between the direction of maximum stress and the direction joining the current voxel centroid with the cell centroid. Using this criterion, the probabilities of adding/removing voxels in the direction where the cell exerts maximum stress are higher/lower so the cell body tends to polarize, as suggested in experiments (Schwarz and Bischofs, 2005). The alignment with stress is included in addition and separately with the parameter $F^{\Delta\sigma}$ in

order to independently control the weights of the stress magnitude and stress gradient factors (equation (5.5)):

$$F_+^{\sigma}=\begin{cases}\dfrac{\sigma_v}{\sigma_{max}}\cos\theta & \theta<\dfrac{\pi}{2}\\ 0 & \dfrac{\pi}{2}\le\theta\end{cases}\qquad F_-^{\sigma}=\begin{cases}0 & \theta<\dfrac{\pi}{2}\\ \dfrac{\sigma_v}{\sigma_{max}}\left|\sin\theta\right| & \dfrac{\pi}{2}\le\theta\end{cases}$$

$$F_+^{\Delta\sigma}=\begin{cases}\cos\theta & \theta<\dfrac{\pi}{2}\\ 0 & \dfrac{\pi}{2}\le\theta\end{cases}\qquad F_-^{\Delta\sigma}=\begin{cases}0 & \theta<\dfrac{\pi}{2}\\ \left|\sin\theta\right| & \dfrac{\pi}{2}\le\theta\end{cases} \tag{5.6}$$

To further clarify this point, a simple 2D representation of the voxel addition process is shown in Figure 5.4. When checking a specific voxel of the cell surface (current), the corresponding value of stress and the position of its neighbours (possible new cell-voxels) are used to compute $p_+$. In the illustration, the top voxel (which is currently part of the ECM) may become cell because $\theta_1$ is lower than 90º so $F_+^{\sigma}$ and $F_+^{\Delta\sigma}$ take a positive value depending on the stress and the alignment. On the other hand, the voxel on the right will not likely appear since $\theta_2$ is higher than 90º so $F_+^{\sigma}$ and $F_+^{\Delta\sigma}$ are 0 and hence $p_+ = p_+^0$. Taking all this into account, the cell tends to migrate to stiffer zones of the ECM (higher cell stress) and in the direction of maximum stress.

### 5.3.2.2. Flow and chemical concentration

It is well known that cells sense the ECM interstitial flow and respond to the concentration of a wide variety of chemical species (Rappel et al., 2002, Zhelev et al., 2004, Shields et al., 2007, Polacheck et al., 2011). To reflect this, both factors are included into the probability functions. The necessary inputs come from the fluid chemical analysis previously described. The parameter representing the chemical concentration ($F^C$) compares the chemical gradient between adjacent voxels ($\Delta C$) and it is normalized by the maximum value of concentration of a particular species ($C_{max}$).

$$F_+^{C}=\begin{cases}\dfrac{\Delta C}{C_{max}} & \Delta C>0\\ 0 & \Delta C<0\end{cases}\qquad F_-^{C}=\begin{cases}\dfrac{\left|\Delta C\right|}{C_{max}} & \Delta C<0\\ 0 & \Delta C>0\end{cases} \tag{5.7}$$

With this definition, the voxels tend to be added in the direction of maximum chemical concentration, appearing at a faster rate the more pronounced the gradient is. Similarly, the voxels tend to be removed more readily at the positions of lower concentration. In sum, the cell body advances in the direction of the chemical gradient. Obviously, in case of repellent species, $F^C$ could be easily reversed to account for opposite effects.

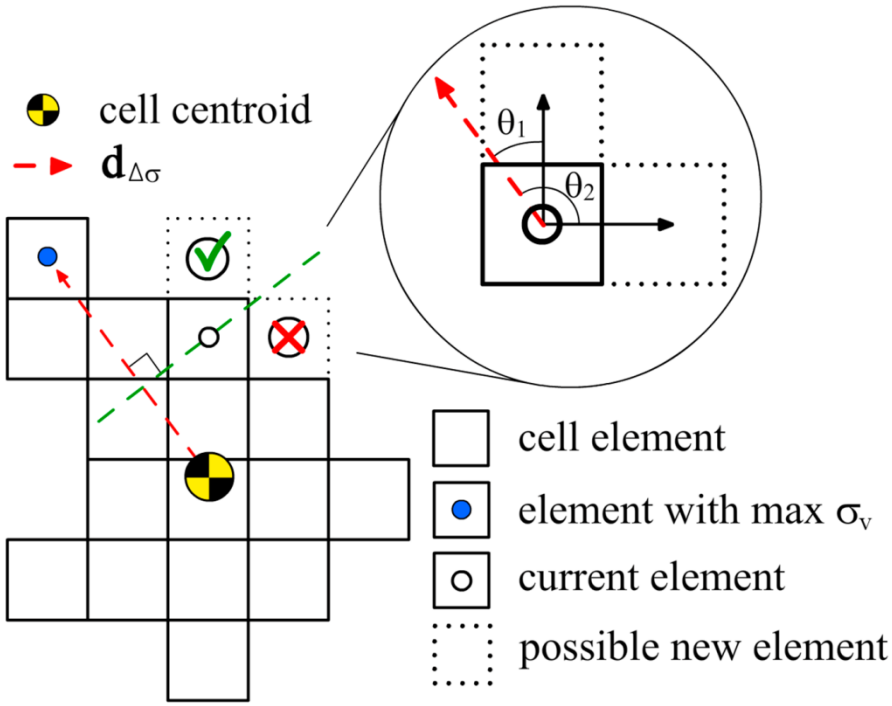


**Figure 5.4:** Schematic example of voxel addition process.
Voxel addition example taking only the stress direction and magnitude into account. When checking a specific voxel (current element), the volumetric stress that it bears ( $\sigma_v$ ) and the angle ( $\theta$ ) that its neighbours form with the direction of maximum stress ( $\mathbf{d}_{\Delta\sigma}$ red arrow) determine the probability of appearance ( $p_+$ ). In the illustration, the top voxel (currently part of the ECM) would have a higher probability than the right one of becoming cell since $\theta_1$ is lower than 90 degrees whereas $\theta_2$ is higher. Note that this is a simplified 2D scheme. In 3D, 6-connectivity is used to compute the voxel addition.

The dependence of cell migration on flow conditions have been recently investigated (Polacheck et al., 2011). It was found that small populations of cells tend to migrate downstream and parallel to the flow direction. Actually, very high flow velocities acting on isolated cells or blocking of some specific receptors may reverse this response,

although these effects are not considered here for simplicity. The flow parameter $F^F$ is then defined as:

$$F_+^F = \begin{cases} \cos\varphi & \varphi < \frac{\pi}{2} \\ 0 & \frac{\pi}{2} \le \varphi \end{cases} \qquad F_-^F = \begin{cases} 0 & \varphi < \frac{\pi}{2} \\ |\sin\varphi| & \frac{\pi}{2} \le \varphi \end{cases} \tag{5.8}$$

where $\varphi$ establishes the alignment of the voxel with the flow direction array at a specific position. Therefore, $\varphi$ is also calculated following the procedure shown in Figure 5.4, but using $\mathbf{d}_{\mathrm{F}}$ instead of $\mathbf{d}_{\Delta\sigma}$.

## 5.4. Results

This section is divided in three main parts. The first one summarizes the results from the microfluidic system simulation, showing the flow velocity field, the streamlines and the pressure gradient across the gel. In the second part shows the effect of the ECM stiffness on the cell stress distribution and cell morphology. Finally, the results focus on cell migration, describing trajectories, speeds and directionality for different situations. Specifically, input factors (mechanics, flow or chemistry) are activated or deactivated in different combinations, and boundary conditions such as gradient directions are varied.

### 5.4.1. Microfluidic simulation

A full 3D microfluidic device is simulated with the conditions described in the FE analysis section. The fluid passes by the input channels and flows through the porous medium (collagen gel) transporting a certain diluted specie, and achieving its peak speed (2.96 μm/s) at the central zone of the gel, between the micropilars, where the cross section is smaller (Figure 5.5A). The velocity field matches quantitatively the results obtained both computational and experimentally by Polacheck et al. (Polacheck et al., 2011), which found a maximum speed of about 3 μm/s. The pressure drop presents a linear decrease through the gel and constant values at the inlet (40 Pa) and outlet (0 Pa) (Figure 5.5B). Similarly, the chemical concentration decreases linearly from a normalized value of 1 mol/m3 at the inlet, to 0 mol/m$^3$ at the outlet (not shown). As pointed before, this simulation accounts for the steady state of the microdevice and it is performed only

once. Then, all the resulting data within a box-like domain in the central part of the gel are interpolated and assigned to the element centroids of the voxel-mesh (***M***) to act as input factors for the migration model.

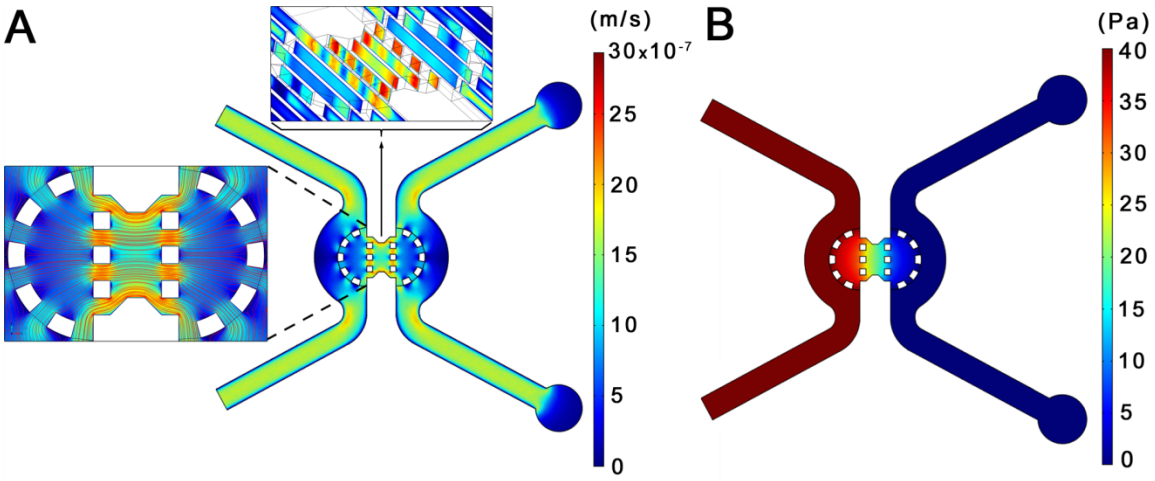


**Figure 5.5:** Fluid chemical analysis in a 3D microdevice.
A) The velocity field present higher values in the gel zone between micropilars, reaching a maximum of 2.93 μm/s. The streamlines in the central part are mostly parallel to the horizontal direction. B) The pressure drop across the microdevice shows a linear decrease through the gel and constant values at the inlet and outlet (40 and 0 Pa respectively). This analysis is computed (using COMSOL) once at the beginning of the simulation and its results are interpolated to a box-like voxelized mesh, where the mechanical analysis is performed and the cell migration is studied.

## 5.4.2. Effects of ECM stiffness

To test the direct effects of ECM stiffness on cell morphology and stress distribution, a box-like domain (300×300×120 μm) with constrained displacements at the boundaries (far enough from the cell to avoid influencing the mechanosensing process) and different ECM stiffness conditions was used. Up to 10 simulations were performed for each set of conditions with mechanical stimulus acting alone (flow and chemical inputs deactivated). These simulations presented some differences due to the stochastic nature of the model, but overall all the results were consistent. For clarity, only one simulation of each set of conditions is presented. For all the cases shown here, the cell was assumed to have an initially spherical shape of ~30 μm (Figure 5.2) and started the simulation in the domain centre. Time simulated was 500 min (100 steps) which is in the usual range of cell migration experiments (Polacheck et al., 2011, Hakkinen et al., 2011). Model parameters

were adjusted to predict speeds similar to migrating fibroblasts observed in experiments (Lo et al., 2000, Friedl and Brocker, 2000, Peyton and Putnam, 2005, Peyton et al., 2011, Hakkinen et al., 2011).

First, the cell is embedded in a homogeneous ECM with constant young modulus of 50 kPa). With no stiffness anisotropy, the ECM displacements are homogeneously distributed, pointing radially to the cell centroid. Similarly, the cell stress is mostly homogeneous, with higher values at the cortex zone (~1.2 kPa) and slightly lower ones in the cytoplasm (Figure 5.6 left). These values are in the order of magnitude of cell stresses found in experiments (Dembo and Wang, 1999, Alberts et al., 2008, Franck et al., 2011, Kraning-Rush et al., 2012, Legant et al., 2013). In addition, considering the surface of each voxel face (9 $\mu m^2$), the magnitude of cell forces would be in the correct range (up to few hundreds of nN) of experimental data (Ghibaudo et al., 2008, Mitrossilis et al., 2009, Trichet et al., 2012). Note that the cortex and cytoplasm zones are under compression whereas the nucleus (assumed passive), is being stretched by the surrounding contracting elements. With such homogeneity, the chance of adding/removing elements at the cell surface is similar in all directions and consequently, the cell migrates in a random fashion (Figure 5.6 middle). Also note that the migration speed depends on the ECM stiffness through the probability functions since higher stiffness lead to higher cell stress (until saturation) and thus to higher migration speeds. In this case, results show ~0.4 μm/min of mean speed and ~0.024 μm/min of effective one (Figure 5.6 right). Mean speed is calculated as the average cell speed at each step, whereas the effective speed takes into account only the initial and final cell location at a certain time. Low effective speed reflects high randomness.

Secondly, two cases with different stiffness conditions are simulated. In case 1, the elastic modulus of the ECM increases linearly with x-coordinate, whereas in case 2, the increase is exponential (Figure 5.7A). The cell centroid at each step is tracked and the 3D and x-y projected trajectories are shown in Figure 5.8A. Overall, in both cases, cell migration pathways were random with a higher net advance in the direction of the gradient stiffness (x-direction). However, cell response was different, moving slightly faster but much more directed in case 2, especially during the first steps. In this case, the stiffness variation (and thus, cell stress) between the front and the back part was very pronounced. According with the probability functions, this corresponds with much higher probability of voxel appearance in +x-direction and of voxel removal in –x-direction,

resulting in fast forward advance. This was reflected on the mean and effective speeds of cell migration (Figure 5.8B). For short times, the mean speeds were similar in both cases (~0.3 μm/min), but the effective speed was much higher in case 2 (0.25 μm/min compared with 0.04 μm/min in case 1), as expected from the trajectory analysis.

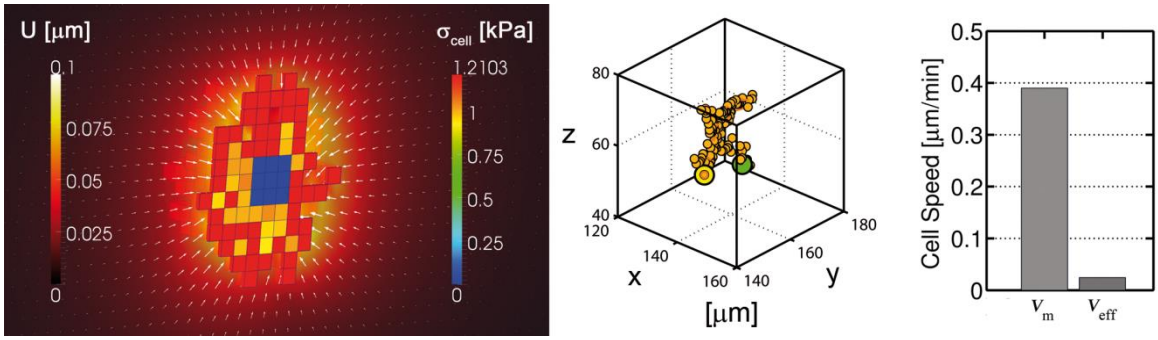


**Figure 5.6:** Cell response for homogeneous ECMs.
Volumetric cell stress, ECM displacement (left), 3D trajectory (middle) and migration speeds (right) for a case with homogeneous stiffness (50 kPa). Left plot shows a cut of the cell body. Cell stress is distributed homogeneously (red cell-voxels) along the cell surface and slightly decreases in the cytoplasm zone. Note that the plot only represents the active stress exerted by the cell elements and not the stress transmitted to the ECM or the nucleus. The nucleus is considered a passive material, thus appearing in blue. ECM displacements are distributed homogeneously, pointing radially to the cell centroid (left legend and white arrows). Middle plot shows cell migration trajectory. Having no guidance, cell moves randomly, which is reflected in the low effective speed.

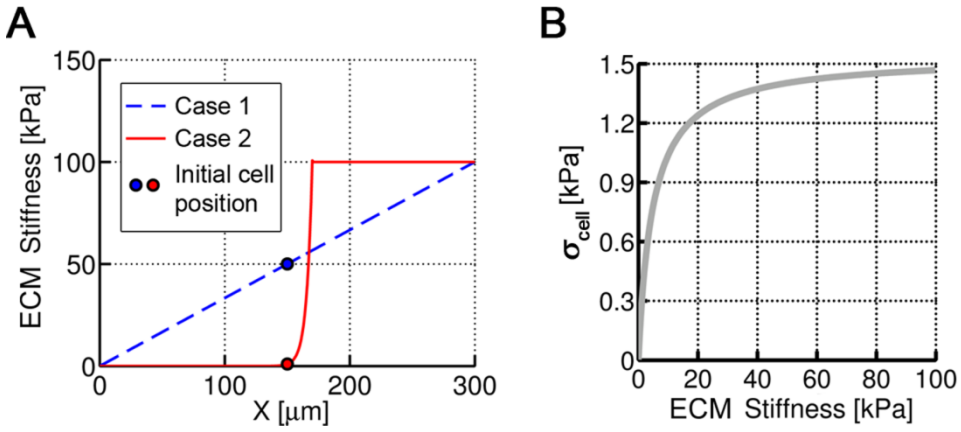


**Figure 5.7:** ECM stiffness gradients and theoretical cell stress.
A) Two different cases are simulated. The ECM stiffness varies linearly with x-coordinate in the first case and exponentially in the second one. The cell starts the simulations at the same location but surrounded by different compliant ECM depending on the gradient type. B) Cell stress depending on ECM stiffness. Note that this curve corresponds with the theoretical solution of the mechano-sensing model in one direction, that is, the stress of one single voxel completely surrounded by an elastic ECM of a specific stiffness.

However, for long-term, both case 1 and 2 presented similar mean (~0.42 μm/min) and effective (~0.06 μm/min) speeds, and the trajectories were mostly random. This is due to cell stress dependence on ECM stiffness. According to the *mechanosensing* model, cell stress increases with ECM stiffness, swiftly for compliant substrates but saturating for higher rigidities (Figure 5.7B). As stated before, pronounced differences between front and rear stress would cause fast and straight movements, whereas small differences would lead to random-like migration. In case 1, cell moved between stiffness of 45-65 kPa, always close to the saturation zone, which explains its non-directional motion.

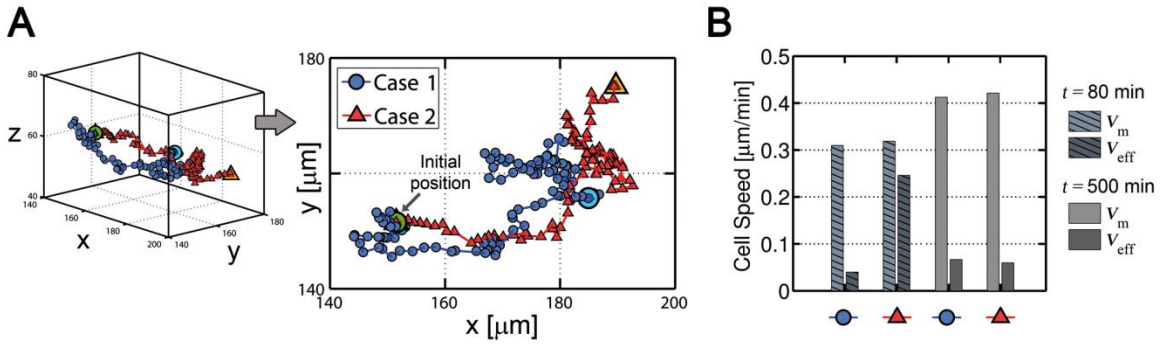


**Figure 5.8:** Migration trajectories and computed speeds.
A) 3D and x-y projected trajectories for: case 1 - linear stiffness gradient, case 2 - exponential stiffness gradient. Initial position is the same for both cases. Light blue circle and orange triangle show the final location of the cell centroid for cases 1 and 2 respectively. B) Cell migration speeds at different times of simulation. Legend in A is used to represent the cases in the x-axis of B. Mean speed is calculated as the average cell speed at each step, whereas the effective speed takes into account only the initial and final cell location at a certain time.

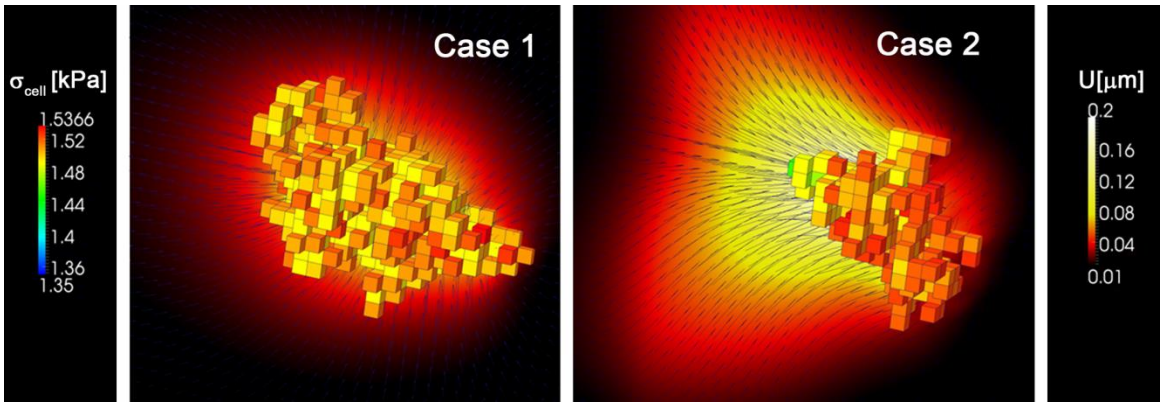


**Figure 5.9:** Cell stress and ECM displacements.
Cell stress (coloured voxels) and ECM displacements (black arrows and cut plane) at t=80 min for case 1 (linear stiffness gradient in x-direction) and case 2 (exponential stiffness gradient in x-direction).

On the other hand, in case 2 the cell started placed in a compliant zone (1 kPa), but quickly found much stiffer surroundings (100 kPa) which highly increased cell stress, decreasing back and rear differences and thus producing stochastic migration. Figure 5.9 shows the stress distribution for both cases at t=80 min which is approximately the time at which the cell arrived to a very stiffer zone, reaching force saturation and thus migrating more randomly. In case 1, cell stress is homogeneously distributed, although the voxels with higher stress corresponded with surface elements preferentially oriented in +x-direction. Cell shape is mainly regular but generally polarized with the gradient direction, and the ECM displacements point radially to the cell centroid. In case 2, however, there exist a clear gradient of cell stress following the ECM stiffness. The cell shown in Figure 5.9 presents a shape which is broader at the front, exerting higher stress, and very thin at the rear. Nevertheless, due to the pronounced stiffness gradient, displacements are much higher at the rear and the ECM is mainly stretched in the x-direction. Overall, cell aspect ratio or shape factor (longer length divided by shorter one) (Figure 5.10A) was similar for both cases, as well as the spreading area (Figure 5.10B), presenting case 2 slightly higher values. This likely happens for the same reasons explained above. The probability functions tend to saturate at high stresses and hence the voxel appearing/disappearing probability is high in all directions. Therefore the aspect ratio is noisy and relatively low, from roundish-like shapes to somewhat elongated (2:1) cells. The algorithm used for calculating the aspect ratio for a voxelized structure is described in Appendix A, Section A.3. Further testing of the model mechanical behavior is collected in Appendix C, Section C.2.

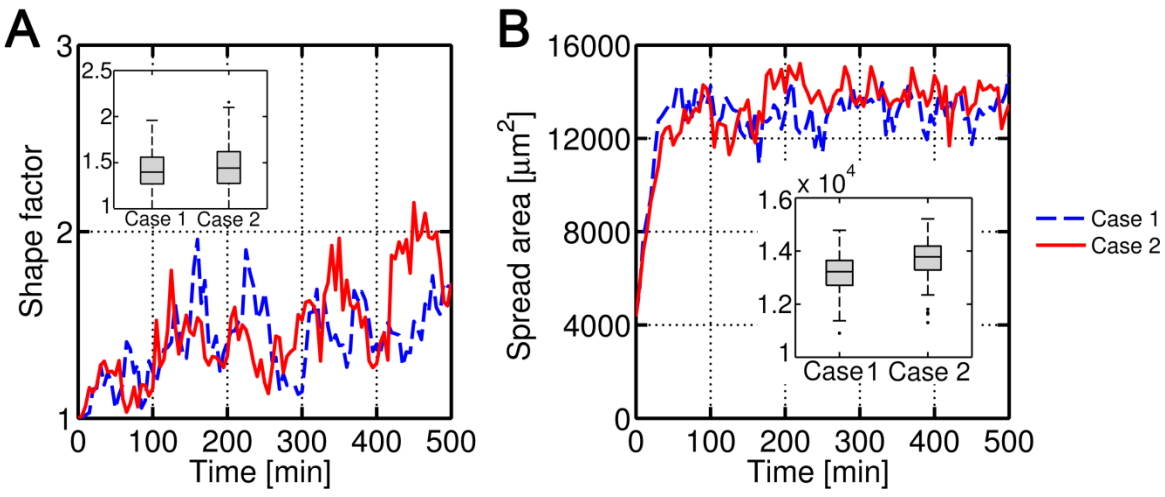


**Figure 5.10:** Cell shape factor and spread area.
A) Cell aspect ratio and spread area B) for case 1 (linear stiffness gradient in x-direction) and case 2 (exponential stiffness gradient in x-direction). B).

### 5.4.2.1. ECM degradation

The matrix metalloproteinases (MMPs) are a family of ECM degrading enzymes which play a major role on cell behaviors such as migration, differentiation or angiogenesis. In fact, localized matrix degradation is thought to contribute to cellular invasiveness in physiological and pathological situations (Linder, 2007). This degradation modifies the morphology and mechanical properties of the ECM, therefore affecting the cell behavior. Computational modeling of such a complex phenomenon requires specific and focused research (Zaman et al., 2007). Nevertheless, the possibility of ECM degradation was added into the codes for possible future development.

As a first approximation, a very simple rule was incorporated: whenever an ECM-voxel (i) is in contact with the cell perimeter it becomes degraded, loosing a certain percentage (*d*) of its original Young's modulus ( $E^i_{\mathrm{ECM}} = E_0(1-d)$ ). To test the effect of such simplification, case 1 (linear stiffness gradient in x-direction) was computed again activating ECM degradation (using *d*=0.01). Results after 80 minutes of simulated time show that both the effective and mean speeds increase when the ECM is degraded (Figure 5.11 left). The reason is that the degradation of the ECM mechanical properties (lower *E*) decreases the probabilities of adding cell elements at the trailing edge. Thus, the cell tends to migrate faster leaving a degraded path on its way (Figure 5.11 right).

Further development of a degradation model might be interesting in the future, although the degradation option was deactivated in the main simulations for simplicity, to isolate the effects of the rest of phenomena.

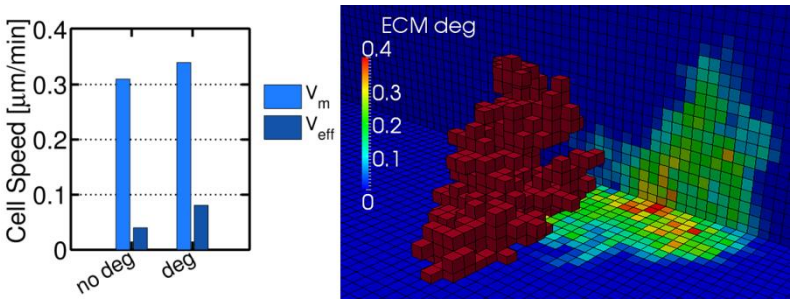


**Figure 5.11:** Cell speeds and ECM degradation.
A) Cell speeds and matrix degradation B) for case 1 (linear stiffness gradient in x-direction) at *t*=80 minutes.Cell speed slightly increases while the cell leaves a degraded path at the trailing edge. Red voxels represent the cell, whereas coloured background shows the percentage of ECM degradation.

### 5.4.3. Migration

To study the resulting patterns depending on input environmental factors by activating/deactivating mechanics, flow or chemistry and using different combinations of gradient directions, 500 min (100 steps) of cell migration were simulated. Five specific cases were distinguished (Figure 5.12): (A) only mechanical inputs activated, applying a linear stiffness gradient (same as case 1 in previous section) on the x-direction, (B) migration is only driven by flow in x-direction, (C) flow and a chemical gradient are both applied in x-direction, (D) flow is applied in x-direction whereas there is a stiffness gradient in y-direction, (E) flow and a chemical gradient are applied in x-direction and a stiffness gradient acts in y-direction. As before, for clarity, only results from one of many performed simulations are shown. Down panel of Figure 5.12 shows the 3D trajectories and the x-y projection. Mean and effective velocities at the end of simulation are plotted for each condition. Although the mean or averaged speed ($V_m$) was similar for all the cases (~0.4 μm/min), the effective speed ($V_{eff}$) was strongly influenced by the boundary conditions. For each case, the directionality of the migration as the angle of each turn in the track relative to the x-direction was determined. Results reflect the sensitivity of the model when applying single or combined factors. Stiffness or flow gradients acting alone (cases A,B), produced more random migration with ~40% of backward movements, which is reflected on effective speeds under 0.1 μm/min. Introducing a second factor on the x-direction (case C), even when another gradient was acting in the y-direction (case E), substantially decreased the randomness. In these cases, only ~10% of the turns went away from the "correct" path, overall achieving effective speeds of ~0.25 μm/min. Interestingly in case D, where the gradients are applied in x and y-directions, the effective speed (~0.16 μm/min) was greater than in cases A or B, probably due to the fact that random deviations were combined with either the direction of the stiffness or the flow gradient.

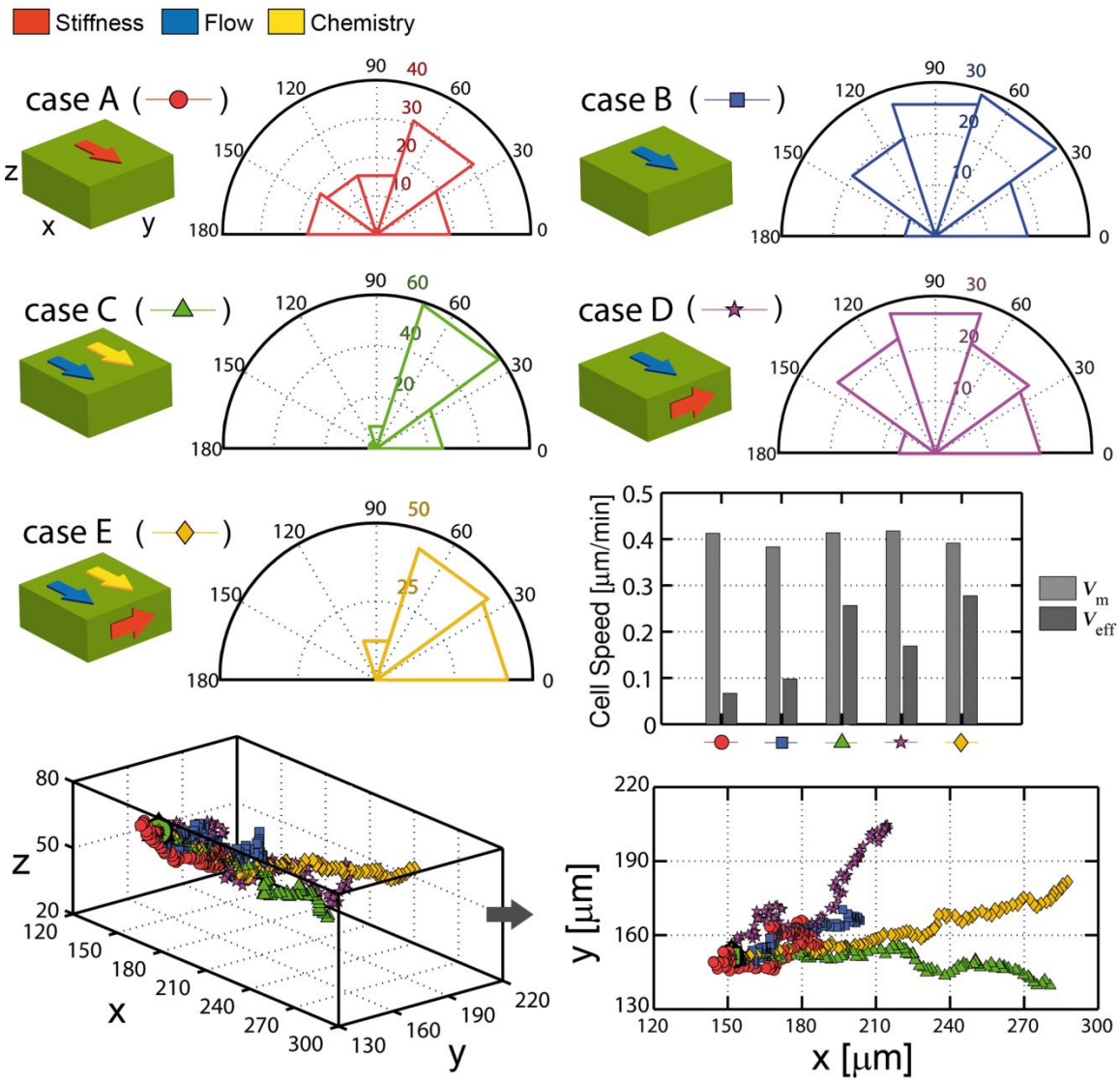


**Figure 5.12:** Cell migration under different environmental conditions.
Mechanical, flow and chemical inputs are activated/deactivated in different combinations and gradient directions. Case A: only the mechanical input is activated, applying a linear stiffness gradient (same as case 1 in previous section) on the x-direction. Case B: flow acts in x-direction. Case C: flow and a chemical gradient are both applied in x-direction. Case D: flow is applied in x-direction and a stiffness gradient in y-direction. Case E: flow and a chemical gradient are applied in x-direction and a stiffness gradient in y-direction. Green box represents the gel and coloured arrows the gradient directions. Migration directionality was determined as the angle of each turn in the track relative to the x-direction.

### 5.4.4. Modeling a porous ECM

So far, all the simulations have considered a continuum matrix through which the cell is able to migrate, completely neglecting morphology or geometrical effects of the ECM. In

this section, a porous mesh is simulated to compute cell migration through the matrix holes. The script used to build such mesh is described in Appendix A, Section A.4.

The domain size is the same as used in previous simulations (300×300×120 μm with voxels of 3 μm) but the mesh is performed randomnly obtaining a porosity of ~0.9 and pore size ~20 μm (Figure 5.13A). The cell is initially placed at the domain center (note that cell's volume is taken into account when building the mesh) (Figure 5.13B). The ECM is still considered as linear elastic for simplicity with homogeneous Young's modulus of 5 kPa, and the cell behavior follows the *mechanosensing* model. In addition, the flow field in x-direction is interpolated from the microfluidic simulation.

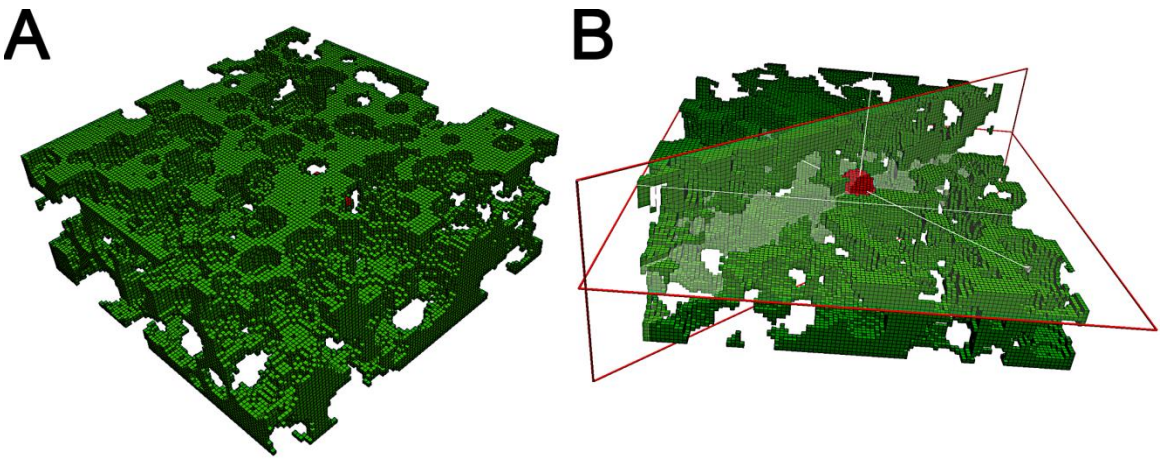


**Figure 5.13:** Example of a porous ECM voxel-mesh.
A) Mesh of porosity ~0.9 and pore size ~20 μm. B). Domain cut using horizontal and diagonal planes showing cell's initial position.

The observed cell behavior was similar to that found in previous simulations using continuum ECM's, presenting, however, some peculiarities. Developed stress was similar to previous cases (~1-1.3 kPa) although ECM displacements were significantly higher (up to 0.9 μm) due to the pores (Figure 5.14). Interestingly, the cell tends to adhere to the pore surface, where the stiffness (and therefore the stress) is higher (Figure 5.14 bottom left). Moreover, the cell contracts its body toward that surface, presenting high displacements at the non-adhered voxels (Figure 5.14 bottom right).

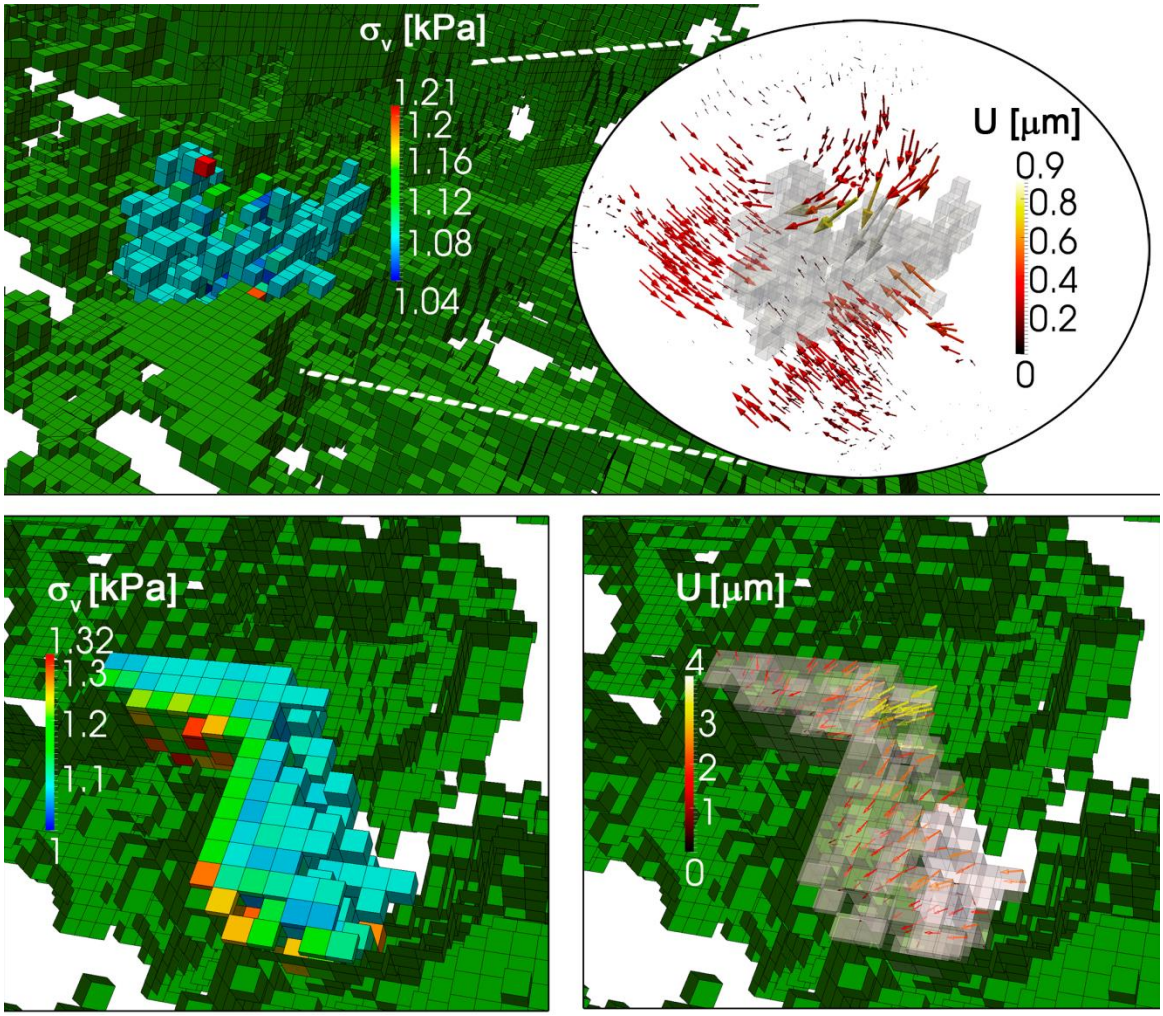


**Figure 5.14:** Cell stress and displacements in a porous ECM.
Top panel shows cell stress and ECM displacements (significantly higher than those in a continuum ECM). Bottom left panel shows cell stress and the cell body adhered to the pore surface (where it develops higher stress). Cell body contracts toward the pore surface (bottom right panel), with high displacements at the free side.

Mean and effective speeds were similar and high (above 0.35 μm/min), indicating a directional migration. In fact, both the trajectory and the angle distribution confirm that the cell moved mainly in x-direction, adhering to the pore surfaces but following the flow lines (Figure 5.15 right plots). Cell shape factor and spreading area present noisy behaviors due to the irregular ECM geometry, although the values are similar to those obtained in a continuum domain.

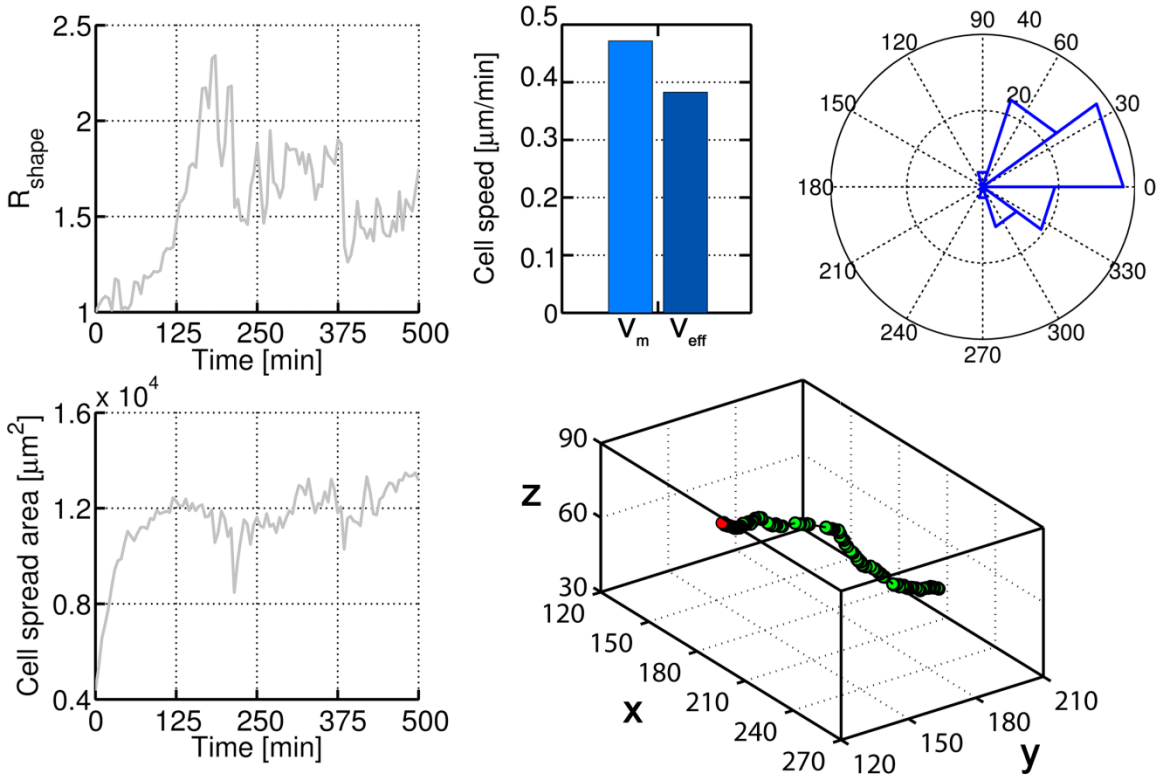


**Figure 5.15:** Cell response in a porous ECM.
Left plots show the cell shape factor and spreading area. Noise is caused by the irregular ECM geometry. Mean and effective speeds are similar, suggesting a directional migration, as confirmed by the trajectory and the angle distribution with respect to x-direction (right plots).

## 5.5. Discussion and conclusions

In this chapter, a phenomenological probabilistic voxel FE model for single cell migration in 3D have been described. Through a set of probability functions and combining different software, the model is able to compute cell migration taking into account different environmental factors evaluated at the cell surface such as mechanical properties of the ECM, chemical gradients, flow and boundary conditions, capturing important migration-related features such as speeds, stresses, ECM-displacements, adhesion area, cell aspect ratio etc. To study the fluid-chemical environment, a full 3D microfluidic device whose geometry and conditions were taken from a recent experiment (Polacheck et al., 2011) is simulated, in which the fluid passes by the input channels and flows through a porous medium. On the other hand, to analyze the mechanical environment, the mechanical equilibrium is solved by using a specific *mechanosensing* model. The macroscopic behavior of the cell emerges naturally from the definition of probabilities at

each voxel (based on the conditions at the macro-scale), allowing the study at the micro and cell scales.

Overall, the model predicts cell migration toward stiffer zones of the ECM (Lo et al., 2000, Saez et al., 2007, Baker et al., 2009, Hakkinen et al., 2011), downstream and parallel to the flow (Polacheck et al., 2011, Shields et al., 2007) and oriented with chemical gradients (Rappel et al., 2002, Zhelev et al., 2004). The parameters of the dynamic functions were adjusted to obtain migration speeds in the range 0-1 μm/min (Lo et al., 2000, Friedl and Brocker, 2000, Peyton and Putnam, 2005, Peyton et al., 2011, Hakkinen et al., 2011) and cell stresses of the order of few kPa as reported experimentally (Dembo and Wang, 1999, Alberts et al., 2008, Franck et al., 2011, Kraning-Rush et al., 2012, Legant et al., 2013). In addition, the effects of combined factors were investigated, confirming that the model responds accordingly in random but controlled fashion.

This approach joins together features from different kind of existing migration models. For instance, similarly to the force-based dynamic approaches, the mechanical equilibrium is locally established taking into account the cell contraction depending on ECM conditions following a *mechanosensing* model (Borau et al., 2011). Note that although this approximation is sensitive to external loads (e.g. hydrostatic pressure or ECM pre-strains), only stress and strain caused by cell contraction are taken into account. Additionally, a 3D lattice is used, like in Monte Carlo studies, which usually permits faster simulations at the expense of quantitative results. Nevertheless, since the cell body is discretized with voxels, this handicap is skipped and the model is able to qualitatively and quantitatively study different aspects of cell migration. Obviously, this simplification implies other disadvantages such as the loss of detail at the cell surface. Finally this approach is based on probabilities. However, unlike purely stochastic models, ECM properties or cell stress can be included to drive migration. In fact, this first approach focuses on fluid direction, chemical gradients and mechanical cues as the main inputs driving cell migration through the probability functions. These tuneable functions allow controling the relative weight of each input parameter (by varying the corresponding $\lambda$ 's), as well as including new factors that affect cell migration. For instance, some experiments (Shields et al., 2007, Polacheck et al., 2011) suggest that cells polarize with the interstitial flow direction and migrate downstream due to a flow-induced gradient of an autocrine chemotactic signal that is detected by specific chemokine receptors. When those receptors are blocked or when the cell population grows (thus disrupting the signalling processes), the migration trend is reversed. This effect could be easily

introduced in the model by simply switching the values of $F^{\mathrm{F}}$ or including a signalling function regulating that specific parameter. Also, the model predicts increasing speed migration (higher probabilities) with ECM stiffness, not considering hindrance or drag effects that may appear in dense ECMs. To account for the biphasic behavior of cell speed versus ECM stiffness, as found in experiments and used in previous models (Palecek et al., 1997, Peyton and Putnam, 2005, Zaman et al., 2005, Dokukina and Gracheva, 2010, Borau et al., 2011), $F^{\sigma}$ could be modified so that the probability of adding/removing voxels decreased as a function of drag ($\sigma_{\mathrm{v}} / \left(\sigma_{\max} f\left(drag\right)\right)$), or a specific $F^{\mathrm{drag}}$ with negative values could be defined. Adding new input factors or enhancing current assumptions is thus possible and easy, although increasing complexity may complicate the interpretation of the results. Nevertheless, with the activation/deactivation of input factors, the model serves as a suitable platform for investigating a wide variety of migration-related phenomena. In fact, in a future development, it will be possible to deep further into some important aspects which are now oversimplified. For instance, ECM degradation could be easily included in the model to study differences between proteolytic and non-proteolytic migration. Additionaly, the ECM architecture could be further explored, studying the effects of porosity and pore size, including features of contact guidance or even reconstructing the geometry from real images. Furthermore, in this kind of environments, blebbing migration usually plays an important role as an alternative mode of migration (Charras and Paluch, 2008). Although the current model is based on the *mechanosensing* assumption (which implies cell-matrix adhesions) and internal pressure driving independent cell protrusions could be easily incorporated. Another simplification is the assumption of a constant difference of maximum stress between the cortex and the cytoplasm. However, the complex reality could be better represented by making the maximum stress magnitude dependent on myosin activation or protein concentration along the different cell parts. Similarly, the stiffness of active cell components ($K_{\mathrm{act}}$) could rely on actin polymerization and cytoskeletal reorganization. These and other phenomena could be incorporated to better reflect the dynamics of cell migration. Nevertheless, it is important to bear in mind the main handicap when working at different scales (microdevice vs. gel vs. cell), which is the computational cost. To solve this, different FE software (COMSOL Multiphysics) including a specific microfluidics module is used, and the steady-state solution of the fluid-chemical problem is computed. Then, this solution is interpolated into a finer mesh

of the central part of the porous gel, where the mechanical analysis and cell migration are computed. Since the model simulates single cell motility, the cell volume does not affect the macro-scale results of the fluid-chemical simulation, and thus it can be neglected permitting considering the stream lines and chemical gradient constant during simulation. In spite of this assumption, the scripts require up to 30 GB of RAM memory, too high for a common personal computer. Furthermore, in case of extending the model to compute collective cell migration, the mentioned simplification would not be valid, making thus necessary a new approach and considerably increasing the computational cost. With all this, another limitation of the current model is the extended use of commercial software (ABAQUS, MATLAB, COMSOL) which restricts the sharing possibilities, although it is intended to remove this dependence in the near future by creating specific hand-coded routines.

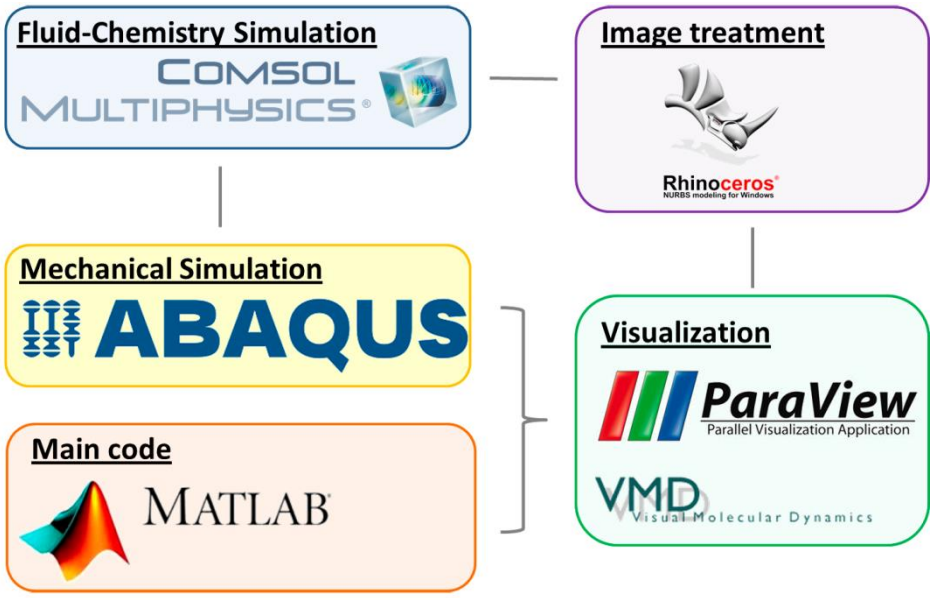


**Figure 5.16:** Different software used.
The methodology described in this chapter uses multiple software. Microfluidic simulations were computed using COMSOL. The mechanical and migration simulations were performed combining ABAQUS with user subroutines and MATLAB scripts. Open Source software (ParaView and VMD) were used for visualization, whereas Rhinoceros was used to smooth some cell geometries (Appendix C, Section C.5).

In sum, this chapter establishes a methodology for testing and designing new experiments; being in particular useful for simulating ongoing microfluidic systems and the study of several basic biological functions such as cell migration, angiogenesis, or organ formation. With all this, it has been developed not just a migration model but a

workbench to investigate cell response to a wide variety of external stimuli. Furthermore, with its modular form, the model can be constantly updated and redefined as advancements are made in clarifying how cellular events take place.

Chapter 6

# LAMELLIPODIUM DYNAMICS

This Chapter describes the key role of lamellipodium dynamics during cell-edge protrusion and retraction cycle, introducing the latest findings in experimental research as well as the most relevant modeling works regarding this issue. Next, a finite-difference model is developed to validate lamellipodium-related phenomena experiments (in general) and vinculin effects on actin rearward flow experiments (specifically). Experiments are conducted and analyzed using several mathematical techniques to extract biological data such as speeds, periodicity, correlations etc. Results are discussed, as well as the possible integration of the model in higher-scale approaches. This work is the result of a PhD stay in the Center for Medical Physics and Technology of Erlangen, led by the professor Ben Fabry.

**Contents**

## 6.1. Introduction

Cells develop fluctuating exploratory motions and migrate by cycles of edge protrusion, adhesion and retraction (Rafelski and Theriot, 2004). Protrusion is thought to be driven by monomeric G-actin polymerizing onto actin filaments (F-actin) at the cell front (Pollard and Borisy, 2003). Two actin modules define the leading edge: the lamellipodium, extended a few microns from the cell border and composed of orthogonal actin filaments (Svitkina, 2007, Urban et al., 2010), evolves a forward-growing lamella, a much broader structure composed of actin bundles in association with myosin II and focal adhesions (FAs) (Koestler et al., 2008). Membrane tension in conjunction with myosin II activity produces a retrograde flow of the entire network toward the cell center and away from the leading edge (Ponti et al., 2004, Giannone et al., 2007). During this process, FAs originate at the lamellipodium, acting like a mechanical clutch to impede actin motion, thus slowing the rearward flow at sites of FA assembly (Giannone et al., 2004, Alexandrova et al., 2008, Hu et al., 2007). The dynamics of lamellipodium, lamella and FA structures during cell crawling have been extensively studied (Giannone et al., 2004, Giannone et al., 2007, Anderson et al., 2008, Burnette et al., 2011); for instance, they found how retrograde flow changes during protrusion and retraction of the leading edge and how flow and edge velocities were related (Figure 6.1).

Nevertheless, the exact interactions between lamellipodium structures are still unclear. Inspired by this riddle, numerous models of protrusion and retraction patterns at the leading edge have arisen in the past years, as reviewed by Ryan et al. (Ryan et al., 2012). Most of these models consider two essential components: (i) a self-reinforcing mechanism promoting actin polymerization, such as membrane curvature (Gov and Gopinathan, 2006) or actin nucleation (Faber et al., 2010), (ii) delayed inhibition resulting in retraction, such as mechanical stress (Wolgemuth, 2005, Kuusela and Alt, 2009), filament-membrane associations (Doubrovinski and Kruse, 2008, Carlsson, 2010) or signaling molecules (Cirit et al., 2010, Tania et al., 2011). More recently, Craig et al. (Craig et al., 2012) developed a set of experiments and proposed a model to study the actin turnover and treadmill in the nerve growth cone, where the cell-substrate adhesion force is negligible. In contrast, other works focus their efforts in elucidating the role of FAs in lamellipodium organization (Shemesh et al., 2009, Shemesh et al., 2012) and their motor-clutch-like behavior (Chan and Odde, 2008). Here, a one-dimensional model is developed to predict and understand how the focal adhesion protein vinculin modulates

actin flow dynamics at the leading edge. This model includes the most relevant lamellipodium components such as actin filaments, myosin motors and FAs, and takes into account actin polymerization, depolymerization, membrane tension, flow friction and periodic myosin motor activation. With a very simple approach, it is able to qualitative capture recent findings regarding lamellipodium dynamics (Giannone et al., 2007, Burnette et al., 2011) and quantitatively test own assays. Finally, new experiments based on the model results and predictions are proposed.

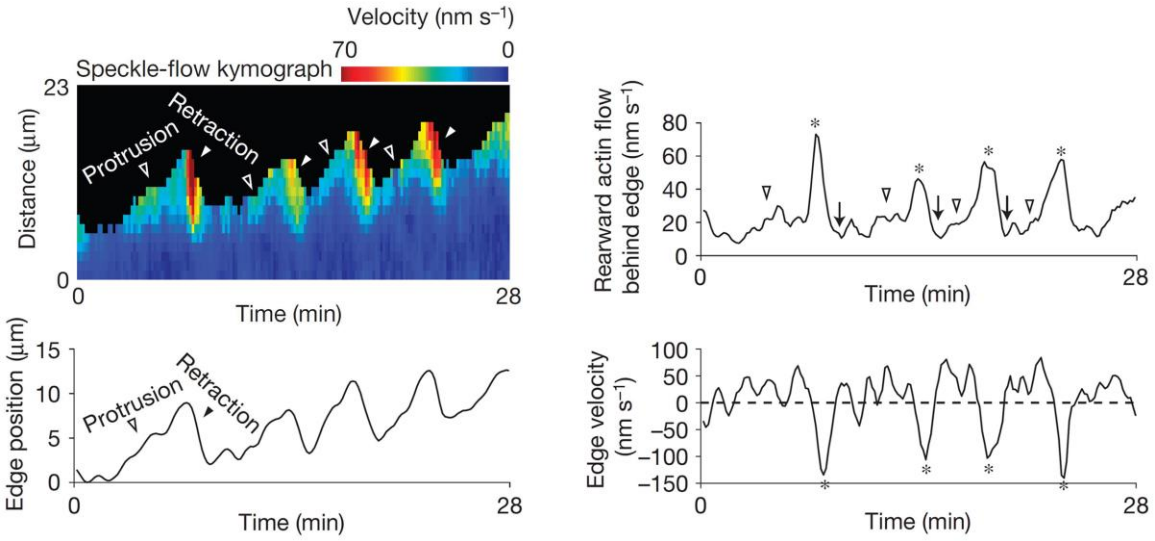


**Figure 6.1:** Cell edge dynamics Adapted from *Burnette et al., 2011*
Experimental results from (Burnette et al., 2011). Top left panel: rearward-speckle-flow kymograph showing the change in retrograde-flow rates during protrusion (open arrows) and retraction (filled arrows) of the leading edge. Edge position, edge velocity and rearward actin flow are plotted over time. Asterisks in edge-velocity and rearward-actin-flow graphs denote retractions and arrowheads denote protrusions corresponding to increases in rearward actin flow. Arrowheads denote slowing rearward actin flow immediately after edge retraction.

## 6.2. Model description

A one-dimensional approach is proposed to model lamellipodium dynamics during cell migration. Main aspects of lamellipodium dynamics such as membrane protrusion and retraction cycles, actin polymerization and depolymerization, retrograde actin flow, activation of myosin motors and focal adhesion forces are taken into account. The general scheme (Figure 6.2) represents a cell lamellipodium of width ( $L_w$ ) attached to a substrate through focal adhesions. Actin flow is driven by the myosin motors pulling from the lamella border and the membrane tension opposing actin polymerization (Watanabe and

Mitchison, 2002, Ponti et al., 2004, Medeiros et al., 2006, Giannone et al., 2007). This retrograde actin flow is slowed down by a drag force depending on the concentration and strength of focal adhesions (Giannone et al., 2004, Hu et al., 2007, Alexandrova et al., 2008). These assumptions and their corresponding equations are described below.

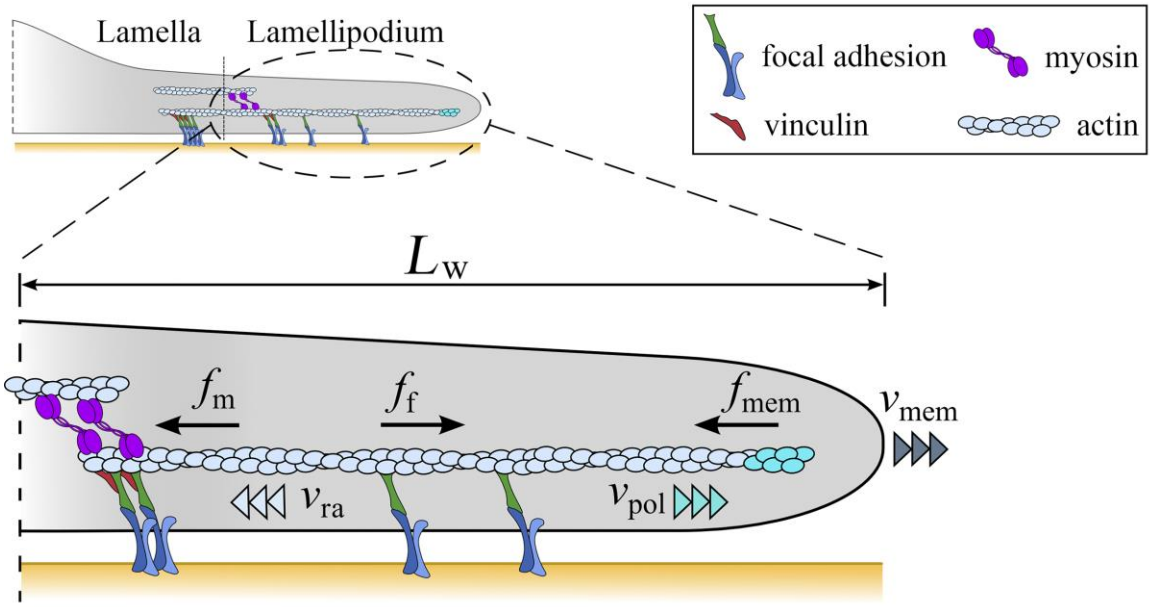


**Figure 6.2:** Lamellipodium model scheme.
Actin retrograde flow is driven by the myosin motors pulling from the lamella border and the membrane tension opposing to actin polymerization. This flow is slowed down by a drag force depending on the concentration and strength of focal adhesions.

## 6.2.1. Forces and kinematics

Rearward actin flow in the lamellipodium is driven by myosin motor forces ( $f_m$ ) pulling periodically from the lamella border, and the build-up of membrane tension ( $f_{mem}$ ) due to actin polymerization. Actin flow ( $v_{ra}$ ) is slowed down by drag forces ( $f_f$ ), with the friction ( $\eta_f$ ) depending on the concentration of actin ( $A_c$ ) and focal adhesions ( $FA_c$ ), and adhesion strength ( $\kappa_{FA}$ )( Figure 6.2).

$$f_m + f_{mem} = f_f = \eta_f v_{ra} \tag{6.1}$$

$$\eta_f = \eta_0 + \eta_{FA} = \eta_0 + \kappa_{FA} FA_c A_c \tag{6.2}$$

where a minimum friction ($\eta_0$) is set to account for other possible friction phenomena such as buckling or fluid attrition. It is considered, for simplicity, that the myosin motor force ($f_m$) presents a constant value when applied. However, this force only acts periodically ($T$) during a certain amount of time ($t_{cont}$) as explained later. In addition, the membrane tension ($f_{mem}$) is assumed to depend on membrane speed as follows:

$$f_{mem} = f_{mem}^0 + c_v v_{mem} \tag{6.3}$$

where $f_{mem}^0$ is the static membrane force, and $c_v$ a viscous coefficient.

With all this, the actin polymerizes at a certain speed ($v_{pol}$) causing the membrane to protrude ($v_{mem}$). Its opposing tension induces, in turn, a retrograde actin flow ($v_{ra}$). Hence, the speeds equilibrium can be expressed as:

$$v_{mem} = v_{pol} - v_{ra} \tag{6.4}$$

## 6.2.2. Actin treadmilling

Motile cells extend the leading edge by assembling a branched network of actin filaments which is later depolymerized and debranched by a core set of proteins such as coffilin (Pollard and Borisy, 2003). Here it is considered that actin polymerizes at the lamellipodium border at a rate $\phi$, and depolymerizes at the lamella border at a rate $\gamma$. Between these two points, the actin concentration ($A_c$) is considered constant for simplicity (Figure 6.3). The polymerization rate can be understood as the speed at which actin is added to the cell edge ($v_{pol}$) to maintain a certain level of actin concentration per length unit ($A_c$):

$$\phi = v_{pol} A_{c,x=L_w} \tag{6.5}$$

Although depolymerization can occur deeper into the cell body, here it is assumed to happen in a narrow zone ($L_d$) at the lamella border. Considering a constant depolymerization rate ($\gamma$) in this zone, yields to the following equation for actin concentration evolution:

$$\frac{\partial A_c}{\partial t} = \begin{cases} -\gamma A_c + v_{ra} \dfrac{\partial A_c}{\partial x} & x < L_d \\ 0 & x > L_d \end{cases} \tag{6.6}$$

Solving equation (6.6) for $\partial A_c/\partial t = 0$ gives the steady-state actin concentration along the lamellipodium:

$$A_c(x) = \begin{cases} A_{c,x=L_d} e^{\left(\frac{-\gamma(L_d - x)}{v_{ra}}\right)} & x < L_d \\ A_{c,x=L_d} = A_{c,x=L_w} & x > L_d \end{cases} \tag{6.7}$$

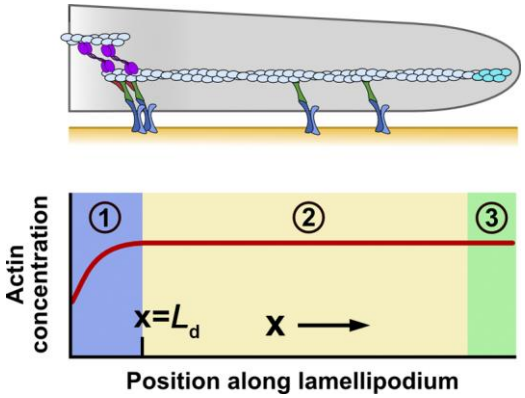


**Figure 6.3:** Actin concentration along lamellipodium.
Actin is polymerized at the cell edge (lamellipodium border) at a rate $\phi$ (3), and depolymerized at the lamella border at a rate $\gamma$ (1). Between these two points (2), the actin concentration ($A_c$) is considered constant.

## 6.2.3. Cyclic contractions

Cell exploratory motions proceed by cycles of protrusion and retraction. During protrusion, the membrane moves forward due to actin polymerization, while producing a rearward actin flow. On the contrary, during retraction, membrane moves backward increasing the actin velocity (Giannone et al., 2004, Giannone et al., 2007, Burnette et al., 2011). These cycles are repeated with periodicity directly proportional to the lamellipodium width and inversely proportional to the actin speed (Giannone et al., 2004, Giannone et al., 2007), suggesting that some signaling complex (e.g. MLCK) travelling with the actin could trigger myosin activity, that in turn would produce the contractions. Here, an unspecified force-induced signaling complex travelling from the leading edge, which triggers myosin contraction at the lamella border is considered. Resuming the retraction phase, the signal activates at the cell tip, initiating a new loop (Figure 6.4). In this way, as suggested by experiments, the period of contractions ($T$) is directly related to the lamellipodium width ($L_w$) and the rearward actin flow speed ($v_{ra}$).

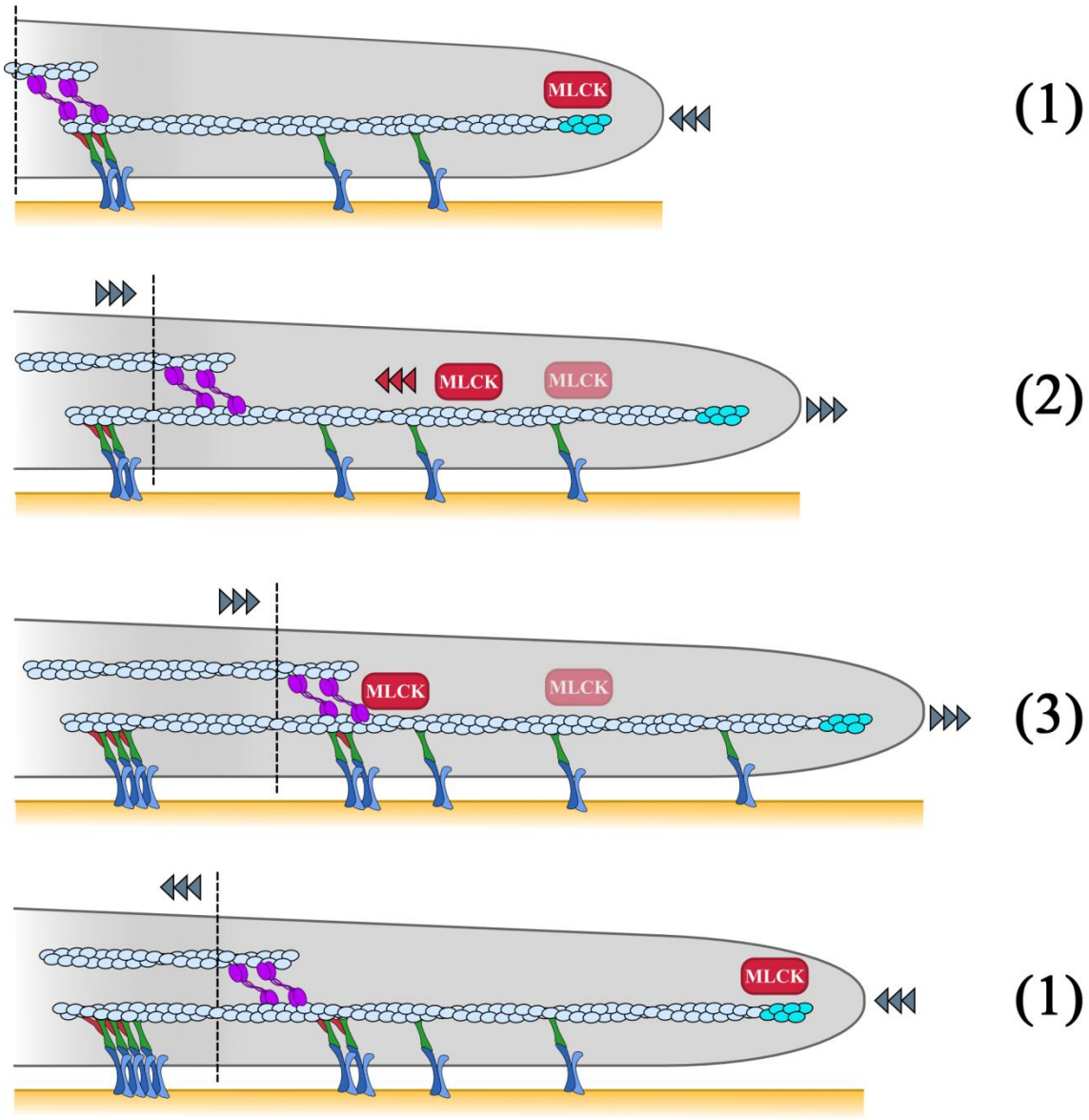


**Figure 6.4:** Cyclic scheme of lamellipodium dynamics.
(1) During the contraction phase, myosin motors generate forces that drive both lamella and leading edge backwards. In this phase, some adhesion sites disappear but others strengthen serving as a firm base for the next protrusion stage. Some force dependent signals (MLCK) are activated at the lamellipodium tip. (2) Protrusion resumes after contraction stage since the polymerization rate overcomes the retrograde actin flow. MLCK is transported rearward by actin flow. (3) The MLCK complex reaches the lamella border, activating the myosin machinery.

## 6.3. Model predictions

The model parameters, which are listed in Table 6-1, are adjusted according to the experimental results from (Thievessen et al., 2013). In this section, model predictions and

general trends are analyzed under different conditions modifying lamellipodium dynamics (via specific drugs) used in literature, qualitatively comparing the computed results with experiments. Next, the model is used to quantitatively reproduce our own experiments regarding vinculin and its interaction with FAs.

| **Variable** | **Symbol** | **Value** | **Units** | **References** |
|---|---|---|---|---|
| Polymerization rate | $\phi$ | 0.0358 | $units_{actin}\ s^{-1}$ | (Craig et al., 2012)* |
| Depolymerization rate | $\gamma$ | 0.0367 | $s^{-1}$ | (Craig et al., 2012)* |
| Depolymerization zone width | $L_d$ | 0.1 | µm | § |
| Actin concentration at the leading edge | $A_{c,x=L_w}$ | 1 | $units_{actin}\ \mu m^{-1}$ | |
| Myosin motors force | $f_m$ | 500 | pN $\mu m^{-1}$ | (Craig et al., 2012)* |
| Membrane static force | $f^0_{mem}$ | 80 | pN $\mu m^{-1}$ | (Craig et al., 2012)* |
| Membrane viscous coefficient | $c_v$ | 1715 | pN s $\mu m^{-2}$ | § |
| Adhesion strength | $\kappa_{FA}$ | 1088 | pN s $units_{actin}^{-1}$ $units_{FA}^{-1}$ | § |
| Minimum friction | $\eta_0$ | 4240 | pN s $\mu m^{-2}$ | § |
| Contraction duration | $t_{cont}$ | 20 | s | (Giannone et al., 2007, Burnette et al., 2011)* |

**Table 6-1:** Model parameters.

*Adapted from literature
§ Estimated parameters

## 6.3.1. Decrease of actin polymerization

To test the influence of actin on lamellipodium protrusive and contractile cycles, Giannone and co-workers (Giannone et al., 2007) used Cytochalasin B, an inhibitor of

actin polymerization. They found that treated cells still generated periodic contractions, although the period increased and the cell edge speed decreased. These experiments established an inverse relationship between actin retrograde flow speed and period between contractions, suggesting that actin alone can trigger such contractions.

This condition is simulated with the model by decreasing $v_{pol}$. In fact, at t=220 s, $v_{pol}$ is decreased to 60% of its original value (arbitrary values). According to equation (6.4) this condition decreases the membrane speed ($v_{mem}$), which in turn combining equations (6.1) and (6.3), slows the retrograde actin flow ($v_{ra}$). As a result, since the lamellipodium width ($L_w$) remains constant, the period of contractions ($T$) increases. This is shown in Figure 6.5, where the leading edge position is represented over time.

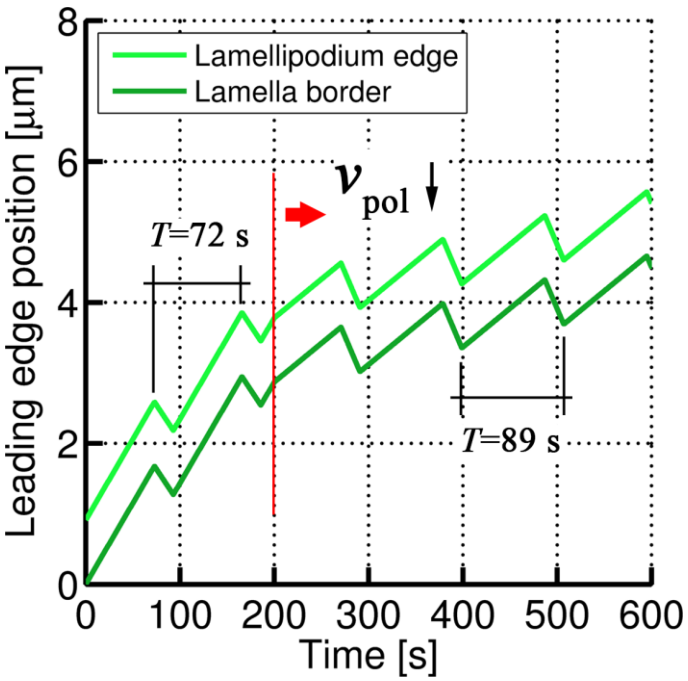


**Figure 6.5:** Leading edge position with decreased polymerization. Actin polymerization is decreased by 40% at t=200 s. This leads to longer periods of contraction and lower actin and membrane speeds, which is translated into a slower advance of the cell leading edge.

## 6.3.2. Myosin inhibition

Blebbistatin (BBI) selectively inhibits myosin motors activity (Straight et al., 2003) and has been used by several authors to study the role of myosin II in lamellipodium dynamics (Giannone et al., 2007, Burnette et al., 2011). Among other complex effects (such as actin arc formation at the lamella border), they found that blebbistatin-treated cells present decreased speeds of edge retraction ($v_{mem}$) and increased retraction duration

($t_{cont}$). Indeed, they conclude that myosin II is essential in the generation of periodic contractions.

This inhibition can be simulated with the model by simply decreasing 50% the maximum force developed by the myosin motors ($f_m$). According to equation (6.1) this is enough to slow the actin retrograde flow ($v_{ra}$) and therefore to decrease the membrane retraction speed ($v_{mem}$ during contraction) as observed in experiments (Giannone et al., 2007)(Figure 6.6).

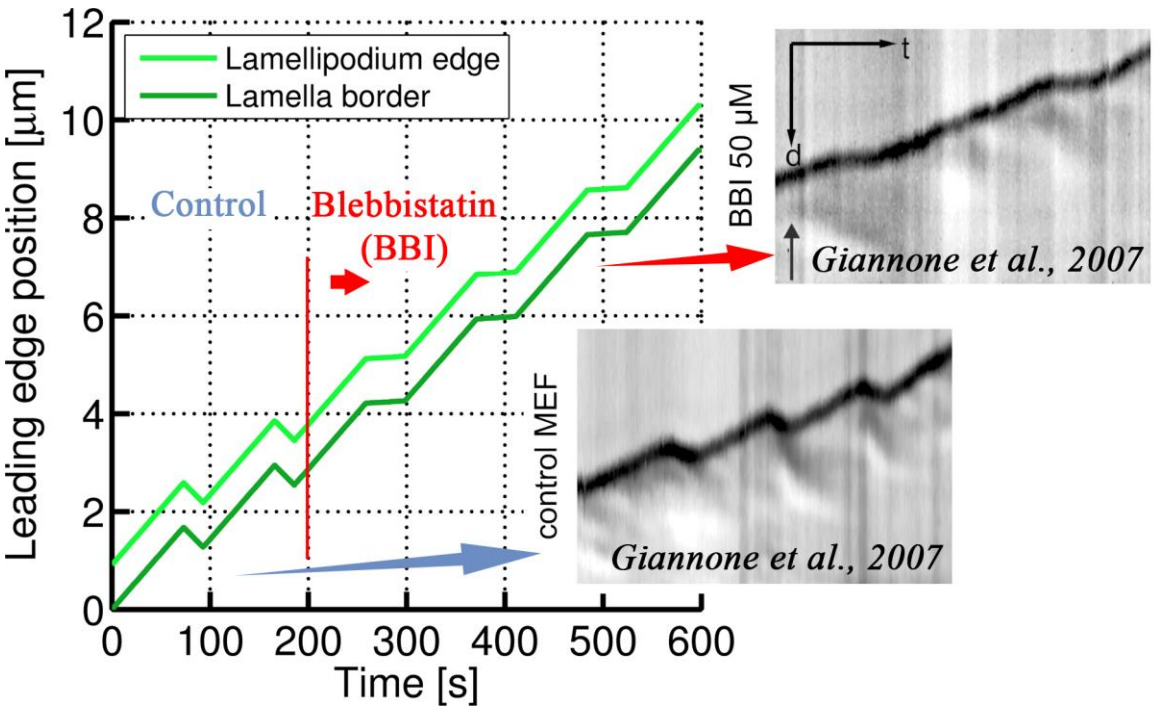


**Figure 6.6:** Leading edge position with myosin inhibition.
Inhibition of myosin produces longer phases of contraction with decreased edge retraction speed.

However, with no further hypothesis, the model does not explain why the retraction duration increases. For that, it is assumed that the amount of ATP (Adenosine TriPhosphate providing energy to motors) is constant, so the energy corresponding to inhibited motors can still be spent by active ones. This extra energy reserve leads to longer phases of contraction. In the model, this is equivalent to the constrain: $f_m t_{cont} = \text{constant}$. In the example shown in Figure 6.7, $f_m$ is reduced to half of its initial value and therefore $t_{cont}$ increases from 20 to 40 seconds, while the global periodicity remains unaffected.

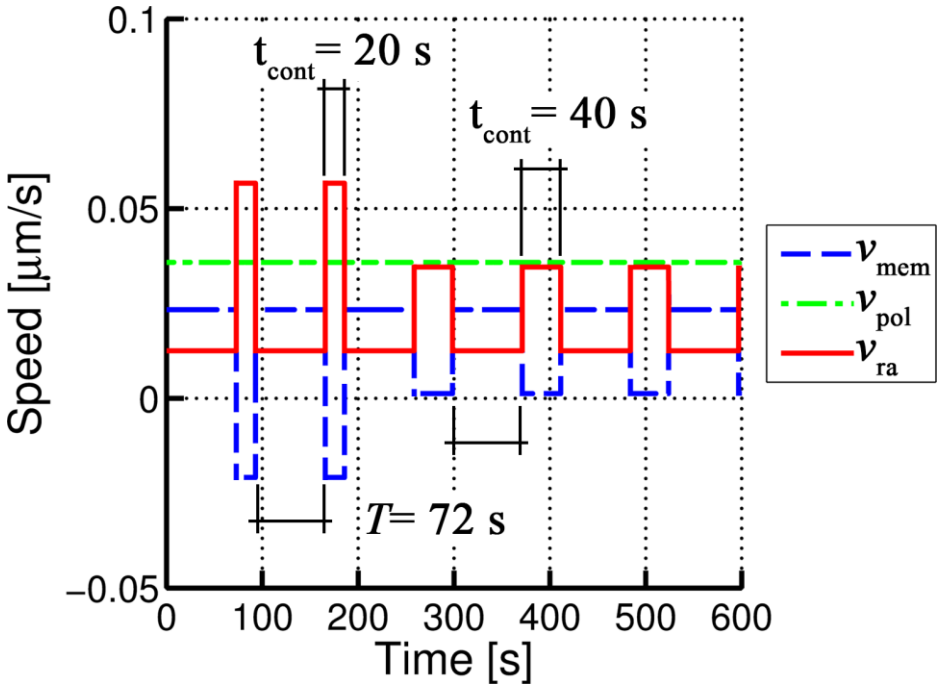


**Figure 6.7:** Model cycles after myosin force inhibition.
Inhibition of myosin force leads to lower speeds of acin rearward flow and membrane retraction. The duration of contraction increases whereas the periodictiy of contractions is unaffected.

### 6.3.3. Decrease of FA friction

Integrin-based FAs are formed in migrating cells near their leading edges. How F-actin flow is coupled to FA is unclear, as well as how F-actin engagement to FA regulates actin cytoskeleton and FA dynamics. The role of vinculin in integrating FA and actin dynamics has been deeply studied by vinculin gene disruption in primary fibroblasts (Thievessen et al., 2013). They show how vinculin promotes nascent FA formation and turnover in lamellipodia, establishes a lamellipodium-lamellum border and engages F-actin flow in maturing FA to generate high ECM traction forces. Characterization of a vinculin point mutation that specifically disrupts F-actin binding showed that vinculin F-actin interaction is critical for these cellular functions. However, FA maturation rate correlated with F-actin flow rate independently of vinculin. Thus, they concluded that vinculin functions as molecular clutch organizing leading edge F-actin, generating ECM traction and promoting FA formation and turnover, while FA maturation is regulated by F-actin flow independently of vinculin.

As stated before, the model was adjusted to fit the experimental results from the aforementioned work (Thievessen et al., 2013). Specifically, vinculin knocked out cells

recovered with wildtype vinculin (Vcl-KO+WT) are taken as the control case (normal conditions) whereas non-transfected vinculin knocked out cells (Vcl-KO) are used to study the effect of FA friction. Apart from fitting experimental data, the model is able to predict untested behaviors. For instance, it is known that Vcl-KO cells present higher retrograde actin flow ($v_{\mathrm{ra}}$) and membrane speeds ($v_{\mathrm{mem}}$) as well as broader lamellipodiums ($L_{\mathrm{w}}$). Since vinculin strengthens FAs, knocking out vinculin decreases the associated friction (decrease of $\kappa_{\mathrm{FA}}$ and hence of $\eta_{\mathrm{FA}}$). According to equations (6.1) and (6.2), $v_{\mathrm{ra}}$ increases if $\eta_{\mathrm{f}}$ is decreased, but this would slow the membrane speed ($v_{\mathrm{mem}}$), opposing to the experimental observations. Thus, the model suggests that modifying friction is not the only effect of vinculin disruption. One possibility is that although the rate of polymerization ($\phi$) may remain constant (constant amount of actin), $v_{\mathrm{pol}}$ may increase. In turn, this would imply that $A_{\epsilon,x=L_{\mathrm{w}}}$ decreases (equation (6.5)).

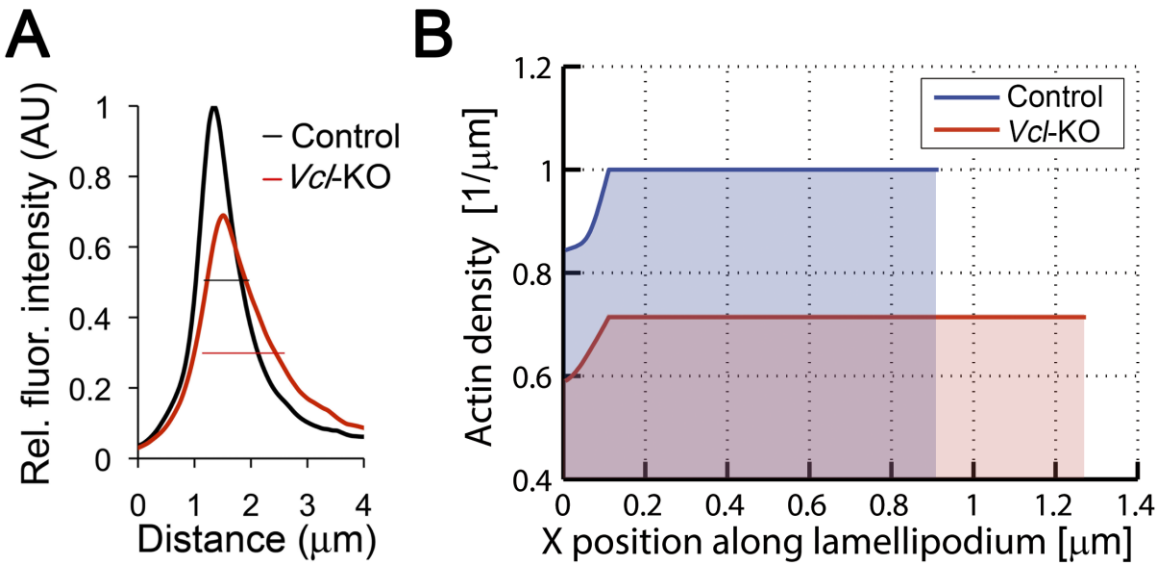


**Figure 6.8:** Cortactin intensity and actin density along lamellipodium
A) Cortactin fluorescence intensity distribution on y-axis/Distance from leading edge on x-axis (Thievessen et al., 2013). B) Actin density along lamellipodium. Control cells present a shorter lamellipodium (0.91 μm) compared to the Vcl-KO cells (1.26 μm) with a less dense network so that the total amount of actin is conserved.

On physical grounds, this is equivalent to a less dense actin network which polymerizes faster. Indeed, qualitative observations of reduced phalloidin fluorescence intensity within lamellipodia lacking vinculin support this possibility. In addition, quantification of the distribution of the actin-binding lamellipodium marker-protein

cortactin (Lai et al., 2008) across fluorescence intensity linescans through the lamellipodium confirmed a reduced peak intensity in the absence of vinculin (Thievessen et al., 2013). Furthermore, if the network density decreases while actin and membrane speeds increase, the lamellipodium must extend to conserve the same amount of actin at the lamellipodium (Figure 6.8).

To compare predictions with experimental data, the control case is disrupted at $t$=200 s where $\kappa_{\mathrm{FA}}$ is decreased by 80% ($\kappa_{\mathrm{FA}} = 0.2\kappa_{\mathrm{FA}}^{0}$) and $v_{\mathrm{pol}}$ is increased by 40% ($v_{\mathrm{pol}} = 1.4v_{\mathrm{pol}}$) simulating vinculin knocking out. The main effect is the substantial increase or rearward actin flow ($v_{\mathrm{ra}}$) from 750 nm/min to 1480 nm/min, as well as the lengthening of the lamellipodium from 0.91 to 1.26 µm according to the criterion of constant amount of actin. Interestingly, the equilibrium actin speed and lamellipodium width produce a shorter period, 51 s compared to 72 s of the control case, as measured in experiments (Figure 6.9). Additionally, Figure 6.10 also ilustrates this behavior and shows a saw-tooth shape of the cell edge, similar to the ruffling patterns reported in Vcl-KO cells (Thievessen et al., 2013).

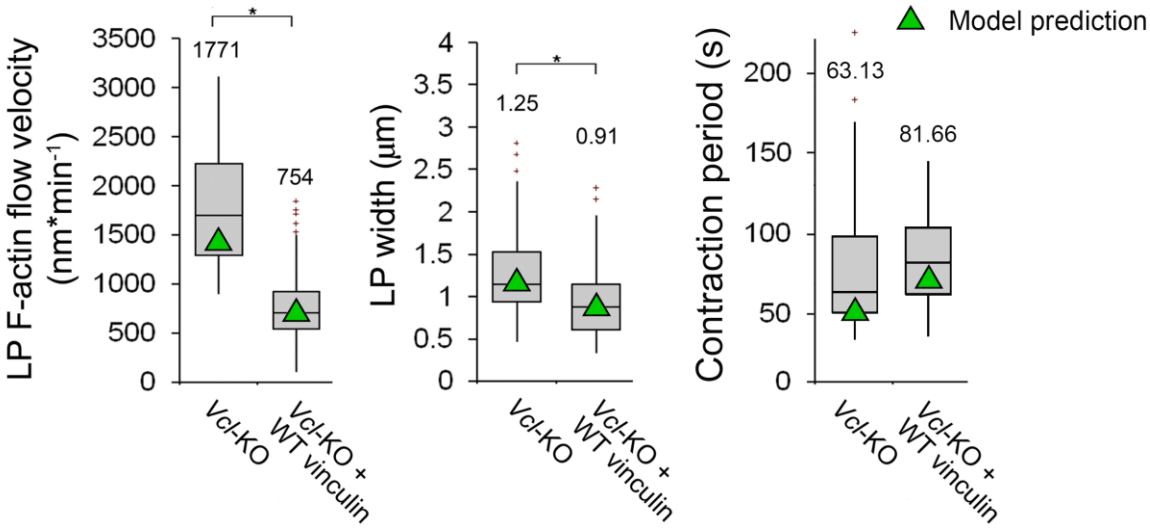


**Figure 6.9:** Model predictions vs. measured data.
Vcl-KO cells and Vcl-KO cells recovered with wildtype vinculin (+WT) are simulated. Model predictions regarding actin flow, lamellipodium width and periodicity are in good agreement with measured experimental data.

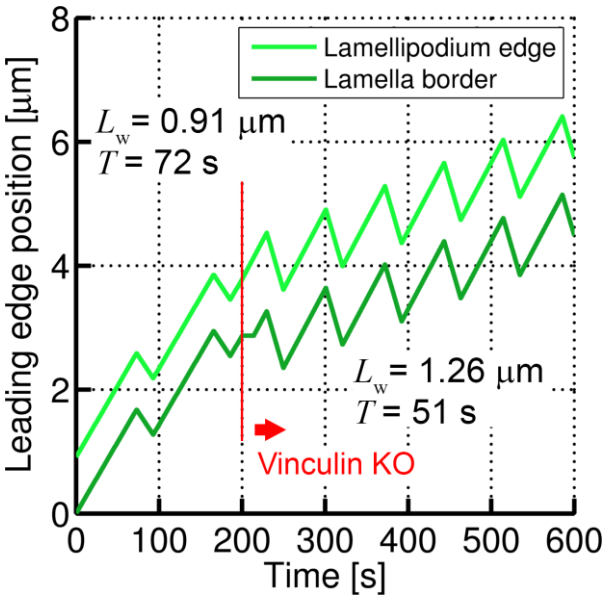


**Figure 6.10:** Leading edge position with vinculin knocked out.
Knocking out vinculin decreases FA friction so that the rearward actin flow increases. Considering a constant amount of actin, the lamellipodium expands, adapting to the new situation. In spite of the larger lamellipodium width and although the membrane speed is enhanced due to polymerization, the period of contraction decreases due to very fast speeds of actin.

The model is also able to capture additional lamellipodium phenomena such as actin waves at the lamella border produced by the rearward actin flow, which has been reported in literature (Giannone et al., 2004). In fact, they found that the periodicity of such actin waves were related with the lamellipodium width and the actin speed, suggesting the transport of some contraction-triggering signal bound to the actin structure. This dependence was confirmed with own experiments, explained in next section, where the lamellipodium width and actin speed was found to follow a linear relationship (correlation coefficient $R^2$: 0.71) as shown in Figure 6.11. Note that results from both the previous work of (Thievessen et al., 2013) and the model were introduced to obtain the fit. Since the lamellipodium width was not measured in the own experiments, it was taken as $L_w = v_{ra} T$. The linear relationship obtained, confirms that such assumption was indeed correct.

To simulate waves of proteins bound to the actin, a transport equation was incorporated, taking into account the protein concentration ($P_c$) and the rate of binding ($k_{on}$) and unbinding ($k_{off}$) of such proteins to the actin:

$$\frac{\partial P_c}{\partial t} = -k_{off} P_c + v_{ra} \frac{\partial P_c}{\partial x} + k_{on} A_c \tag{6.8}$$

This equation implies a double dependence on both the actin speed and actin concentration, although the periodicity of the protein waves is the same as that of the actin, as shown in Figure 6.12, in qualitative agreement with literature (Giannone et al.,

2004). This simple approach could be used to simulate the transport of multiple proteins, and could be refined to account for the complex interactions between them, although at the moment is out of the scope of this Thesis.

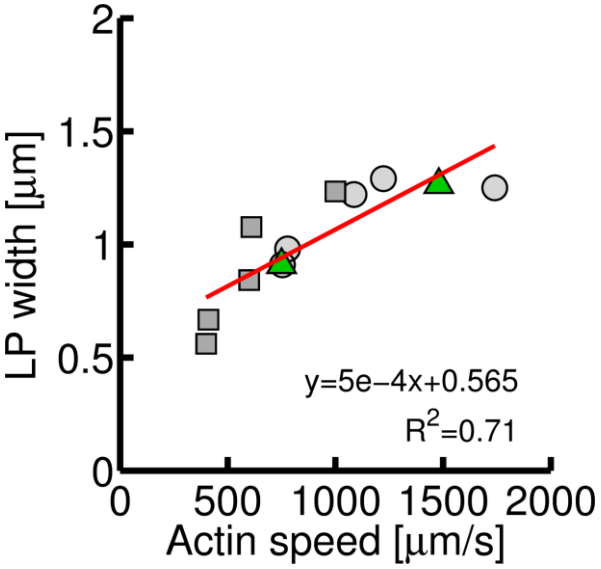


**Figure 6.11:** Lamellipodium width and actin speed relationship.
Actin speed correlates linearly with the lamellipodium width, suggesting that $T = v_{ra}/L_w$ is a reasonable assumption. Light grey circles represent experimental results from (Thievessen et al., 2013). Dark grey squares represent experimental results from current experiments. Green triangles show the model predictions for the control and Vcl-KO cases.

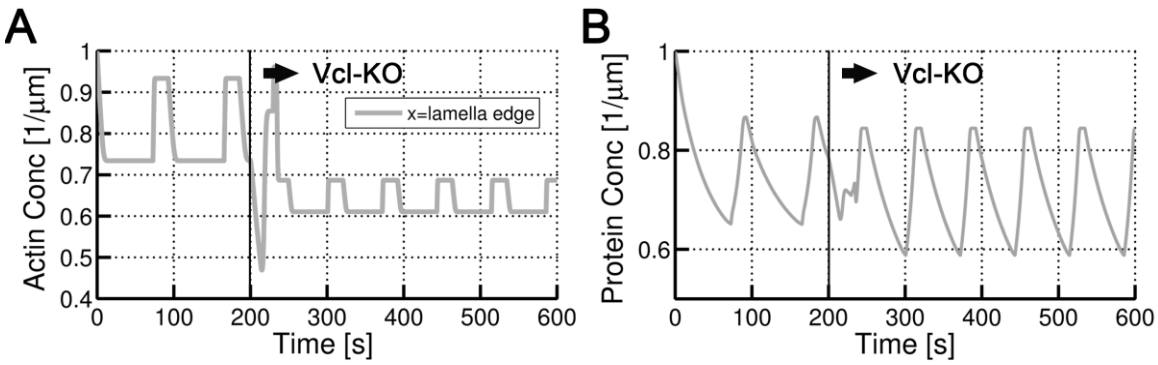


**Figure 6.12:** Actin and protein concentration at the lamella border.
Changes in retrograde actin flow during contractions produce actin and bound protein waves at the lamella border, more frequently when vinculin is knocked out. Note that the system requires ~30 s for adaptation to a sudden change in friction conditions. After that period, a new steady state is achieved.

## 6.4. Experimental assays

The role of vinculin and its interaction with actin in modulating leading edge FA dynamics has been studied in detail in (Thievessen et al., 2013). In fact, to test whether

vinculin promotes nascent FA formation and/or disassembly by interacting with actin, lamellipodial FA was analyzed in Vcl-KO cells expressing WT, dAB, PA-dAB and PA:

- **WT:** Vcl-KO cells rescued with wildtype (normal) vinculin. Equivalent to plain control cells.
- **dAB:** full length protein but actin binding deficient. Giving back the full protein just with one point mutant (aminoacid switch) restores all other activities of vinculin (signaling or interactions with other proteins) except actin binding, allowing to test if the effect of the vinculin knockout is the result of loss of actin-integrin connection.
- **PA-dAB:** pre-activated actin binding deficient vinculin. Actin binding is required for the opening of the vinculin molecule (the molecule only binds actin and talin simultaneously to transmit force from actin to integrin when it is open/activated). When the molecule cannot bind actin (such as dAB) it does not fully open and hence, using dAB proteins alone to test the role of actin binding does not clarify whether the observed effects of the dAB mutant are due to (i) lack of actin binding or (ii) lack of vinculin activation. Pre-activating the vinculin allows testing the isolated effects of vinculin-actin interaction.
- **PA:** pre-activated vinculin. Vinculin activation induces effects on focal adhesions and potentially actin itself. A further control condition (PA) was included to see whether an effect observed in the PA-dAB mutant is the result of the PA and not the dAB mutation.

In their study, however, some aspects such as the periodicity or the correlation between actin and leading edge speeds were not analyzed. For that, different algorithms were developed in this Thesis to measure lamellipodium dynamics including actin and membrane speeds during protrusion/retraction cycles as well as the periodicity of contractions. More details are given in Appendix A, Section A.6 and A.7.

### 6.4.1. Results

The experiments previously described were repeated with a different set of cells and analyzed using the aforementioned scripts. Results confirmed the behaviors found in

(Thievessen et al., 2013). Vcl-KO cells exhibited remarkably faster actin flow speeds, especially during retraction phases, whereas Cells expressing dAB or PAdAB showed increased actin velocities compared to the WT and PA cells, suggesting that actin-vinculin interaction is critical to engage lamellipodial actin flow. Overall, membrane speed was slower during retraction and actin speed was higher (except in the WT cells where it remained practically constant) in agreement with the model assumptions. In addition, membrane speeds were similar for all cells, both during protrusion and retraction cycles, indicating that knocking out vinculin may alter the polymerization conditions as predicted by the model. The periodicity of lamellipodium retractions was not significantly affected by the mutations neither in the membrane nor in the actin measurements (Figure 6.14). In fact, averaging the periods of actin and membrane retraction cycles for all the studied cases, leads to a mean periodicity of ~90 s (86.9 s 87.2 s for membrane and actin respectively). The correlation of both curves gave and averaged period of ~72 s with a correlation of $R^2$=0.79 (Figure 6.15). The low variability of periods, together with the strong changes in actin rearward flow speeds, support the assumption that lamellipodium adapts its width depending on the situation so that $T = v_{\mathrm{ra}}/L_{\mathrm{w}}$ remains more or less stable. Interestingly, the phase delay between membrane and actin movements is overall contained within the range 0 to -90º when averaging all the cases, although WT cells present small positive phases (~30º). Negative delays mean that the membrane follows the actin, a finding that has not been reported yet in any other experimental study.

## 6.5. Materials and methods

This section briefly summarizes the main mathematical, computational and experimental techniques used in the simulations and during experimental data acquisition. Nevertheless, more specific and detailed methods can be found in Appendix A, Section A.6 and in (Thievessen et al., 2013) as indicated later.

### 6.5.1. Mathematical approach

All the model variables are interrelated through the presented equations and thus it is possible to find the analytical solution for the steady state of the system. However, in order to account for time-dependent parameters or sudden changes of specific conditions (e.g. enhancement or inhibition of polymerization, myosin activity etc.) the equations are computed using a finite-differences approach. The lamellipodium is discretized $N$ elements of size $dx$ and evolves in time-steps of $dt$ .

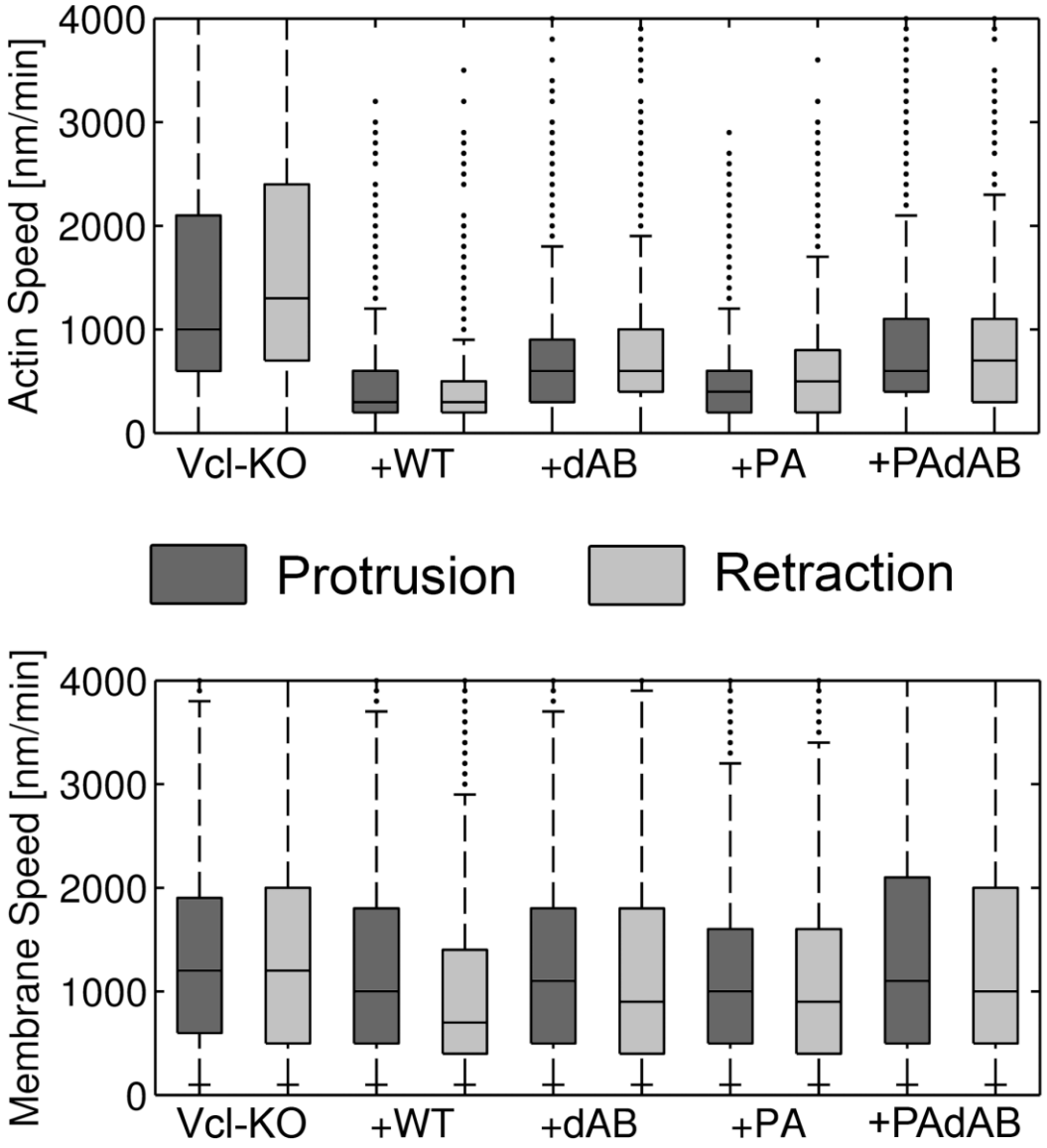


**Figure 6.13:** Actin and membrane speeds during protrusion/retraction cycles.
Vcl-KO cells show remarkably higher actin flow velocities, although the results are more spread compared with the rest of cases. Cells expressing dAB or PAdAB show increased actin velocities compared to the WT and PA cells, suggesting that actin-vinculin interaction is critical to engage lamellipodial actin flow. Overall, membrane speed is slower during retraction phases.

From initial conditions, the actin retrograde flow speed ($v_{ra}$) is computed using equation (6.1), then the change of actin concentration due to diffusion and depolymerization can be calculated as:

$$\begin{aligned} \Delta A_c^{i,j} &= -\gamma A_c^{i,j} + v_{ra}\left(A_c^{i+1,j} - A_c^{i,j}\right)\Big/ dx \\ A_c^{i,j} &= A_c^{i,j-1} + \Delta A_c^{i,j} dt \end{aligned} \tag{6.9}$$

where *i* represents the spatial discretization along the lamellipodium and *j* the temporal one.

Knowing the actin density distribution allows computing the total amount of actin at the lamellipodium at each time step (and therefore the friction and other related parameters):

$$\int_{x=0}^{x=Lw} A_c(x,t)dx \simeq \sum_{i=1}^{i=N} A_c^{i,j}\Big|_{j=t} \tag{6.10}$$

With all the variables updated, the new actin and membrane speeds are calculated as well as the leading edge position. Next, a new temporal step proceeds.

## 6.5.2. Experimental methods

Due to the computational character of this Thesis and the lack of space, the experimental methods used to perform the previous assays are not included. Nevertheless, they are described in detail in (Thievessen et al., 2013).

## 6.5.3. Measurements

### 6.5.3.1. Actin flow and edge position

Experiments provide images of actin density at the cell edge and its evolution over time. By means of image pattern correlation techniques, the actin rearward flow as well as the membrane movement can be measured. In short, a small region of the cell edge is manually selected and a hand-coded MATLAB script computes the velocity field distinguishing between cell body and background (Figure 6.17). Detailed information of specific functions and procedures used for these measurements is provided in Appendix A, Section A.6.

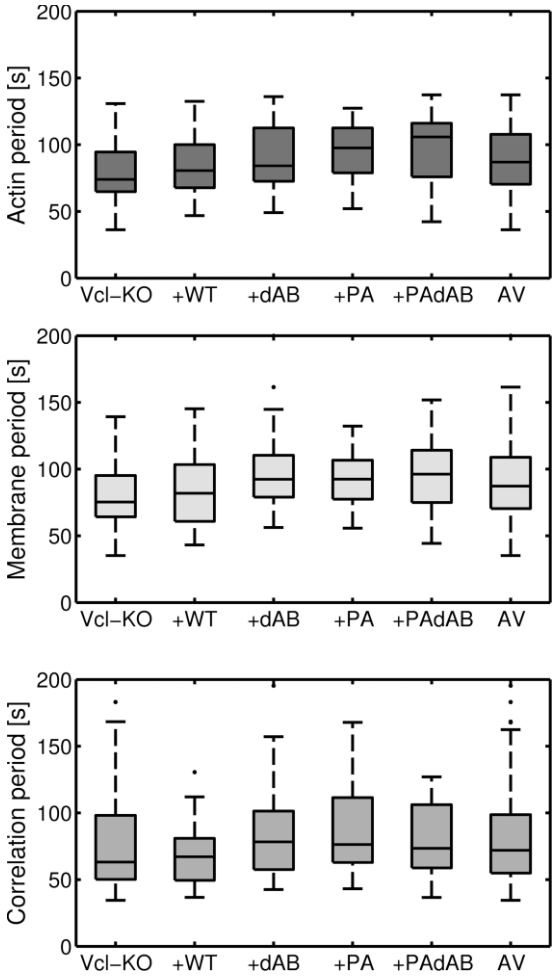


**Figure 6.14:** Actin and membrane periodicity.
Both actin and membrane speed curves have similar periodicity (in the range ~70-100 s) for all the studied cases (slightly higher for the PAdAB mutants), whereas their correlation presents slightly lower periods (~70 s). AV tick shows the average of all cases.

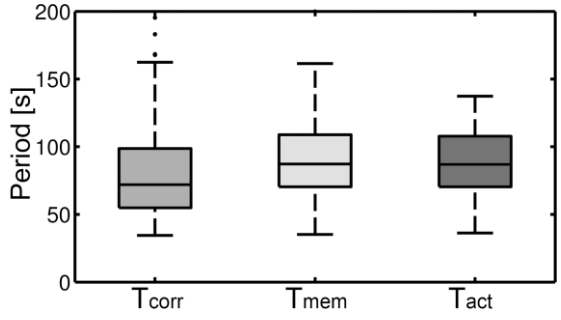


**Figure 6.15:** Averaged periodicity.
Averaged periodicity of membrane and actin speeds is ~90 s (86.9 s 87.2 s for membrane and actin respectively), whereas the correlation of both curves gives and averaged period of ~72 s with a correlation of $R^2$=0.79.

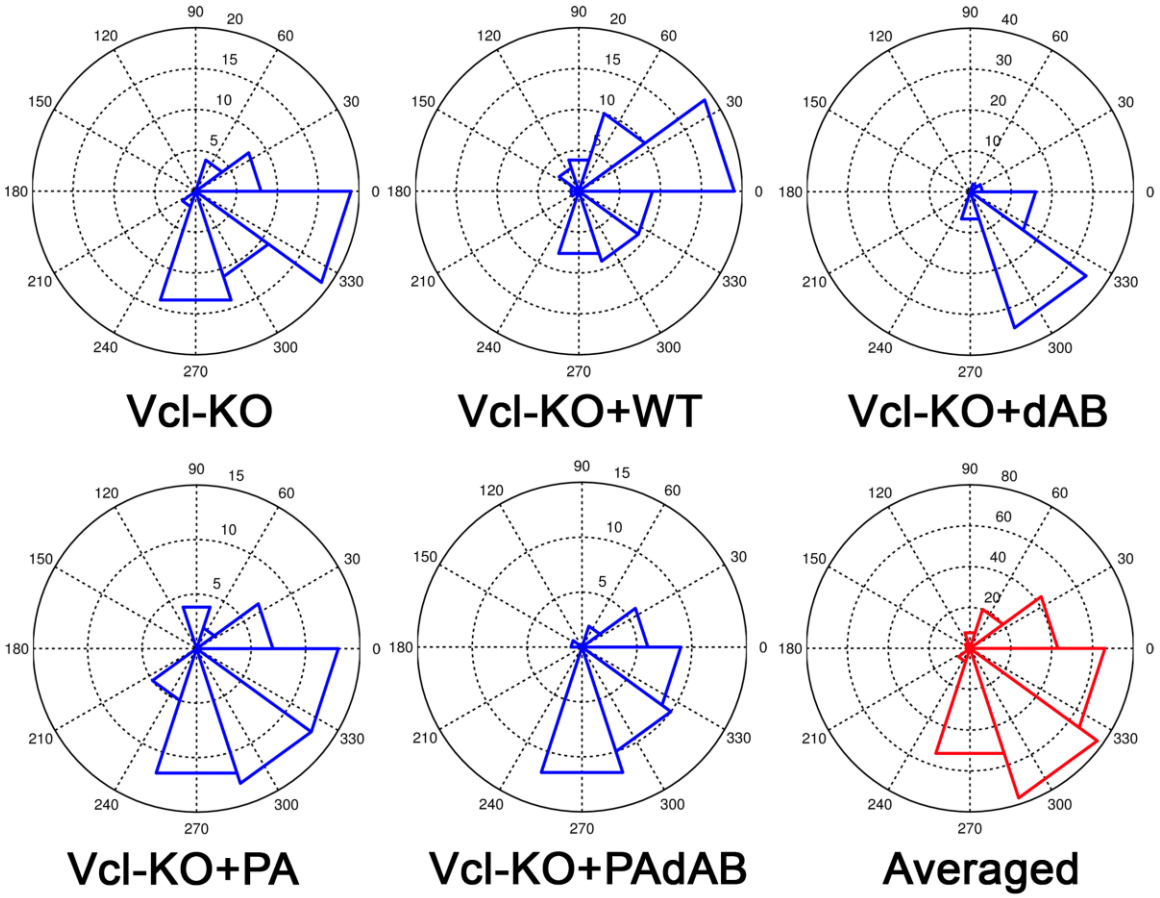


**Figure 6.16:** Actin-membrane velocities phase delay.
Except in the WT cells, the phase between actin and membrane speed curves is mainly constrained in the range 0 to -90º, indicating that membrane movements follow the actin.

### 6.5.3.2. Actin and membrane speeds correlation

With the aforementioned script, actin and membrane speeds over time are recorded to perform statistical analysis. Studying the correlation of both curves and performing a Fourier analysis not only allows finding periodic patterns (repeated cycles of edge protrusion/retraction) but also the phase delay that indicates whether actin follows the membrane movements or *vice-versa* (Figure 6.18). More details regarding this tool can be found in Appendix A, Section A.7.

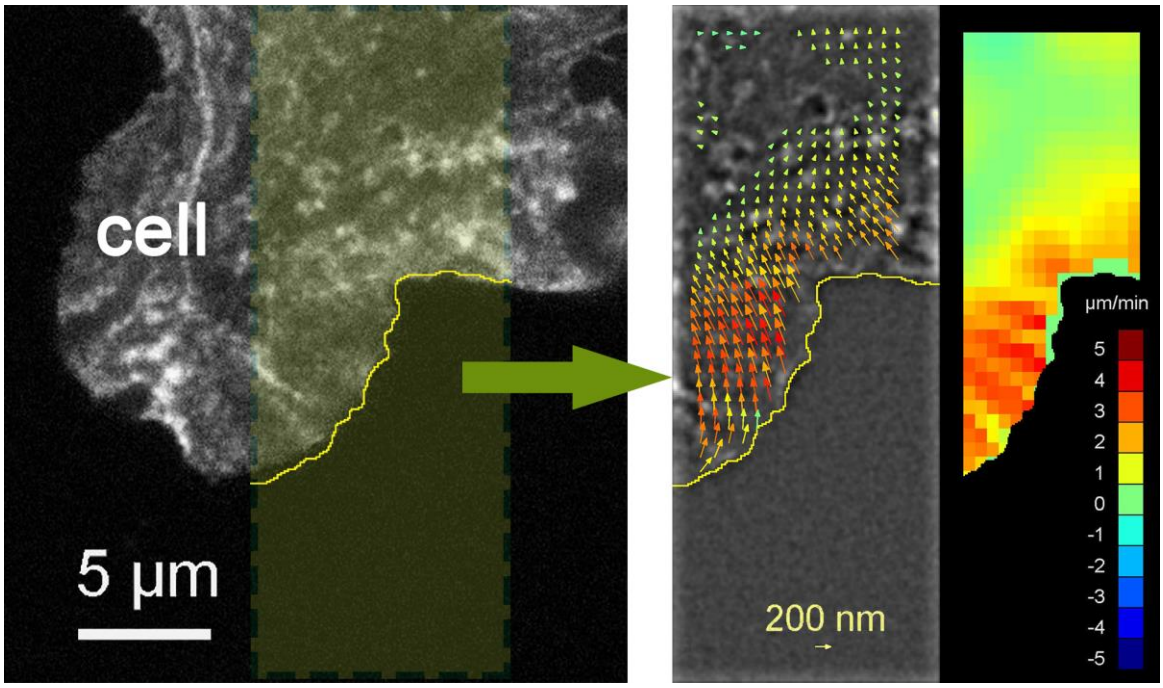


**Figure 6.17:** Actin flow and membrane speed measurement.
A small section of cell edge is selected to measure actin and membrane dynamics. A detailed description of the methods used for this purpose can be found in Appendix A, Section A.6.

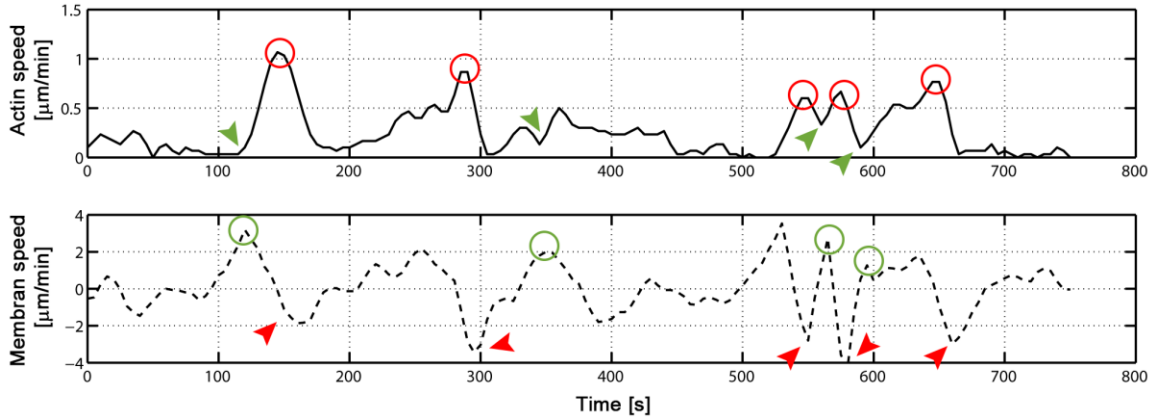


**Figure 6.18:** Actin and membrane speeds over time.
Actin and membrane velocities are measured from experimental movies: actin retrograde flow peaks (red circles) correlate with membrane retractions (red arrows), whereas higher protrusion velocities (green circles) correspond with local minimums of actin speed (green arrows). This allows finding periodic patterns and phase delays between noisy curves.

## 6.6. Discussion

In this Chapter, a continuum approach for modeling lamellipodium dynamics and the role of vinculin engaging rearward actin flow has been described. All the variables have a physical meaning, and the main assumptions of the model are based on experimental observations (Giannone et al., 2004, Giannone et al., 2007, Burnette et al., 2011): (i) cell migration proceeds by cycles of edge protrusion and retraction, (ii) actin polymerizes at the cell tip, pushing the membrane and producing a retrograde actin flow, (iii) this flow is faster at the lamellipodium and slows down at the lamella, probably due to friction of actin with mature FAs and depolymerization of the network, (iv) myosin II contributes to the rearward actin flow producing cyclic contractions of the whole network, (v) the period of this contractions is proportional to the lamellipodium width and inversely proportional to the actin speed, suggesting that some triggering signal travels with the actin flow to the lamella border from the cell edge (vi) nascent FAs appear during the contraction phase. With all this, the model is able to predict general behaviors of lamellipodium dynamics such as protrusion/retraction cycles or periodic myosin activation, and more specific effects such as the decrease of membrane speed and increase of the retraction period when polymerization is inhibited or the increase of contraction duration when myosin activity is reduced (Giannone et al., 2007). Some additional hypotheses (e.g. lamellipodium width adaptation to maintain a constant amount of actin) were introduced to fulfill previous experimental results (Thievessen et al., 2013). In turn, these hypotheses predicted some untested behaviors (the increase of polymerization when knocking out vinculin), which were later confirmed by further experiments.

Since the model uses a finite-differences method in 1D, the computational cost is notably low, allowing really fast simulations (of the order of minutes) in a personal computer. The drawback, however, is the lack of details and the use of averaged values (e.g. constant friction along the lamellipodium). In any case, its simplicity facilitates its incorporation into more complex models, so that combining this approach with particle-based of finite element methods would allow for very detailed simulations in 3D migrating cells.

Additionally, different algorithms based on matrix convolution and function correlation have been developed to measure lamellipodium dynamics from experiments, such as actin and membrane speeds, their correlation, periodicity of contractions and phase delay between actin and membrane evolution. With these scripts, 61 different

movies were analyzed (4-6 measurements per movie) in which Vcl-KO cells were fully or partially recovered by expressing WT, PA, dAB and PAdAB. Results confirmed the general trends observed previously (Thievessen et al., 2013) and provided new findings regarding the periodicity of actin and membrane retraction cycles as well as the phase delay between both curves. Knocking out vinculin produced increased speeds of actin rearward flow compared to the rest of cases. WT and PA showed slower actin velocities whereas dAB and PAdAB cells presented intermediate speeds. This, together with the low variability of periods, supports the observation that a decrease of friction produces larger lamellipodiums and higher speeds while the periodicity of contractions is not affected, so that $T \sim L_w / v_{ra}$ . Interestingly, 73% of all the analyzed cells showed negative phases (0 to -90º) meaning that the membrane movements follows the actin. This percentage increases to 82% if WT cells are not considered, since half of these WT mutants present positive phases. Averaging all the values of the WT cells gives a phase delay of 2.4º which means that actin and membrane are practically synchronized. Further experiments with these and other type of cells would be necessary to confirm this finding which has not been reported yet in other research works.

Chapter 7

# CLOSURE

This chapter summarizes the work accomplished throughout the previous chapters, recapitulating the main conclusions and highlighting the original contributions of this Thesis. Finally, several open future lines are proposed.

**Contents**

## 7.1. Summary

The main objective of this Thesis was the development of numerical and computational models to achieve a better understanding of the mechanisms leading to cell migration. With this purpose, continuum, discrete and finite element-based approaches were used. For instance, to study the effect of mechanical factors (substrate stiffness, geometry and boundary conditions) on cell migration within a 3D ECM, a FE single cell migration model based on *mechanosensing* and including the major phases of the migratory cycle was developed and described in Chapter 2. The model was capable of simulating the preferential movement of an individual cell under different mechanical conditions, predicting speeds and migratory patterns similar to experiments. In this approach, the mechanical behavior of the whole cell body was simplified to two springs in parallel and a contractile actuator in series (equivalent to a third pre-compressed spring), implying the increase of cell exerted stress with ECM stiffness until saturation as observed experimentally. Additionally, using a balance of forces together with the assumption that the ECM friction increases with stiffness (due to higher material densities), the bi-phasic behavior of cell speed was also captured. The model was also tested to study a specific experiment where a blunted micro-needle is introduced in the substrate near the cell to modify the local state of stress in the ECM and is moved toward or away from the cell (causing the cell to move away and toward the needle respectively). The simulations suggested that the cell feels the spatial stretching or compression caused in the ECM by external loads. Hence, if the microneedle pulls, the compressive forces of the cell oppose the needle forces and the cell feels higher rigidity. However, if the micro-needle pushes, the compression forces of the cell follow the same direction as those of the micro-needle, causing the cell to sense more compliance in the direction of the micro-needle, even though Young's modulus is homogeneous in all directions. Sensitivity analysis of the model parameters, suggested that actin stiffness is one of the major parameters controling cell response. In a more complex structure such as the real cell body, this role would correspond to the CSK organization. In fact, it has been observed in experiments how some cell structures (FAs, stress fibers, actin rings etc.) react to mechanical changes of environmental conditions, therefore adapting the CSK to the new situation. To better understand these mechanisms, a more detailed modeling of the CSK network taking into account its main constituents was required, giving way to the next approach, addressed in Chapter 3.

To explore the role of the internal structure of cell CSK and its response to ECM stiffness, a Brownian-dynamics particle-based computational model was used to polymerize a 3D cross-linked actin network and test its contractility. By only including the dynamics of molecular motors and ACPs, the simulated actin network exhibited macroscopic contractile behaviors similar to experiments, indicating that microscopic properties of individual constituents govern the network responses. In fact, it was found that molecular motors play a central role in *mechanosensing*. While not negating the significance of other factors such as actin dynamics and structures, biochemical signaling, and adhesions dynamics in the cell's response and adaptation to mechanical cues, it was demonstrated here that actomyosin machinery can be one of several possible key mechanisms for cell rigidity-sensing phenomena. As a matter of fact, among all the studied factors, those affecting motor dynamics were the most influential in network behavior. Confirming experimental evidence, the model predicted that cell stress is proportional to ECM stiffness for compliant substrates and becomes relatively constant (saturates) for stiffer ECMs. The existence of a transition to a slower rate of stress increase can be explained by the mechanisms that cause the motors to slow or stall: (i) all of the next binding sites in a barbed-end direction are already occupied (blocking), (ii) reaching the motor stall force, or (iii) reaching the barbed end of an actin filament. It was demonstrated here that only a small fraction of motors reached the barbed end of a filament for all the studied ECM stiffness, so this would have little direct influence on the saturation stress. Blocking, on the other hand, was observed over the entire range of substrates, but was especially prevalent at compliant ECMs due to the greater distance that motors needed to walk before reaching their maximum force, combined with the tendency for all constituents (filaments, motors, and ACPs) to increase in density under large compressions. For stiffer substrates, material strains were smaller and motors walked shorter distances before attaining the stall force. For high ECM stiffnesses, the stress saturated as determined by the stall force that motors could exert maximally while at lower stiffnesses, the stress was limited by the blocking effect which progressively decreased as the ECM rigidity increased. This transition from blocking to limitation due to motor stall force constitutes a mechanism by which cells can sense substrate stiffness. This mechanism was further confirmed by varying actin concentration and average filament length. In sum, this work elucidated one mechanism by which cells can modulate their properties and respond to the surrounding environment via cytoskeleton contractility. Although the model was based on molecular-level processes, macroscopic

behaviors of the active cross-linked actin networks agreed well with the response of cells probed in experimental quantitative studies and served as validation for the previous *mechanosensing* model assumptions. In addition, the model can be used to study a wide variety of actin-related phenomena such as CSK stiffening/softening, creep network response or ring formation in cytokinesis among others. Nevertheless, detailed modeling allows very specific and accurate analysis but entails high computational costs. For instance, one single simulation of a small domain using 8 CPUs in parallel can last several weeks. This duration is not reasonable to properly study the migration of a whole cell, since the simulation would be longer than a real experiment. Hence, a phenomenological law able to reproduce the macroscopic features of the CSK becomes necessary.

To incorporate the findings at the micro-scale (intracellular) into the macro-scale (cell) model hypothesis, the temporal network stabilization caused by motor stalling was introduced into the *mechanosensing* model by means of a continuum regulatory function, reproducing the force build-up and saturation. This assumption, contained in Chapter 4, allowed performing simulations lasting seconds instead of weeks, making the approach suitable to be included in finite element models with longer time and length scales. Despite its simplicity, the model was able to successfully simulate multiple rigidity-sensing conditions and its results were in good correspondence with experiments and the computational results obtained with the actin network model. As before, this suggests that although intracellular signaling or other complex chemical phenomena play important roles in cell behavior, the *mechanosensing* process is precisely depending on mechanics. Similar to the model described in Chapter 2, the whole cell body was represented with two springs in parallel, however, the time dependence was introduced in the contractile actuator in series. In other words, the actuator was equivalent to a third pre-stressed spring whose equilibrium length was brought to zero through a decay clock. This three-spring configuration allowed distinguishing between active and passive responses of the cell. Mechanistically, the addition of the series spring (actin stiffness) with the acto-myosin actuator permitted to capture the linearity of cell force with respect to substrate stiffness for compliant substrates, and its saturation for higher rigidities. In addition, relative values between the actin stiffness and the rigidity of the CSK passive components regulated the cell response under different mechanical conditions, playing the actin stiffness a predominant role at high substrate stiffness. This also would allow simulating more complex phenomena such as stress-fiber rigidization, network disruption etc. in

comparison with the usual two-spring configurations used in other works. Finally, sudden changes in substrate stiffness were analyzed, finding that cell reaction occurs almost instantaneously suggesting that the CSK adaptation is a purely mechanistic process, in agreement with model assumptions and experimental observations. The accuracy obtained in the numerical results suggested that a one-dimensional approach was adequate to model the *mechanosensing* process, at least for the simple scheme proposed in the simulated experiments. Nevertheless, the implementation of this theory in 3D and in combination with models of cell migration would provide a strong impetus for the development of future models with applications in wound healing, tissue engineering or cancer metastasis. Indeed, since cell migration requires the integration of multiple processes, this kind of model should include the effects of environmental factors on cell migration other than mechanical cues, such as chemical conditions or fluid flow. Although these processes may be interrelated in reality, their isolation is useful to study their individual effects on cell behavior.

With this purpose, a phenomenological probabilistic voxel FE model for single cell migration in 3D was developed. Through a set of probability functions and combining different software, the model was able to compute cell migration taking into account different environmental factors such as mechanical properties of the ECM, chemical gradients, flow and boundary conditions. In fact, to study the fluid-chemical conditions surrounding a cell embedded in a porous medium, a real micro-fluidic device was simulated using FEM. Then, these results were extracted and interpolated into a finer mesh composed of voxels where the mechanical analysis and the migration were computed. While particle-based approaches are useful for detailed analysis, phenomenological laws are necessary to study longer time and length scales. By discretizing both the ECM and the cell body with voxels, and considering that each cell-voxel follows the *mechanosensing* behavior described in previous chapters, the model was able to predict macroscopic aspects of cell migration such as trajectories, velocities, adhesion area, cell aspect ratio, cell stresses etc, for times scales of the order of hours. Additionally, by defining the individual behavior of each of the cell constituents (voxels) through probability functions, the macroscopic behavior emerged naturally. Furthermore, these tunable functions allowed controling the relative weight of each input factor (mechanics, flow and chemistry) as well as including new factors that may affect cell migration. Migration was computed assuming both continuum and porous ECMs.

Compared with a continuum approximation, a porous ECM geometry affected cell

migration, guiding the cell through the pores and modifying the mechanosensing process. Although a continuum ECM was enough to capture general migratory trends, considering contact guidance and hydrostatic pressure among other factors, would be necessary for more realistic simulations of 3D cell motility. In short, a methodology for testing and designing new experiments was here established; being in particular useful for simulating ongoing microfluidic systems and the study of several basic biological functions such as cell migration, angiogenesis, or organ formation. Additionally, the modular form of the model permits it to be constantly updated and redefined as research advancements shed new lights on cell behavior.

The models and approaches used during this Thesis have been mainly focused on cell response to external stimuli, however, internal conditions are equally important modulating cell activity. For instance, cell migration and exploratory motions proceed by cycles of edge protrusion and retraction driven by actin polymerization pushing against the membrane. In turn, this produces a retrograde actin flow that influences FA formation and maturation that bind the CSK to the substrate and determine the cell-matrix interactions and therefore the migration. Hence, a continuum approach for modeling lamellipodium dynamics and the role of vinculin engaging rearward actin flow has been developed. Basing the main assumptions on experimental observations and using parameters with physical meaning, the model was able to predict general behaviors of lamellipodium dynamics such as protrusion/retraction cycles or periodic myosin activation, and more specific effects such as the decrease of membrane speed and increase of the retraction period when polymerization is inhibited or the increase of contraction duration when myosin activity is reduced. Apart from reproducing experimental results, the model was useful to predict untested phenomena and design new experiments. For example, the initial model hypotheses were not enough to reproduce at the same time the increase of membrane and actin speeds and the widening of the lamellipodium when knocking out vinculin, thus suggesting that other conditions different from the FA friction might be altered. Assuming that the polymerization increases while the total amount of actin remains constant, allowed reproducing the effects on Vcl-KO cells. This assumption was later supported by further experiments where reduced phalloidin fluorescence intensity within lamellipodia lacking vinculin was qualitative observed, or where the quantification of the distribution of the actin-binding lamellipodium marker-protein cortactin across fluorescence intensity linescans through the lamellipodium confirmed a reduced peak intensity in the absence of vinculin. The model used a finite-differences

method in 1D, where the lamellipodium was discretized in length and time. Thus, the computational cost was notably low, allowing really fast simulations (of the order of minutes) at the expense of details and the use of averaged values. This simple approach will facilitate its possible incorporation into more complex models. For instance, the combination of the current model with particle-based of finite element methods (where each particle or element behaved following the model equations) would allow for very detailed simulations in 3D migrating cells. Additionally, different algorithms based on matrix convolution and function correlation were developed to measure lamellipodium dynamics from our own experiments. Using hand-coded scripts instead of commercial software allowed a complete control and the adaptation of the routines depending on necessities. With these codes, actin and membrane speeds, their correlation, the periodicity of contractions and phase delay between actin and membrane evolution were measured. Results confirmed the general trends observed in previous works and provided new findings regarding the periodicity of actin and membrane retraction cycles as well as the phase delay between both curves. In fact, knocking out vinculin produced increased speeds of actin rearward flow compared to the rest of cases. WT and PA cells showed slower actin velocities whereas dAB and PAdAB cells presented intermediate speeds, suggesting that actin-vinculin interaction is critical to engage lamellipodial actin flow. This, together with the low variability of periods, supports the observation that a decrease of friction produces larger lamellipodiums and higher speeds while the periodicity of contractions is not affected, so that the period of contractions can be considered proportional to the lamellipodium width and inversely proportional to the actin flow velocity. A high percentage of all the analyzed cells (73%) showed negative phase delays (0 to -90º) between actin and membrane speed curves, meaning that overall, the membrane movements follow the actin. Since this finding has not been reported yet in other research works, further experiments with these and other type of cells would be necessary to confirm it.

## 7.2. Conclusions

The main conclusions of this Thesis are grouped by chapters and can be summarized as follows:

- *Mechanosensing* and cell migration modeling in 3D

1. *Mechanosensing* is one of the main regulatory mechanisms to direct cell movement. Mechanical cues alone such as ECM stiffness or boundary conditions may be enough to drive cell migration.
2. The *mechanosensing* behavior of the whole cell body can be simplified to two springs in parallel and a contractile actuator in series (which is equivalent to a third pre-compressed spring). This simple scheme, while still subject to further improvement, implies the increase of cell exerted stress with ECM stiffness until saturation.
3. Actin stiffness is one of the major factors controling cell *mechanosensing* response. In a complex structure such as the cell's CSK, mainly composed of actin filaments, the organization and adaptation of its components to external conditions determine cell behavior. To properly understand these mechanisms, a simple approach is not enough and hence a more detailed modeling of actin networks taking into account their main constituents becomes necessary.
4. Cells contract their surroundings to test the ECM compliance. The simulations suggest that the cell may not actually feel forces, but the spatial stretching or compression caused in the ECM by itself or external loads.

- Modeling of cross-linked actin networks dynamics
  1. At least two structural components are necessary to simulate actin networks: actin filaments and actin cross-linkers. By only including the dynamics of molecular motors and ACPs, the simulated actin network exhibits macroscopic contractile behaviors similar to experiments, suggesting that microscopic properties of individual constituents are capable of simulating the network responses.
  2. According to this model, molecular motors play a central role in *mechanosensing*. Among all the studied factors, those affecting motor dynamics were the most influential in network behavior.
  3. Cell-generated stress is proportional to ECM stiffness for compliant substrates and becomes relatively constant (saturates) for stiffer ECMs. The existence of a transition to a slower rate of stress increase can be explained by the mechanisms that cause the motors to slow or stall: (i) all of the next binding sites in a barbed-end direction are already occupied (blocking), (ii) reaching the motor stall force, or (iii) reaching the barbed end of an actin filament. This

transition from blocking to limitation due to motor stall force constitutes a mechanism by which cells can sense substrate stiffness.

4. Agent-based computational models are very useful to study in detail a wide variety of actin-related phenomena such as *mechanosensing* or others such as CSK stiffening/softening, creep network response or ring formation in cytokinesis among others. However, computational costs are extremely high even using parallelized approaches, making them unsuitable for simulating the whole CSK.

- Time-dependence of *mechanosensing* processes
  1. Time-dependence is essential for capturing realistic cell *mechanosensing* processes. Introducing an internal variable representing the evolution of motor stalling into a mechanical model is enough to reproduce experimental results, allowing simulations lasting seconds instead of weeks, and thus making the approach suitable to be included in finite element models with longer time and length scales. Nevertheless, except for specific (and non-biological) conditions such as sudden changes of substrate stiffness, the long term *mechanosensing* response of cells is governed by the saturation of forces determined by the mechanical equilibrium.
  2. Motor stalling increases exponentially until saturation with a relaxation time independent of substrate stiffness. Although experimentally it was found that relaxation was substrate-dependent at short time scales, the model confirmed that such dependence is negligible for the long term.
  3. The *mechanosensing* behavior of the whole cell body can be represented with two springs in parallel and a contractile actuator in series, equivalent to a third pre-stressed spring whose equilibrium length is brought to zero through a decay clock.
  4. This three-spring configuration allows distinguishing between active and passive responses of the cell, permiting to capture the linearity of cell force with respect to substrate stiffness for compliant substrates, and its saturation for higher rigidities, and allowing the simulation of more complex phenomena such as stress-fiber rigidization, network disruption etc.

5. Cell reaction to sudden changes in substrate stiffness occurs almost instantaneously, suggesting that the CSK adaptation is a purely mechanistic process.

- Modeling 3D cell migration depending on multiple environmental factors
  1. Phenomenological laws are adequate to study long time and length scales. Discretizing both the ECM and the cell body with voxels, and considering that each cell-voxel follows the *mechanosensing* behavior described in previous chapters, is sufficient to study macroscopic aspects of cell migration such as trajectories, velocities, adhesion area, cell aspect ratio, cell stresses etc for times scales of the order of hours.
  2. By defining the individual behavior of each of the cell constituents (voxels) through probability functions, the macroscopic behavior emerges naturally.
  3. The consideration of the cell body in a full microdevice simulation does not affect the overall fluid-chemical results. Therefore, except when modeling cell populations, the cell body can be neglected and the steady state solution can be assumed throughout the mechanical and migration simulations, permitting to decouple the calculations and saving computational efforts. Nevertheless, due to the usually irregular geometry of the cell body, the effect of the fluid flow and chemical concentrations along the cell surface should be taken into account for a proper detailed consideration of such factors.
  4. Compared with a continuum approximation, a porous ECM geometry affects cell migration, guiding the cell through the pores and modifying the *mechanosensing* process. Although a continuum ECM is enough to capture general migratory trends, considering contact guidance and hydrostatic pressure among other factors, would be necessary for more realistic simulations of 3D cell motility.

- Simulating lamellipodium dynamics and effects of FAs
  1. A continuum 1D approach for modeling lamellipodium dynamics and the role of vinculin engaging rearward actin flow is suitable to predict general behaviors of cell exploratory motions such as protrusion/retraction cycles or periodic myosin activation, and more specific effects such as the decrease of

membrane speed and increase of the retraction period when polymerization is inhibited or the increase of contraction duration when myosin activity is reduced.

2. Matrix convolution and function correlation are powerful mathematical tools that can be applied to measure lamellipodium dynamics from experiments via image treatment.
3. Knocking out vinculin alters the friction and the polymerization conditions at the lamellipodium. Assuming that the polymerization increases while the total amount of actin remains constant, allows reproducing the effects on Vcl-KO cells.
4. Knocking out vinculin produces increased speeds of actin rearward flow compared to the rest of studied cases. WT and PA cells show slower actin velocities whereas dAB and PAdAB cells present intermediate speeds suggesting that actin-vinculin interaction is critical to engage lamellipodial actin flow.
5. A decrease of friction produces larger lamellipodiums and higher speeds while the periodicity of contractions is not affected. Hence, the period can be considered proportional to the lamellipodium width and inversely proportional to the actin flow velocity.
6. Overall, the membrane movements follow the actin. Since this finding has not been reported yet in other research works, further experiments with these and other type of cells would be necessary to confirm it.

## 7.3. Original contributions

The foremost original contributions of this Thesis are the following:

- Formulation of a 3D migration model based on *mechanosensing*, that is to say, depending on ECM mechanical properties, loads and boundary conditions.
- 3D FE numerical simulations to determine cell migratory patterns, forces and speeds for different constrains and external forces.

- Adaptation of an agent-based Brownian dynamics computational model to study the dynamic mechanics of rigidity-sensing in a cross-linked actin network via particle-interaction simulations.

- Extension of the *mechanosensing* hypothesis to include the time-dependent response in a macroscopic approach of the active mechanical behavior of the cell, analyzing the influence of mechanical parameters and studying the system response to sudden changes in substrate stiffness.
- Development of a phenomenological probabilistic voxel FE model for single cell migration in 3D taking into account several factors that affect cell migration: mechanics, fluid flow and chemistry.
- 3D FE simulations of a microfluidic system to determine flow and chemical gradients through a porous material.
- Formulation of a continuum model to describe lamellipodium dynamics and study the influence of FAs in actin rearward flow.
- Adaptation of a tool to measure actin flow and cell membrane movement from speckle microscopy images and development of a methodology to analyze retraction periodicity and correlation between actin and membrane speeds.
- Analysis of the effect of several drugs inhibiting or enhancing polymerization, myosin activity as well as alteration of FAs strength via vinculin knocking out.

### 7.3.1. Publications in peer-reviewed journals

The publications on international journals achieved during the Thesis period are listed below:

1. **BORAU, C.**, KAMM, R.D. & GARCÍA-AZNAR, J.M. 2011. Mechano-sensing and cell migration: a 3D model approach. *Physical Biology*, 8, 066008.
2. **BORAU, C.**, KIM, T., BIDONE, T., GARCIA-AZNAR, J.M. & KAMM, R.D. 2012. Dynamic mechanisms of cell rigidity sensing: insights from a computational model of actomyosin networks. *PLoS One*, 7, e49174.
3. **BORAU, C.**, GARCIA-AZNAR, J.M. & KAMM, R.D. 2013. A time-dependent phenomenological model for cell mechano-sensing. *(Under review)*

4. **BORAU, C.**, POLACHECK, W.J., GARCIA-AZNAR, J.M. & KAMM, R.D. 2013. Probabilistic voxel-FE model for single cell motility in 3D *(In process)*
5. **BORAU, C.**, THIEVESSEN, I., GARCIA-AZNAR, J.M. & FABRY, B. 2013. Modeling lamellipodium dynamics and effects of vinculin on rearward actin flow. *(In process)*.

### 7.3.2. Congress and conference contributions

The following communications have been presented during the development of this Thesis:

1. **BORAU, C**., DOWEIDAR, M.H., GARCÍA-AZNAR, J.M., Mechanosensing and Cell Migration: 3D modeling. *XXVIII Congreso Anual de la Sociedad Española de Ingeniería Biomédica (CASEIB)*, Madrid (Spain) 2010.
2. GARCÍA-AZNAR, J.M., **BORAU, C**., KAMM, R. D., Three-Dimensional modelling of cell migration due to active mechanosensing. *TERMIS-EU*, Galway (Ireland), 2010.
3. GARCÍA-AZNAR, J.M., **BORAU, C**., KAMM, R. D., Modeling of cell migration and mechano-sensing in 3D. *17th Congress of the European Society of Biomechanics (ESB)*, Edinburgh (UK), 2010
4. **BORAU, C.**, KAMM, R. D., KIM, T, GARCÍA-AZNAR, J.M., Exploring Rigidity Sensing and Acto-myosin based Contractility: a 3-D Actin Network Computational Model. *4th European Cell Mechanics Meeting (CellMech)*. Amsterdam (Netherlands) 2011.
5. GARCÍA-AZNAR, J.M., **BORAU, C.**, KAMM, R. D., Modelling mechanosensing in cell-material interaction: implications for tissue engineering. *TERMIS-EU Annual Meeting*, Granada (Spain), 2011.
6. **BORAU, C.**, KAMM, R. D., KIM, T, GARCÍA-AZNAR, J.M., Computational Model of 3-D Cross-linked Actin Networks: mechanosensing behaviour of cells. *II International Conference on Particle-based Methods. Fundamentals and Applications (PARTICLES)*. Barcelona (Spain), 2011.
7. GARCÍA-AZNAR, J.M., **BORAU, C.**, KIM, T, KAMM, R. D., Computational Model of 3-D Cross-linked Actin Networks: Mechanosensing Behaviour of Cells. *II International conference on particle based methods Fundamentals and applications (PARTICLES)*, Barcelona (Spain), 2011.

8. GARCÍA-AZNAR, J.M., **BORAU, C.**, KAMM, R. D., Models of cell migration: implications for tissue engineering. *II International Conference on Tissue Engineering (ICTE)*, Lisbon (Portugal), 2011.
9. **BORAU, C.**, KAMM, R. D., KIM, T, GARCÍA-AZNAR, J.M., Acto-myosin system Contraction: computational study of 3D actin networks and their response to extracellular matrix stiffness. *I Reunión del Capítulo Nacional Español de la Sociedad Europea de Biomecánica (ESB-Cap Esp)*, Zaragoza (Spain), 2011.
10. KAMM, R. D., **BORAU, C.**, KIM, T, GARCÍA-AZNAR, J.M., Computational insights into cytoskeletal rheology. *Biophysical Society Meeting*, Baltimore, MD, (USA), March, 2011.
11. KAMM, R. D., **BORAU, C.**, KIM, T, GARCÍA-AZNAR, J.M., Computational models of the cytoskeleton and a look forward to simulation of mechanotransduction. *Microscale Modeling in Biomechanics and Mechanobiology*, Ericeira (Portugal), 2011.
12. KAMM, R. D., **BORAU, C.**, KIM, T, GARCÍA-AZNAR, J.M., A Computational, Brownian Dynamics Simulation of Cytoskeletal Mechanics, *The 1st KIAS Conference on Subcellular Dynamics*, Seoul (Korea), 2011.
13. KAMM, R. D., **BORAU, C.**, KIM, T, GARCÍA-AZNAR, J.M., The unique biomechanical properties of the cell: Insights from computational modeling. *Nanyang Technological University*, 2011.
14. **BORAU, C.**, KAMM, R. D., KIM, T, GARCÍA-AZNAR, J.M., Cell cytoskeleton dynamics: mechanosensing properties. *I3A -Jornada de jóvenes investigadores*, Zaragoza (Spain), 2012.
15. GARCÍA-AZNAR, J.M., **BORAU, C.**, KIM, T, KAMM, R. D., Mechanosensing: from a discrete to a continuum approach. *8th European Solid Mechanics Conference*, Graz (Austria), 2012.
16. **BORAU, C.**, KAMM, R. D., GARCÍA-AZNAR, J.M., Computational model of 3D single cell migration: a mechano-chemical approach. *18th Congress of the European Society of Biomechanics (ESB)*, Lisbon (Portugal), 2012.
17. KAMM, R. D., **BORAU, C.**, KIM, T, GARCÍA-AZNAR, J.M., Biomechanical properties of the cell: Insights from computational modeling. *Society of Physical Regulation and Biomolecular Modeling*, San Juan (Puerto Rico), 2012.

18. KAMM, R. D., **BORAU, C.**, KIM, T, GARCÍA-AZNAR, J.M., The unique biomechanical properties of the cell: Insights from computational modeling. *Worcester Polytechnic Institute (WPI)*, Worcester, MA (USA), 2012.
19. KAMM, R. D., **BORAU, C.**, KIM, T, GARCÍA-AZNAR, J.M., The unique biomechanical properties of the cell: Insights from computational modeling. *International Federation for Medical & Biological Engineering (IFMBE)*, Beijing (China), 2012.
20. GARCÍA-AZNAR, J.M., **BORAU, C.**, BIDONE, T., KIM, T, KAMM, R. D., Modeling 3D actin networks: dynamics of cell mechanosensing. *III International Conference on Particle-based Methods Fundamentals and Applications*, Stuttgart (Germany), 2012
21. **BORAU, C.**, THIEVESSEN, I. GARCÍA-AZNAR, J.M., FABRY, B., Lamellipodium dynamics and rearward actin flow depend on vinculin. *19th Congress of the European Society of Biomechanics (ESB)*, Patras (Greece), 2013. (Candidate to the ESB Student Awards)

## 7.4. Future lines of work

The variety of approaches presented in this Thesis is only a small contribution to the understanding of cell behavior. Results and conclusions obtained throughout this work raise new questions and suggest possible lines of research that need to be explored. The most important can be listed as follows:

- Extension of individual cell migration models to simulate cell populations

  Single cell migration models presented in Chapter 2 and 5 are useful for isolating effects of specific parameters influencing cell migration, however, cell-cell interactions give rise to complex changes in multicellular tissue structures and processes, including epithelial regeneration or angiogenesis. Hence, the incorporation of such intercellular interactions would extend enormously the potential of the models. Although some technical issues should be considered, the present approaches are ready to incorporate larger populations of cells.

- Study of additional actin structures relevant for cell behavior.

There exist many actin structures involved in different cell processes that can be studied with the Brownian dynamics model described in Chapter 3. For instance, stress fibers (consisting of actin filaments cross-linked with proteins and myosin II motors) are essential to distribute cell forces along the CSK, and play an important role in cell contractility and morphogenesis. The development of realistic myosin minifilaments (instead of the kinetic adaptation of myosin V) would be required to properly study the stress fiber formation. Also, contractile actin rings appearing in Cytokinesis (the cytoplasm division during cell proliferation) could be objective of modeling. In these rings, myosin II constricts the cell membrane forming a cleavage furrow until abscission occurs. Hydrolysis of ATP and microtubule structures should be incorporated to analyze this phenomenon. Additionaly, actin arcs at the leading edge serve as structural elements where nascent focal adhesion mature and form the base for the protrusion events that take place in cell exploratory motions. Combining the particle-based model with the theoretical assumptions described in Chapter 6, would allow a very detailed analysis of cell lamellipodium dynamics.

- Enhacement of cell-ECM interactions

  Cell-matrix interactions are mediated via transmembrane receptors (integrings) and focal adhesions, acting as signal transductors and presenting complex and dynamic behaviors. Their detailed modeling has not been considered in the models described in this Thesis. For instance, in the migration model presented in Chapter 5, the whole cell surface is considered adhered to the ECM, and therefore all the perimeter elements extert contractile forces. In reality, only some parts of the cells are attached to the substrate and only some of those parts include strong focal adhesion complexes able to exert noticeable forces. Hence, a detailed modeling of focal adhesion maturation would be required to fully understand their role in cell motility. Furthermore, mechanisms such as actin polymerization or internal hydrostatic pressure, especially importants when ECM pores are small, have neither been included and should be accounted to properly simulate 3D cell migration.

- Distinguishing cell parts

  In the 3D simulations of Chapter 3 and Chapter 5, three different parts of the cell body are considered: nucleous, cytoplasm and cortex. They are roughly mimicked by varying the developed stress or deactivating the contractile behavior in the case of the nucleus. This was done for simplicity and indeed to prepare the codes for future development, however, the complex behavior of the CSK could be better reflected in several ways. For instance the actin stiffness could be related with actin polymerization (or with actin density) usually more prominent at the cell edge. Also, the concentration of ACPs would determine the strength of the network links, therefore affecting the global rigidity. In the same way, the concentration of myosin would influence the maximum force exerted at each cell zone, and the distribution of FAs would determine whether such force is transmitted to the ECM or absorbed by the CSK passive components.

- Use of realistic cell and ECM geometries

  Voxel approaches are useful to study general trends of cell behavior with large length and time scales, however, important details may be lost with the simplifications. For instance, cell membrane curvature may trigger cell polymerization in specific parts, driving the advance of filopods and other exploratory structures and regulating the tension that produces the rearward actin flow at the lamellipodium. A model using surface finite elements could combine the advantages of FE meshes (reliable and fast calculations) preserving the details of the irregular curvature of the cell membrane.

- Include formation and maturation of FAs in the lamellipodium model

  While continuum approaches allow for fast simulations to investigate general trends, detailed modeling becomes necessary to analyze complex phenomena such as the FA formation and maturation during lamellipodium protrusion/retraction cycles. This process is critical since mature FAs form a firm basis at the lamella border, allowing the protrusion by slowing down the actin flow and transmitting forces to the substrate. Hence, the explicit incorporation of FAs formation

depending on actin speed and/or density, substrate stiffness or other parameters such as protein concentration would provide more accurate results.

- Combine continuum approaches with particle-based or FE methods

  The main handicap of the continuum 1D approach describing lamellipodium dynamics is the lack of details and the use of averaged variables. However, its simplicity permits a very easy combination of the model with particle-based or FE approximations, allowing complex simulations in 3D with reasonable computational costs. Hence, a cell model incorporating *mechanosensing* features (as described in previous chapters) and whose mechanical properties depend on evolving parameters such as actin or FA concentration, polymerization, myosin activation etc. would be a very interesting and detailed approach that would allow studying phenomena both at the micro and macro scales at once.

# A

# APPENDIX A: SOME COMPUTATIONAL ALGORITHMS

This appendix describes some unusual algorithms, not commonly used in computation neither included in commercial software. The codes developed for this Thesis are extense and heterogeneous, so only a minimal part is compiled here for specific interest or just for curiosity. In addition, some methods used in the Thesis that were not fully described in the corresponding chapter to facilitate the reading, are extended here.

## A.1 Finding a point inside an irregular hexahedron

Chapter 2 develops a 3D migration approach where a cell changes its position ($\mathbf{x}_{\text{cell}}$) during the simulation. The model uses FEM to obtain the displacement/strain/stress field produced by the contractile cell embedded on a tridimensional matrix. Hence, the element containing the cell needs to be known at the beginning of each step. For simplicity, a domain meshed with regular hexahedrons was used in the simulations, however, the main code allows working with irregular meshes as long as the elements have 8 nodes. For this reason, a script able to find a point ($\mathbf{x}_{\text{cell}}$) inside an irregular hexahedron was developed.

To compute the mechanical problem, a FEM software (ABAQUS) and a user subroutine are used. Specifically, the subroutine UEL permits to describe each element behavior by defining its mechanical properties and the desired shape functions. One of the UEL's peculiarities is that it goes through all the mesh elements (one by one), building the global stiffness matrix and computing the displacements until the equilibrium is reached. Thus, the point-finder script needs to take this into account.

First, when the main code (the UEL) enters each element (lets call it JELEM using ABAQUS nomenclature), it checks if the cell is inside the limits of a sphere of radius $d_s$, which is the length of the longest diagonal of the hexahedron (Figure A.1A). If not, the

UEL skips all the code related with the cell behavior and considers the JELEM element as ECM. This fast checking saves enormous amount of computational time, especially with very refined meshes. Nevertheless, if the cell is found within the sphere, it still may be inside or outside the hexahedron. Therefore, a second check is performed. In this procedure, the intersection (if existing) of the direction joining $\mathbf{x}_{\text{cell}}$ with the element centroid ($\mathbf{x}_{\text{JELEM}}$) and the 6 planes forming the hexahedron is calculated ($\mathbf{x}_{\text{int}}^{i}$). From all the intersections found, the closest to $\mathbf{x}_{\text{cell}}$ is selected ($\mathbf{x}_{\text{int}}^{\text{closest}}$). Note that only the intersections in the same direction that the vector joining the cell and the element centroid can be candidates, that is to say, if $\mathbf{x}_{\text{cell}}-\mathbf{x}_{\text{int}}^{\text{closest}}$ forms 0 degrees with $\mathbf{x}_{\text{cell}}-\mathbf{x}_{\text{JELEM}}$, $\mathbf{x}_{\text{int}}^{\text{closest}}$ is valid. Otherwise, if the angle is 180 degrees, $\mathbf{x}_{\text{int}}^{\text{closest}}$ is invalid. Then, the script checks whether the distance from the cell to the intersection ($d_{\text{cell-int}}=\left\|\mathbf{x}_{\text{cell}}-\mathbf{x}_{\text{int}}^{\text{closest}}\right\|$) is higher or lower than the distance from the cell to the element centroid ($d_{\text{cell-JELEM}}=\left\|\mathbf{x}_{\text{cell}}-\mathbf{x}_{\text{JELEM}}\right\|$). If $d_{\text{cell-int}}<d_{\text{cell-JELEM}}$, it means that the cell is outside the hexahedron, otherwise the cell is inside (Figure A.1B). The decision tree is shown in . Obviously if the cell is finally found in a specific element, the UEL does not search it in the remaining elements in the current step.

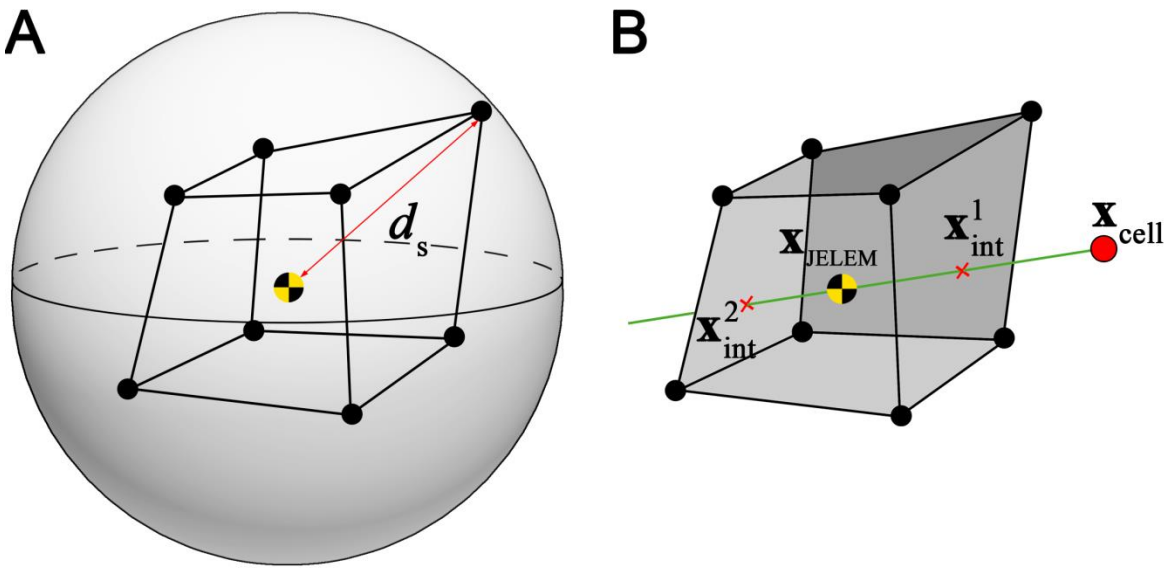


**Figure A.1:** Point-finder script scheme.
A) Preliminar checking to ensure that the cell is within a sphere around the element. B) Plane-intersection method to elucidate whether the cell is inside or outside the hexahedron.

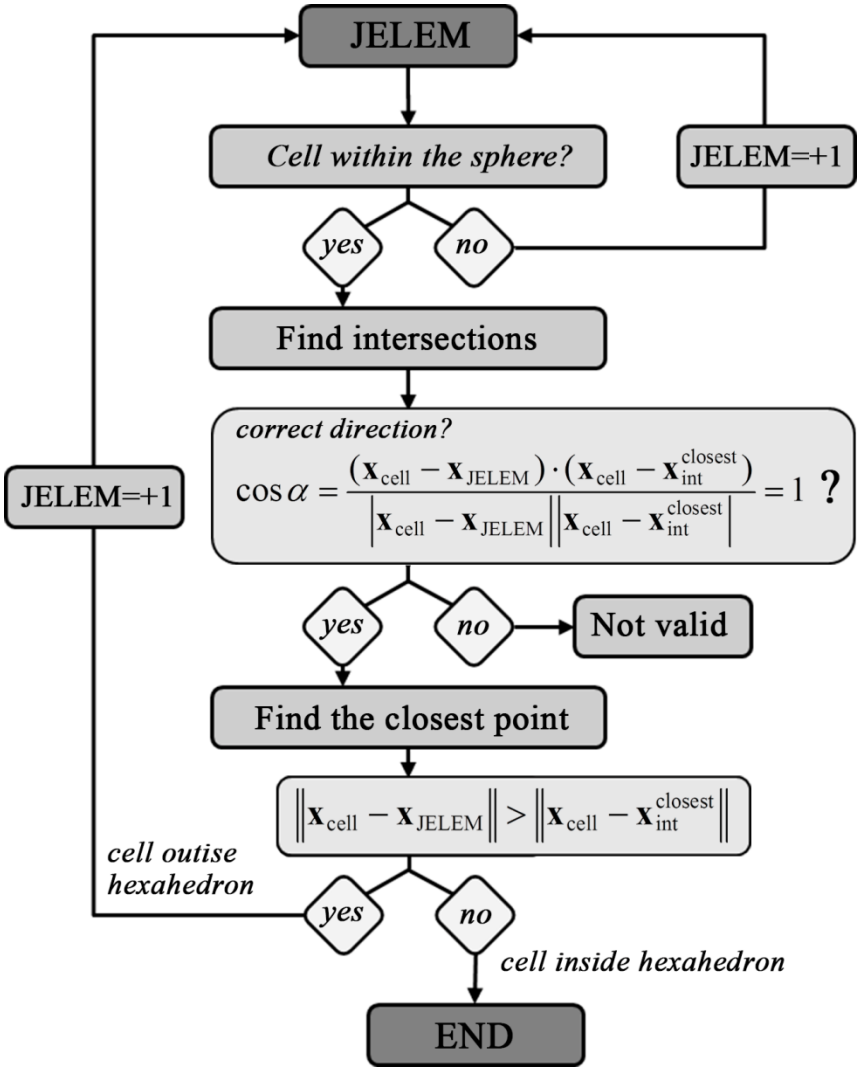


**Figure A.2:** Decision tree of the point-finder script.

## A.2 Computing cell orientation using FE shape functions

The cell's CSK orientation described in Chapter 2 is assumed to depend on the direction of minimum cell strain. However, solving the system to find the principal strain directions $(\boldsymbol{\varepsilon} - \lambda_i \mathbf{I})\mathbf{d}_{\varepsilon i} = 0$ does not define the + or – direction of $\mathbf{d}_{\varepsilon}$. Hence, it becomes necessary an additional calculation to compute the migration direction, or more specifically in which direction the cell centroid moves (that is the criterion chosen as described in the migration model and schematically showed in 1D in Figure 2.3B).

In a cubical hexahedron element of 8 nodes (C3D8) the shape functions (*N*) are described as follows:

$$N_i = \frac{1}{8}\left(1+\xi\xi_i\right)\left(1+\eta\eta_i\right)\left(1+\tau\tau_i\right) \tag{A.2.1}$$

where $\xi$, $\eta$, $\tau$ are the coordinates in the natural system of the element (from 0 to 1). The shape function matrix is therefore built:

$$\mathbf{N} = \begin{bmatrix} N_1 & 0 & 0 & N_2 & 0 & 0 & ... & N_8 & 0 & 0 \\ 0 & N_1 & 0 & 0 & N_2 & 0 & ... & 0 & N_8 & 0 \\ 0 & 0 & N_1 & 0 & 0 & N_2 & ... & 0 & 0 & N_8 \end{bmatrix} \tag{A.2.2}$$

and permits the projection of any variable from the nodes to any point of the element:

$$\mathbf{x}\left(x,y,z\right) = \mathbf{N}\left(\xi,\eta,\tau\right)\mathbf{x}_{\text{nod}}\left(x,y,z\right) \tag{A.2.3}$$

The model defines two points ($\mathbf{p}_1, \mathbf{p}_2$) proximal to the element centroid ($\mathbf{x}_{\text{JELEM}}$) and contained in the direction of minimum strain ($\mathbf{d}_\varepsilon$):

$$\begin{aligned} \mathbf{p}_1\left(x,y,z\right) &= \mathbf{x}_{\text{JELEM}} + \frac{\mathbf{d}_\varepsilon}{m} \\ \mathbf{p}_2\left(x,y,z\right) &= \mathbf{x}_{\text{JELEM}} - \frac{\mathbf{d}_\varepsilon}{m} \end{aligned} \tag{A.2.4}$$

where *m* is an arbitrary constant defining the proximity. These points are defined in the global coordinate system but needed in the natural one. Hence, the equation (A.2.3) is solved using a Newton-Rhapson approach to find the corresponding $\xi$, $\eta$, $\tau$ values.

Once the points are defined in the natural system, the displacements are projected from the element nodes onto the calculated points.

$$\begin{aligned} \mathbf{u}_{\text{p1}} &= \mathbf{N}\left(\xi_{\text{p1}},\eta_{\text{p1}},\tau_{\text{p1}}\right)\mathbf{u}_{\text{nod}} \\ \mathbf{u}_{\text{p2}} &= \mathbf{N}\left(\xi_{\text{p2}},\eta_{\text{p2}},\tau_{\text{p2}}\right)\mathbf{u}_{\text{nod}} \end{aligned} \tag{A.2.5}$$

In turn, these displacements are projected on the minimum strain direction ($\mathbf{u}_{\text{p1}}^{d\varepsilon} = \left|\mathbf{u}_{\text{p1}}\right|\cos(\theta)$, where $\theta$ is the angle between $\mathbf{u}_{\text{p1}}$ and $\mathbf{d}_\varepsilon$). The point with minimum displacement will define the movement of the cell centroid in minimum strain direction,

and therefore the cell front. Note that the displacement of the centroid is not directly calculated (using $\xi = \eta = \tau$ =0.5) to avoid rare cases where $\mathbf{u}_{\text{JELEM}}$ is completely perpendicular to $\mathbf{d}_{\varepsilon}$.

## A.3 Cell aspect ratio using voxels

Cell aspect ratio or shape factor indicates the extent of cell's body elongation during migration. The voxelization approach used in the model described in Chapter 5 permits the computation of this factor even when the cell presents very irregular shapes with numerous protuberances or exploring arms.

Knowing the geometrical distribution, the computation of the aspect ratio is equivalent to the finding of the minimum and maximum inertia directions:

$$\text{AR}_{\text{cell}} = \frac{d_{\min \text{I}}}{d_{\max \text{I}}} \tag{A.3.1}$$

where $d_{\max \text{I}}$ and $d_{\min \text{I}}$ correspond to maximum distances separating cell voxels measured in the direction of maximum and minimum inertia respectively (Figure A.3).

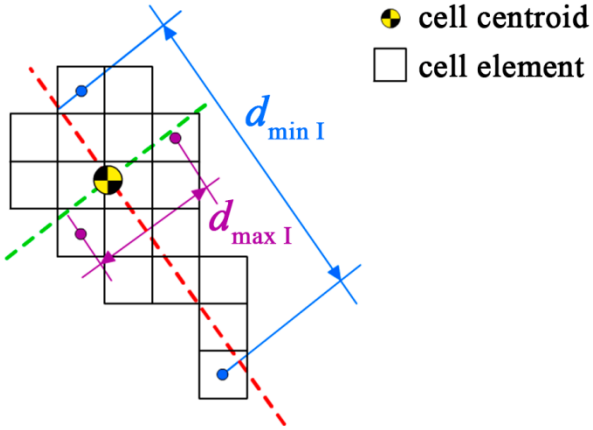


**Figure A.3:** Geometric scheme of cell aspect ratio calculation. The distance between the most separated voxels projected on the direction of minimum/maximum inertia determines $d_{\min \text{I}}$ and $d_{\max \text{I}}$ respectively. The fraction of these quantities defines the cell aspect ratio and gives an idea of the cell's elongation.

Therefore, to obtain the principal inertia directions, the inertia tensor $\mathbf{I}_{\text{m}}$ must be defined:

$$\mathbf{I}_{\text{m}} = \begin{pmatrix} I_{xx} & I_{xy} & I_{xz} \\ I_{yx} & I_{yy} & I_{yz} \\ I_{zx} & I_{zy} & I_{zz} \end{pmatrix} \tag{A.3.6}$$

where

$$\begin{aligned} I_{xx} &= \int_V \rho(y^2+z^2)dxdydz \qquad I_{xy} = I_{yx} = \int_V -\rho(xy)dxdydz \\ I_{yy} &= \int_V \rho(x^2+z^2)dxdydz \qquad I_{xz} = I_{zx} = \int_V -\rho(xz)dxdydz \\ I_{zz} &= \int_V \rho(x^2+y^2)dxdydz \qquad I_{yz} = I_{zy} = \int_V -\rho(yz)dxdydz \end{aligned} \tag{A.3.3}$$

and particularized for a cube of edge *a* and mass density $\rho$:

$$\begin{aligned} I_{xx} &= I_{yy} = I_{zz} = \frac{1}{12}a^3\rho(a^2+a^2) = \frac{1}{6}\rho a^5 \\ I_{xy} &= I_{yx} = I_{xz} = I_{zx} = I_{yz} = I_{zy} = 0 \end{aligned} \tag{A.3.4}$$

Since all the voxels are exactly equaly sized, equal voxel mass is assumed. Therefore, knowing the inertia tensor of a single voxel, the global inertia tensor for the whole cell body can be determined through the Steiner Theorem:

$$\begin{aligned} I_{xx\_\text{cell}} &= \sum_{i=1}^{n}\left(I_{xx\_i} + M\left((y_i - y_{CG})^2 + (z_i - z_{CG})^2\right)\right) \\ I_{yy\_\text{cell}} &= \sum_{i=1}^{n}\left(I_{yy\_i} + M\left((x_i - x_{CG})^2 + (z_i - z_{CG})^2\right)\right) \\ I_{zz\_\text{cell}} &= \sum_{i=1}^{n}\left(I_{zz\_i} + M\left((x_i - x_{CG})^2 + (y_i - y_{CG})^2\right)\right) \\ I_{xy\_\text{cell}} &= \sum_{i=1}^{n}\left(I_{xy\_i} - M\left((x_i - x_{CG}) + (y_i - y_{CG})\right)\right) \\ I_{xz\_\text{cell}} &= \sum_{i=1}^{n}\left(I_{xz\_i} - M\left((x_i - x_{CG}) + (z_i - z_{CG})\right)\right) \\ I_{yz\_\text{cell}} &= \sum_{i=1}^{n}\left(I_{yz\_i} - M\left((y_i - y_{CG}) + (z_i - z_{CG})\right)\right) \end{aligned} \tag{A.3.5}$$

where *n* is the number of individual voxels, *M* is the mass of each voxel and CG stands for the centre of gravity of the cell, calculated geometrically:

$$\mathbf{x}_{CG} = \frac{\sum_{i=1}^{n} \mathbf{x}_{CG\_i}}{n} \tag{A.3.7}$$

After the calculation of $\mathbf{I}_{\mathrm{m}}$, the principal directions of inertia are computed solving $(\mathbf{I}_{\mathrm{m}} - \lambda_i \mathbf{I})\mathbf{d}_i = 0$ (note that $\mathbf{I}$ is the identity tensor), therefore obtaining $\mathbf{d}_{\mathrm{p}}$ and $\mathbf{I}_{\mathrm{p}}$:

$$\mathbf{I}_{\mathrm{p}} = \begin{pmatrix} I_1 & 0 & 0 \\ 0 & I_2 & 0 \\ 0 & 0 & I_3 \end{pmatrix} \tag{A.3.8}$$

where $I_1$ and $I_3$ are the inertia values in the directions of maximum ($d_{\max \mathrm{I}}$) and minimum ($d_{\min \mathrm{I}}$) inertia respectively.

## A.4 Building a porous mesh

Extracting the real geometry from a porous material is a hard task even with the latest techniques of image processing. In addition, it is difficult to control and measure important features of these materials such as the porosity and the pore size of a specific region.

For this purpose, a voxel-mesh generator script was developed to build "porous-meshes" in order to roughly mimic a 3D porous geometry. This MATLAB script is able to construct meshes of the desired voxel-size, with the desired porosity and mean pore size. For the simulations performed in Chapter 5 of this Thesis, a box-like domain of (300×300×120 μm) was used.

First, the script generates a full voxelized mesh of the desired size. Then, it makes an initial hole at the domain center where the cell will be placed in the migration simulations. Next, spherical-like holes of minimum size 1 voxel and maximum size $p_{\mathrm{s}}$ (specified pore size) are placed at random until the desired porosity is achieved. MATLAB functions such as *bwmorph(…,'bridge')* or *bwareaopen* are used to fill small gaps or remove small "floating" objects.

This simple script allows for rapid building of different geometries than can be used to test the model assumptions under different situations, as shown in Figure A.4.

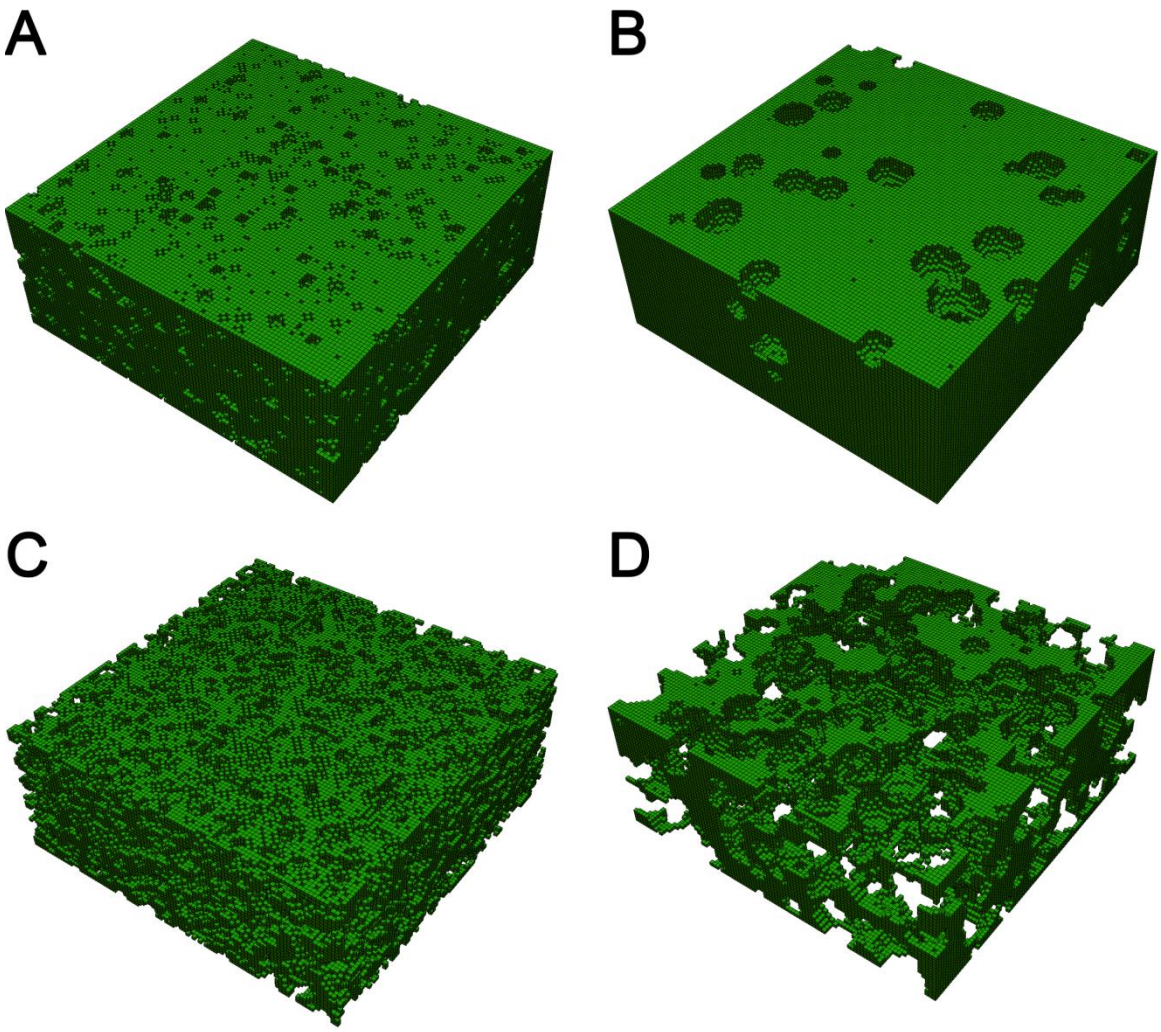


**Figure A.4:** Porous meshes with different porosity and pore size.
A) Porosity=0.2, Pore size=5 μm, B) Porosity=0.2, Pore size=20 μm, C) Porosity=0.8, Pore size=5 μm, D) Porosity=0.8, Pore size=20 μm. Visualization using ParaView.

## A.5 Making 3D movies

The own codes used in the model described in Chapter 5, allow the postprocessing of output data in multiple ways. At each simulation step, all the required parameters are recorded in text files, formatted for different visualization software. Specifically, ParaView and Visual Molecular Dynamics (VMD) are used in this Thesis (both are Open Source).

ParaView directly imports geometry and mesh for different time steps, permitting to visualize scalar or vector field evolution and recording them into movie files. The

geometry is not smoothed, so if the mesh is made of voxels, the movie shows moving voxels. This can be enhanced using VMD.

VMD allows importing individual nodes and the connectivity among them. Although this software is focused on visualization of proteins or other molecules, it also offers the possibility of working with any kind of particles (useful for instance to visualize cross-linked actin networks as described in Chapter 3).

In the migration codes, a specific script generates a file with the VMD format, including the cell centroid and the position of the perimeter nodes at each step. With this "geometry" and the "surf" visualization mode, the voxel structure is nicely transformed into a 3D form that can be recorded to make an enhanced migration movie.

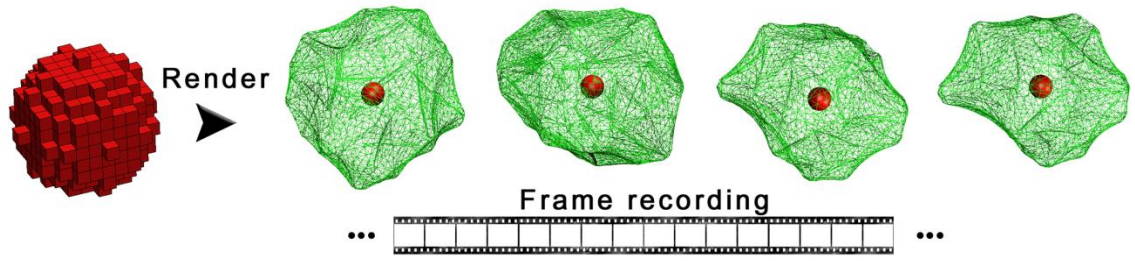


**Figure A.5:** Rendering of voxel structures with VMD.

## A.6 Measuring actin flow with matrix convolution

In mathematics, convolution is an operation on two functions ($f * g$) that gives the area overlap between the two functions as a function of the amount that one of the original functions is translated (Figure A.6). In particular, it is defined as the integral of the product of the two functions after one is reversed and shifted.

In image processing, 2D-convolution can be used to filter images (bi-dimensional matrices of pixels), obtaining different results depending on selected filters. For instance, these filters can serve to sharpen the original image, blur it, detect or enhance edges or produce emboss effects depending on their pixel value distribution. Additionally, convolution can be used to find complicated patterns or compare the similarities (pixel overlap) between two images.

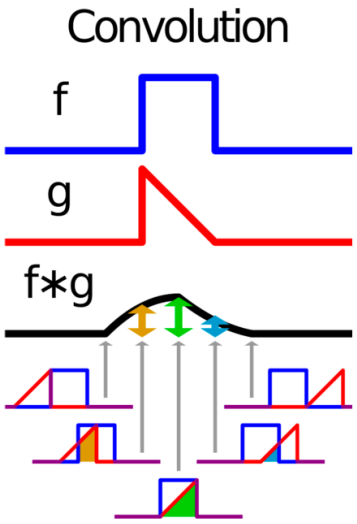


**Figure A.6:** Convolution of functions.
Convolution gives the area overlap between two functions as a function of translation. Adapted from *http://en.wikipedia.org/wiki/Convolution (accessed: 13/05/2013)*

In this Thesis, the actin rearward flow in the lamellipodium is computed using images of actin intensity at the cell edge and the convolution of matrices coded in a MATLAB script. Specifically, the movement of *speckles* (intensity patterns) is studied through comparison of small windows between consecutive images as explained below.

The MATLAB script consists of 8 main points:

At the beginning:

1) All the images are readed and stored as two-dimensional matrices. Since they are usually too big for processing, the user is asked to select a small region by hand (Figure A.7)
2) Two low-pass filters are defined. Specifically, Gaussian filters of size 9 and 21 pixels and standard deviation 1 and 7 pixels respectively are used in the current example (Figure A.8). The MATLAB function *fspecial('gaussian',size,sigma)* was used for this purpose.

Next, for $i$=1 to the total number of images ( $n_{images}$ ):

*3)* The two low-pass filters are applied to clean the noise and enhance the speckle intensity obtaining two filtered images using matrix convolution. Specifically, the function *conv2(…,'same')* from MATLAB was used (Figure A.9).

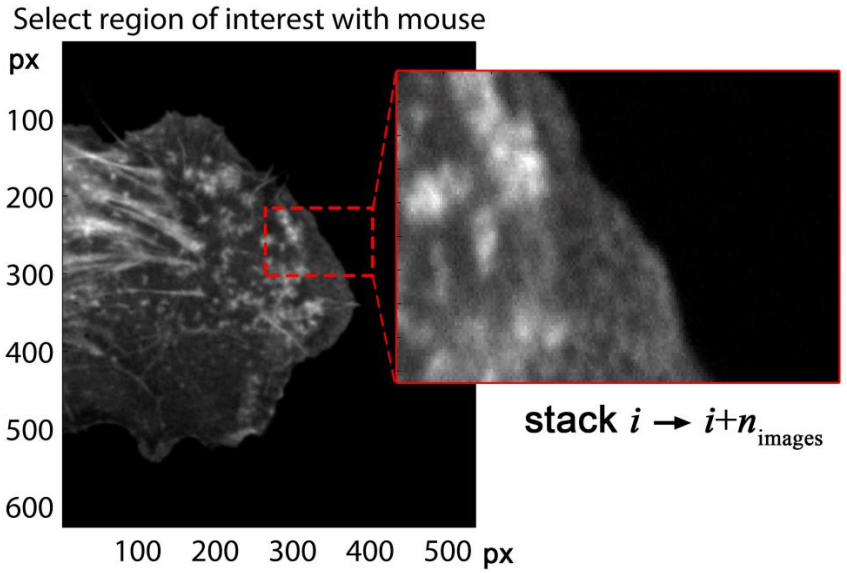


**Figure A.7:** Region selection for image processing.
The script opens the first image and asks the user to select a region of interest. Then, the selected window is cut from $n_{images}$ and stacked for post-processing.

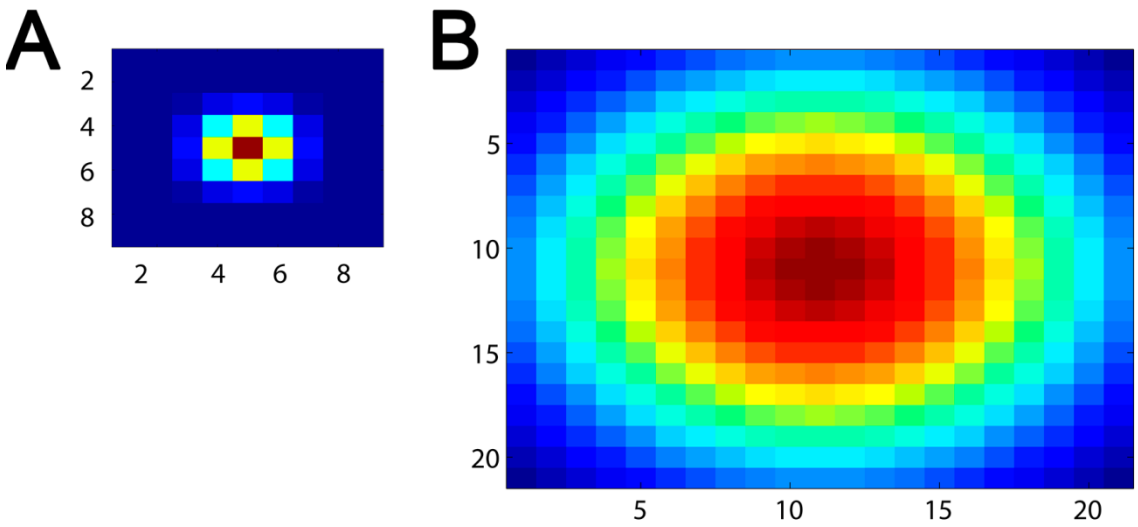


**Figure A.8:** Gaussian low-pass filters.
A) A low-pass Gaussian filter of low standard deviation (1) is used to clean the noise from the image. B) A low-pass Gaussian filter of high standard deviation (9) is used to smooth the image.

4) The original image is band-passed by subtracting the two low-pass filtered images and appliying again matrix convolution, thus obtaining the final image where the speckle movement is tracked (Figure A.10).
5) Small templates from the current image (*i*) are sought in a limited surrounding space of the next image (*i*+1), finding the pixel correlation between template

and search windows. High correlation indicates that pixels from image *i* are likely moving to a specific location of image *i*+1.

6) Small templates from the next image (*i*+1) are sought in a limited surrounding space of the current image (*i*), finding the pixel correlation between template and search windows (Figure A.10). High correlation indicates that pixels from image *i*+1 are likely coming from a specific location of image *i*.
7) Both the correlation matrices of the "move to" and "came from" searchers are averaged and correlated using convolution to find the speckle displacements.
8) Knowing the time step between images, the actin velocity field is computed and stored for post-processing (Figure A.11).

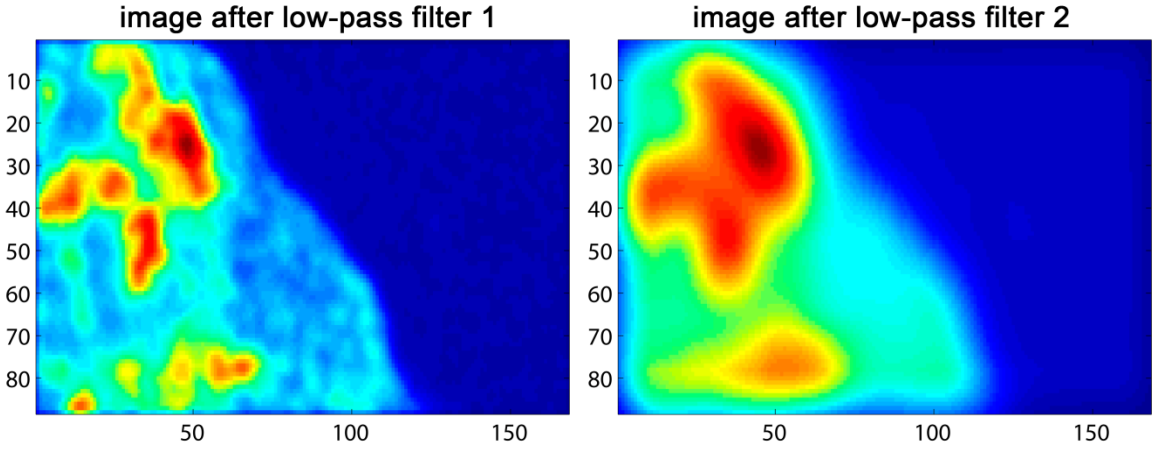


**Figure A.9:** Image after applying low-pass filters.

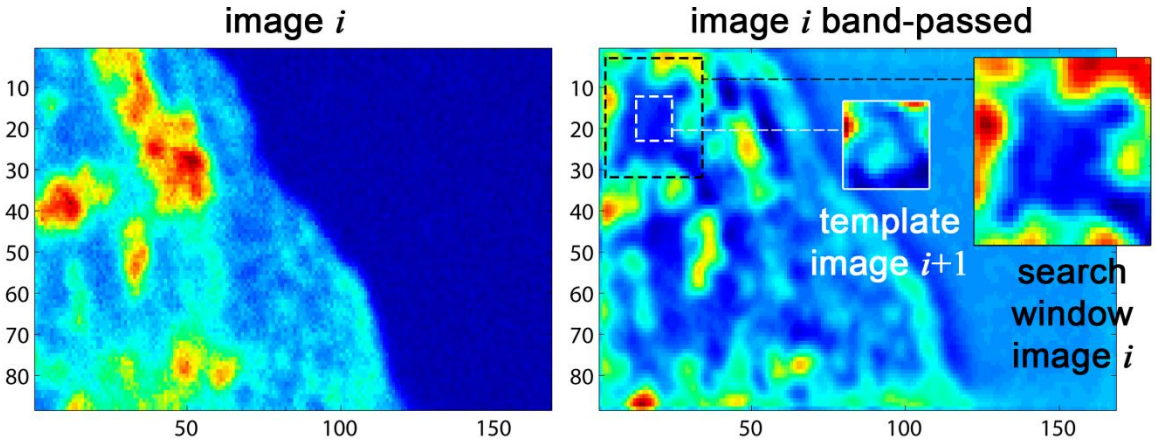


**Figure A.10:** Original and band-passed image.
Right panel shows the *i* band-passed image. A small template from image *i* is sought into a surrounding region of image *i*+1 to find where the template is moving to. In addition, a small template from image *i*+1 is sought into a surrounding region of image *i* (search window) to determine where the template is coming from.

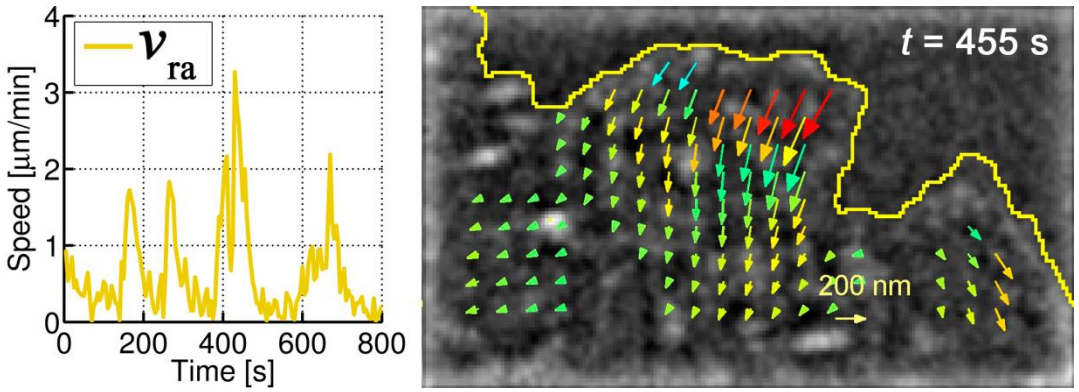


**Figure A.11:** Actin speed measurement.
Speckle tracking permits to find the displacement field at the cell edge (coloured arrows) for each time step, as well as the measurement of actin rearward flow magnitude.

## A.7 Function correlation and Fourier analysis

The cross-correlation of a signal is a mathematical tool for finding repeating patterns, such as the presence of a periodic signal which has been buried in noise. It is often used in signal processing for analyzing functions or series of values. The auto-correlation is just a cross-correlation of a signal with itself (Figure A.12).

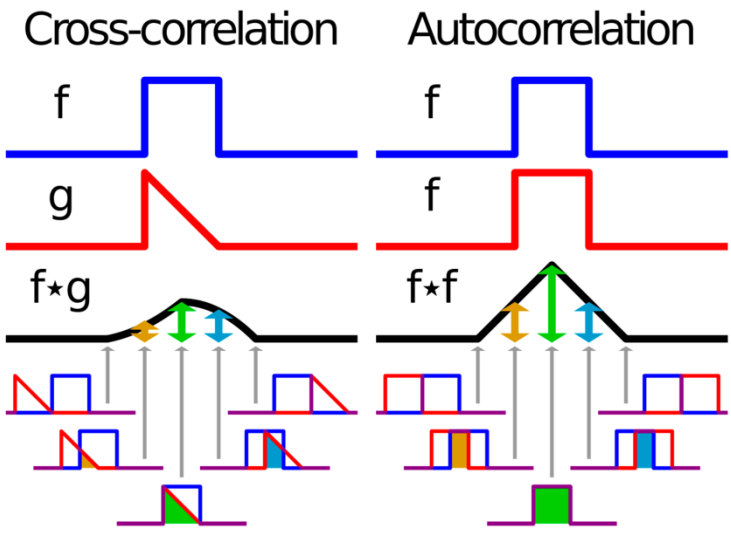


**Figure A.12:** Cross-correlation of functions.
Adapted from *http://en.wikipedia.org/wiki/Autocorrelation (accessed: 13/05/2013)*

In Chapter 6 matrix-convolution methods (described in previous section) are used to find the actin-speckle movements. As a result, the evolution of rearward actin flow and

membrane speed is recorded ($v_{ra}$ and $v_{mem}$ respectively). These curves are significantly noisy and it is sometimes difficult to extract useful conclusions. Nevertheless, experiments from literature suggest that both $v_{ra}$ and $v_{mem}$ present periodic behaviors, although it is not clear whether the actin flow follows the membrane movement or viceversa. Hence, in order to find periodic behaviors of these curves, the following scheme is used:

1) Auto-correlate the membrane speed to roughly find a global period ($T_{glob,mem}$).
2) Correlate small windows (of size $T_{glob,mem}$) of the membrane speed signal with the whole signal to find the periodicity more precisely. The periods found are averaged ($T_{av,mem}$) (Figure A.13).
3) Auto-correlate the actin speed to roughly find a global period ($T_{glob,ra}$).
4) Correlate small windows (of size $T_{glob,ra}$) of the membrane speed signal with the whole signal to find the periodicity more precisely. The periods found are averaged ($T_{av,ra}$).
5) Correlate small windows (of size $T_{glob,mem}$) of the actin speed signal with the whole membrane speed signal (actin speed curve sliding onto the membrane one) to find the correlation curve.
6) Find the periodicity of the correlation (frequency) and the phase delay between actin and membrane speed curves using different-sized windows of the correlation curve.

For the points from 1 to 5, the function *normxcorr2* included in MATLAB is used. This function uses an algorithm that compares the "shapes" of the curves regardless the magnitude, hence being very useful to find repeated patterns.

For the 6$^{th}$ point, the fast Fourier transform function (*fft*), also included in MATLAB, is used. This function is an excellent tool to find the frequency components of a sampled signal. Here, it is used to find the periodicity and strength of the correlation between actin and membrane speeds, as well as the delay between those curves.

Following this simple scheme, allows rapid and automatic analysis and comparison of large amounts of input data. The usage of appropriate filters (e.g. requirement of a minimum value of correlation) permits to discard meaningless samples, being really useful for experimental analysis.

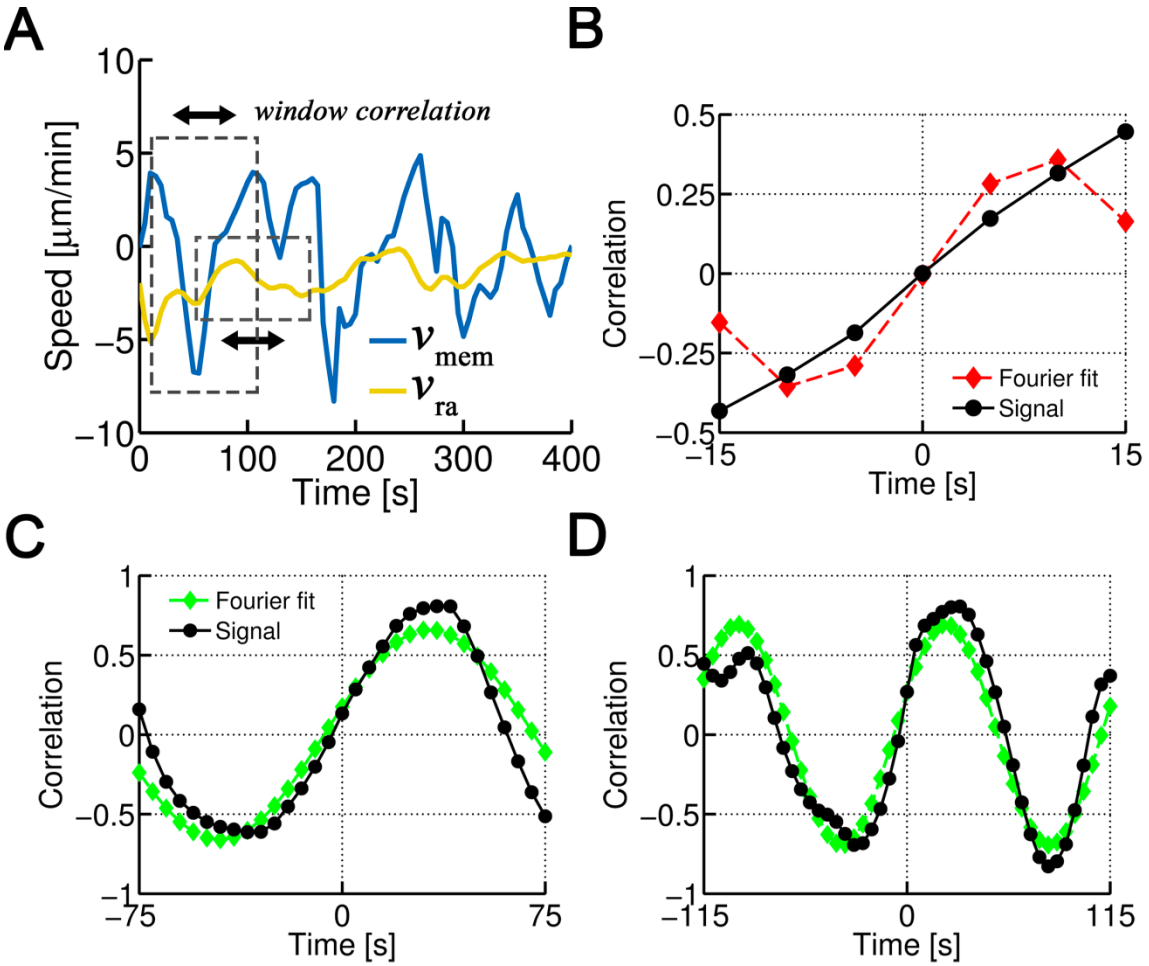


**Figure A.13:** Example of membrane and actin speeds correlation fit.
A) The membrane ($v_{mem}$) and actin ($v_{ra}$) speed periodicity is studied through cross-correlations of different-sized windows (grey dotted lines). B) Different sections of the correlation curve (black line) are fit using the Fourier transform (red line). Usually short sections (small windows) lead to poor Fourier fits, indicating that the pattern periodicity (if exists) is larger than the chosen range. Larger windows (C and D) permit better fits and allow determining realistic periods and phase delays between $v_{mem}$ and $v_{ra}$. Note that the delay is the switch of the correlation from $t$=0. To find the correlation the actin speed curve slides on the membrane speed curve. Hence, negative phases mean that membrane follows the actin.

# B

# APPENDIX B: INFLUENCE OF MYOSIN-HEADS

Molecular motors in the agent-based model described in Chapter 3 mimic a myosin minifilament consisting of numerous myosin II molecules. Although the kinetic properties of a single molecule of myosin V have been experimentally tested, a precise analytical model for describing the walking rate of a minifilament is not well-known due to both difficulty in measurements and the dependence of the walking rate on the number of myosin heads involved with walking action.

In order to simulate a more realistic situation with stress and contraction comparable to those observed in cells, a sensitivity analysis is performed to computationally obtain the kinetic properties of a minifilament depending on the number of myosin heads.

As described in Chapter 3, motors in the model unbind following Bell's equation:

$$k_{\mathrm{u,M}} = k_{\mathrm{u,M}}^{0} \exp\left( \frac{\lambda_{\mathrm{u,M}} \left| \vec{F}_{\mathrm{s}} \right|}{k_{\mathrm{B}} T} \right) \tag{B.1}$$

where $k_{\mathrm{u,M}}^{0} = 0.02\ \mathrm{s}^{-1}$ is the zero-force unbinding rate coefficient and $\lambda_{\mathrm{u,M}} = 2.6\mathrm{e}^{-9}$ is the mechanical compliance of the bond measured experimentally for myosin V (Uemura et al., 2004). Hence, the probability of unbinding is written as follows:

$$p_{\mathrm{u,M}} = 1 - \exp\left(-k_{\mathrm{u,M}} dt\right) \tag{B.2}$$

which essentially means that high forces or longer times increase the unbinding probability of molecular motors.

A MATLAB script was developed for this analysis. The program distributes the total force acting on the entire filament among the different myosin heads. Therefore when a head detaches, the rest of heads, still bound, bear more force, increasing the probability of unbinding.

This analysis is focused on exploring how varying the number of myosin heads, and other parameters such as the time step ( $dt$ ) and the probability of rebinding ( $p_{\text{reb}}$ ) affect the unbinding rate of the whole minifilament ( $k_{\text{u,Fil}}$ )(Figure B.1).

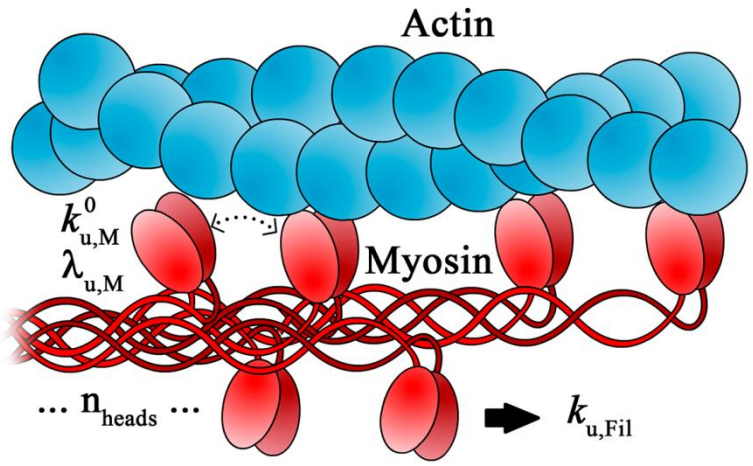


**Figure B.1:** Scheme of myosin minifilament.
A myosin minifilament consists of numerous myosin II molecules. The number of heads forming the filament determines its kinetic properties.

## B.1 Influence of the time step

The time step affects the unbinding rate of motors but only at high forces. The reason, as stated before, is that the probability of unbinding of a myosin head increases with force. If the time step is too big, the unbinding event will happen at a 100% of probability in that step, giving unaccurate values of unbinding rate. This behavior is shown in Figure B.2, where $k_{\text{u,M}}$ converges asymptotically to $1/dt$ .

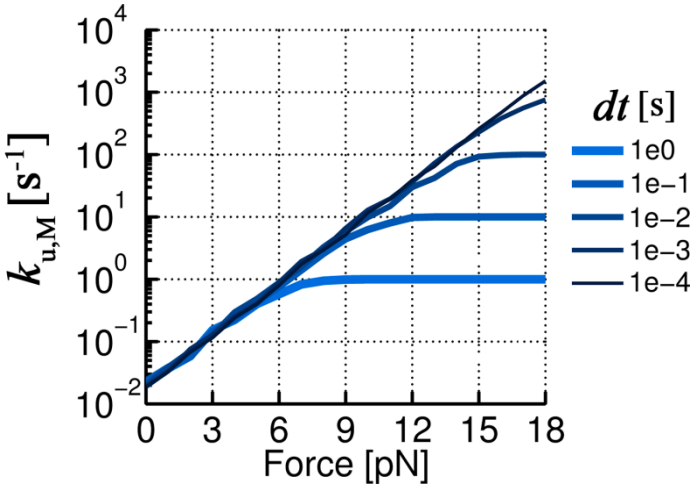


**Figure B.2:** Influence of time step on unbinding rate of single motors.
One single head is repeteadly subjected to different forces until unbinding occurs. The unbinding rate ( $k_{\text{u,M}}$ ) is then calculated as $1/(n \cdot dt)$, where $n$ is the number of repetitions until unbinding. When $dt$ and forces are high, the unbinding occurs at $n$=1.

Additionally, the effects of different values of $dt$ with different number of myosin heads at zero-force are analyzed. As expected, $k^0_{u,M}$ is not affected by $dt$ at any number of heads due to the null force. Nevertheless, $k^0_{u,M}$ decreases as the number of heads decreases (note that rebinding was deactivated for this study) (Figure B.3).

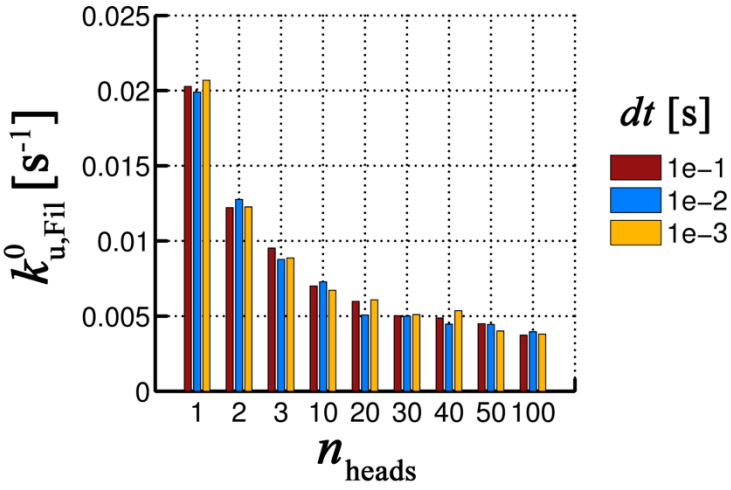


**Figure B.3:** Influence of time step at zero-force and several heads.

At zero-force, the unbinding rate of the minifilament ( $k^0_{u,Fil}$ ) is unnafected by $dt$ .
However, the unbinding rate decreases as the number of heads composing the minifilament increases.

## B.2 Influence of the number of heads

Varying the number of heads produces a dramatic and non-linear change in the rate of unbinding of the whole minifilament ( $k_{u,Fil}$ ). As in the previous study, the probability of rebinding is set to zero, so once a head unbinds, it remains detached. This permits to isolate the effects of the number of heads, since the probability of rebinding is taken into account in the next section. $k_{u,Fil}$ is calculated as $1/(n \cdot dt)$ with $dt = 0.001\,\text{s}$ and $n$ the number of steps until complete unbinding of the filament.

The results show that $k_{u,Fil}$ is strongly affected by the number of heads at low forces (Figure B.4A) but more markedly at high ones (Figure B.4B). Increasing the number of heads leads to a decrease in the rate of unbinding of the filament, since the force born per head is lower and consequently the probability of unbinding of each head decreases. Interestingly, the rate of unbinding doesn't vary proportionally to the number of heads, probably produced by the cascade effect that fastly increases the force per head when a certain amount of heads becomes detached. This behavior is clearly observed in with $k_{u,Fil}$ decreasing exponentially with $n_{heads}$ .

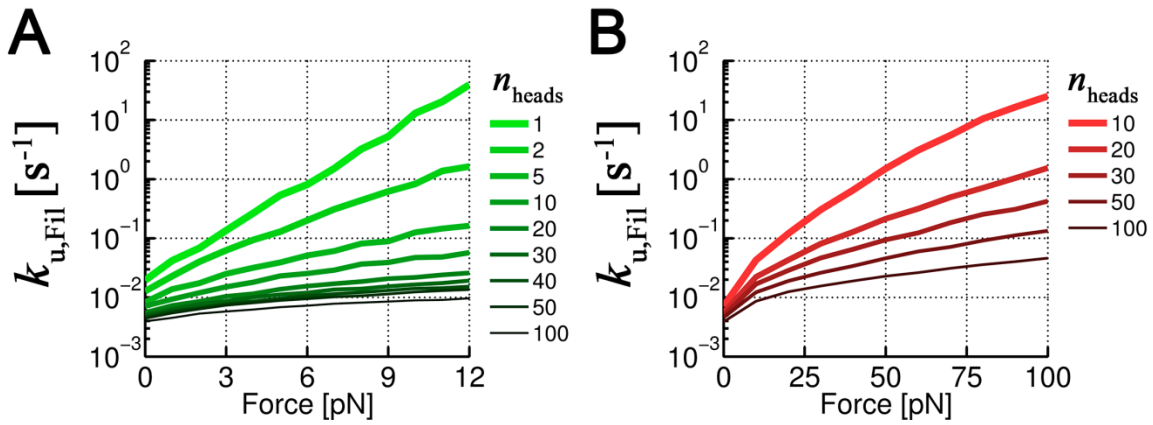


**Figure B.4:** Influence of the number of heads on filament kinetics.
Influence of $n_{heads}$ at A) low forces and B) high forces. The rate of unbinding of the minifilament $k_{u,Fil}$ is not proportional to $n_{heads}$ and varies dramatically specially for higher forces.

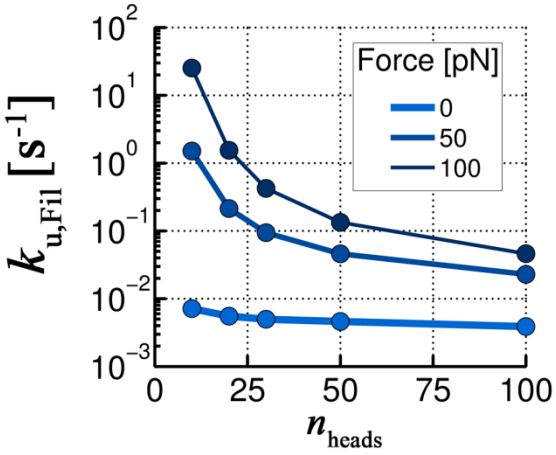


**Figure B.5:** Effect of force and number of heads.
The unbinding rate of the minifilament decreases exponentially with the number of myosin heads, more dramatically for higher forces.

## B.3 Influence of rebinding

Rebinding of myosin heads affects enormously the rate of total unbinding of the minifilament, diminishing the cascade effect and therefore increasing the life-time of the bond.

To study the effects of rebinding, the ratio between unbinding and rebinding probabilities ( $p_u$ and $p_{reb}$ respectively) is varied over the range [0-1]. It is important to note that while $p_u$ depends on force, $p_{reb}$ doesn't (since a free head does not feel any force). For this reason, the study is performed at a constant value of force, specifically at zero-force to see the effect of $p_{reb}/p_u$ on $k^0_{u,Fil}$ .

The maximum number of heads studied is 20 since for higher values, the computational time increases too much. In fact, with ( $p_{reb}/p_u$ ~1) and more than 20 heads, $k^0_{u,Fil}$ goes beyond 1e$^{-10}$ s$^{-1}$ and the complete unbinding of the myosin minifilament might never happen. The dependence of $k^0_{u,Fil}$ on both $p_{reb}/p_u$ and $n_{heads}$ is shown in Figure B.6. The ratio $p_{reb}/p_u$=0 corresponds with the results discussed in previous sections. As could be expected, at higher ratios and higher number of heads, the minifilament remains bound to the actin more time, so the rate of unbinding decreases. This behavior is consistent for different values of forces.

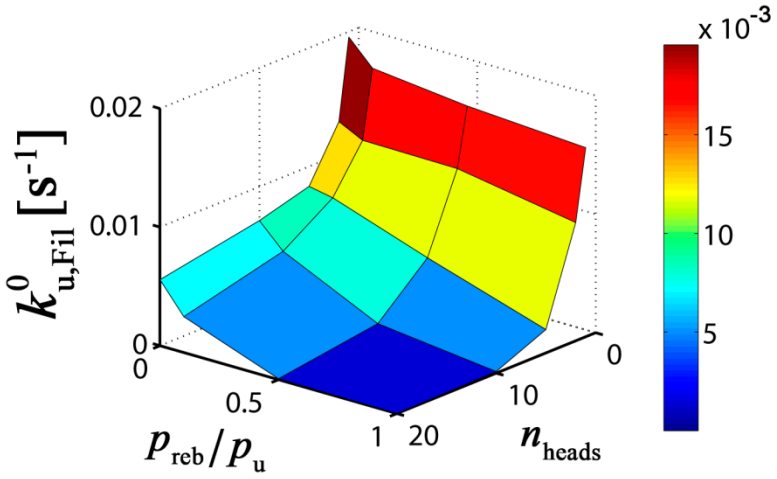


**Figure B.6:** Influence of rebinding probability and number of heads.

## B.4 Minifilament properties

The analysis conducted so far allows understanding the role of the number of myosin heads, and the influence of several parameters on the general behavior of a myosin minifilament.

Using the parameters of one single myosin head in the model described in Chapter 3 would lead to low cell contraction compared to experiments. With $k^0_{u,M} = 0.02$ s$^{-1}$ and $\lambda_{u,M} = 2.6e^{-9}$, all the motors would unbind with insignificant forces and the whole network would collapse. Hence, it is assumed that each molecular motor actually represents a minifilament with multiple heads and therefore with lower rates and sensitivity of unbinding. Specifically, it was found that $k^0_{u,M} = 2e^{-5}$ s$^{-1}$ and $\lambda_{u,M} = 2.6e^{-10}$ were appropriate to achieve more realistic results. To justify these adjustment, the target curve

(Bell's equation using those values, Figure B.7B) was fit by varying the number of heads and the probability of rebinding of each head.

Note that the probability of rebinding should be independent of the force acting on the filament, however, it is really difficult to properly fit the Bell's curve with a constant value of $p_{\text{reb}}$ and for any $n_{\text{heads}}$. Also note that $k_{\text{u,Fil}}$ (and consequently $p_{\text{u}}$) changes very quickly with the applied force and the number of heads. Hence, if $p_{\text{reb}}$ remains constant, it affects $k_{\text{u,Fil}}$ much more when $p_{\text{reb}}$ is comparable to $p_{\text{u}}$. In other words, if $p_{\text{reb}}$ is low/high, $k_{\text{u,Fil}}$ is influenced at low/high forces when $p_{\text{u}}$ is also low/high. In sum, the curve becomes destabilized and it is not possible to exactly fit it with a constant value of rebinding probability. For this reason, $p_{\text{reb}}$ is systematically adjusted for each level of force and for different number of heads. Interestingly, with low number of heads, $p_{\text{reb}}$ must increase with force to fit the curve. On the other hand, to do so with high number of heads, $p_{\text{reb}}$ must decrease, suggesting that there exists an optimum value of $n_{\text{heads}}$ which fits the target curve with an almost constant value of $p_{\text{reb}}$.

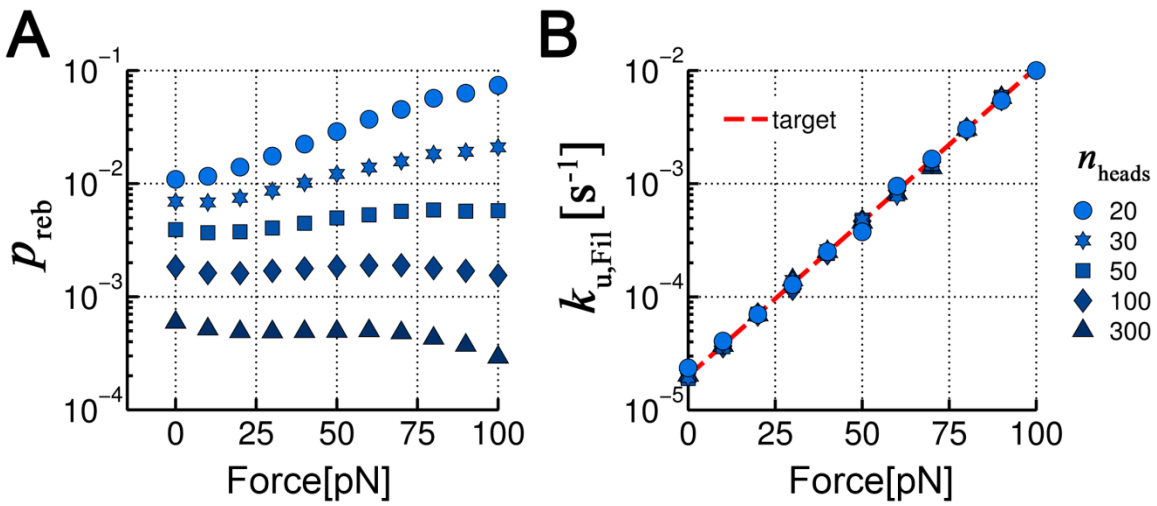


**Figure B.7:** Bell's equation fit with multiple myosin heads and different rebinding probabilities.
A) The probability of rebinding ($p_{\text{reb}}$) at each level of force and $n_{\text{heads}}$ that fits the Bell's equation. The trend for low $n_{\text{heads}}$ is $p_{\text{reb}}$ increasing with force, whereas for high $n_{\text{heads}}$, $p_{\text{reb}}$ decreases. B) Bell's curve (target) fit for several $n_{\text{heads}}$ and $p_{\text{reb}}$. Legend is shared with A.

With all this, it can be concluded that a minifilmaent of myosin II with a number of heads between 50 and 100 and a constant probability of rebinding between 0.002 and 0.004 would be equivalent to the motor kinetics used in the Brownian-dynamics model (Chapter 3), hence justifying the use of $k^{0}_{\mathrm{u,M}} = 2\mathrm{e}^{-5}$ $\mathrm{s}^{-1}$ and $\lambda_{\mathrm{u,M}} = 2.6\mathrm{e}^{-10}$ instead of the experimental values found for single myosin V motors.

# C

# APPENDIX C: ADDITIONAL MODEL VALIDATIONS

The migration model described in Chapter 5 studies the cell behavior depending on different environmental factors through probability functions. In this Appendix, the randomness of these probability functions is firstly tested to check the consistency of the model. Next, the mechanical conditions are isolated to properly check the model parameters, and the fluid and chemical factors are independently studied. Following, the probability functions are subjected to a sensitivity analysis. Finally, some assumptions of the microfluidic simulation are tested with detailed simulations at the cell scale.

## C.1 Model randomness

To check whether the random functions used in the model are truly stochastic, a simple analysis is performed for validation. This study consists of 100 simulations of cell migration, each of them including 50 steps. The cell starts at the same position in all the simulations, and its final position is recorded. The angle histograms of the effective trajectories projected on the coordinate planes as well as the 3D point cloud of the final positions are shown in Figure C.1. Their homogeneous distribution demonstrates that the computed trajectories are indeed random.

The same procedure is used to check the migration behavior when the cell is forced to migrate in a certain direction (manually specifying the direction of maximum stress). Specifically, the cell is forced to migrate in the x-direction, although the random direction remains activated. As previously, the angle histograms of the effective trajectories projected on the coordinate planes and the 3D point cloud are shown in Figure C.2. The directional pattern in the forced direction confirms the proper behavior of the probability functions and permits the adjustment of parameters, preparing the model for further testings.

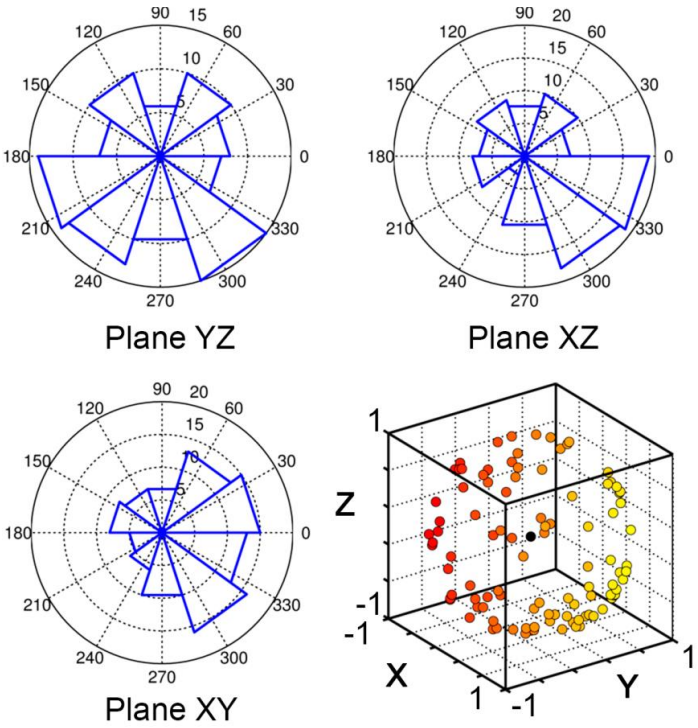


**Figure C.1:** Angle histograms and final cell positions in purely random migration.
Angle histograms of random migration simulations projected on the coordinate planes. The random distribution confirms the stochastic nature of the cell movement. The 3D distribution (bottom right panel) shows the spherical arrangement of cell final positions (red to yellow shaded points) with respect to the initial location (black circle).

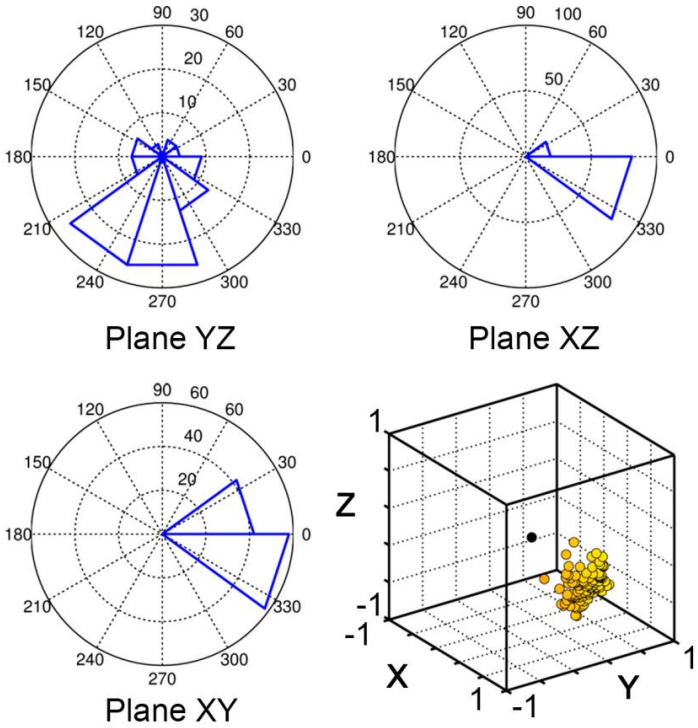


**Figure C.2:** Angle histograms and final positions in forced plus random migration.
Angle histograms of forced plus random migration simulations projected on the coordinate planes. The directional distribution confirms the proper behavior of the model, with most of the trajectories comprissed in a small range of angles with respect the forced direction (x-direction). The 3D distribution (bottom right panel) shows the accumulation of cell final positions (red to yellow shaded points) at the +X location with respect to the initial position (black circle).

## C.2 Mechanical testing

Ideally, a cell embedded in a homogeneous ECM would feel very similar conditions along its surface. In the model, however, geometry and morphology due to the voxel-based approach affect importantly the mechanical conditions and therefore the *mechanosensing* process. To validate the mechanical factors used in the probability functions, it becomes necessary to perform a simpler analysis where the mechanical effects are completely isolated. Here, geometrical and morphological effects are neglected by considering a constant stress along the cell surface regardless its position and shape. Furthermore, this assumption allows skipping the FE-based mechanical calculation permitting a faster analysis and therefore the computation of many repetitions.

Three different cases are considered: (i) forced movement in a specific direction, (ii) forced movement plus a random component, (iii) purely random migration. For each of these cases, three values of cell stress are taken into account: (j) high stress,1.5 kPa (corresponding with stiff ECMs, $E > 200$ kPa), (jj) intermediate stress, 0.6 kPa (corresponding with ECMs of $E \sim 3$ kPa), (jjj) low stress, 0.1 kPa (corresponding with compliant ECMs $E < 0.4$ kPa). Each simulation comprises 50 steps of 5 minutes and it is repeated 10 times to avoid errors due to random effects.

As in Chapter 5, the model parameters are adjusted to obtain cell speeds in the experimental range observed in fibroblasts (Lo et al., 2000, Friedl and Brocker, 2000, Peyton and Putnam, 2005, Peyton et al., 2011, Hakkinen et al., 2011). Results show that in forced migration (stablishing the direction of maximum stress in the desired direction) both the effective and mean speeds increase with cell stress (equivalent to increasing ECM stiffness)(Figure C.3A). As might be expected with random effects deactivated, the effective speed is similar to the mean speed since the cell migrates in a straight fashion parallel to the forced direction.

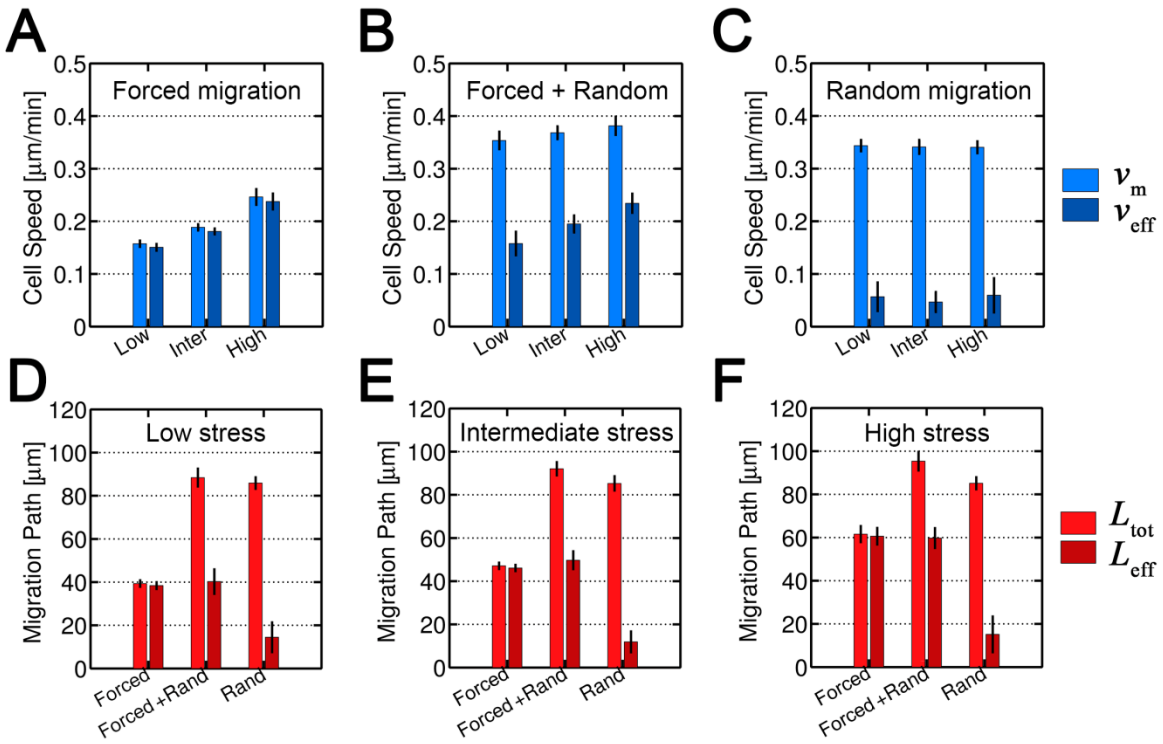


**Figure C.3:** Cell speeds and migration path lengths.
A) Cell speed increases with stress in the case of forced migration. Effective and mean speeds present similar values. B) A random direction is added to the forced one. As a result the effective speed is lower than the mean speed, although they still rise with increasing stress. C) Purely random migration. The effective speed decreases due to unidirectional movements independently of cell stress. D) Migration paths for low, E) intermediate and F) high stress. The cell migrate through longer distances when forced and random directions act together, however, the effective advanced distance from the initial point is similar to the case of forced migration for all levels of stress.

This trend is also observed in Figure C.3 with travelled path lengths increasing with stress. When a random direction is added, the mean speed is increased, whereas the effective one is maintained (Figure C.3B). In the case of purely random migration, the mean speed is much higher than the effective one and its value is logically independent of cell stress (Figure C.3C). Overall, the migration path lengths present similar patterns for all levels of stress (although travelled distances increase with stress) and each subcase (Figure C.3D-F). Interestingly, the total distance in random migration is higher than in the forced case and for any cell stress. This is probably due to the the fact that forced migration makes cells elongate in the chosen migration direction, compared with the more spherical cells produced by random migration. Hence, there are few surface cell elements at the front and back parts where new voxels will likely appear/disappear. This is equivalent to a decreased probability of advance, and consequently the computed paths

are shorter. Supporting this idea, the cell shape factor (or aspect ratio) is notably higher in forced migration for all levels of stress as shown in Figure C.4 (top panels). Interestingly, for high levels of stress, the shape factor becomes noisy and presents a lower mean value than in cases of lower stress.

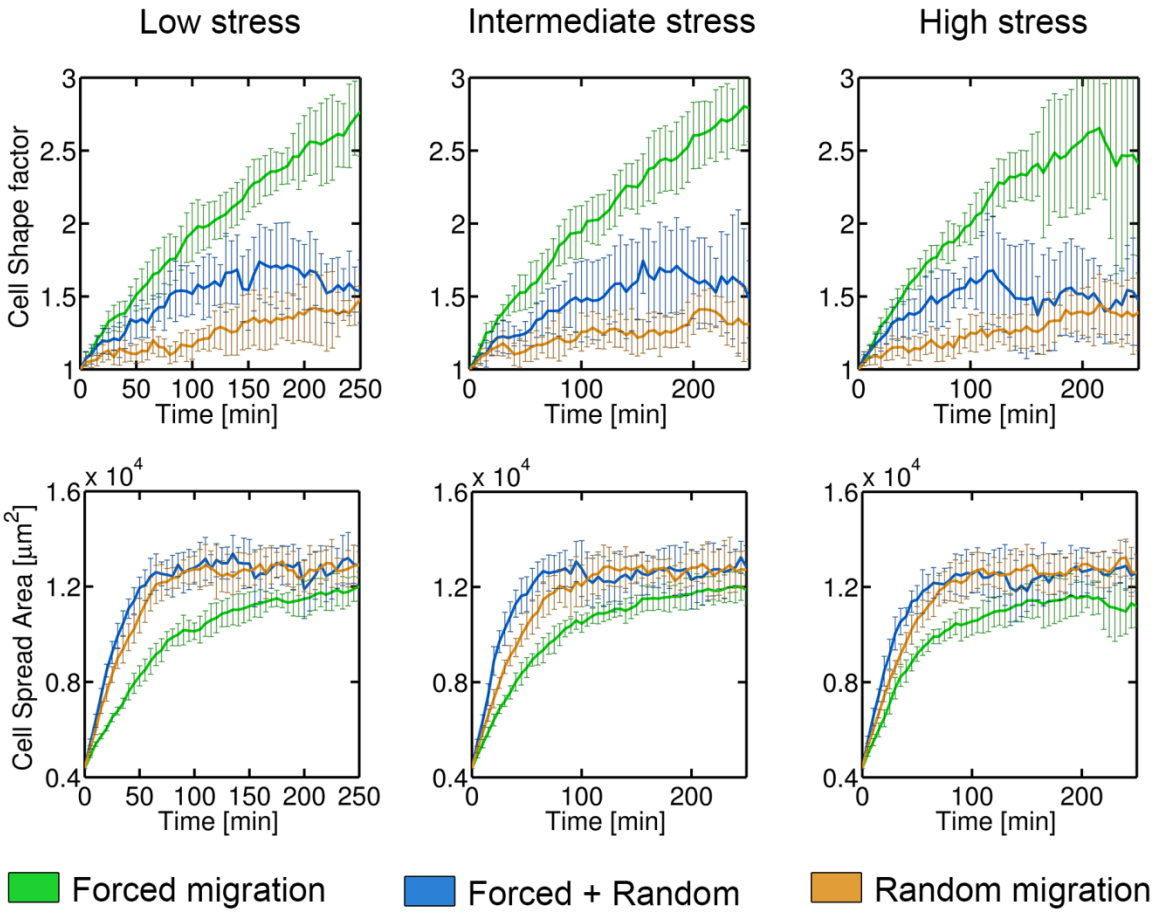


**Figure C.4:** Cell shape factor and spread area for different stress levels.
Cell shape factor is higher in forced migration for all levels of cell stress, producing elongated cells in the chosen direction (top panels) and leading to smaller spreading areas (bottom panels) compared to other cases.

This happens because the probability functions saturate at high stresses and hence the voxel appearing/disappearing probability is still high even in different directions to the forced one. Consequently, the cell becomes less elongated. In random migration cases, cells present very low aspect ratio (close to 1), which implies rounded shapes. Furthermore, this is accompanied by slightly higher adhesion area (peripheral voxel faces in contact with the ECM) in comparison with forced migration (Figure C.4 bottom panels).

While the values of the cell shape factor are in agreement with those found in literature (what they call cell axial ratio), the computed spread area is ~10 fold higher than experimental measurements (Hakkinen et al., 2011). As explained in Chapter 5, this area is calculated as the sum of all the cell voxel faces (each of 9 $\mu m^2$) in contact with the ECM, and its value is limited by the maximum number of cell voxels (specifically it is allowed an increase of 10% of the initial volume). Hence, the difference with respect to experimental values relies basically on the overestimation produced by a voxelized structure compared to a smoother surface. For instance, a sphere of radius 15 μm has an area of ~2828 $\mu m^2$, whereas when that same sphere is voxelized, its area increases to 4374 $\mu m^2$. Furthermore, the discrepancy becomes higher when the cell elongates and presents small protrusions that increase considerably the computed area. Nevertheless, the general trend is similar to the quick increase and saturation of adhesion area found in cells on micropilar substrates (Trichet et al., 2012).

## C.3 Fluid-chemical factors testing

Similarly to the previous analysis, the migration behavior is tested under isolated conditions of fluid and chemical inputs. As described in Chapter 5, the flow direction at each point as well as the chemical species concentration field are taken into account, extracting their values from a FE simulation of a whole microdevice. The validation is performed distinguishing 5 different cases:

1) Chemical gradient in x-direction.
2) Chemical gradient and fluid flow in x-direction.
3) Low chemical gradient and fluid flow in x-direction.
4) Chemical gradient and fluid flow in x-direction with cell receptors blocked
5) Low chemical gradient and fluid flow in x-direction with cell receptors blocked.

As before, 10 simulations (50 steps) of each case are computed. Cases 4 and 5 are equivalent to 2 and 3 except that the probabilities regarding fluid flow are reversed (receptors blocked). In other words, cells prefer to migrate upstream. This behavior was observed experimentally (Shields et al., 2007, Polacheck et al., 2011) and the explanation is that tumor cells utilize interstitial flow to create and amplify autologous transcellular chemokine gradients. When specific receptors are blocked (e.g. CCR7), cells are unable to detect such autologous gradients and tend to migrate upstream probably due to their preference for higher pressures.

Resulting speeds (Figure C.5) show that a chemical gradient acting alone produces random migrations, with effective speeds much lower than mean ones. This is due to the definition of $F^C$ that considers the concentration variation ($\Delta C$) between adjacent voxels. Since the chemical gradient was computed for the whole microdevice (from $C = 0$ to 1 at the inlet and outlet boundaries respectively), $\Delta C$ was very low in the cell length scale. Nevertheless, the sensitivity constant for this factor ($\lambda^C$) is three orders of magnitude higher than the other constants to account for this phenomenon (Table 5-2).

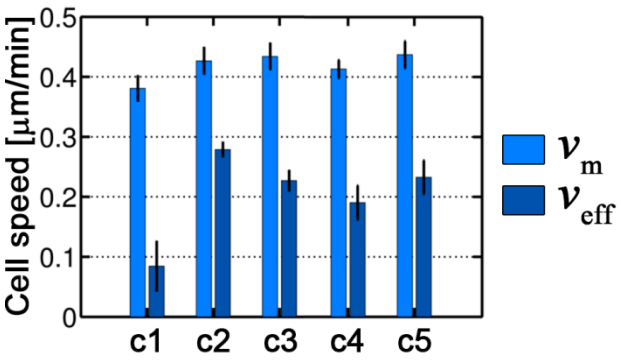


**Figure C.5:** Cell mean and effective speeds for different fluid-chemical conditions.
c1: Chemical gradient in x-direction.
c2: Chemical gradient and fluid flow in x-direction.
c3: Low chemical gradient and fluid flow in x-direction.
c4: Chemical gradient and fluid flow in x-direction with cell receptors blocked.
c5: Low chemical gradient and fluid flow in x-direction with cell receptors blocked.

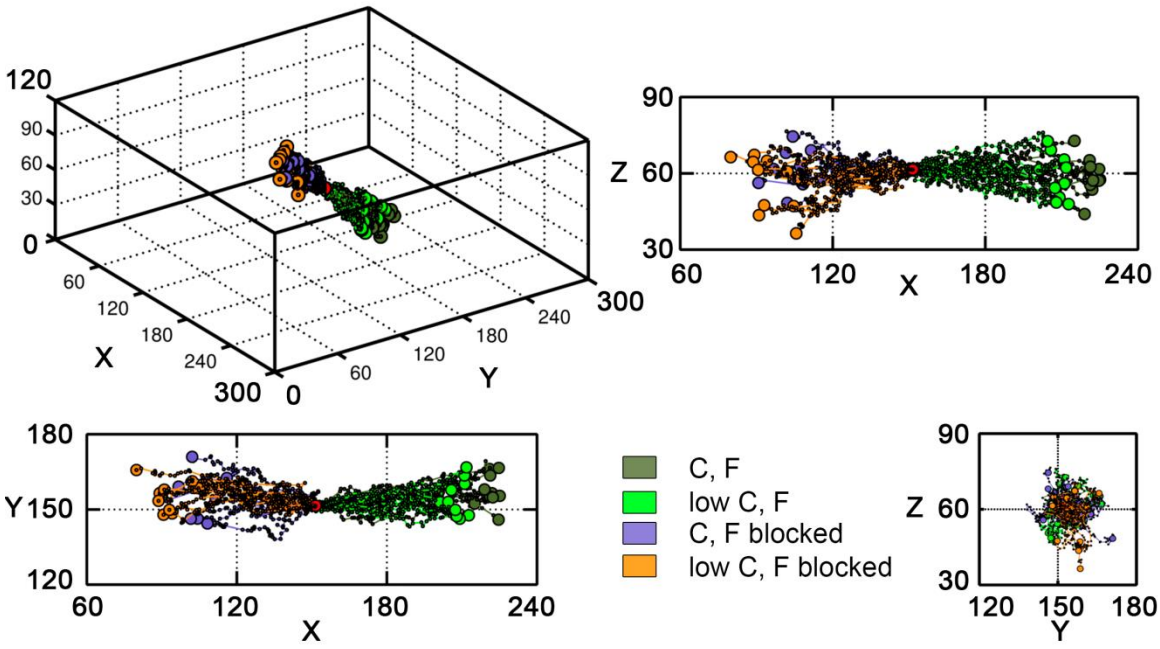


**Figure C.6:** Migration trajectories for different flow-chemical conditions.
For each case, 10 repetitions of 50 steps were simulated. Cell initial position (red circle) was the same for all the simulations.

When the fluid flow factor is activated (case 2 and 3) the effective speed increases notably, meaning that the cell migrates aligned with the flow direction. This increase is smaller in case 3 where the chemical gradient is lower. Blocking the cell receptors (reversing the effect of $F^{\mathrm{F}}$) leads to similar migration results, indicating that in these simulations the fluid flow factors dominate the chemical ones. Since chemical gradient pushes the cell in opposite direction than the fluid flow, a lower chemical gradient (case 5) leads to higher effective speeds. The 3D trajectories as well as the coordinate plane projection of each case are shown in Figure C.6 (except case 1 for clarity).

## C.4 Probability functions sensitivity analysis

A sensitivity analysis is performed to better understand the effect of each separate factor on the probability of adding/removing voxels:

$$\begin{aligned} p_+ &= p_+^0 + p_+^{\max}\left(1 - e^{-k_+^0\left(\lambda_+^\sigma F_+^\sigma + \lambda_+^{\Delta\sigma} F_+^{\Delta\sigma} + \lambda_+^{\mathrm{C}} F^{\mathrm{C}} + \lambda_+^{\mathrm{F}} F_+^{\mathrm{F}}\right)dt}\right) \\ p_- &= p_-^0 + p_-^{\max}\left(1 - e^{-k_-^0\left(\lambda_-^\sigma F_-^\sigma + \lambda_-^{\Delta\sigma} F_-^{\Delta\sigma} + \lambda_-^{\mathrm{C}} F^{\mathrm{C}} + \lambda_-^{\mathrm{F}} F_-^{\mathrm{F}}\right)dt}\right) \end{aligned} \tag{C.4.1}$$

Due to the number of factors and high variety of combinations, $\sigma_{\mathrm{v}}$ is represented in the x-axis while varying other parameters. First, the number of factors involved and activated at the same time is explored. For this analysis all the factors have the same weights ($\lambda F$ : constant). In addition, to consider the maximum probability in each case, all the $F$ 's depending on angles are considered aligned, that is, cosines and sines equal to 1. Figure C.7 shows the probability of adding and removing voxels as a function of the cell stress and the active factors. In both cases, $p_*$ increases exponentially with $\sigma_{\mathrm{v}}$ since $F_*^\sigma$ has a linear dependence with cell stress. Adding new factors increases substantially the probabilities, but saturates when all the factors are acting at the same time (darker lines).

Secondly the effect of the alignment is tested. In particular, chemical and flow inputs are deactivated, taking only into account cell stress magnitude and gradient factors ($F_*^\sigma$ and $F_*^{\Delta\sigma}$). In case of a voxel completely perpendicular with the maximum stress direction ($\cos(\theta) = 0$ or $\sin(\theta) = 0$ for adding or removing probabilities respectively), the exponent becomes null and hence $p_* = p_*^0$. As the alignment increases, so does the probability, more notably for higher stresses (Figure C.8).

Next the effect of the sensitivity constants ($\lambda$) is analyzed. Specifically $\lambda_*^{\sigma}$ is varied while $\lambda_*^{\Delta\sigma}$ is held constant and $\lambda_*^{C} = \lambda_*^{F} = 0$. Note that considering a perfect alignment ($\cos(\theta) = 1$, $\sin(\theta) = 1$ for adding/removing) and the control value of $\lambda_*^{\Delta\sigma}$ produces an offset of 0.3 and 0.15 (0.4 and 0.25 when adding $p_*^0$) in the probabilities of adding/removing voxels respectively, as can be seen in Figure C.9. Due to this offset the functions are closer to saturation, explaining the minor changes produced in $p_*$ (especially in $p_-$) for bigger variations of $\lambda_*^{\sigma}$. This is particularly important when all the factors are activated.

Finally the adding/removing rate ($k_*^0$) is varied. Since this parameter affects equally and at the same time to all the factors, small changes produce noticeable effects. These effects, however, are stronger for low rate values. For higher ones, the exponential function saturates producing very slight changes on the probability. Note that in Figure C.10 the saturation is enhanced due to the consideration of perfect alignment (and therefore higher $F$ values) as previously.

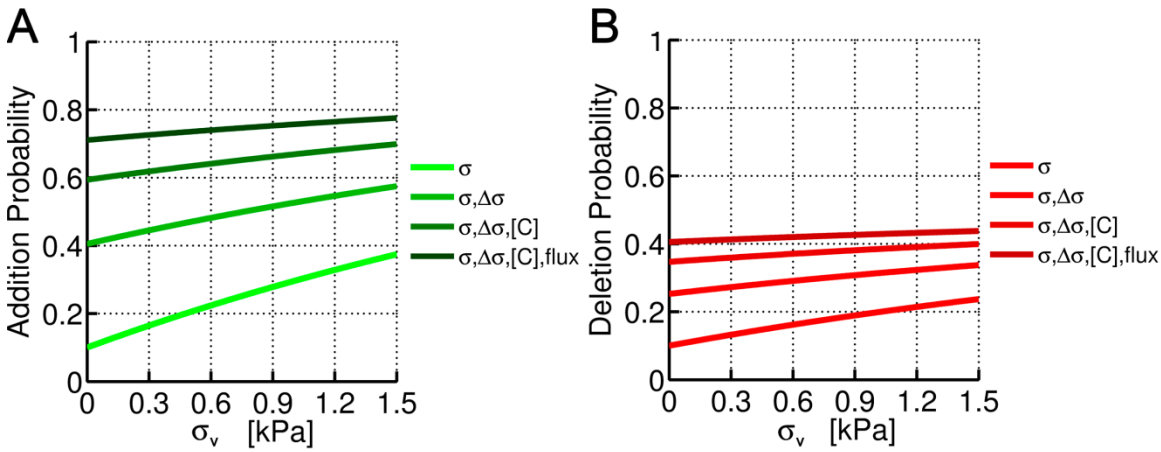


**Figure C.7:** Effect of the number of factors on the probability functions.
A) Adding voxels probability. B) Removing voxels probability.

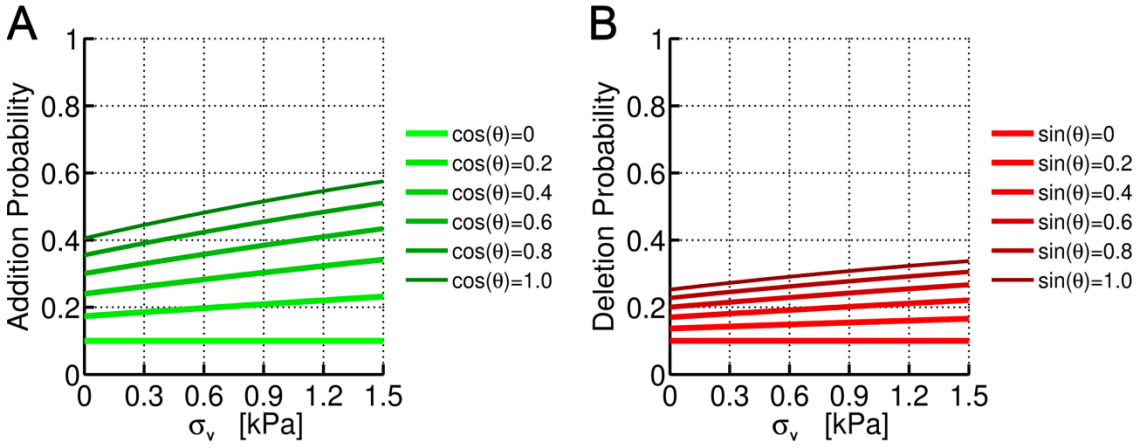


**Figure C.8:** Effect of the alignment on the probability functions.
A) Adding voxels probability. B) Removing voxels probability.

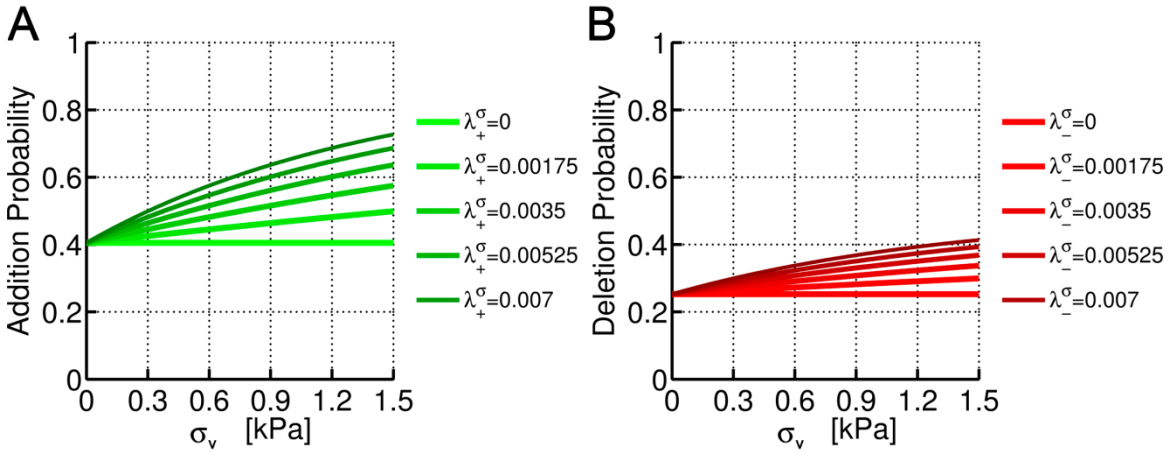


**Figure C.9:** Effect of the sensitivity constants on the probability functions.
A) Adding voxels probability. B) Removing voxels probability.

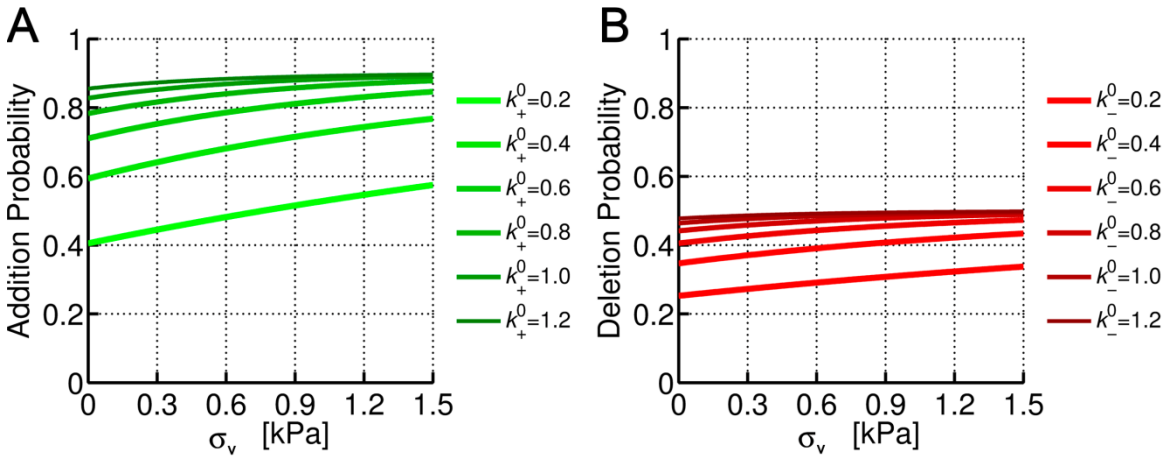


**Figure C.10:** Effect of the adding/removing rate on the probability functions.
A) Adding voxels probability. B) Removing voxels probability.

## C.5 Fluid-chemical simulation with cell body embedded in a porous ECM

To ensure that the body of a single cell embedded in a porous ECM does not affect the fluid and chemical fields of the whole microdevice, a specific analysis taking the cell geometry from a previous simulation of the migration model was performed. Since in this model the cell body is discretized with voxels the surface was smoothed and the resultant geometry was imported in COMSOL to perform the computation (Figure C.11). Note that in this particular case each voxel is 1 $\mu m^3$ instead of 9 $\mu m^3$ as used in the simulations of Chapter 5. Hence, the cell was ~20 µm length in the chosen frame.

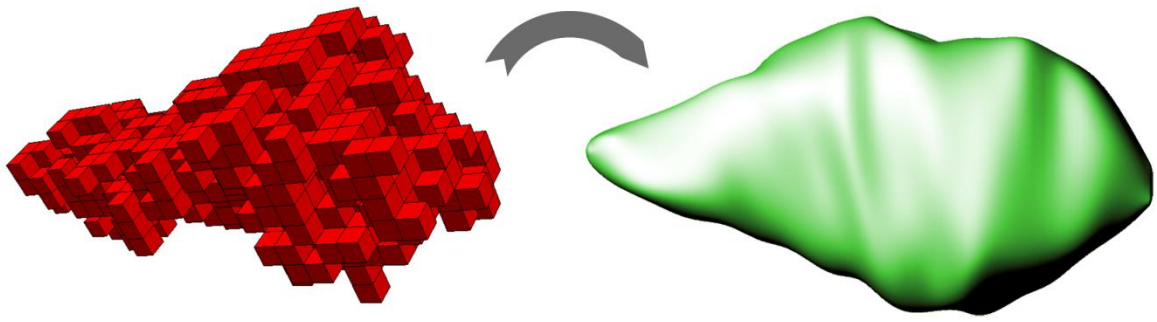

**Figure C.11:** Cell geometry smoothing.
The voxelized-cell body from the migration model (left) is smoothed (right) to perform the fluid-chemical simulation.

For the analysis a cubical domain of 60×60×60 µm is used, and the smoothed cell geometry is embedded in the central part (Figure C.12). Periodic conditions are established in lateral boundaries, and no-slip condition is considered at the cell surface. Speed-pressure inputs and porous material properties are taken from the microdevice simulation, choosing a zone of maximum fluid velocities to enhance the effects of the cell body. A tetrahedral mesh is used in the whole domain, with finer elements at the cell surface. As in the main microfluidic simulation, the steady-state solution is computed using the FEM software COMSOL.

The results show how both the speed magnitude and stream lines are slightly affected by the cell inclusion into the porous material (Figure C.13A). Changes in flow velocity are only noticeable within 1-2 µm from the cell surface, a negligible distance

compared with the dimensions of the whole collagen which are of the order of mm. Similarly, chemical (Figure C.13B) and pressure (Figure C.14) gradients are practically unaffected, maintaining a linear increasing fashion with x-direction. In sum, this confirms the assumption that the cell body can be neglected in the simulation of the whole microdevice. Nevertheless, the slight changes occurring at the cell surface due to its geometry could be, in reality, critical for the cell to choose a migration direction. Such detailed considerations are, for the moment, out of scope of the model presented in Chapter 5.

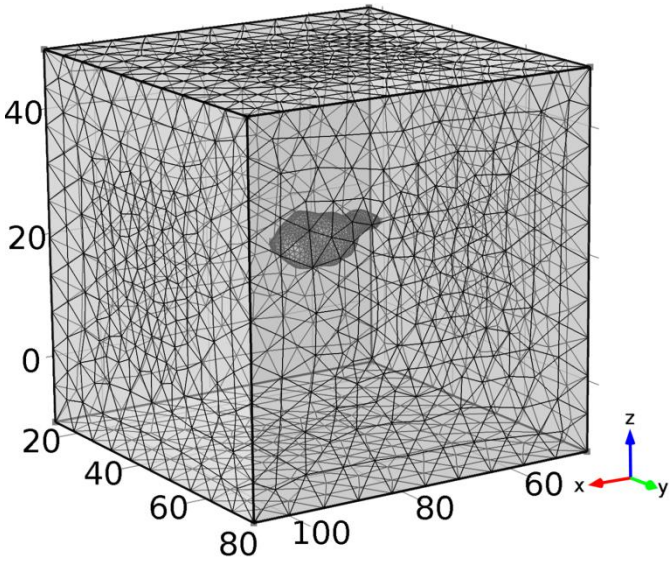


**Figure C.12:** Tetrahedral mesh used in the simulations.
The cell body is embedded in a cubical domain of 60×60×60 µm. Finer elements are used at the cell surface.

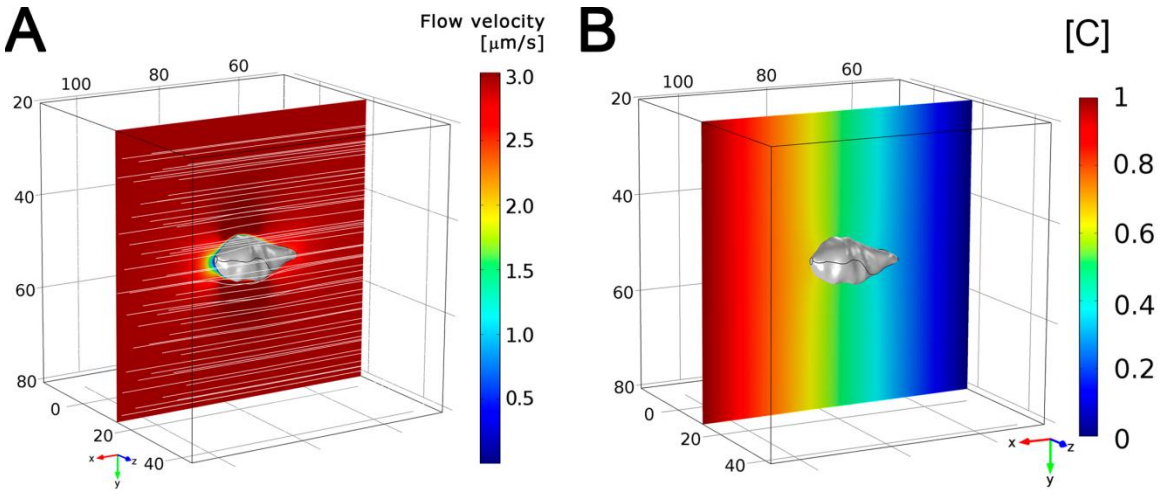


**Figure C.13:** Flow velocity and ECM chemical concentration.
A) Flow velocity field and stream lines (white) around the embedded cell body (gray). Speeds are shown in a middle cut plane. B) Normalized chemical gradient along the ECM.

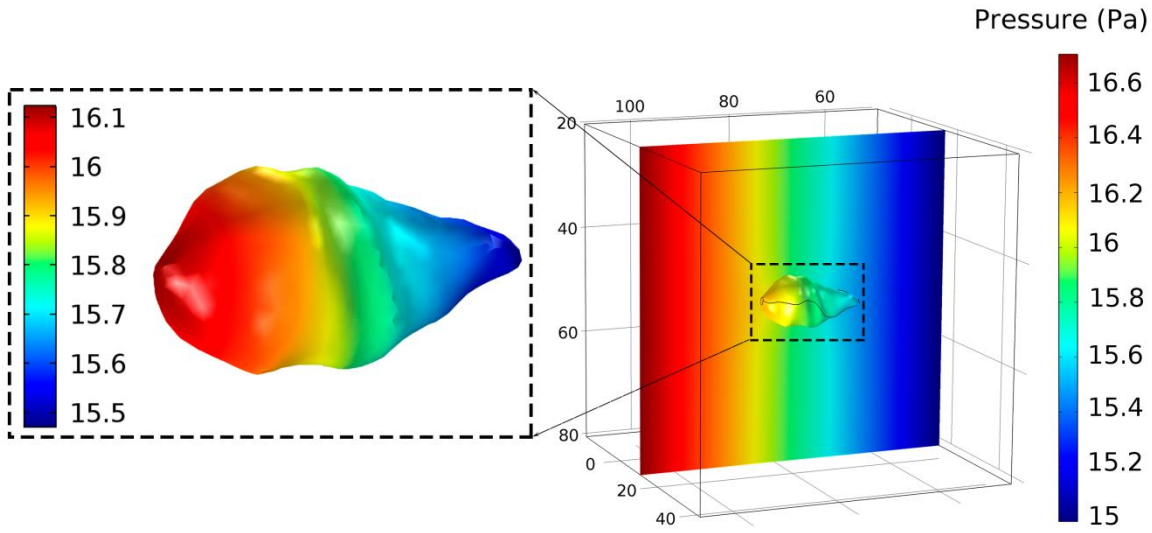


**Figure C.14:** Pressure gradient along the ECM and cell surface.
The pressure changes linearly along the porous ECM, slightly affected by the cell body inclusion. Detail of pressure along cell surface is magnified.

Additional simulations aer performed to check how the flow velocity affects the concentration of autologous chemokine gradients around the cell. The same geometry and boundary conditions of the previous analysis are used but adding a normalized concentration at the cell surface. The steady state is computed for the experimental value of flow speed (Figure C.15A) and multiplying such speed 10 (Figure C.15B) and 100 fold (Figure C.15C). Although these last values may be not physiologically relevant, the computation is still useful to check the consistency of the model. As might be expected, higher flow velocities drags the chemokine factor downstream. Cell receptors would detect higher concentrations in that direction and therefore its body would align and migrate following the fluid flow.

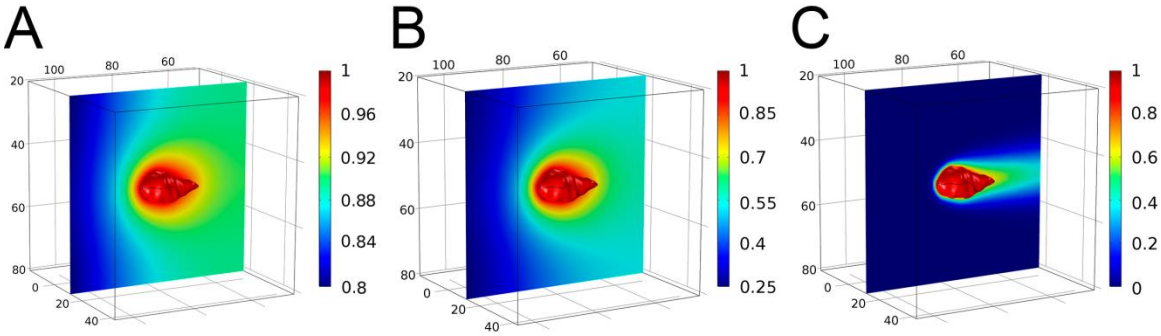


**Figure C.15:** Autologous chemokine concentration for different flow speeds.
The experimental value of flow speed A) is multiplied 10 fold B) and 100 fold C)..

# BIBLIOGRAPHY


AHMADI, A., LIVERPOOL, T. B. & MARCHETTI, M. C. 2005. Nematic and polar order in active filament solutions. *Phys Rev E Stat Nonlin Soft Matter Phys,* 72**,** 060901.

ALBERTS, B., JOHNSON, A., LEWIS, J., RAFF, M., ROBERTS, K. & WALTER, P. 2008. *Molecular Biology of the Cell*, Garland science.

ALBERTS, J. B. & ODELL, G. M. 2004. In silico reconstitution of Listeria propulsion exhibits nano-saltation. *PLoS Biol,* 2**,** e412.

ALEXANDROVA, A. Y., ARNOLD, K., SCHAUB, S., VASILIEV, J. M., MEISTER, J. J., BERSHADSKY, A. D. & VERKHOVSKY, A. B. 2008. Comparative dynamics of retrograde actin flow and focal adhesions: formation of nascent adhesions triggers transition from fast to slow flow. *PLoS One,* 3**,** e3234.

ANDERSON, T. W., VAUGHAN, A. N. & CRAMER, L. P. 2008. Retrograde flow and myosin II activity within the leading cell edge deliver F-actin to the lamella to seed the formation of graded polarity actomyosin II filament bundles in migrating fibroblasts. *Mol Biol Cell,* 19**,** 5006-18.

ARCIERO, J. C., MI, Q., BRANCA, M. F., HACKAM, D. J. & SWIGON, D. 2011. Continuum model of collective cell migration in wound healing and colony expansion. *Biophys J,* 100**,** 535-43.

ASTROM, J. A., KUMAR, P. B. S. & KARTTUNEN, M. 2009. Aster formation and rupture transition in semi-flexible fiber networks with mobile cross-linkers. *Soft Matter,* 5**,** 2869-2874.

ASTROM, J. A., KUMAR, P. B. S., VATTULAINEN, I. & KARTTUNEN, M. 2008. Strain hardening, avalanches, and strain softening in dense cross-linked actin networks. *Phys Rev,* 77**,** 051913.

ATILGAN, E., WIRTZ, D. & SUN, S. X. 2005. Morphology of the lamellipodium and organization of actin filaments at the leading edge of crawling cells. *Biophys J,* 89**,** 3589-602.

ATILGAN, E., WIRTZ, D. & SUN, S. X. 2006. Mechanics and dynamics of actin-driven thin membrane protrusions. *Biophys J,* 90**,** 65-76.

ATIYEH, B. S., GUNN, S. W. & HAYEK, S. N. 2005. State of the art in burn treatment. *World J Surg,* 29**,** 131-48.

BAKER, E. L., BONNECAZE, R. T. & ZAMAN, M. H. 2009. Extracellular Matrix Stiffness and Architecture Govern Intracellular Rheology in Cancer. *Biophys J,* 97**,** 1013-1021.

BELOUSSOV, L. V., LOUCHINSKAIA, N. N. & STEIN, A. A. 2000. Tension-dependent collective cell movements in the early gastrula ectoderm of Xenopus laevis embryos. *Dev Genes Evol,* 210**,** 92-104.

BERSHADSKY, A. D., BALABAN, N. Q. & GEIGER, B. 2003. Adhesion-dependent cell mechanosensitivity. *Annu Rev Cell Dev Biol,* 19**,** 677-695.

BESSER, A. & SCHWARZ, U. S. 2010. Hysteresis in the cell response to time-dependent substrate stiffness. *Biophys J,* 99**,** L10-2.

BISCHOFS, I. B. & SCHWARZ, U. S. 2003. Cell organization in soft media due to active mechanosensing. *Proc Natl Acad Sci U S A,* 100**,** 9274-9279.

BLAKNEY, A. K., SWARTZLANDER, M. D. & BRYANT, S. J. 2012. The effects of substrate stiffness on the in vitro activation of macrophages and in vivo host

response to poly(ethylene glycol)-based hydrogels. *J Biomed Mater Res A,* 100**,** 1375-86.

BORAU, C., KAMM, R. D. & GARCIA-AZNAR, J. M. 2011. Mechano-sensing and cell migration: a 3D model approach. *Phys Biol,* 8**,** 066008.

BORAU, C., KIM, T., BIDONE, T., GARCIA-AZNAR, J. M. & KAMM, R. D. 2012. Dynamic mechanisms of cell rigidity sensing: insights from a computational model of actomyosin networks. *PLoS One,* 7**,** e49174.

BORDELEAU, F., MYRAND LAPIERRE, M. E., SHENG, Y. & MARCEAU, N. 2012. Keratin 8/18 regulation of cell stiffness-extracellular matrix interplay through modulation of Rho-mediated actin cytoskeleton dynamics. *PLoS One,* 7**,** e38780.

BOTTINO, D., MOGILNER, A., ROBERTS, T., STEWART, M. & OSTER, G. 2002. How nematode sperm crawl. *J Cell Sci,* 115**,** 367-384.

BOYDEN, S. 1962. The chemotactic effect of mixtures of antibody and antigen on polymorphonuclear leucocytes. *J Exp Med,* 115**,** 453-66.

BURNETTE, D. T. B. D. T., MANLEY, S., SENGUPTA, P., SOUGRAT, R., DAVIDSON, M. W., KACHAR, B. & LIPPINCOTT-SCHWARTZ, J. 2011. A role for actin arcs in the leading-edge advance of migrating cells. *Nat Cell Biol,* 13**,** 371-U88.

BUXBOIM, A., IVANOVSKA, I. L. & DISCHER, D. E. 2010. Matrix elasticity, cytoskeletal forces and physics of the nucleus: how deeply do cells 'feel' outside and in? *J Cell Sci,* 123**,** 297-308.

CARLSSON, A. E. 2001. Growth of branched actin networks against obstacles. *Biophys J,* 81**,** 1907-23.

CARLSSON, A. E. 2010. Dendritic actin filament nucleation causes traveling waves and patches. *Phys Rev Lett,* 104**,** 228102.

CARLSSON, A. E. & SEPT, D. 2008. Mathematical modeling of cell migration. *Methods Cell Biol,* 84**,** 911-37.

CIRIT, M., KRAJCOVIC, M., CHOI, C. K., WELF, E. S., HORWITZ, A. F. & HAUGH, J. M. 2010. Stochastic Model of Integrin-Mediated Signaling and Adhesion Dynamics at the Leading Edges of Migrating Cells. *PLoS Comput Biol,* 6.

CRAIG, E. M., VAN GOOR, D., FORSCHER, P. & MOGILNER, A. 2012. Membrane tension, myosin force, and actin turnover maintain actin treadmill in the nerve growth cone. *Biophys J,* 102**,** 1503-13.

CROW, A., WEBSTER, K. D., HOHLFELD, E., NG, W. P., GEISSLER, P. & FLETCHER, D. A. 2012. Contractile equilibration of single cells to step changes in extracellular stiffness. *Biophys J,* 102**,** 443-51.

CUKIERMAN, E., PANKOV, R., STEVENS, D. R. & YAMADA, K. M. 2001. Taking cell-matrix adhesions to the third dimension. *Science,* 294**,** 1708-1712.

CUKIERMAN, E., PANKOV, R. & YAMADA, K. M. 2002. Cell interactions with three-dimensional matrices. *Curr Opin Cell Biol,* 14**,** 633-639.

CURTZE, S., DEMBO, M., MIRON, M. & JONES, D. B. 2004. Dynamic changes in traction forces with DC electric field in osteoblast-like cells. *J Cell Sci,* 117**,** 2721-9.

CHAN, C. E. & ODDE, D. J. 2008. Traction dynamics of filopodia on compliant substrates. *Science,* 322**,** 1687-91.

CHARRAS, G. & PALUCH, E. 2008. Blebs lead the way: how to migrate without lamellipodia. *Nat Rev Mol Cell Biol,* 9**,** 730-6.

CHEN, N., GLAZIER, J. A., IZAGUIRRE, J. A. & ALBER, M. S. 2007. A parallel implementation of the Cellular Potts Model for simulation of cell-based morphogenesis. *Comput Phys Commun,* 176**,** 670-681.

CHOPARD, B., OUARED, R., DEUTSCH, A., HATZIKIROU, H. & WOLF-GLADROW, D. 2010. Lattice-Gas Cellular Automaton Models for Biology: From Fluids to Cells. *Acta Biotheor,* 58**,** 329-340.

CHUNG, B. G., LEE, K. H., KHADEMHOSSEINI, A. & LEE, S. H. 2012. Microfluidic fabrication of microengineered hydrogels and their application in tissue engineering. *Lab Chip,* 12**,** 45-59.

CHUNG, S., SUDO, R., VICKERMAN, V., ZERVANTONAKIS, I. K. & KAMM, R. D. 2010. Microfluidic Platforms for Studies of Angiogenesis, Cell Migration, and Cell-Cell Interactions. *Ann Biomed Eng,* 38**,** 1164-1177.

DAMANIA, D., SUBRAMANIAN, H., TIWARI, A. K., STYPULA, Y., KUNTE, D., PRADHAN, P., ROY, H. K. & BACKMAN, V. 2010. Role of Cytoskeleton in Controlling the Disorder Strength of Cellular Nanoscale Architecture RID B-6689-2009. *Biophys J,* 99**,** 989-996.

DAWES, A. T., BARD ERMENTROUT, G., CYTRYNBAUM, E. N. & EDELSTEIN-KESHET, L. 2006. Actin filament branching and protrusion velocity in a simple 1D model of a motile cell. *J Theor Biol,* 242**,** 265-79.

DE, R., ZEMEL, A. & SAFRAN, S. A. 2007. Dynamics of cell orientation. *Nat Phys,* 3**,** 655-659.

DE, R., ZEMEL, A. & SAFRAN, S. A. 2008. Do cells sense stress or strain? Measurement of cellular orientation can provide a clue. *Biophys J,* 94**,** L29-L31.

DEMBO, M. & WANG, Y. L. 1999. Stresses at the cell-to-substrate interface during locomotion of fibroblasts. *Biophys J,* 76**,** 2307-2316.

DESHPANDE, V. S., MCMEEKING, R. M. & EVANS, A. G. 2006. A bio-chemo-mechanical model for cell contractility. *Proc Natl Acad Sci U S A,* 103**,** 14015-20.

DICKINSON, R. B. & PURICH, D. L. 2002. Clamped-filament elongation model for actin-based motors. *Biophys J,* 82**,** 605-17.

DISCHER, D. E., JANMEY, P. & WANG, Y. L. 2005. Tissue cells feel and respond to the stiffness of their substrate. *Science,* 310**,** 1139-1143.

DOKUKINA, I. V. & GRACHEVA, M. E. 2010. A Model of Fibroblast Motility on Substrates with Different Rigidities. *Biophys J,* 98**,** 2794-2803.

DOU, Y., ARLOCK, P. & ARNER, A. 2007. Blebbistatin specifically inhibits actin-myosin interaction in mouse cardiac muscle. *AM J Physiol-Cell Ph,* 293**,** C1148-C1153.

DOUBROVINSKI, K. & KRUSE, K. 2008. Cytoskeletal waves in the absence of molecular motors. *Epl,* 83.

EHRBAR, M., SALA, A., LIENEMANN, P., RANGA, A., MOSIEWICZ, K., BITTERMANN, A., RIZZI, S. C., WEBER, F. E. & LUTOLF, M. P. 2011. Elucidating the Role of Matrix Stiffness in 3D Cell Migration and Remodeling. *Biophys J,* 100**,** 284-293.

ELLIOTT, C. M., STINNER, B. & VENKATARAMAN, C. 2012. Modelling cell motility and chemotaxis with evolving surface finite elements. *J R Soc Interface,* 9**,** 3027-44.

ENGLER, A., BACAKOVA, L., NEWMAN, C., HATEGAN, A., GRIFFIN, M. & DISCHER, D. 2004a. Substrate compliance versus ligand density in cell on gel responses. *Biophys J,* 86**,** 617-628.

ENGLER, A. J., GRIFFIN, M. A., SEN, S., BONNETNANN, C. G., SWEENEY, H. L. & DISCHER, D. E. 2004b. Myotubes differentiate optimally on substrates with tissue-like stiffness: pathological implications for soft or stiff microenvironments. *J Cell Biol,* 166**,** 877-887.

ENGLER, A. J., SEN, S., SWEENEY, H. L. & DISCHER, D. E. 2006. Matrix elasticity directs stem cell lineage specification. *Cell,* 126**,** 677-689.

EVEN-RAM, S. & YAMADA, K. M. 2005. Cell migration in 3D matrix. *Curr Opin Cell Biol,* 17**,** 524-532.

FABER, M., ENCULESCU, M. & FALCKE, M. 2010. Filament capping and nucleation in actin-based motility. *Eur Phys J-Spec Top,* 191**,** 147-158.

FERRER, J. M., LEE, H., CHEN, J., PELZ, B., NAKAMURA, F., KAMM, R. D. & LANG, M. J. 2008. Measuring molecular rupture forces between single actin filaments and actin-binding proteins. *Proc Natl Acad Sci U S A,* 105**,** 9221-9226.

FLAHERTY, B., MCGARRY, J. P. & MCHUGH, P. E. 2007. Mathematical models of cell motility. *Cell Biochem Biophys,* 49**,** 14-28.

FOUCARD, L. & VERNEREY, F. J. 2012. A thermodynamical model for stress-fiber organization in contractile cells. *Appl Phys Lett,* 100**,** 13702-137024.

FOUCHARD, J., MITROSSILIS, D. & ASNACIOS, A. 2011. Acto-myosin based response to stiffness and rigidity sensing. *Cell Adh Migr,* 5**,** 16-9.

FRALEY, S. I., FENG, Y., KRISHNAMURTHY, R., KIM, D.-H., CELEDON, A., LONGMORE, G. D. & WIRTZ, D. 2010. A distinctive role for focal adhesion proteins in three-dimensional cell motility. *Nat Cell Biol,* 12**,** 598-604.

FRANCK, C., MASKARINEC, S. A., TIRRELL, D. A. & RAVICHANDRAN, G. 2011. Three-dimensional traction force microscopy: a new tool for quantifying cell-matrix interactions. *PLoS One,* 6**,** e17833.

FREYMAN, T. M., YANNAS, I. V., YOKOO, R. & GIBSON, L. J. 2002. Fibroblast contractile force is independent of the stiffness which resists the contraction. *Exp Cell Res,* 272**,** 153-162.

FRIEDL, P. & BROCKER, E. B. 2000. The biology of cell locomotion within three-dimensional extracellular matrix. *Cell Mol Life Sci,* 57**,** 41-64.

FRIEDL, P. & GILMOUR, D. 2009. Collective cell migration in morphogenesis, regeneration and cancer. *Nat Rev Mol Cell Biol,* 10**,** 445-57.

FRIEDL, P., HEGERFELDT, Y. & TUSCH, M. 2004. Collective cell migration in morphogenesis and cancer. *Int J Dev Biol,* 48**,** 441-9.

FRIEDL, P., SAHAI, E., WEISS, S. & YAMADA, K. M. 2012. New dimensions in cell migration. *Nat Rev Mol Cell Biol,* 13**,** 743-7.

GANZ, A., LAMBERT, M., SAEZ, A., SILBERZAN, P., BUGUIN, A., MEGE, R. M. & LADOUX, B. 2006. Traction forces exerted through N-cadherin contacts. *Biol Cell,* 98**,** 721-30.

GARDEL, M. L., NAKAMURA, F., HARTWIG, J. H., CROCKER, J. C., STOSSEL, T. P. & WEITZ, D. A. 2006. Prestressed F-actin networks cross-linked by hinged filamins replicate mechanical properties of cells. *Proc Natl Acad Sci U S A,* 103**,** 1762-7.

GERBAL, F., CHAIKIN, P., RABIN, Y. & PROST, J. 2000. An elastic analysis of Listeria monocytogenes propulsion. *Biophys J,* 79**,** 2259-75.

GHASSEMI, S., MEACCI, G., LIU, S., GONDARENKO, A. A., MATHUR, A., ROCA-CUSACHS, P., SHEETZ, M. P. & HONE, J. 2012. Cells test substrate rigidity by local contractions on submicrometer pillars. *Proc Natl Acad Sci U S A,* 109**,** 5328-33.

GHIBAUDO, M., SAEZ, A., TRICHET, L., XAYAPHOUMMINE, A., BROWAEYS, J., SILBERZAN, P., BUGUIN, A. & LADOUX, B. 2008. Traction forces and rigidity sensing regulate cell functions. *Soft Matter,* 4**,** 1836-1843.

GIANNONE, G., DUBIN-THALER, B. J., DOBEREINER, H. G., KIEFFER, N., BRESNICK, A. R. & SHEETZ, M. P. 2004. Periodic lamellipodial contractions correlate with rearward actin waves. *Cell,* 116**,** 431-43.

GIANNONE, G., DUBIN-THALER, B. J., ROSSIER, O., CAI, Y., CHAGA, O., JIANG, G., BEAVER, W., DOBEREINER, H. G., FREUND, Y., BORISY, G. & SHEETZ, M. P. 2007. Lamellipodial actin mechanically links myosin activity with adhesion-site formation. *Cell,* 128**,** 561-75.

GOV, N. S. & GOPINATHAN, A. 2006. Dynamics of membranes driven by actin polymerization. *Biophys J,* 90**,** 454-69.

GRACHEVA, M. E. & OTHMER, H. G. 2004. A continuum model of motility in ameboid cells. *Bull Math Biol,* 66**,** 167-93.

GROH, A. & WAGNER, M. 2011. Biased three-dimensional cell migration and collagen matrix modification. *Math Biosci,* 231**,** 105-119.

GUO, B. & GUILFORD, W. H. 2006. Mechanics of actomyosin bonds in different nucleotide states are tuned to muscle contraction. *Proc Natl Acad Sci U S A,* 103**,** 9844-9849.

HÄCKER, A. 2011. A mathematical model for mesenchymal and chemosensitive cell dynamics. *J Math Biol***,** 1-41.

HAKKINEN, K. M., HARUNAGA, J. S., DOYLE, A. D. & YAMADA, K. M. 2011. Direct Comparisons of the Morphology, Migration, Cell Adhesions, and Actin Cytoskeleton of Fibroblasts in Four Different Three-Dimensional Extracellular Matrices. *Tiss Eng Pt A,* 17**,** 713-724.

HARJANTO, D. & ZAMAN, M. H. 2010. Computational study of proteolysis-driven single cell migration in a three-dimensional matrix. *Ann Biomed Eng,* 38**,** 1815-25.

HARLEY, B. A. C., KIM, H. D., ZAMAN, M. H., YANNAS, I. V., LAUFFENBURGER, D. A. & GIBSON, L. J. 2008. Microarchitecture of three-dimensional scaffolds influences cell migration behavior via junction interactions. *Biophys J,* 95**,** 4013-4024.

HARUNAGA, J. S. & YAMADA, K. M. 2011. Cell-matrix adhesions in 3D. *Matrix Biol,* In Press, Corrected Proof.

HAYAKAWA, K., SATO, N. & OBINATA, T. 2001. Dynamic reorientation of cultured cells and stress fibers under mechanical stress from periodic stretching. *Exp Cell Res,* 268**,** 104-14.

HENG, Y. W. & KOH, C. G. 2010. Actin cytoskeleton dynamics and the cell division cycle RID A-2215-2011. *Int J Biochem,* 42**,** 1622-1633.

HILL, A. V. 1938. The heat of shortening and the dynamic constants of muscle. *P Roy Soc Lond B Bio,* 126**,** 136-195.

HOFMANN, M., GUSCHEL, M., BERND, A., BEREITER-HAHN, J., KAUFMANN, R., TANDI, C., WIIG, H. & KIPPENBERGER, S. 2006. Lowering of tumor interstitial fluid pressure reduces tumor cell proliferation in a xenograft tumor model. *Neoplasia,* 8**,** 89-95.

HU, K., JI, L., APPLEGATE, K. T., DANUSER, G. & WATERMAN-STORER, C. M. 2007. Differential transmission of actin motion within focal adhesions. *Science,* 315**,** 111-5.

HUXLEY, A. F. 1957. Muscle structure and theories of contraction. *Prog Biophys Biophys Chem,* 7**,** 255-318.

ILINA, O. & FRIEDL, P. 2009. Mechanisms of collective cell migration at a glance. *J Cell Sci,* 122**,** 3203-3208.

INGBER, D. E. 2010. From Cellular Mechanotransduction to Biologically Inspired Engineering. *Ann Biomed Eng,* 38**,** 1148-1161.

JANMEY, P. A., WINER, J. P., MURRAY, M. E. & WEN, Q. 2009. The Hard Life of Soft Cells. *Cell Motil Cytoskeleton,* 66**,** 597-605.

JOYCE, J. A. & POLLARD, J. W. 2009. Microenvironmental regulation of metastasis. *Nat Rev Cancer,* 9**,** 239-52.

KASZA, K. E., ROWAT, A. C., LIU, J. Y., ANGELINI, T. E., BRANGWYNNE, C. P., KOENDERINK, G. H. & WEITZ, D. A. 2007. The cell as a material. *Curr Opin Cell Biol,* 19**,** 101-107.

KATSUMI, A., NAOE, T., MATSUSHITA, T., KAIBUCHI, K. & SCHWARTZ, M. A. 2005. Integrin activation and matrix binding mediate cellular responses to mechanical stretch. *J Biol Chem,* 280**,** 16546-9.

KAVERINA, I., KRYLYSHKINA, O., BENINGO, K., ANDERSON, K., WANG, Y. L. & SMALL, J. V. 2002. Tensile stress stimulates microtubule outgrowth in living cells. *J Cell Sci,* 115**,** 2283-2291.

KIM, T., HWANG, W. & KAMM, R. D. 2009a. Computational Analysis of a Cross-linked Actin-like Network. *Exp Mech,* 49**,** 91-104.

KIM, T., HWANG, W. & KAMM, ROGER D. 2011. Dynamic Role of Cross-Linking Proteins in Actin Rheology. *Biophys J,* 101**,** 1597-1603.

KIM, T., HWANG, W., LEE, H. & KAMM, R. D. 2009b. Computational Analysis of Viscoelastic Properties of Crosslinked Actin Networks. *PLoS Comput Biol,* 5**,** e1000439.

KOBAYASHI, T. & SOKABE, M. 2010. Sensing substrate rigidity by mechanosensitive ion channels with stress fibers and focal adhesions. *Curr Opin Cell Biol,* 22**,** 669-76.

KOESTLER, S. A., AUINGER, S., VINZENZ, M., ROTTNER, K. & SMALL, J. V. 2008. Differentially oriented populations of actin filaments generated in lamellipodia collaborate in pushing and pausing at the cell front. *Nat Cell Biol,* 10**,** 306-13.

KOLLMANNSBERGER, P. & FABRY, B. 2011. Linear and Nonlinear Rheology of Living Cells. *Ann Rev Mater Res,* 41**,** 75-97.

KOVACS, M., TOTH, J., HETENYI, C., MALNASI-CSIZMADIA, A. & SELLERS, J. R. 2004. Mechanism of blebbistatin inhibition of myosin II. *J Biol Chem,* 279**,** 35557-35563.

KRANING-RUSH, C. M., CALIFANO, J. P. & REINHART-KING, C. A. 2012. Cellular traction stresses increase with increasing metastatic potential. *PLoS One,* 7**,** e32572.

KRUSE, K., JOANNY, J. F., JULICHER, F., PROST, J. & SEKIMOTO, K. 2005. Generic theory of active polar gels: a paradigm for cytoskeletal dynamics. *Eur Phys J E Soft Matter,* 16**,** 5-16.

KUNG, C. 2005. A possible unifying principle for mechanosensation. *Nature,* 436**,** 647-54.

KUUSELA, E. & ALT, W. 2009. Continuum model of cell adhesion and migration. *J Math Biol,* 58**,** 135-61.

LADOUX, B., ANON, E., LAMBERT, M., RABODZEY, A., HERSEN, P., BUGUIN, A., SILBERZAN, P. & MEGE, R.-M. 2010. Strength dependence of cadherin-mediated adhesions. *Biophys J,* 98**,** 534-42.

LAI, F. P., SZCZODRAK, M., BLOCK, J., FAIX, J., BREITSPRECHER, D., MANNHERZ, H. G., STRADAL, T. E., DUNN, G. A., SMALL, J. V. &

ROTTNER, K. 2008. Arp2/3 complex interactions and actin network turnover in lamellipodia. *EMBO J,* 27**,** 982-92.

LAMMERMANN, T. & SIXT, M. 2009. Mechanical modes of 'amoeboid' cell migration. *Curr Opin Cell Biol,* 21**,** 636-44.

LAUFFENBURGER, D. A. & HORWITZ, A. F. 1996. Cell migration: A physically integrated molecular process. *Cell,* 84**,** 359-369.

LEGANT, W. R., CHOI, C. K., MILLER, J. S., SHAO, L., GAO, L., BETZIG, E. & CHEN, C. S. 2013. Multidimensional traction force microscopy reveals out-of-plane rotational moments about focal adhesions. *Proc Natl Acad Sci U S A,* 110**,** 881-6.

LI, S., HUANG, N. F. & HSU, S. 2005. Mechanotransduction in endothelial cell migration. *J Cell Biochem,* 96**,** 1110-26.

LIM, C. T., ZHOU, E. H. & QUEK, S. T. 2006. Mechanical models for living cells - A review. *J Biomech,* 39**,** 195-216.

LINDER, S. 2007. The matrix corroded: podosomes and invadopodia in extracellular matrix degradation. *Trends Cell Biol,* 17**,** 107-17.

LO, C. M., WANG, H. B., DEMBO, M. & WANG, Y. L. 2000. Cell movement is guided by the rigidity of the substrate. *Biophys J,* 79**,** 144-152.

MANOUSSAKI, D. 2003. A mechanochemical model of angiogenesis and vasculogenesis. *Esaim-Math Model Num,* 37**,** 581-599.

MARCQ, P., YOSHINAGA, N. & PROST, J. 2011. Rigidity sensing explained by active matter theory. *Biophys J,* 101**,** L33-5.

MARTINAC, B. 2004. Mechanosensitive ion channels: molecules of mechanotransduction. *J Cell Sci,* 117**,** 2449-60.

MASKARINEC, S. A., FRANCK, C., TIRRELL, D. A. & RAVICHANDRAN, G. 2009. Quantifying cellular traction forces in three dimensions. *Proc Natl Acad Sci U S A,* 106**,** 22108-22113.

MCGARRY, J. P., FU, J., YANG, M. T., CHEN, C. S., MCMEEKING, R. M., EVANS, A. G. & DESHPANDE, V. S. 2009. Simulation of the contractile response of cells on an array of micro-posts. *Philos T R Soc A,* 367**,** 3477-3497.

MCMAHON, T. 1985. Muscles, Reflexes, and Locomotion. *Percept Motor Skill,* 60**,** 679-679.

MEDEIROS, N. A., BURNETTE, D. T. & FORSCHER, P. 2006. Myosin II functions in actin-bundle turnover in neuronal growth cones. *Nat Cell Biol,* 8**,** 215-26.

MERKS, R. M. H. & KOOLWIJK, P. 2009. Modeling Morphogenesis in silico and in vitro: Towards Quantitative, Predictive, Cell-based Modeling. *Math Model Nat Pheno,* 4**,** 149-171.

MITROSSILIS, D., FOUCHARD, J., GUIROY, A., DESPRAT, N., RODRIGUEZ, N., FABRY, B. & ASNACIOS, A. 2009. Single-cell response to stiffness exhibits muscle-like behavior. *Proc Natl Acad Sci U S A,* 106**,** 18243-18248.

MITROSSILIS, D., FOUCHARD, J., PEREIRA, D., POSTIC, F., RICHERT, A., SAINT-JEAN, M. & ASNACIOS, A. 2010. Real-time single-cell response to stiffness. *Proc Natl Acad Sci U S A,* 107**,** 16518-16523.

MOGILNER, A. 2009. Mathematics of cell motility: have we got its number? *J Math Biol,* 58**,** 105-34.

MOGILNER, A. & EDELSTEIN-KESHET, L. 2002. Regulation of actin dynamics in rapidly moving cells: a quantitative analysis. *Biophys J,* 83**,** 1237-58.

MOGILNER, A. & OSTER, G. 2003. Polymer motors: pushing out the front and pulling up the back. *Curr Biol,* 13**,** R721-33.

MOREO, P., GARCIA-AZNAR, J. M. & DOBLARE, M. 2008. Modeling mechanosensing and its effect on the migration and proliferation of adherent cells. *Acta Biomater,* 4**,** 613-621.

MUNEVAR, S., WANG, Y. L. & DEMBO, M. 2004. Regulation of mechanical interactions between fibroblasts and the substratum by stretch-activated Ca2+ entry. *J Cell Sci,* 117**,** 85-92.

NOVAK, I. L., SLEPCHENKO, B. M., MOGILNER, A. & LOEW, L. M. 2004. Cooperativity between cell contractility and adhesion. *Phys Rev Lett,* 93.

OUAKNIN, G. Y. & BAR-YOSEPH, P. Z. 2009. Stochastic collective movement of cells and fingering morphology: no maverick cells. *Biophys J,* 97**,** 1811-21.

PACHECO, P. S. 1997. *Parallel programming with MPI*, Morgan Kaufmann Publishers, Inc. San Francisco California.

PALECEK, S. P., LOFTUS, J. C., GINSBERG, M. H., LAUFFENBURGER, D. A. & HORWITZ, A. F. 1997. Integrin-ligand binding properties govern cell migration speed through cell-substratum adhesiveness. *Nature,* 385**,** 537-40.

PALSSON, E. 2001. A three-dimensional model of cell movement in multicellular systems. *Future Gener Comp Sy,* 17**,** 835-852.

PANKOV, R., ENDO, Y., EVEN-RAM, S., ARAKI, M., CLARK, K., CUKIERMAN, E., MATSUMOTO, K. & YAMADA, K. M. 2005. A Rac switch regulates random versus directionally persistent cell migration. *J Cell Biol,* 170**,** 793-802.

PARKHURST, M. R. & SALTZMAN, W. M. 1992. Quantification of human neutrophil motility in three-dimensional collagen gels. Effect of collagen concentration. *Biophys J,* 61**,** 306-15.

PELHAM, R. J. & WANG, Y. L. 1997. Cell locomotion and focal adhesions are regulated by substrate flexibility. *Proc Natl Acad Sci U S A,* 94**,** 13661-13665.

PESKIN, C. S., ODELL, G. M. & OSTER, G. F. 1993. Cellular motions and thermal fluctuations: the Brownian ratchet. *Biophys J,* 65**,** 316-24.

PETRIE, R. J., DOYLE, A. D. & YAMADA, K. M. 2009. Random versus directionally persistent cell migration. *Nat Rev Mol Cell Biol,* 10**,** 538-549.

PETRIE, R. J., GAVARA, N., CHADWICK, R. S. & YAMADA, K. M. 2012. Nonpolarized signaling reveals two distinct modes of 3D cell migration. *J Cell Biol,* 197**,** 439-55.

PETTET, G. J., PLEASE, C. P., TINDALL, M. J. & MCELWAIN, D. L. 2001. The migration of cells in multicell tumor spheroids. *Bull Math Biol,* 63**,** 231-57.

PEYTON, S. R., KALCIOGLU, Z. I., COHEN, J. C., RUNKLE, A. P., VAN VLIET, K. J., LAUFFENBURGER, D. A. & GRIFFITH, L. G. 2011. Marrow-Derived stem cell motility in 3D synthetic scaffold is governed by geometry along with adhesivity and stiffness. *Biotechnol Bioeng,* 108**,** 1181-1193.

PEYTON, S. R. & PUTNAM, A. J. 2005. Extracellular matrix rigidity governs smooth muscle cell motility in a biphasic fashion. *J Cell Physiol,* 204**,** 198-209.

POLACHECK, W. J., CHAREST, J. L. & KAMM, R. D. 2011. Interstitial flow influences direction of tumor cell migration through competing mechanisms. *Proc Natl Acad Sci U S A,* 108**,** 11115-11120.

POLACHECK, W. J., ZERVANTONAKIS, I. K. & KAMM, R. D. 2012. Tumor cell migration in complex microenvironments. *Cell Mol Life Sci*.

POLLARD, T. D. & BORISY, G. G. 2003. Cellular motility driven by assembly and disassembly of actin filaments. *Cell,* 112**,** 453-65.

PONTI, A., MACHACEK, M., GUPTON, S. L., WATERMAN-STORER, C. M. & DANUSER, G. 2004. Two distinct actin networks drive the protrusion of migrating cells. *Science,* 305**,** 1782-6.

RAFELSKI, S. M. & THERIOT, J. A. 2004. Crawling toward a unified model of cell mobility: spatial and temporal regulation of actin dynamics. *Annu Rev Biochem,* 73**,** 209-39.

RANGARAJAN, R. & ZAMAN, M. H. 2008. Modeling cell migration in 3D: Status and challenges. *Cell Adh Migr,* 2**,** 106-9.

RAPAPORT, D. C. 2002. *The Art of Molecular Dynamics Simulation,* Cambridge University Press.

RAPPEL, W. J., THOMAS, P. J., LEVINE, H. & LOOMIS, W. F. 2002. Establishing direction during chemotaxis in eukaryotic cells. *Biophys J,* 83**,** 1361-7.

RASSIER, D. E., MACINTOSH, B. R. & HERZOG, W. 1999. Length dependence of active force production in skeletal muscle. *J Appl Physiol,* 86**,** 1445-1457.

REN, Y., EFFLER, J. C., NORSTROM, M., LUO, T., FIRTEL, R. A., IGLESIAS, P. A., ROCK, R. S. & ROBINSON, D. N. 2009. Mechanosensing through cooperative interactions between myosin II and the actin crosslinker cortexillin I. *Curr Biol,* 19**,** 1421-8.

RICHERT, L., ENGLER, A. J., DISCHER, D. E. & PICART, C. 2004. Elasticity of native and cross-linked polyelectrolyte multilayer films. *Biomacromolecules,* 5**,** 1908-16.

RIDLEY, A. J., SCHWARTZ, M. A., BURRIDGE, K., FIRTEL, R. A., GINSBERG, M. H., BORISY, G., PARSONS, J. T. & HORWITZ, A. R. 2003. Cell migration: integrating signals from front to back. *Science,* 302**,** 1704-9.

RIVELINE, D., ZAMIR, E., BALABAN, N. Q., SCHWARZ, U. S., ISHIZAKI, T., NARUMIYA, S., KAM, Z., GEIGER, B. & BERSHADSKY, A. D. 2001. Focal contacts as mechanosensors: Externally applied local mechanical force induces growth of focal contacts by an mDia1-dependent and ROCK-independent mechanism. *J Cell Biol,* 153**,** 1175-1185.

RONAN, W., DESHPANDE, V. S., MCMEEKING, R. M. & MCGARRY, J. P. 2012. Numerical investigation of the active role of the actin cytoskeleton in the compression resistance of cells. *J Mech Behav Biomed Mater,* 14C**,** 143-157.

ROUSSOS, E. T., CONDEELIS, J. S. & PATSIALOU, A. 2011. Chemotaxis in cancer. *Nat Rev Cancer,* 11**,** 573-587.

RUEGG, C., VEIGEL, C., MOLLOY, J. E., SCHMITZ, S., SPARROW, J. C. & FINK, R. H. A. 2002. Molecular motors: Force and movement generated by single myosin II molecules. *News Physiol Sci,* 17**,** 213-218.

RYAN, G. L., WATANABE, N. & VAVYLONIS, D. 2012. A review of models of fluctuating protrusion and retraction patterns at the leading edge of motile cells. *Cytoskeleton (Hoboken),* 69**,** 195-206.

SABEH, F., SHIMIZU-HIROTA, R. & WEISS, S. J. 2009. Protease-dependent versus -independent cancer cell invasion programs: three-dimensional amoeboid movement revisited. *J Cell Biol,* 185**,** 11-9.

SAEZ, A., BUGUIN, A., SILBERZAN, P. & LADOUX, B. 2005. Is the mechanical activity of epithelial cells controlled by deformations or forces? *Biophys J,* 89**,** L52-L54.

SAEZ, A., GHIBAUDO, M., BUGUIN, A., SILBERZAN, P. & LADOUX, B. 2007. Rigidity-driven growth and migration of epithelial cells on microstructured anisotropic substrates. *Proc Natl Acad Sci U S A,* 104**,** 8281-8286.

SANZ-HERRERA, J. A., MOREO, P., GARCIA-AZNAR, J. M. & DOBLARE, M. 2009. On the effect of substrate curvature on cell mechanics. *Biomaterials,* 30**,** 6674-86.

SCHAFER, A. & RADMACHER, M. 2005. Influence of myosin II activity on stiffness of fibroblast cells. *Acta Biomater,* 1**,** 273-280.

SCHLUTER, D. K., RAMIS-CONDE, I. & CHAPLAIN, M. A. 2012. Computational modeling of single-cell migration: the leading role of extracellular matrix fibers. *Biophys J,* 103**,** 1141-51.

SCHMIDT, C. E., HORWITZ, A. F., LAUFFENBURGER, D. A. & SHEETZ, M. P. 1993. Integrin Cytoskeletal Interactions In Migrating Fibroblasts Are Dynamic, Asymmetric, and Regulated. *J Cell Biol,* 123**,** 977-991.

SCHWARZ, U. S. & BISCHOFS, I. B. 2005. Physical determinants of cell organization in soft media. *Med Eng Phys,* 27**,** 763-772.

SCHWARZ, U. S., ERDMANN, T. & BISCHOFS, I. B. 2006. Focal adhesions as mechanosensors: The two-spring model. *Biosystems,* 83**,** 225-232.

SEN, S., ENGLER, A. J. & DISCHER, D. E. 2009. Matrix Strains Induced by Cells: Computing How Far Cells Can Feel. *Cell Mol Bioeng,* 2**,** 39-48.

SHEMESH, T., BERSHADSKY, A. D. & KOZLOV, M. M. 2012. Physical model for self-organization of actin cytoskeleton and adhesion complexes at the cell front. *Biophys J,* 102**,** 1746-56.

SHEMESH, T., GEIGER, B., BERSHADSKY, A. D. & KOZLOV, M. M. 2005. Focal adhesions as mechanosensors: a physical mechanism. *Proc Natl Acad Sci U S A,* 102**,** 12383-8.

SHEMESH, T., VERKHOVSKY, A. B., SVITKINA, T. M., BERSHADSKY, A. D. & KOZLOV, M. M. 2009. Role of focal adhesions and mechanical stresses in the formation and progression of the lamellipodium-lamellum interface [corrected]. *Biophys J,* 97**,** 1254-64.

SHIELDS, J. D., FLEURY, M. E., YONG, C., TOMEI, A. A., RANDOLPH, G. J. & SWARTZ, M. A. 2007. Autologous chemotaxis as a mechanism of tumor cell homing to lymphatics via interstitial flow and autocrine CCR7 signaling. *Cancer Cell,* 11**,** 526-38.

SILVER, F. H. & SIPERKO, L. M. 2003. Mechanosensing and mechanochemical transduction: how is mechanical energy sensed and converted into chemical energy in an extracellular matrix? *Crit Rev Biomed Eng,* 31**,** 255-331.

SIMPSON, K. J., SELFORS, L. M., BUI, J., REYNOLDS, A., LEAKE, D., KHVOROVA, A. & BRUGGE, J. S. 2008. Identification of genes that regulate epithelial cell migration using an siRNA screening approach. *Nat Cell Biol,* 10**,** 1027-1038.

SIMPSON, M. J., TOWNE, C., MCELWAIN, D. L. S. & UPTON, Z. 2010. Migration of breast cancer cells: Understanding the roles of volume exclusion and cell-to-cell adhesion. *Phys Rev E,* 82**,** 041901.

SOARES E SILVA, M., DEPKEN, M., STUHRMANN, B., KORSTEN, M., MACKINTOSH, F. C. & KOENDERINK, G. H. 2011. Active multistage coarsening of actin networks driven by myosin motors. *Proc Natl Acad Sci U S A,* 108**,** 9408-9413.

SOON, L., MOUNEIMNE, G., SEGALL, J., WYCKOFF, J. & CONDEELIS, J. 2005. Description and characterization of a chamber for viewing and quantifying cancer cell chemotaxis. *Cell Motil Cytoskeleton,* 62**,** 27-34.

STRAIGHT, A. F., CHEUNG, A., LIMOUZE, J., CHEN, I., WESTWOOD, N. J., SELLERS, J. R. & MITCHISON, T. J. 2003. Dissecting temporal and spatial control of cytokinesis with a myosin II Inhibitor. *Science,* 299**,** 1743-7.

SVITKINA, T. 2007. Electron microscopic analysis of the leading edge in migrating cells. *Methods Cell Biol,* 79**,** 295-319.

TABER, L. A., SHI, Y., YANG, L. & BAYLY, P. V. 2011. A Poroelastic Model for Cell Crawling Including Mechanical Coupling between Cytoskeletal Contraction and Actin Polymerization. *J Mech Mater Struct,* 6**,** 569-589.

TANIA, N., PROSK, E., CONDEELIS, J. & EDELSTEIN-KESHET, L. 2011. A Temporal Model of Cofilin Regulation and the Early Peak of Actin Barbed Ends in Invasive Tumor Cells. *Biophys J,* 100**,** 1883-1892.

TEE, S. Y., FU, J., CHEN, C. S. & JANMEY, P. A. 2011. Cell shape and substrate rigidity both regulate cell stiffness. *Biophys J,* 100**,** L25-7.

THIEVESSEN, I., BERLEMON, S., PLEVOCK, K. M., PLOTNIKOV, S. V., THOMPSON, P. M., ZEMLJIC-HARPF, A., ROSS, R. S., DAVINDSON, M. W., DANUSER, G., CAMPBELL, S. L. & WATERMAN-STORER, C. M. 2013. Vinculin-actin interation mediates engagement of actin retrograde flow to focal adhesions, but is dispensable for actin-dependent focal adhesion maturation. *Biophys J,* (submitted).

TREPAT, X. & FREDBERG, J. J. 2011. Plithotaxis and emergent dynamics in collective cellular migration. *Trends Cell Biol,* 21**,** 638-46.

TRICHET, L., LE DIGABEL, J., HAWKINS, R. J., VEDULA, S. R., GUPTA, M., RIBRAULT, C., HERSEN, P., VOITURIEZ, R. & LADOUX, B. 2012. Evidence of a large-scale mechanosensing mechanism for cellular adaptation to substrate stiffness. *Proc Natl Acad Sci U S A,* 109**,** 6933-8.

UEMURA, S., HIGUCHI, H., OLIVARES, A. O., DE LA CRUZ, E. M. & ISHIWATA, S. I. 2004. Mechanochemical coupling of two substeps in a single myosin V motor. *Nat Struct Mol Biol,* 11**,** 877-883.

UJIHARA, Y., NAKAMURA, M., MIYAZAKI, H. & WADA, S. 2012. Contribution of actin filaments to the global compressive properties of fibroblasts. *J Mech Behav Biomed Mater,* 14C**,** 192-198.

URBAN, E., JACOB, S., NEMETHOVA, M., RESCH, G. P. & SMALL, J. V. 2010. Electron tomography reveals unbranched networks of actin filaments in lamellipodia. *Nat Cell Biol,* 12**,** 429-35.

VERNEREY, F. J. & FARSAD, M. 2011. A constrained mixture approach to mechano-sensing and force generation in contractile cells. *J Mech Behav Biomed Mater,* 4**,** 1683-99.

VICKERMAN, V., BLUNDO, J., CHUNG, S. & KAMM, R. D. 2008. Design, fabrication and implementation of a novel multi-parameter control microfluidic platform for three-dimensional cell culture and real-time imaging. *Lab Chip,* 8**,** 1468-1477.

VON PHILIPSBORN, A. C., LANG, S., LOESCHINGER, J., BERNARD, A., DAVID, C., LEHNERT, D., BONHOEFFER, F. & BASTMEYER, M. 2006. Growth cone navigation in substrate-bound ephrin gradients. *Development,* 133**,** 2487-95.

WALCOTT, S. & SUN, S. X. 2010. A mechanical model of actin stress fiber formation and substrate elasticity sensing in adherent cells. *Proc Natl Acad Sci U S A,* 107**,** 7757-7762.

WANG, J. H., GOLDSCHMIDT-CLERMONT, P. & YIN, F. C. 2000. Contractility affects stress fiber remodeling and reorientation of endothelial cells subjected to cyclic mechanical stretching. *Ann Biomed Eng,* 28**,** 1165-71.

WANG, N., NARUSE, K., STAMENOVIC, D., FREDBERG, J. J., MIJAILOVICH, S. M., TORIC-NORRELYKKE, I. M., POLTE, T., MANNIX, R. & INGBER, D. E. 2001. Mechanical behavior in living cells consistent with the tensegrity model RID B-6966-2008. *Proc Natl Acad Sci U S A,* 98**,** 7765-7770.

WANG, S. & WOLYNES, P. G. 2012. Active contractility in actomyosin networks. *Proc Natl Acad Sci U S A,* 109**,** 6446-51.

WANG, Y. & MCNIVEN, M. A. 2012. Invasive matrix degradation at focal adhesions occurs via protease recruitment by a FAK-p130Cas complex. *J Cell Biol,* 196**,** 375-385.

WATANABE, N. & MITCHISON, T. J. 2002. Single-molecule speckle analysis of actin filament turnover in lamellipodia. *Science,* 295**,** 1083-6.

WEBSTER, K. D., CROW, A. & FLETCHER, D. A. 2011. An AFM-Based Stiffness Clamp for Dynamic Control of Rigidity. *PLoS One,* 6**,** e17807.

WOLF, K., MAZO, I., LEUNG, H., ENGELKE, K., VON ANDRIAN, U. H., DERYUGINA, E. I., STRONGIN, A. Y., BROCKER, E. B. & FRIEDL, P. 2003. Compensation mechanism in tumor cell migration: mesenchymal-amoeboid transition after blocking of pericellular proteolysis. *J Cell Biol,* 160**,** 267-77.

WOLGEMUTH, C. W. 2005. Lamellipodial contractions during crawling and spreading. *Biophys J,* 89**,** 1643-9.

WONG, H. C. & TANG, W. C. 2011. Finite element analysis of the effects of focal adhesion mechanical properties and substrate stiffness on cell migration. *Journal of Biomech,* 44**,** 1046-50.

XU, K., BABCOCK, H. P. & ZHUANG, X. 2012. Dual-objective STORM reveals three-dimensional filament organization in the actin cytoskeleton. *Nat Methods,* 9**,** 185-8.

YAMAOKA, H., MATSUSHITA, S., SHIMADA, Y. & ADACHI, T. 2012. Multiscale modeling and mechanics of filamentous actin cytoskeleton. *Biomech Model Mechanobiol,* 11**,** 291-302.

YANG, T. Y. & ZAMAN, M. H. 2007. Free energy landscape of receptor-mediated cell adhesion. *J Chem Phys,* 126**,** 045103.

YANG, T. Y. & ZAMAN, M. H. 2010. Estimation of Cellular Adhesion Forces Using Mean Field Theory. *Cell Mol Bioeng,* 3**,** 190-194.

YEUNG, T., GEORGES, P. C., FLANAGAN, L. A., MARG, B., ORTIZ, M., FUNAKI, M., ZAHIR, N., MING, W., WEAVER, V. & JANMEY, P. A. 2005. Effects of substrate stiffness on cell morphology, cytoskeletal structure, and adhesion. *Cell Motil Cytoskeleton,* 60**,** 24-34.

YOSHIGI, M., HOFFMAN, L. M., JENSEN, C. C., YOST, H. J. & BECKERLE, M. C. 2005. Mechanical force mobilizes zyxin from focal adhesions to actin filaments and regulates cytoskeletal reinforcement. *J Cell Biol,* 171**,** 209-15.

ZAMAN, M. H. 2007. A multiscale probabilisitic framework to model early steps in tumor metastasis. *Mol Cell Biomech,* 4**,** 133-41.

ZAMAN, M. H., KAMM, R. D., MATSUDAIRA, P. & LAUFFENBURGER, D. A. 2005. Computational model for cell migration in three-dimensional matrices. *Biophys J,* 89**,** 1389-1397.

ZAMAN, M. H., MATSUDAIRA, P. & LAUFFENBURGER, D. A. 2007. Understanding effects of matrix protease and matrix organization on directional persistence and translational speed in three-dimensional cell migration. *Ann Biomed Eng,* 35**,** 91-100.

ZAMAN, M. H., TRAPANI, L. M., SIEMESKI, A., MACKELLAR, D., GONG, H., KAMM, R. D., WELLS, A., LAUFFENBURGER, D. A. & MATSUDAIRA, P. 2006. Migration of tumor cells in 3D matrices is governed by matrix stiffness along with cell-matrix adhesion and proteolysis *Proc Natl Acad Sci U S A,* 103**,** 13897-13897.

ZEMEL, A., DE, R. & SAFRAN, S. A. 2011. Mechanical consequences of cellular force generation. *Curr Opin Solid St M,* 15**,** 169-176.

ZEMEL, A., REHFELDT, F., BROWN, A. E. X., DISCHER, D. E. & SAFRAN, S. A. 2010a. Cell shape, spreading symmetry, and the polarization of stress-fibers in cells. *J Phys-Condens Mat,* 22**,** 194110.

ZEMEL, A., REHFELDT, F., BROWN, A. E. X., DISCHER, D. E. & SAFRAN, S. A. 2010b. Optimal matrix rigidity for stress-fibre polarization in stem cells. *Nat Phys,* 6**,** 468-473.

ZHAO, M., PU, J., FORRESTER, J. V. & MCCAIG, C. D. 2002. Membrane lipids, EGF receptors, and intracellular signals colocalize and are polarized in epithelial cells moving directionally in a physiological electric field. *Faseb J,* 16**,** 857-9.

ZHELEV, D. V., ALTERAIFI, A. M. & CHODNIEWICZ, D. 2004. Controlled pseudopod extension of human neutrophils stimulated with different chemoattractants. *Biophys J,* 87**,** 688-95.

ZHU, J. & CARLSSON, A. E. 2006. Growth of attached actin filaments. *Eur Phys J E Soft Matter,* 21**,** 209-222.